

GUSTAVO RODOVALHO BORIOLLO

**Light steel framing façades: mechanical behavior of cementitious boards and
numerical structural modeling for high building applications**

São Paulo

2021

GUSTAVO RODOVALHO BORIOLO

Light steel framing façades: mechanical behavior of cementitious boards and
numerical structural modeling for high building applications

Revised version

(The original version is available for consultation at the Escola Politécnica da
Universidade de São Paulo)

Thesis submitted to the *Escola Politécnica
da Universidade de São Paulo* to obtain the
Doctor of Science degree

Field of studies: Structural Engineering

Advisor: Prof. Dr. Túlio N. Bittencourt

São Paulo

2021

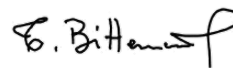
I authorize the reproduction and total or partial dissemination of this work by any conventional or electronic means for the purposes of study and research, as long as the source is cited.

This copy was revised and amended in relation to the original version, under the sole responsibility of the author and with the consent of his advisor.

São Paulo, May 21st, 2021.



Author



Advisor

Catálogo-na-publicação

Boriolo, Gustavo Rodvalho

Light steel framing façades: mechanical behavior of cementitious boards and numerical structural modeling for high building applications / G. R. Boriolo -- versão corr. -- São Paulo, 2021.

202 p.

Tese (Doutorado) - Escola Politécnica da Universidade de São Paulo. Departamento de Engenharia de Estruturas e Geotécnica.

1.light steel frame 2.lightweight facades 3.fiber cement 4.cracking modeling 5.numerical modeling I.Universidade de São Paulo. Escola Politécnica. Departamento de Engenharia de Estruturas e Geotécnica II.t.

GUSTAVO RODOVALHO BORIOLO

Light steel framing façades: mechanical behavior of cementitious boards and
numerical structural modeling for high building applications

Thesis submitted to the *Escola Politécnica
da Universidade de São Paulo* to obtain the
Doctor of Science degree

São Paulo

2021

BORIOLO, G. R. **Light steel framing façades: mechanical behavior of cementitious boards and numerical structural modeling for high building applications.** 2021 (Revised version). Tese (Doutorado) – Escola Politécnica, Universidade de São Paulo, São Paulo, 2021. 202 p.



Janus

Universidade de São Paulo

ATA DE DEFESA

Aluno: 3144 - 6852781 - 1 / Página 1 de 1

Ata de defesa de Tese do(a) Senhor(a) Gustavo Rodovalho Boriolo no Programa: Engenharia Civil, do(a) Escola Politécnica da Universidade de São Paulo.

Aos 23 dias do mês de março de 2021, no(a) realizou-se a Defesa da Tese do(a) Senhor(a) Gustavo Rodovalho Boriolo, apresentada para a obtenção do título de Doutor intitulada:

"Fachadas estruturadas em aço leve: comportamento mecânico de placas cimentícias e modelagem numérica estrutural para edifícios de grande altura"

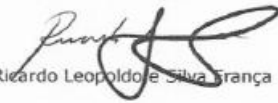
Após declarada aberta a sessão, o(a) Sr(a) Presidente passa a palavra ao candidato para exposição e a seguir aos examinadores para as devidas arguições que se desenvolvem nos termos regimentais. Em seguida, a Comissão Julgadora proclama o resultado:

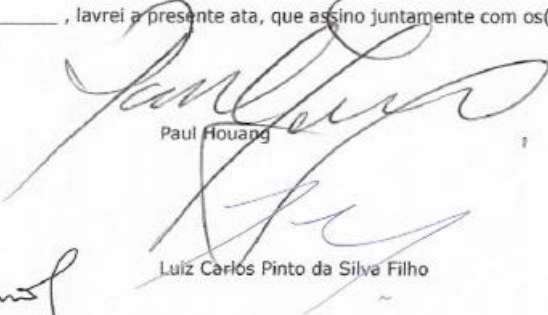
Nome dos Participantes da Banca	Função	Sigla da CPG	Resultado
Túlio Nogueira Bittencourt	Presidente	EP - USP	Aprovado
Ricardo Leopoldo e Silva França	Titular	EP - USP	Aprovado
Paul Houang	Titular	Externo	Aprovado
Vanderley Moacyr John	Titular	EP - USP	Aprovado
Luiz Carlos Pinto da Silva Filho	Titular	UFRGS - Externo	Aprovado

Resultado Final: Aprovado

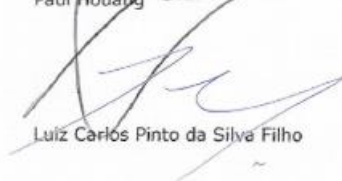
Parecer da Comissão Julgadora *

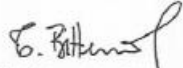
Eu, Elias Alves de Almeida _____, lavrei a presente ata, que assino juntamente com os(as) Senhores(as). São Paulo, aos 23 dias do mês de março de 2021.


Ricardo Leopoldo e Silva França


Paul Houang


Vanderley Moacyr John


Luiz Carlos Pinto da Silva Filho


Túlio Nogueira Bittencourt
Presidente da Comissão Julgadora

* Obs: Se o candidato for reprovado por algum dos membros, o preenchimento do parecer é obrigatório.

À minha família.

AGRADECIMENTOS

Agradeço primeiramente aos meus pais, Nelson e Isabel, pelo exemplo que sempre me deram. Apesar das dificuldades, sempre tiveram a clareza de que a “educação muda as pessoas e as pessoas transformam o mundo”, e nunca pouparam esforços para me garantir a educação formal de alto nível à qual, infelizmente, eles mesmos não puderam ter acesso.

À minha irmã Caroline e à Teca, um agradecimento especial pelo companheirismo diário, e, mais ainda, por suas participações durante este trabalho. À primeira, agradeço pelas ajudas na busca lexical, e à outra, pela companhia leal em cada segundo que estive escrevendo. À minha mui estimada prima Karina, meus sinceros agradecimentos pelo intenso auxílio na revisão final deste texto.

Agradeço ao professor Túlio por todos esses anos de orientação. Obrigado por ter me apresentado à pesquisa ainda na Iniciação Científica. Agradeço a amizade, os conselhos e as oportunidades que me deu ao longo de minha trajetória acadêmica.

À Saint-Gobain, manifesto a minha gratidão, na pessoa de meu diretor Gabriel Gorescu, pela confiança em mim depositada. A realização deste trabalho só foi possível graças ao financiamento e à estrutura que me foram oferecidos. Aproveito ainda para agradecer a todos os colegas do Grupo e, em especial, aos amigos técnicos, pesquisadores e as equipes de administração e patrimônio da SGR Brasil.

Agradeço à Embaixada da França no Brasil que, por meio do seu Consulado em São Paulo, cofinanciou este projeto através do programa “*Docteurs en Entreprise*”.

Agradeço ainda aos membros do Comitê de Tese que me acompanharam ao longo deste trabalho. Aos professores Vanderley John, Henrique Campelo, Ricardo França e ao meu ex-diretor Paul Houang o meu muito obrigado pelas discussões técnicas, pela ajuda e pela disponibilidade que tiveram nesse período.

Aos amigos e à minha família, um pedido de desculpas pelas vezes em que não pude estar presente. Saibam que foram vocês que me ajudaram a não desanimar e que sempre estiveram ao meu lado para compartilhar as alegrias, mas, sobretudo, para me dar suporte nas dificuldades. Meu muito obrigado pelo apoio e pela presença.

Agradeço, por fim, à Força criadora de quem tudo provém e cujo amor inspira, motiva e dá suporte a todas as minhas ações dia após dia.

ABSTRACT

BORIOLO, G. R. **Light steel framing façades: mechanical behavior of cementitious boards and numerical structural modeling for high building applications.** 2021 (Revised version). Tese (Doutorado) – Escola Politécnica, Universidade de São Paulo, São Paulo, 2021. 202 p.

This work presents a framework to assess the mechanical behavior of lightweight façades in high buildings. This framework is based on the definition of a set of structural requirements for the steel frame structure, the fiber cement boards and their fixing system. These requirements have been proposed and verified considering both the ultimate and the serviceability limit states (ULS and SLS), and differentiating the global and local structural behaviors under wind loads action and hygrothermal dimensional variations. Design wind loads have been proposed based on a documental comparison of different international standards for wind action on buildings. The behavior of the boards and the screws was experimentally characterized in different conditions of humidity and aging. Several finite element models were created in ABAQUS to simulate the materials behavior and to predict the mechanical performance of the façade system. It has been verified that aging improves the ultimate strength of the fiber cement material, also moisture changes this material behavior by rising its ductility and degrading its final strength. The modeling strategy has been proven to be capable to provide decent results to predict the façade performance. It has been demonstrated that the XFEM and the Hashin bi-linear models have limits to simulate a fiber cement board. Moreover, the Concrete Damage Plasticity has been confirmed as a convenient formulation to capture the cracking mechanisms of the board, having a good fit, even in the post-peak behavior. The numerical results have shown that the fixing system definition is crucial to prevent cracks. Minimum edge distances must be respected to mitigate these risks, and the use of pre-drilling is helpful to avoid any stress concentration due to shrinkage. Numerical simulations have also been performed to define an optimized configuration for a 30-floor building façade considering a critical wind load. These simulations, in a specific and illustrative case, have resulted in studs of 200mm spaced at each 400mm and with non-winged screws at each 400mm.

Keywords: light steel frame, lightweight facades, fiber cement, cracking modeling, numerical modeling

RESUMO

BORIOLO, G. R. **Light steel framing façades: mechanical behavior of cementitious boards and numerical structural modeling for high building applications**. 2021 (Revised version). Tese (Doutorado) – Escola Politécnica, Universidade de São Paulo, São Paulo, 2021. 202 p.

Este trabalho apresenta a estruturação de critérios para avaliação do comportamento mecânico de fachadas leves em edifícios altos. Esta estruturação consiste na definição de requisitos estruturais para a estrutura metálica, para as placas de fibrocimento e para o sistema de fixação. Estes requisitos foram propostos considerando os estados limites último e de serviço, além de diferenciar os comportamentos local e global do sistema submetido à ação do vento e aos efeitos de variação higrotérmica. Uma proposta de cálculo da carga de vento para diferentes alturas foi realizada a partir do comparativo entre diferentes normas internacionais de ação do vento em edifícios. As placas e os parafusos foram caracterizados em diferentes idades e condições de umidade. Modelos numéricos, em elementos finitos, foram criados no programa ABAQUS para simular o comportamento dos materiais e para avaliar a performance mecânica do sistema. Os resultados mostraram que o envelhecimento melhora o desempenho mecânico do fibrocimento, e pode ainda promover um ganho no desempenho do sistema ao longo do tempo desde que as fixações sejam corretamente projetadas. Por outro lado, a umidade é crítica para o material. A modelagem numérica mostrou-se capaz de simular corretamente o comportamento dos materiais. Algumas técnicas numéricas como o XFEM e o modelo de Hashin apresentaram limitações na modelagem da placa de fibrocimento. No entanto, o modelo CDP teve um bom desempenho nas diferentes situações avaliadas e mostrou-se conveniente para simular o material. Os resultados numéricos confirmaram ainda que a fixação das placas pode reduzir ou aumentar o risco de aparecimento de fissuras. Distâncias mínimas dos parafusos às bordas e o uso de pré furos devem ser considerados para reduzir estes riscos. Além disso, uma solução otimizada de fachada foi definida através de simulações numéricas indicado, no caso específico estudado, o uso de perfis com alma de 200mm espaçados a cada 400mm e com parafusos sem asa a cada 400mm.

Palavras-chave: LSF, fachada leve, placa cimentícia, modelos de fissuração, modelagem numérica

LIST OF FIGURES

Figure 1: Proposed framework of design requirements and thesis scope summary.	31
Figure 2: Chapters scheme.	32
Figure 3: Lightweight façades fixing typologies: a) Infill wall and b) Continuous or curtain wall.	35
Figure 4: Examples of inserts. a) Inserts on slabs. b) Inserts on edge beam.	36
Figure 5 : a) Cladding system; b) Complete building envelope.	37
Figure 6 : Vertical section of a ventilated cladding system.	38
Figure 7: Exterior wall finish systems: a) DAFS; b) EWIS.	39
Figure 8: Steel cold-formed profiles. a) C-section studs and b) U-section studs.	41
Figure 9: : Light steel framing structural components.	41
Figure 10: The Alan G. Davenport wind loading chain.	50
Figure 11: Wind profile - Mean speed and gusting.	52
Figure 12: Schema of wind pressure distribution on buildings plans.	60
Figure 13: Building examples with standard plans. a) Rectangular building. b) H-plan building.	62
Figure 14: Proposal for design wind loads and criteria to façade design, based on Brazilian standards requirements.	70
Figure 15: Layout of Hatschek machine. Example of production process using three cylinder sieves.	75
Figure 16: Cross section view of a generic laminated material.	77
Figure 17: 3-point bending test configuration.	82

Figure 18: a) Partially debonded fiber configuration with combined elastic and frictional behavior. b) Interface shear stress distribution along a fiber immediately after cracking.	85
Figure 19: Idealized representation of the stress field around an advancing crack.	87
Figure 20: Water jet cutting machine. Samples preparation.	88
Figure 21: Mass stabilization during sample conditioning	89
Figure 22: Test apparatus and sample positioning for the three-point bending test.	89
Figure 23: Load-displacement average curve for the three-point bending test in different hygrometric conditions.	91
Figure 24: a) Geometry of dogbone-shaped specimens. b) Test apparatus to direct tensile test in a specimen with strain gage.	92
Figure 25: Tensile average response of the board in wet and in ambient conditions.	93
Figure 26: Multiple cracking process due to fiber-bridging in the direct tensile test.	94
Figure 27: RILEM work of fracture testing set-up.	95
Figure 28: Work of fracture results. Load versus displacement average curves for samples with different notch lengths and in different conditioning states.	95
Figure 29: TG and DTG curves of new samples.	99
Figure 30: TG and DTG curves of PP fibers.	100
Figure 31: TG and DTG curves of aged samples.	100
Figure 32: Comparative of the flexural behavior of aged and new samples in ambient condition.	103
Figure 33: Bowing effect in function of the depth of hygrometric variation on a laminated board.	106
Figure 34: Traction-separation law for cohesive damage in ABAQUS.	112

Figure 35: Boundary conditions of 3-point bending model.	117
Figure 36: Load-displacement simulated flexural response using XFEM and Hashin model.	119
Figure 37: Load-displacement response of the 3-point bending test simulated by the CDP model.	120
Figure 38: Geometry and boundary conditions to the direct tensile test.	121
Figure 39: Load-displacement curve. Direct tensile response using XFEM and Hashin model.	121
Figure 40: Force-displacement response of the direct tensile test simulated by the CDP model.	123
Figure 41: Example of fixing and gliding points positioning.....	128
Figure 42: Fixing system using rivets. a) Sliding point. b) Fixed point using a rivet sleeve.	128
Figure 43: Fixing system using screws. a) Sliding point. b) Fixed point using washers.	128
Figure 44: Self-drilling screws. a) Flat head with wings, b) Wafer head without wings.	129
Figure 45: Localization of the maximum stressed connecting point due to in-plane loads...	130
Figure 46: Field of displacements generated by a shrinkage loading.....	131
Figure 47: Influence area and symmetric boundary conditions of the corner fixing.....	132
Figure 48: Position of the fixing point – distance to free edges and screwed hole diameter.	132
Figure 49: Fasteners model using springs supports and coupled nodes.	134
Figure 50: Influence of fastener stiffness on cracking results.....	135
Figure 51: Examples of cracking path in real façades cases.	136
Figure 52: Influence of edge distances on cracking results.	137
Figure 53: Pre-drill schema.	138

Figure 54: Effect of pre-drilling considering 10mm of edges distances.	139
Figure 55: Combined effect of pre-drilling and minimum edge distance for pre-drilled solution 1.....	140
Figure 56: Combined effect of pre-drilling and minimum edge distance for pre-drilled solution 2.....	141
Figure 57: Screws driven through board samples.....	142
Figure 58: Test assembly for measuring screw pull-through resistance. a) Board positioning with screw threads up. b) Test starting with board blocked by the support fixture.	143
Figure 59: Load-displacement pull-through curves.....	145
Figure 60: Load-displacement linear model example.....	147
Figure 61: Load-displacement piecewise linear model example.....	148
Figure 62: Load-displacement curvilinear model example.....	149
Figure 63: Numerical modeling of pull-through test. Calibration of the screw-board interaction behavior.	150
Figure 64: Numerical calibration of winged screws pull-through.....	152
Figure 65: Numerical calibration of no-winged screws using a monotonic curvilinear function.	153
Figure 66: Numerical calibration of no-winged screws using a piecewise function.	153
Figure 67: Mesh detailing. 5mmx5mm S4 elements.	157
Figure 68: Boundary conditions of a simply-supported C-stud. Model 1.....	158
Figure 69: Mises equivalent stress of Model 1.....	159
Figure 70: Displacement field of Model 1.	159
Figure 71: Boundary conditions with insert geometry simulation. Model 2.....	161

Figure 72: Stress increasing with reduced web-insert contact.	162
Figure 73: Influence of insert width in stress concentration.	162
Figure 74: Boundary conditions considering lateral in-plane restraints provided by screws. Model 3.....	163
Figure 75: Stress increasing in function of screws spacing.	163
Figure 76: Design criteria for a 30-floor building lightweight façade.....	164
Figure 77: Façade frame geometry.	166
Figure 78: External wind load.	167
Figure 79: Boundary conditions. Inserts positioning.....	168
Figure 80: Connectors interactions.	168
Figure 81: Local ULS analysis considering studs and screws distance of 400mm x 300mm.	170
Figure 82: Local ULS analysis considering studs and screws distance of 400mm x 400mm.	171
Figure 83: Local ULS analysis considering studs and screws distance of 400mm x 600mm.	171
Figure 84: Façade panel configuration of 400mm x 600mm under a horizontal load of 3,0kPa.	172
Figure 85: Local ULS analysis considering studs and screws distance of 600mm x 300mm.	173
Figure 86: Global ULS analysis considering studs and screws distance of 600mm x 150mm.	173
Figure 87: Façade panel of 400mm x 300mm in wetting condition, under a horizontal load of 3,0kPa.	174

Figure 88: Local ULS analysis in wet condition, with studs and screws distance of 400mm x 300mm. 175

Figure 89: Local ULS analysis in wet condition, with studs and screws distance of 400mm x 270mm. 175

Figure 90: Summary of façades design validation for a 30-floor building using winged screws. 178

LIST OF TABLES

Table 1: Lightweight façade classification.....	39
Table 2: Brazilian standard specifications and definitions for structural cold-formed steel (CFS) profiles to LSF constructions.	42
Table 3: Usual dimensions adopted to LSF profiles.....	42
Table 4: Maximum design horizontal loads calculated on ULS for a 3-meters high C-stud profile following the Brazilian standard ABNT NBR 14762:2010.	44
Table 5: Brazilian categories of fiber cement boards without asbestos for external use according to its mechanical strength.	45
Table 6: Maximum design horizontal load supported in ULS by a fiber cement board.....	45
Table 7: Maximum vertical screw spacing to support horizontal loads.	47
Table 8: Basic wind speeds parameters for different national codes.....	56
Table 9: Wind speed parameters in different international codes.	57
Table 10: Wind-induced pressures from different international codes.....	58
Table 11: Internal pressure coefficient definitions from different national codes.....	61
Table 12: Wind speed and dynamic pressure defined by the Brazilian standard.	63
Table 13: Wind speed and dynamic pressure defined by the European standard.	64
Table 14: Wind speed and dynamic wind pressure defined by the ASCE standard.....	64
Table 15: Wind speed and dynamic wind pressure defined by the Australian-New Zealand standard.....	65
Table 16: Summary of dynamic wind pressure results.	65
Table 17: Critical external pressure coefficients by different standards.....	66
Table 18: Critical and usual internal pressure coefficients by different standards.....	67

Table 19: Characteristic wind-induced pressures for a 90m-height building.....	68
Table 20: Critical design wind-induced pressures based on Brazilian standards.	70
Table 21: Raw materials composition of fiber cement board.....	88
Table 22: Flexural characterization of a 10mm-board in different hygrometric conditions following ABNT NBR 15498:2016. Average results from five samples for each condition.	91
Table 23: Tensile characterization of a 10mm-board in wet and ambient conditions. Average results from three samples for each condition.	93
Table 24: Fracture energy and crack initiation stress (σ_{cr}) obtained by the RILEM method. Average results from three samples for each condition.	95
Table 25: Chemical composition of raw materials by XRF.	97
Table 26: Total calcium and magnesium oxides in new and aged samples by XRF analysis.	98
Table 27: Mass change observed for the different TG peaks for new and aged samples.	100
Table 28: Bulk density and water absorption changes after natural aging.....	102
Table 29: Comparative flexural results of boards after natural aging.....	103
Table 30: Fracture flexural parameters defined to XFEM and Hashin numerical simulations.	118
Table 31: Maximum load and energy predicted by XFEM and Hashin numerical simulations.	118
Table 32: Tensile plastic material behavior definition based on the flexural experimental data.	119
Table 33: Maximum load and energy predicted by CDP numerical simulations.....	120
Table 34 : Compressive plastic parameters of fiber cement board for the CDP model.....	122

Table 35: Tensile plastic material behavior definition based on the direct tensile experimental data.	122
Table 36 : Maximum load and energy predicted by CDP simulation.....	123
Table 37: Comparative between experimental and numerical ultimate strength (σ_u) results.	125
Table 38: Equivalent influence lengths for a 1200mmx3000mm rectangular board.	133
Table 39: Pull-through strength results for new samples.....	144
Table 40: Pull-through strength results for aged samples.	145
Table 41: Linear model parameters for flat head winged screws pull-through on fiber cement boards.	146
Table 42: Piecewise linear model parameters for wafer head screws without wings pull-through on fiber cement boards.	148
Table 43: Curvilinear model parameters for wafer head screws without wings pull-through on fiber cement boards.	149
Table 44: Numerical model parameters to simulate a flat head winged screwed connection.	151
Table 45: Input parameters for the numerical models of wafer head screws without wings.	152
Table 46: Maximum design horizontal loads calculated by means of FEM for a 3-meters high C-stud.	160
Table 47: Suggested profiles for LSF façades studs. Minimum geometries.	160
Table 48: Requirements validation framework.	165

LIST OF ABBREVIATIONS

ABNT	Associação Brasileira de Normas Técnicas
AR	alkali-resistance
AS	Australian standard
ASCE	The American Society of Civil Engineers
ASTM	American Society for Testing and Materials
BC	boundary condition
BOP	bend over point
CBCA	Centro Brasileiro da Construção em Aço
CDP	concrete damage plasticity
CFS	cold-formed steel
CI	carbonation index
DAFS	direct-applied finish system
DIC	digital image correlation
DTG	first thermogravimetric derivative
EAD	European Assessment Document
EIFS	external insulation finish system
EN	European standard
EPS	expanded polystyrene
ETICS	external thermal insulation composite system
EWIS	external wall insulation systems
FEA	finite element analysis
FEM	finite element model
FPZ	fracture process zone
FVHF	Association for Materials and Components for Rear-Ventilated Facades
ITZ	interfacial transition zone
LEFM	linear elastic fracture mechanics
LOI	loss of ignition
LOP	limit of proportionality
LSF	light steel framing
MOE	modulus of elasticity
MOR	modulus of rupture
MWFRS	main wind force-resisting system

NBR	Brazilian standard
NZS	New-Zealander standard
OSB	oriented strand board
PE	polyethylene
PP	polypropylene
PU	polyurethane
PVA	polyvinylacohol
RH	relative humidity
RILEM	The International Union of Laboratories and Experts in Construction Materials, Systems and Structures
SLS	serviceability limit state
TG	thermogravimetric
TGA	thermogravimetric analysis
UK	United Kingdom
ULS	ultimate limit state
USA	United States of America
UTS	ultimate tensile strength
XFEM	extended finite element method
XPS	extruded polystyrene
XRF	X-ray fluorescence
ZAR	high-resistant zincked steel

LIST OF SYMBOLS

a	notch length
b	width
c_{pe}	external pressure coefficient
c_{pi}	internal pressure coefficient
c_r	roughness coefficient (EN standard)
c_o	orographic coefficient (EN standard)
c_e	exposure coefficient (EN standard)
d_{st}	studs distance
d_f	fiber damage index
d_m	matrix damage index
d_s	shear damage index
e	potential flow eccentricity
f_y	yield steel strength
f_u	ultimate tensile steel strength
g	wind peak factor
h	façade panel height
k_i	equivalent fastener stiffness
l	span
l_{cr}	crack length
m	mass fraction content
m_i	initial mass
m_f	final mass
n_{screw}	number of screws
p_s	wind-induced pressure
\bar{p}	hydrostatic tensor
\bar{q}	Mises equivalent stress
q	wind dynamic pressure
q_{wd}	design wind load
q_{wk}	characteristic wind load
s_{screw}	screw distance
s_{ver}	screw vertical distance to the free edge

s_{hor}	screw horizontal distance to the free edge
t	board thickness
t_{hyg}	depth of hygrothermal variation
v_b	reference wind speed (EN standard)
v_m	wind speed (EN standard)
w_c	maximum vertical displacement in the 3-point bending test
w_{abs}	water absorption
$A_{dom,open}$	area of dominant openings
$A_{suction}$	area of suction
A_{open}	area of openings
A_{total}	total area
C_p	pressure coefficient
C_{fig}	aerodynamic shape factor
C_{dyn}	dynamic factor
E_y	elastic steel modulus
E_L	elastic longitudinal modulus
E_T	elastic transverse modulus
E_m	elastic matrix modulus
E_f	elastic fibers modulus
E_x	flexural stiffness
$F_{d,pull-through}$	pull-through design strength
$F_\alpha(x)$	crack-tip function
F_f^t	fiber tensile failure
F_f^c	fiber compression failure
F_m^t	matrix tensile failure
F_m^c	fiber compression failure
G	shear modulus
G	gust factor
G_{LT}	shear modulus
G_c	critical strain energy release rate
G_f	fracture energy
$H(x)$	Heavside function

$K_y L$	buckling length in y-direction
$K_z L$	buckling length in z-direction
K_z	exposure coefficient (ASCE code)
K_{zt}	topographic coefficient (ASCE code)
K_d	directionality coefficient (ASCE code)
K_l	local pressure factor
K_a	area reduction factor
K_p	porous cladding reduction factor
K_c	fracture toughness
L_{board}	board length
M	terrain/height multiplier (AS/NZ standard)
M_s	shielding multiplier (AS/NZ standard)
M_t	topographic multiplier (AS/NZ standard)
M_d	directional multiplier (AS/NZ standard)
$N_i(x)$	nodal shape function
P_{max}	maximum load
R	radius of curvature
S_1	topographic factor (NBR standard)
S_2	roughness factor (NBR standard)
S_3	importance factor (NBR standard)
S^L	longitudinal shear strength
S^T	transverse shear strength
U	wind speed
\bar{U}	mean wind speed
\hat{U}	expected wind gust
$V_{sit,\beta}$	directional wind speed (AS/NZ standard)
$V_{des,\theta}$	design wind speed (AS/NZ standard)
V_R	regional wind speed (AS/NZ standard)
V_0	basic wind speed (NBR standard)
V_k	characteristic wind speed (NBR standard)
V	volume fraction content
V_f	fiber volume fraction

X^T	longitudinal tensile strength
X^C	longitudinal compressive strength
Y^T	transverse tensile strength
Y^C	transverse compressive strength
α	thermal expansion coefficient
β	moisture expansion coefficient
γ_f	design load factor
γ_r	strength reduction factor
γ_s	pull-trough safety factor
δ_h	horizontal displacement
δ_{eq}^0	initial damage equivalent displacement
δ_{eq}^f	complete damage equivalent displacement
δ_{free}	free in-plane displacement
ε_{sh}	dimensional variation
$\varepsilon_{sh,cr}$	initial crack shrinkage
ε_{mu}	matrix crack strain
$\tilde{\varepsilon}_t^{pl}$	tensile plastic strain
$\tilde{\varepsilon}_c^{pl}$	compressive plastic strain
ζ_i	equivalent influence length in the direction i
ν	Poisson's coefficient
ρ	specific density
ρ_{air}	air density
σ_{adm}	allowable stress
σ_u	time wind speed fluctuation
σ_{xx}	normal stress
σ_{xz}	shear stress
σ_c	composite stress
σ_m	matrix stress
σ_f	fiber stress
σ_{cr}	crack initiation stress
σ_{t0}	uniaxial tensile stress
σ_c^y	compressive yield stress

σ_t^y	tensile yield stress
σ_u	ultimate stress strength
τ_{fu}	frictional fiber shear stress
τ_{au}	fiber-matrix shear strength
ψ	dilatation angle
ΔT	variation of temperature
ΔRH	variation of relative humidity
\emptyset_{screw}	screw diameter
\emptyset_{drill}	drill diameter
\underline{a}_i	crack contour component of the nodal enriched vector
\underline{b}_i^α	crack-tip component of the nodal enriched vector
\underline{u}	displacement vector
\underline{M}	resultant moments
\underline{N}	membrane forces
$\underline{\varepsilon}$	strain tensor
$\underline{\varepsilon}^{pl}$	plastic strain tensor
$\underline{\varepsilon}^\sigma$	plane stress strain tensor
$\underline{\varepsilon}_m$	field of membrane strains
$\underline{\sigma}$	Cauchy stress tensor
$\underline{\sigma}^\sigma$	plane stress Cauchy tensor
$\underline{\varphi}$	field of surface curvatures
$\underline{\underline{A}}$	membrane stiffness matrix
$\underline{\underline{B}}$	membrane-bending-torsion coupling matrix
$\underline{\underline{C}}$	elastic stiffness tensor
$\underline{\underline{C}}_d$	damaged elasticity tensor
$\underline{\underline{D}}$	bending stiffness matrix
$\underline{\underline{Q}}$	local reduced stiffness matrix
<i>dof</i>	degree of freedom
%wt.	weight fraction

CONTENTS

INTRODUCTION	27
Context and motivations	27
Objectives.....	30
Description of chapters	32
1. LIGHT STEEL FRAMING FAÇADES	34
1.1. LSF façades assembly – construction process and fixing typologies	35
1.2. Façade typologies and finishing systems	37
1.3. Design parameters.....	40
1.4. Concluding remarks	48
2. WIND LOADS ON FAÇADES	49
2.1. Wind actions on buildings.....	50
2.2. International standard comparison.....	55
2.3. Comparative example	62
2.4. Design wind load and design criteria – Brazilian standard.....	68
2.5. Concluding remarks	71
3. FIBER CEMENT BOARDS.....	72
3.1. Manufacturing Hatschek process.....	74
3.2. Constitutive law of fiber cement materials and fracture process.....	76
3.3. Mechanical characterization	87
3.4. Durability analysis	96
3.5. Concluding remarks	107
4. NUMERICAL MODELING OF FIBER CEMENT BOARDS.....	109
4.1. Failure simulation techniques	110
4.2. Numerical modeling of experimental tests.....	116
4.3. Concluding remarks	124

5. FIXING SYSTEM	126
5.1. Screw-board interaction	127
5.2. In-plane loads.....	129
5.3. Pull-through loads.....	142
5.4. Concluding remarks	154
6. NUMERICAL MODELING OF A FAÇADE PANEL	156
6.1. Structural frame modeling.....	157
6.2. Requirements validation framework.....	164
6.3. Façade modeling	165
6.4. Design parameters optimization	169
6.5. Concluding remarks	177
CONCLUSIONS	179
General remarks.....	179
Wind loads.....	179
Fiber cement boards.....	180
Fixing system	182
Façade model.....	182
Final statement.....	183
Suggestions for future researches	183
REFERENCES	185

INTRODUCTION

Context and motivations

Context

Industrialization is a current demand of the construction sector in the Brazilian market. New production process, new materials and new construction technologies are demanded to increase productivity and to reach a sustainable chain. In addition, these new process can allow costs reduction and improve competitiveness¹. The construction activity usually presents a productivity index lower than other economic activities. In Brazil, the civil construction productivity is estimated around 30% of the average productivity in developed countries.² These best productivity results can be obtained by the combination of different factors such as cultural aspects, qualified workforce, R&D investments and the promotion of industrialized solutions.

The proposal of new production processes to the different parts of a building is important to achieve the industrialization of the construction market. Among the different building subsystems, façades are pointed by constructors as a crucial one. The façade system design plays an important role, since it is the building image and due to its urban interaction.³ In addition, the façades are easily degraded once they are in direct contact and interaction with the external environment.

Different authors stated the façades production process as the critical path on the construction planning^{3; 4; 5}. These same authors estimated that traditional façades represent around 9% to 15% of the global costs of the building construction. Despite being significant, the costs are difficult to control because the traditional production process also imply material loss, waste generation and low productivity^{4; 6; 7}.

In this context, lightweight façades are becoming an interesting alternative to traditional masonry and concrete blocks. These façades, already largely used in North America and in Europe, presents a technological solution to improve building performance. Industrialized façades enable, in addition, cost savings, reduction of wasting and productivity improvement with the acceleration of the construction time.

On the other hand, the introduction of a new system in the construction market always represents a change of paradigms and needs a cultural change to be fully accepted and adopted³. Constructors and construction market specialists have noticed that the technical knowledge on lightweight industrialized systems are not

sufficiently spread in the Brazilian market yet.⁵ Even with a slow increase on the number of scientific and technical production related to this subject in Brazil, there still is a technical gap in terms of structural requirements definition, such as design loads prediction or durability assessment of materials and systems.^{3; 5; 8}

A proper design requirements definition, in order to predict and avoid pathologies, is important to ensure and to set a cultural confidence in a lightweight façade performance. However, the assessment of a complete façade system is not trivial. Composed by different materials, a façade is a complex subsystem and to ensure its performance and durability, it demands a proper characterization of each element and the prevention of a large list of possible pathologies such as crackings, fiber cement degradation, steel corrosion or fixings fatigue due to cyclic loads.

In Brazil, technical catalogues and even the few national standards related to lightweight systems are mainly inspired by the international experience with only a few of local return of experience in Brazilian sites. Among these rare public reports, Antunes (2010) and Handa (2019) presented the main pathologies observed in lightweight façades in Brazil^{7; 9}. They observed that cracking is the main damage related to the system, mainly over the joints, but also over the boards or even over the coating and finish systems. Even if the cracking process is initially an aesthetic problem, it may become a structural problem after its evolution over the years.

The main reported pathologies in façades are related to the mechanical response of the system. As a system, the mechanical analysis of a lightweight façade must be done in a multiscale approach, simultaneously assessing materials performance and the behavior of their connections and assembled parts. Numerical tools, such as Finite Element Models, have been widely developed and applied on the evaluation of different materials, including crack and damage analyses. However, these technologies are generally driven and used to simulate high performance materials and rarely applied to assess a complete system, such as façades, or even their external boards or other components.

Therefore, a scientific characterization of lightweight façades systems and their components is a helpful way to promote the reliability of these industrialized systems and to contribute to widespread the technical knowledge for a proper implementation of these façades. A better understanding of the system and of its mechanical behavior, including an appropriate numerical modeling and a review of some standards

considerations will help in the definition of design requirements, contributing to improve life-cycle of the systems and their components.

Motivations

The previously described scenario prompts a vast range of studies for lightweight façades systems. Working on this subject is **endorsing a sustainable production process whilst improving quality in the civil construction**. The proposal of a scientific methodology to **support design requirements and technical assembly choices** plays a double technical and economical role, contributing to ensure the reliability of these non-traditional systems and meeting the construction market demands by the promotion of an industrialized façade production process.

Lightweight and dry constructions systems have already been implemented and widely used in Europe and North America. However, in Brazil, these solutions have been sluggishly implemented and there is still a gap to fulfill. Even if drywalls have consolidated their place on the internal partitions market, lightweight external façades are not among the first choices of constructors yet. As the implementation of these façades are still considered in phase of learning, technical supports and **predictive models are requested to ensure performance**, quality and durability of the system.

The performance of an external façade system must be assessed by the verification of its structural stability, its mechanical strength, its water and air tightness capacity, its thermoacoustic behavior and the moisture and condensation risks on the system. **Large displacements and cracking are important warning evidences** of design deviations and degradation of each of those performance attributes, apart from thermoacoustic and moisture assessment. Therefore, a proper design must consider the limitation of those displacements and cracks over the complete system and on its components. This analysis can be held using numerical tools and the design parameters can be validated using these appropriate simulation models.

The potential market that is starting to adopt lightweight façades solutions is the residential market, where high buildings are quite common, i.e. buildings with around 25 to 30 floors. This application implies on façades subjected to important wind loads, despite the weathering exposition inherent to an external system. In case of lightweight elements, the **wind action represents a significant risk** if it is not properly predicted and the system is not appropriately designed to withstand these loads.

Furthermore, the weathering exposure submits the façade to hygrothermal loads, generated by heat-rain cycles. Moreover, in Brazil, fiber cement boards are the usual external sheathing board in lightweight façades. These boards may present, depending on their formulation and production process, a sensitive dimensional variation related to the heat-rain cycles and to their aging, such as an irreversible shrinkage caused by carbonation. This **in-plane movement can lead to a progressive cracking** over the boards, mainly near to fixing points. This cracking risk can be assessed in function of the constitutive law of the boards.

To reduce structural risks on façades systems, the definition of the appropriate wind load magnitude and its correspondent structural design are indispensable, as well as the assessment of the fasteners mechanical behavior. In addition, the dimensional variation of the boards must also be considered, since it can modify the mechanical behavior of fixings and cause cracks, facilitating the pullout of the boards.

The effects of these combined actions have not been broadly explored in the literature yet. Moreover, it can be found no or a few studies regarding the mechanical interaction between the fiber cement board and the façade frame subjected to wind and hygrothermal action. Reference standards recommend experimental tests and validation for each new configuration. It motivates the proposal of an assessment methodology based on numerical simulations to predict the mechanical behavior of a façade system and to validate some design parameters, such as profile dimensions and screw distances.

Objectives

General objective

The main objective of this work is to postulate a design framework to assess the mechanical behavior of lightweight façades in high buildings. The façade design is based on the definition of structural requirements for the steel frame structure, the fiber cement boards and their fixing system. A numerical modelling strategy is presented to support the requirements validation through computational simulations.

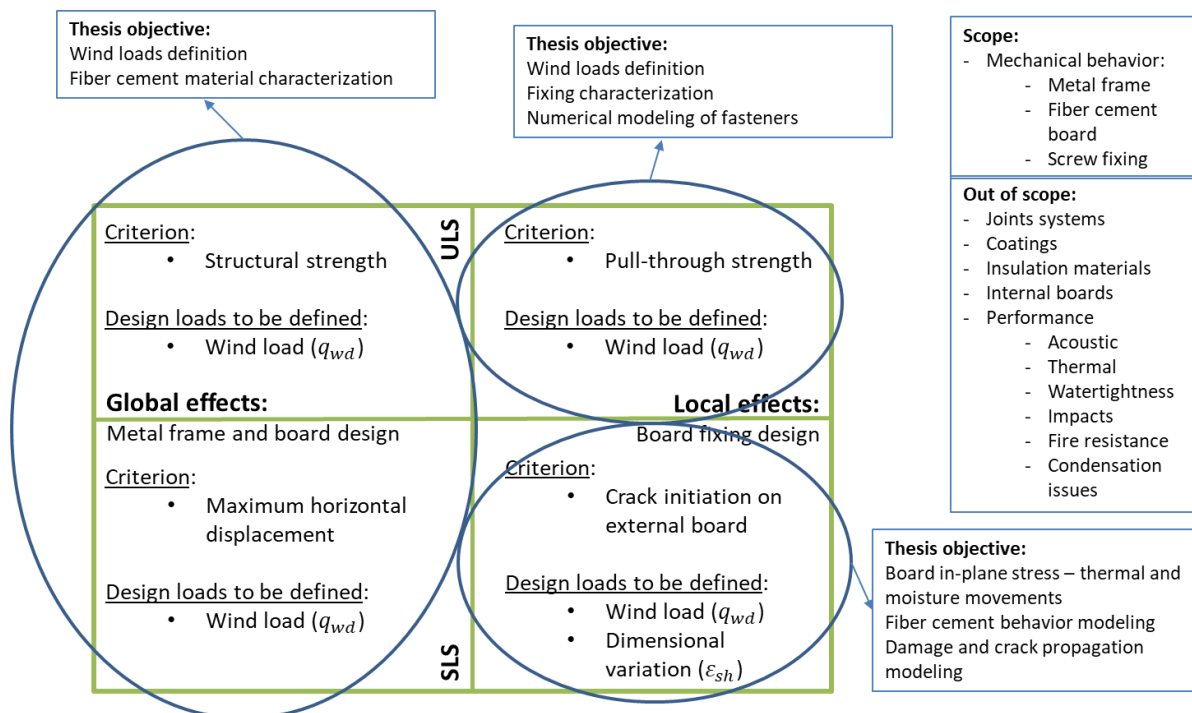
These requirements are proposed and verified considering both ultimate and serviceability limit states (ULS and SLS) and differentiating the global and local structural behaviors under wind loads action and hygrothermal dimensional variations.

The numerical modeling creation and the macro analysis of the façade system depend on several specific objectives that are proposed below and summarized in the Figure 1.

Specific objectives

- Understand the different typologies of façades and the main design parameters;
- Set a framework of structural criteria to define the design wind loads;
- Characterize the mechanical behavior of a fiber cement board, including aging;
- Propose a numerical model to simulate the fiber cement board behavior, predicting cracks;
- Characterize and simulate the fixing system behavior and the board-screw interactions before and after aging;
- Assess the effects of dimensional in-plane variation on fiber cement boards, considering different boundary conditions based on the fixing behavior;
- Propose a numerical model to simulate a façade panel submitted to wind and hygrothermal loads and validate some design parameters, such as profile dimensioning and screw distancing.

Figure 1: Proposed framework of design requirements and thesis scope summary.

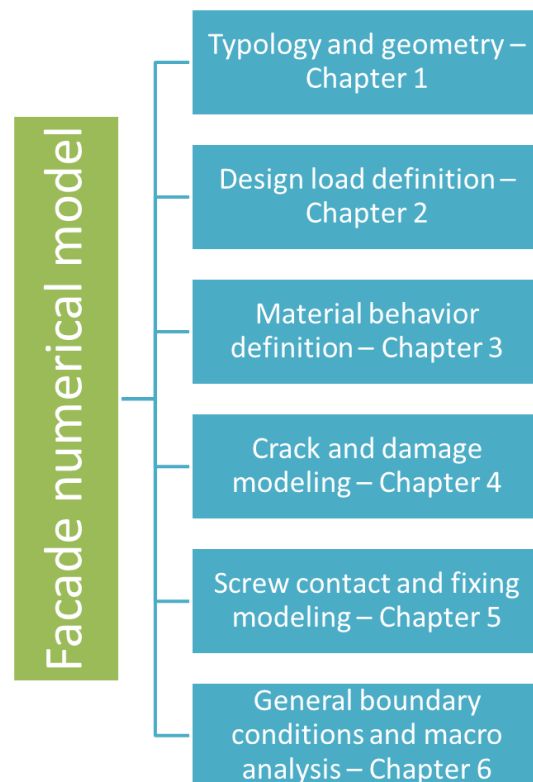


Source: author.

Description of chapters

This thesis is organized into six chapters, besides this introduction, general conclusions and suggestions for future researches. Each chapter presents a discussion with a specific literature review and an analytical, experimental or numerical analysis in order to define one step or input of the complete numerical model of a façade, as illustrated in Figure 2.

Figure 2: Chapters scheme.



Source: author.

The first chapter presents what a Light Steel Framing (LSF) façade is, describing the different typologies and the main design parameters. The chapter shows a first pre-design definition of maximum loads considering different LSF stud profiles, fiber cement boards strength and screws spacing based on an analytical analysis, technical recommendations and national standards requirements.

The main considerations on the definition of wind design loads on façades are exposed in chapter 2. Herein, local and global wind effects are presented through an international standard comparison and an analytical comparative case analysis. The chapter is concluded by a proposal of design wind loads (for SLS and ULS) for façades design, adjusting the current Brazilian code requirements.

The characterization of a fiber cement board is addressed in chapter 3, introducing its formulation basis as well as its production process. A theoretical and analytical formulation is presented to describe the mechanical behavior of these boards and the influence of fibers on the cementitious matrix. An experimental characterization focused on the tensile behavior of these boards is reported in order to set the constitutive curves of the material in different hygrometric conditions. Moreover, a durability analysis is held considering aging effects, such as carbonation, on the mechanical behavior of the boards. Finally, a literature definition of irreversible and cyclic dimensional variations magnitude is stated closing this chapter.

In chapter 4, numerical models are introduced to simulate fiber cement boards, considering damage and cracking. Numerical analyses using the Abaqus formulation for the eXtended Finite Element Model (XFEM), the Hashin damage and the Concrete Damage Plasticity model are performed and compared with the experimental results. Advantages and disadvantages of each numerical strategy are presented for the definition of the tensile behavior parameters of fiber cement boards.

Chapter 5 outlines the different fixing systems and their characteristics to fasten the cementitious board on the metallic frame. The influence of each of them in the fastening stiffness is introduced, and an experimental characterization is performed to assess the pull-through resistance of the fiber cement board using self-drilling screws with or without wings. Lastly, the chapter ends assessing, by numerical modeling, the effects of the dimensional variations on the board based on the different fixing stiffness.

The sixth chapter defines the final modeling of the façade panel, and shows the results of several numerical simulations. Different techniques to model the structural frame are discussed in this chapter. In addition, the influence of board aging on the global behavior of the system is assessed. Therefore, the numerical performed analyses provide the definition of optimized screws and studs design configurations.

After the chapters, general conclusions are postulated along with suggestions for complementation of this work and future researches. Here it is important to highlight that no joint treatment was studied in this work and no monolithic rendering or coating were neither considered; accordingly, the conclusions presented in this work cannot be directly extrapolated to those applications.

1. LIGHT STEEL FRAMING FAÇADES

Numerical model input definition: Façade typology and geometry

Light steel framing buildings, or LSF, are lightweight constructions structured on light cold-formed steel profiles with frame connection. The implementation of this construction system depends on the technical qualification of the different market players. Technical literature, national standards and labor qualification are essential elements to improve the development of LSF system on a national market. ^{3; 10}

The LSF system is being widely used in USA, Japan, New Zealand and in various countries in Europe. In UK and in France, for example, steel construction represents about 7% of the construction market of housing and residential buildings. LSF is used in almost 3% of buildings in those countries. ^{11; 12}

In Brazil, reinforced concrete buildings or structural masonry represent 87% of the construction market. LSF constructions still represent a negligible amount on the market, less than 0,1%, but it is expected that they increase in the next years ¹³. The recent national economic problems have slowed down this growth, but constructions are restarting slowly. Residential buildings are the most important consumers of LSF profiles ⁸. However, the knowledge regarding dry construction systems has not been widely spread into the Brazilian construction market yet.

A LSF system may be divided into three main subsystems: floor, walls and roof. The complete system is traditionally used in single-story buildings or low-rise multi-story buildings. The LSF structure may provide stability for buildings up to 10 story height, depending on wind loading exposure ¹⁴. On high-rise buildings, however, the LSF system may be recommended for external façades, without any height limitation if properly designed. ^{13; 14}

LSF façades increase productivity and lead to a reduction of up to 3 months on the construction schedule when compared to traditional masonry in high buildings ⁴. In addition, LSF production reduces waste generation, water consumption and work-force on site. ^{4; 15; 16; 17}

Another benefit of LSF façades is the large portfolio of typologies, finishing system and modulation design choices allowed due to the flexibility of this system. ¹⁸ This chapter presents the main LSF façade typologies, including the most used production processes, the finishing options and an overview on the most important

design parameters regarding the mechanical behavior considerations of the frame and their fixing systems.

1.1. LSF façades assembly – construction process and fixing typologies

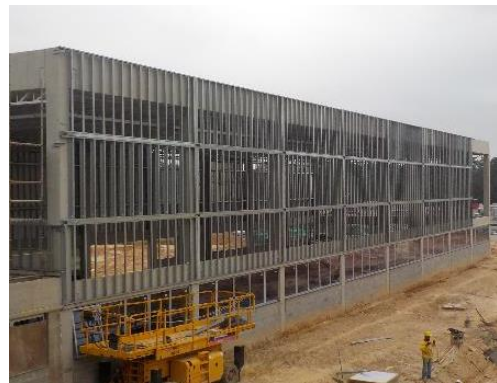
In high buildings, the light steel framing façade structure is a secondary structure assembled on the main structure. A façade panel may be classified as a non-load bearing wall if it is designed to be a self-supported structure resisting to cladding weight and wind loads. If the façade panel is additionally subjected to axial loads from floors or roof, it is classified as a load bearing wall. Lightweight façade panels on high rise buildings are usually designed as non-load bearing walls.¹¹

The relative position of the façade structure to the main structure defines the system as an infill wall or as a curtain wall (also called over-sail or continuous wall). Figure 3 illustrates both fixing typologies.

Figure 3: Lightweight façades fixing typologies: a) Infill wall and b) Continuous or curtain wall.



(a)



(b)

Source: author.

Infill walls are façade panels built between the floors of the main structure of the building. Usually these panels are constructed element-by-element, cut and installed on site, following the so-called stick-built process. The façade loads (self-weight, cladding weight and wind loads) are transmitted directly to the main structure by the contact between the steel tracks and the slab. If there is a rigid connection (structural screws) between the metal frame and the main structure, the façade panels must absorb the vertical displacements of the slabs. To avoid these effects, decoupling the displacements, the upper track is connected on the studs without any restriction on vertical displacement.^{17; 18}

When the façade structure is assembled externally to the main building structure, it is called a **curtain wall** system. These walls are independent from the main construction, they are an external envelope to the building, as a skin façade. A curtain wall must be designed to be a self-supported structure, absorbing its own displacements, the self-weight and wind loads. The façade panels may be fabricated directly on site (stick-built process) or prefabricated in a factory and then assembled on site. The curtain façade is connected to the main structure by specific inserts bolted on the edge beams or on the slabs (in case of flat slab constructions). Figure 4 illustrates the inserts connection on the main structure. These inserts are usually semi-rigid connections allowing the vertical displacement of the façade frame and restricting its horizontal displacement. ^{17; 19}

Figure 4: Examples of inserts. a) Inserts on slabs. b) Inserts on edge beam.



(a)



(b)

Source: a) Halfen Curtain Wall. b) author.

Cardoso (2016, p. 88) classifies the façade production methods in three degrees of industrialization. The infill walling is on the first level of industrialization because this process still retains some aspects of handmade constructions. The continuous walling, assembled on a stick-built process is on the second level of industrialization, since the façade structure is more independent from the main structure and the production process is more optimized than the infill one. The third level of industrialization is achieved by the use of prefabricated panels, since the façade is completely produced in a factory by industrialized means. ³

The construction market longs for the most industrialized solution available. Actually, curtain wall systems are desirable for allowing eventual vertical alignment corrections on the building or redressing geometrical heterogeneities of beams and

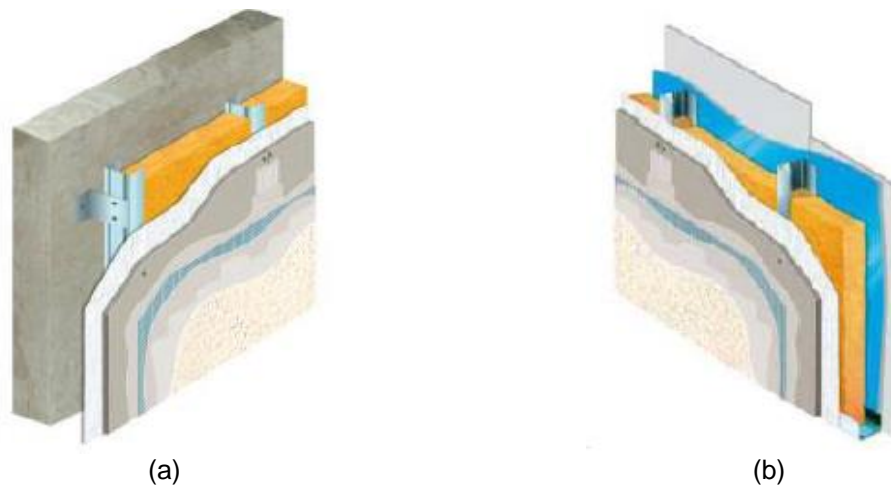
columns. However, curtain façades are more expensive than infill walls and their assembly process is more complex.

1.2. Façade typologies and finishing systems

An exterior wall structured in LSF is a multilayer system, composed by different elements. Internal and external boards, weather resistive barrier, insulation, coatings, sealants and glass fiber meshes can be combined over the LSF structure, setting the complete façade system. ²⁰

Lightweight façade systems may be adopted either as the complete **building envelope** (a wall separating the interior and the exterior of the building) or as external wall **claddings** (mechanically fixed to external masonry or concrete walls, for example, in new or existing buildings). Figure 5 presents a standard design of a cladding system fixed on a concrete wall and a standard design of a complete building envelop. ^{21; 22; 23}

Figure 5 : a) Cladding system; b) Complete building envelope.

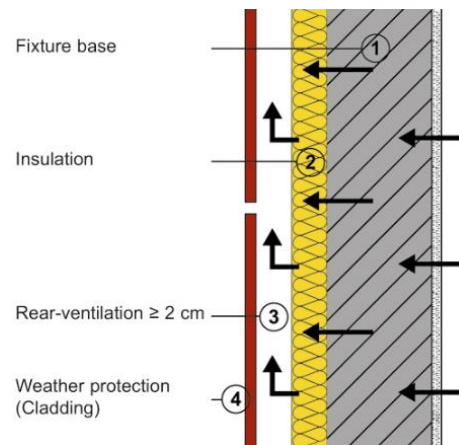


Source: a) EAD 090119-00-0404, b) EAD 090120-00-0404.

The design of both typologies must be able to ensure a correct mechanical, thermal and acoustical performance as well as be watertight, avoiding moisture problems. Different design solutions can be proposed to improve the thermal performance of the building and the moisture management on the façade system. The use of a ventilated air cavity on the façade composition is often adopted to permit the dry-out of the water that could penetrate by condensation or rain. A façade is called a **ventilated façade** when there are ventilation openings at the bottom and at the top edge of the system and if the ventilation air gap is at least 2 cm. A simplified schema of a ventilated façade can be seen in Figure 6. ²⁴

The choice of the finishing system on an exterior wall is directly linked to aesthetic aspects of the building. Besides protecting the complete façade system, the finishing must fulfill durability and maintenance requirements. In some cases, the finishing system can also contribute to enhance the energetic performance of the building. Exterior sidings, in vinyl or fiber cement materials for example, can be used as a finishing.

Figure 6 : Vertical section of a ventilated cladding system.



Source: FVHF (Association for Materials and Components for Rear-Ventilated Façades).

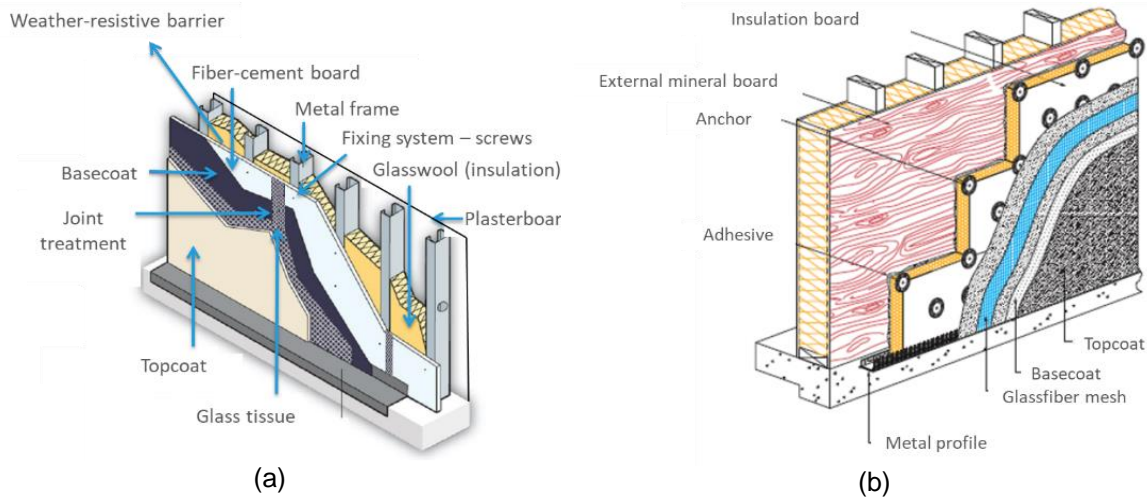
For coated finishing systems, the first choice will be the use of open or closed joints systems. In the case of closed joints, there are two different applications: **Direct-Applied Finish System (DAFS)** and **External Wall Insulation Systems (EWIS)**. In the first one (DAFS), the coating is applied directly over the external mineral board. In EWIS, also referred to as EIFS (External Insulation Finish System) or as ETICS (External Thermal Insulation Composite System), an external insulation board is included over the external mineral board and the coating is applied over the external insulation board. ^{25; 26}

The composition of both finishing systems are essentially the same. As shown in Figure 7, the typical components of the system are:

- Internal gypsum board;
- Metal frame structure;
- Insulation – glasswool or rockwool for example;
- Weather-resistive barrier, screwed on the metal frame;
- External mineral board – fiber cement board, for example – fixed over the weather resistive barrier and fastened to the metal frame;

- Coating system: may be composed by a basecoat, a primer and a topcoat
- Glass fiber mesh – embedded in the basecoat - usually used if the joint treatment or the basecoat is a cementitious based material

Figure 7: Exterior wall finish systems: a) DAFS; b) EWIS.



Source: author, adapted from EAD 040089-00-0404.

In EWIS, the system additionally comprises an insulation board made on EPS, XPS, PU, foam plastic or other insulation material. This board can be mechanically fixed on the external mineral board by anchors or chemically bonded by specific adhesives.²⁵

Table 1 summarizes the different classifications of a lightweight façade system according to its typology, production process and finishing system. It can be easily observed that different systems can be proposed and designed, and yet have a lightweight composition.

Table 1: Lightweight façade classification.

Construction process	stick-built or pre-fabricated
Fixing typology	infill or curtain wall
Functionality	complete envelop or external claddings
Ventilation	ventilated or non-ventilated
Finishing system	siding; DAFS or EWIS

Source : author.

This work focuses on the behavior of a curtain wall, non-ventilated façade enveloping the building. However, modeling the different façades compositions quickly

become a rough task due to the several variables. For this reason, this study concentrates on assessing the mechanical behavior of the fiber cement boards and its fixations on the metal frame structure. No finish system was taken into account on the numerical models, even if it is known that coatings and joint treatments can play an important role on the design of these façade panels. A specific study need to be done for the design of those finishing systems or joint treatments, the behavior of these components can be properly considered to avoid any cracking risk on the system.

1.3. Design parameters

The design of an LSF façade, in this work, consists on the mechanical design of the metal frame structure and its fixing systems, including the fixation on the main structure of the building and the board screwing on the frame. This way, each component must attend their specific standard requirements, ensuring the performance of the complete façade panel. Some technical definitions were standardized by the market as usual profile sections, vertical studs spacing, board geometry, screwing recommendations, among other definitions.

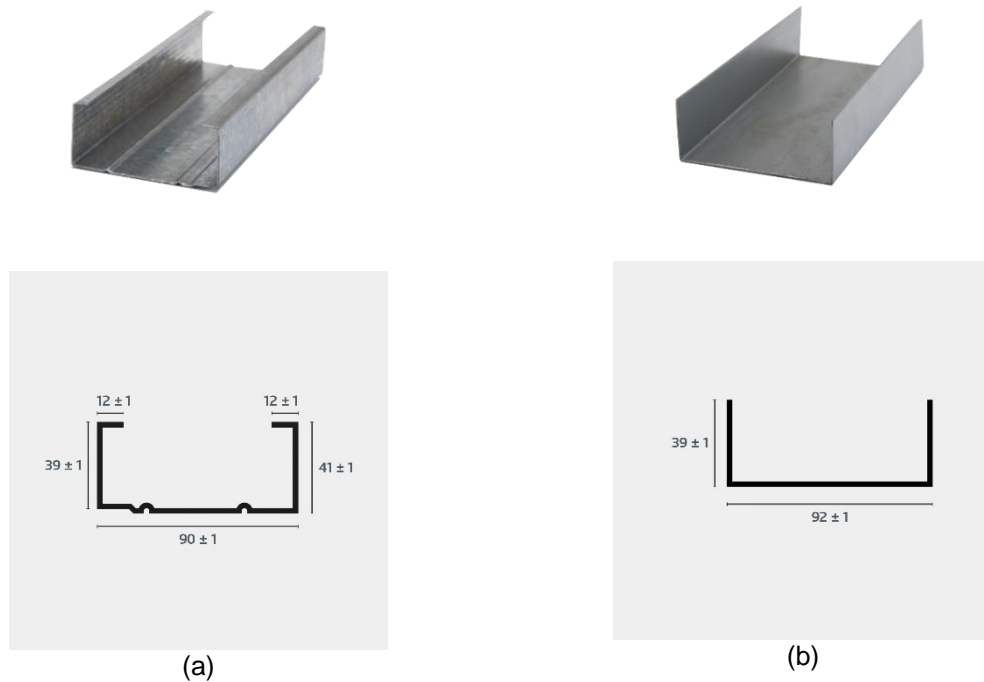
The main design parameters, their standard requirements and the usual definitions are presented for the metallic frame, the fiber cement board, the screws and the inserts. The influence and optimization of each parameter will be presented in the following chapters.

1.3.1. Cold-formed steel profiles

The metallic structure is basically composed by the connection between horizontal U tracks and vertical C studs. Typical profile sections are illustrated in Figure 8. Bracing straps or horizontal blockings are also commonly used to assure the stability of the frame, as shown in Figure 9.

The steel profiles are cold-formed and mechanically defined by their yield strength (f_y), their tensile strength (f_u) and their elastic moduli (E_y). All these metallic profiles must be protected against corrosion, mainly because they will be used on external conditions. To avoid rusting, the profiles are zinc-coated or zinc/aluminum-coated by the hot-dip process. ¹⁰

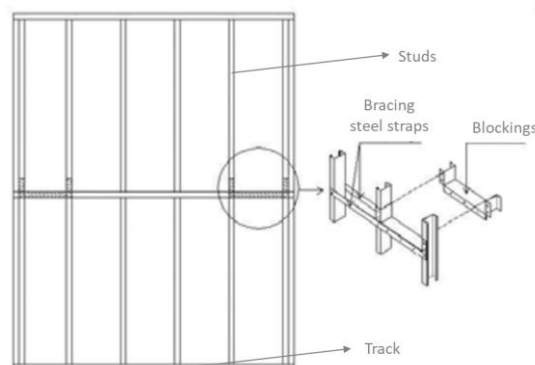
Figure 8: Steel cold-formed profiles. a) C-section studs and b) U-section studs.



Source: Ananda Metais.

Table 2 shows the main material definitions adopted and specified by Brazilian standards for steel cold-formed structural profiles. The usual geometrical dimensions for LSF profiles are indicated in Table 3. Combining depths and thickness it is possible to find the optimized design of the metal profile for different configurations and loads. A 50mm-width profile may be convenient because it facilitates the board screwing, even if it does not have a significant contribution in terms of mechanical strength. ^{27; 28; 29; 30}

Figure 9: : Light steel framing structural components.



Source: adapted from Manual de Steel Frame – Engenharia of CBCA.

Table 2: Brazilian standard specifications and definitions for structural cold-formed steel (CFS) profiles to LSF constructions.

Yield strength (f_y)	$\geq 230 \text{ MPa}$
f_u/f_y	$\geq 1,08$
Elastic modulus (E_y)	200 GPa
Poisson's coefficient (ν)	0,3
Shear modulus (G)	77 GPa
Thermal coefficient (α)	$1,2 \cdot 10^{-5} \text{ }^\circ\text{C}^{-1}$
Specific density (ρ)	7850 kg/m^3
Galvanized coating	$\geq 275 \text{ g/m}^2$ if zinc-coated $\geq 150 \text{ g/m}^2$ if zinc/aluminum-coated

Source: ABNT NBR 15523:2010.

A wall structured on LSF is then composed by studs that transmit the loads vertically through their webs. The studs are usually assembled on 400mm or 600mm each. These modulations are chosen due to the standard dimensions of the boards.

Table 3: Usual dimensions adopted to LSF profiles.

	Vertical studs	Horizontal tracks
Web depth	90mm, 140mm or 200mm	92mm, 142mm or 202mm
Flange width	40mm or 50mm	40mm
Stiffeners length	12mm	-
Thickness	0,8mm, 0,95mm or 1,25mm	

Source: author.

These parameters are necessary to the design of the metal frame structure. The standard profile nomenclature for C-studs contains the complete geometry description of the profile. Profile name is presented, in millimeters, on the form *Web depth x Flanges width x Stiffeners length x Thickness*. For example, a C-stud profile 90 x 40 x 12 x 0,95 is a 0,95mm-thickness profile with a 90mm-depth web and 40mm-width flanges with stiffeners of 12mm. ³⁰

1.3.2. Metal frame dimensioning considerations

For the structural design of the frame, each stud is considered as a wire pinned supported at its extremities. The studs must be designed at combined bending and compression load in the ULS. In the case of a non-load bearing wall, the compression

loads are the self-weight of the steel structure, of the boards and its finishing systems, and the bending is a result of the wind pressure applied on the façade.³¹

As described at 1.3.1, C-studs are an open thin-walled cross-section cold-formed steel profile. Under compression forces, the studs are susceptible to flexural buckling. For this cross section (C-profiles), the shear center and the centroid are not coincident and then the studs are also subjected to lateral-torsional buckling effects (also called lateral buckling or flexural-torsional buckling). Bracing straps or blockings are recommended to reduce or avoid these lateral-torsional effects and can contribute to reduce, in addition, flexural buckling on the minor principal axis direction.³¹

The LSF profiles may also fail by local and/or distortional buckling. Although they present a stable post-critical behavior, the local phenomena can occur combined with global flexural and/or torsional buckling and this combined failure mode presents an unstable post-critical behavior. For these reasons, it is important to highlight that the design of LSF profiles cannot be based on the yield strength of the material. Usually, buckling occurs at a lower stress than the yield one and then buckling verifications become the limiting design criteria.^{31; 32}

In summary, all vertical studs may be designed avoiding failure due to each buckling mode (flexural, torsional, lateral-torsional, local and distortional) and their interaction effects on the effective material strength. Based on these assumptions and following the design equations recommended on the national standards, it is possible to define the maximum horizontal pressure, represented by the maximum wind pressure, which can be withstanding by each profile presented in the Brazilian standards.

Table 4 presents the maximum design wind pressure that can be supported by the most usual cross-sections profiles for a 3-meters high LSF stud. The use of a steel profile ZAR 230 ($f_y = 230 \text{ MPa}$) was assumed. Bracing straps were used at the middle of studs to reduce their buckling length on the minor principal axis direction and on the torsional buckling ($K_y L = K_z L = 1,5m$, studs with no flexural or warping end restraint). The maximum supported pressure was also calculated considering the studs common spacing of 400mm and 600mm. The Ultimate Limit State (ULS) was considered with its corresponding design factors and a total vertical load less than 60 kg/m². The

mechanical contribution of the sheathing board and of its coating system were not taking into account in this calculation. ^{29; 32}

Table 4: Maximum design horizontal loads calculated on ULS for a 3-meters high C-stud profile following the Brazilian standard ABNT NBR 14762:2010.

C-stud LSF profile (ZAR 230)	Maximum design wind pressure - q_{wd} (kPa)	
	400 mm	600 mm
90 x 40 x 12 x 0.8	1,4	0,9
90 x 40 x 12 x 0.95	1,8	1,2
90 x 50 x 12 x 0.95	2,1	1,3
90 x 40 x 12 x 1.25	2,5	1,6
140 x 40 x 12 x 0.95	2,9	1,8
140 x 50 x 12 x 0.95	3,3	2,2
200 x 40 x 12 x 0.95	3,7	2,4
200 x 50 x 12 x 0.95	4,4	2,9
140 x 40 x 12 x 1.25	4,6	3,0
200 x 40 x 12 x 1.25	6,2	4,0

Source : author.

1.3.3. Exterior board

The exterior board is commonly a mineral board. Fiber cement, glassmat plasterboards, OSB or metal plates are the traditional materials used by the market. The standard dimensions of these boards are 1200mm x 2400mm, and they may vary depending on the needs of the project. These boards must resist wind loads and mechanical impacts besides ensure the watertightness of the façade. Furthermore, these elements are specified to facilitate the maintenance and ensure the durability of the system. ³³

To be used on external façades, these boards must present a minimum mechanical strength, measured by its flexural strength. For fiber cement boards, the Brazilian standard requires a minimum average of 4 MPa on flexural strength, measured by the modulus of rupture (MOR) of the board in both longitudinal and transverse directions and on saturated specimens it means after 24 hours of water immersion. Depending on the flexural strength results, the standard defines a specific board category as shown in Table 5. ³⁴

Table 5: Brazilian categories of fiber cement boards without asbestos for external use according to its mechanical strength.

Boards Class A (external use)	Minimum average flexural strength required - σ_{adm}
Category 1	-
Category 2	4 MPa
Category 3	7 MPa
Category 4	13 MPa
Category 5	18 MPa

Source: ABNT NBR 15498 :2015.

For the different boards categories, it is possible to determine the maximum design wind pressure allowed when these boards are applied on a metal frame structure with studs spaced by 400mm or 600mm. In the ULS, a design load factor of 1,4 ($\gamma_f = 1,4$) and a design strength reduction factor of 1,4 ($\gamma_r = 1,4$) were applied. The strength reduction factor for the fiber cement material was adopted similarly to the design factor recommended for concrete structures, considering the variability of the mechanical properties of a fiber cement board. For a first approach, the board applied on the frame subjected to wind pressure can be considered as a simply supported beam with a span equal to the studs spacing under a distributed load. Then, the maximum allowed load is done by (1).

$$q_{wd} \leq \gamma_f \frac{8}{l^2} \frac{bt^2}{6} \frac{\sigma_{adm}}{\gamma_r} \quad (1)$$

Table 6: Maximum design horizontal load supported in ULS by a fiber cement board.

Fiber cement boards without asbestos – Class A (ABNT NBR 15498:2015)	Maximum design wind pressure - q_{wd} (kPa)	
	400 mm	600 mm
Category 2	1,7	0,8
Category 3	3,0	1,3
Category 4	5,5	2,5
Category 5	7,7	3,4

Source: author.

Where q_{wd} is the design wind pressure, b is equal to 1m, l is the span or in this case the studs spacing, t is the board-thickness, σ_{adm} is the minimum required stress

of the board and γ_f and γ_r are the ULS factors. The results of (1) for the different board categories are exposed in Table 6. ¹⁹

Fiber cement boards are sensitive to hygrometric conditions. Usually these boards present an important level of water absorption (~30% in mass). Additionally, its dimensional variation by hygrometric effects is relevant. The hygrometric movements of the board can become the most critical effects on a board during its service life.

1.3.4. Screws fixing

The external fiber cement boards are usually fastened over the metal frame by self-drilling screws with or without wings measuring 4,2mm x 32mm. Some technical catalogs recommend a minimum edge distance of 10mm of the screws on the fiber cement board. Other suppliers recommend a minimum edge distance of 15mm within the board, which implies the use of a 50mm-flange width studs. ^{35; 36}

These screws must be dimensioned to prevent the pull through of the board due to wind actions and the sliding of the board due to its self-weight. In addition, the fixing system must be designed to avoid the collapse of the board edges by shear effects and to allow the in-plane displacements of the board, avoiding stress concentration caused by the hygrothermal dimensional variations of the fiber cement material.

Admitting a uniform distribution of horizontal loads (q_{wd}) on the façade and on each screw, it can be defined the number of screws (n_{screw}) required on each stud. In the equation (2), d_{st} is the studs' distance, L_{board} is the length of a single board (usually the same length of the stud, to avoid horizontal joints) and $F_{d,pull-through}$ is the pull-through design strength of a screw on the board.

$$n_{screw} \geq \frac{q_{wd} L_{board}}{F_{d,pull-through}} \quad (2)$$

Additionally, it can be calculated, as shown in (3), the maximum vertical screw distance (s_{screw}) to support a specified horizontal pressure. For the horizontal screw distance, the same stud spacing length will be assumed. Adopting the results obtained in 1.3.4 and a pull-through design value equal to 502 N, the maximum screw spacing is summarized in Table 7 for the different frame choices.

$$s_{screw} \leq \frac{L_{board}}{n_{screw} - 1} \quad (3)$$

Besides the verification of the pull-through screw strength in relation to wind forces, it is important to understand the stiffness of these screwed connections and its influence on the stress concentration on the board. During the aging of the material, these connections can become stiffer and imply on more important stress concentration due to hygrothermal movements of the board. A numerical study of these effects is presented in chapter 5.

Table 7: Maximum vertical screw spacing to support horizontal loads.

C-stud LSF profile (ZAR 230)	Maximum screw spacing – s_{screw} (cm)	
	400 mm	600 mm
90 x 40 x 12 x 0.8	100	150
90 x 40 x 12 x 0.95	75	75
90 x 50 x 12 x 0.95	75	75
90 x 40 x 12 x 1.25	60	60
140 x 40 x 12 x 0.95	50	50
140 x 50 x 12 x 0.95	43	43
200 x 40 x 12 x 0.95	38	38
200 x 50 x 12 x 0.95	30	33
140 x 40 x 12 x 1.25	30	30
200 x 40 x 12 x 1.25	23	23

Source: author.

1.3.5. Inserts

Depending on the choice of the fixing system, different types of inserts may be proposed. The optimized choice is also made based on the material of the main structure of the building. The inserts elements must be able to withstand mainly the wind pressure and suction and to transmit the loads arriving on the façade system to the main structure of the building. In addition, these anchor elements should be capable to absorb and accommodate differential displacements between the main structure and the façade system, besides compensating plumb line deviations.

In the case of an infill wall, the bottom track is attached to the floor and the upper track is attached to the upside of the floor above. This attachment may be provided by structural screws. The number of screws and their spacing must be specified according to the structural project, considering the applied loads and the combination of actions, disposed in a double line 40mm each, or by bolts, fastened 1200mm each.

For a curtain wall system, special inserts designed on steel L section profiles are bolted on the main structure and screwed on the web of studs. Figure 4 has shown an example of these inserts. Depending on the project, it is possible to bolt all studs, or the inserts may be spaced, for example, 1200mm each. The design of the inserts and the number of bolts must be specified depending on the structural framing dimensions and wind loads considerations. Usually, if correctly calculated, they are not the most critical point to the system due to the large portfolio of bolts in terms of traction strength available on the market. ¹⁹

1.4. Concluding remarks

Light steel framing façades have been gradually introduced in the Brazilian market. Their benefits, such as the productivity increase, the waste generation reduction and the construction time optimization, have motivated constructors to move on this industrialization way. As a modular system, these façades can be used from different manners.

By combining different construction process, fixing typologies and even different finishing systems, these LSF façades can be used as the building envelope or as an external cladding. The choice of the desired façade functionality implies on its typology definition and, consequently, on the setting of the design variables and parameters. For example, the design of a curtain wall differs from an infill wall project, especially for the inserts and structural fixing design.

This work is based on the analysis of a curtain wall system, considering the façade as the complete building envelope and without any rendering system or joint treatment. Hence, the main parameters were defined to ensure a proper façade performance assessment:

- Metal profile: must be designed to withstand its self-weight and wind loads;
- External board: it has to be characterized to define an adjusted numerical model able to simulate its constitutive behavior;
- Screw fixing: must be designed to resist the pull-through forces, even considering their interaction with the board and aiming to prevent cracking;
- Structural inserts: must be designed to support the façade panel and to anchor it in the main structure of the building.

2. WIND LOADS ON FAÇADES

Numerical model input definition: Design loads

High and slender buildings with lighter and more flexible architectural systems are increasingly present on cities. The preference for these slender buildings implies a higher importance on wind actions considerations. Static and dynamic horizontal loads become the design criteria for lightweight and flexible structures, even though these loads have a few or no influence on the design of heavy constructions.

Lightweight façades systems are even more susceptible when subjected to horizontal loads. The façade system shall be able to withstand the wind and, in case of load-bearing walls, they might be able to carry and transfer the wind loads and the structural loads. Load or non-load-bearing façades, both must be designed to carry the static and dynamics effects of wind-induced pressure and suction.

The description of wind-induced effects on buildings depends on the evaluation of meteorological parameters and on the aerodynamics description of the building ³⁸. The wind velocity field is described as statistical functions and the wind-induced pressure is determined by aerodynamics admittance with spatial coherence ³⁹. The statistical description of the wind velocity field and its relation with wind-induced pressure has started with Davenport, in the 1960s, and, since then, it has been studied for many authors. ^{37; 38; 39}

Furthermore, for façades elements analysis the consideration of local wind effects will be necessary. These local effects are associated with the peaks of wind velocity field. Different techniques and methods to calculate extreme wind speeds and extreme values for peak loads are presented on the literature ^{40; 41; 42; 43}. The differentiation between local effects and global effects is important on the analysis and on the design of small elements as façades fixing systems for example.

Wind speed fluctuations can also generate dynamic effects on the structure. This study is focused on the static effects of wind loads and their influence on façade elements design, assuming that dynamic effects will be covered by the design of the main structure of the building.

National building codes were written defining and detailing national techniques to describe wind velocity fields and define wind-induced pressures. Many recognized standards follow the same reasoning, but sometimes they adopt different statistical

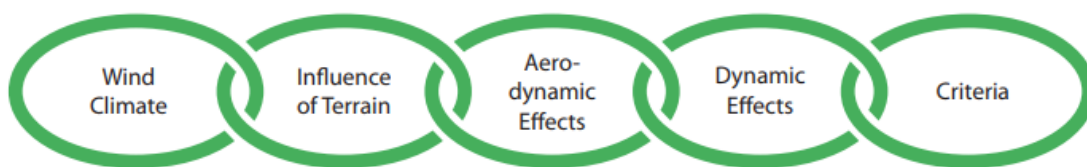
techniques and different aerodynamic considerations. Regarding wind-induced pressure on façades elements, for example, the differentiation between global and local wind effects is not always clearly presented. ⁴⁴

This chapter presents the parameters and coefficients widely used to describe the wind action on buildings, including a discussion about the main techniques and considerations to calculate the wind-induced pressures. A comparison between four international codes will illustrate the convergence and the differences on the literature regarding wind actions analysis, especially regarding the considerations of static wind effects on façades elements design. An example of wind pressure calculation closes the chapter showing the quantitative difference using the different codes and their specifications for local and global wind effects.

2.1. Wind actions on buildings

Davenport (1982) proposes a sequence of steps to assess wind load on buildings. The so called **Davenport wind loading chain**, illustrated by the Figure 10, shows that wind-induced loads are the result of two effects: a natural-one which considers, for example, the meteorology, terrain conditions and neighborhood effects and a geometrical-one, addressing the building shape and dimensions and the building aerodynamic influences. ^{45; 46}

Figure 10: The Alan G. Davenport wind loading chain.



Source: Irwin et al. (2013)

The natural effects depend on the expression of wind climate and the influence of terrain. A description of the wind velocity field determines the important parameters of mean speed, turbulence intensity and wind fluctuations acting on the building. The terrain conditions, as surface roughness, combined with the wind velocity field define the wind dynamic pressure. ^{45; 47}

This dynamic wind flow in relation to the building turns into a wind-induced pressure. To define the induced pressure on a surface the Bernoulli's equation is used

for an inviscid, barotropic and steady flow. And then, the wind-induced pressure on a surface is expressed by a general equation (4).⁴⁸

$$p_s = qC_p = \frac{1}{2}\rho_{air}U^2C_p \quad (4)$$

Where p_s is the pressure on a surface; q is the wind dynamic pressure; C_p is the pressure coefficient, which will be described in details in section 2.1.2; ρ_{air} is the air density and U is the wind speed.

Equation (4) shows that the wind speed and a pressure coefficient must be defined to obtain the wind pressure acting on a building. The first parameter will be defined contemplating meteorological aspects, dimensions of the building and terrain considerations. The second one will be calculated in function of the geometry of the building and its aerodynamic aspects.⁴⁹

Wind flow presents general characteristics around a high-rise building. On the windward face, the stagnation point is located at a height of 70-80% of the total building height. The flow downs below this stagnation point at the windward wall. Side walls can be subjected to high local pressures and the leeward face is subjected to a low level of suction.³⁹

2.1.1. Characteristic wind speed

2.1.1.1. Wind speed definition

The wind speed is composed by the so-called basic wind speed multiplied by different coefficients considering the local of the building construction, the neighborhood, the topography and statistical effects.⁴⁹

The wind velocity field varies with height, and its profile depends on the terrain roughness and on the proximity of obstacles as trees, higher buildings and others. Mathematical laws are used to describe the wind speed variation on height. Often, national standards use a logarithmic law or a power law to describe the wind velocity profile above the surface. The logarithmic law is considered the most accurate expression in strong wind conditions near the surface, whereas the power law is more convenient to calculate resultant forces and moments because it is an easily integrated function.³⁹

Besides its spatial variability, the wind speed is a random variable time-dependent. Mathematically, the wind can be modeled as a stochastic process by a

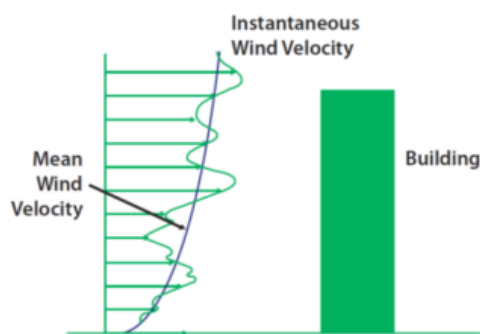
time-dependent function. As a random process the wind speed can be represented by defining a mean (\bar{U}) and a fluctuation (σ_u) on the time, according to equation (5). The mean wind speed depends on the averaging period (usually taken as ten minutes or one hour, for example) and the fluctuation is represented by a peak factor (g) that indicates local speed values on the time. Figure 11 represents the wind profile acting on a building. ³⁷

$$\hat{U} = \bar{U} + g\sigma_u \quad (5)$$

The mean wind speed usually corresponds to global wind effects on the buildings. The peak factor, in contrast, is related to local effects and defines the peak values, or the expected peak gust (\hat{U}), of the wind speed function. The ratio of the peak gust to the mean wind speed within an averaging period is called gust factor (G). The estimation of peak values defines the gust factor and the peak gust. ^{41; 42; 43}

Considering these different parameters on the wind speed definition, most national standards define a basic wind speed by geographic location in a country. The basic wind speed is the wind speed measured under controlled conditions, that is, at same height, in a flat and opened terrain and calculated with a specified gust factor and recurrence time. The particularities of each specific building are then contemplated by several coefficients. These coefficients aim to adapt the standard wind velocity to the specific situation, considering the shape and dimensions of the building for example. ³⁹

Figure 11: Wind profile - Mean speed and gusting.



Source: Irwin et al. (2013)

Basic wind speeds are obtained by a statistical treatment of historical data on recorded wind speeds. The statistical analysis must be based on an extreme value distribution. Fisher and Tippett were the first to propose an analysis of the largest values for a random variable. They identified three types of distributions to represent extreme

values. Gumbel, at the beginning of 1950s, adopted the distribution Fisher and Tippet type I applied on his wind studies. This distribution, then called the Gumbel distribution, became the most used in several national standards. These statistical distributions need a separation of the recorded data by storm type to present a good fit. As well as the Gumbel distribution, in some cases the distribution Type II or even Type III can be used. They are known as the Frechet distribution and the Weibull distribution, respectively. Distributions Type I and Type II are unbounded, whereas distribution Type III has an upper limit. ^{38; 40; 41}

Besides the distribution type, basic wind speeds depend on the measuring length or the averaging time. Usually, national standards take an average time of 3 seconds or 10 minutes. It was demonstrated by Zhou et al., in 2002, that the basic wind speed defined in a 3s measurement is equal to 1,48 times of the wind speed taken in a 10min register. ⁵⁰

2.1.2. Aerodynamics pressure coefficients

When a flow with a specific velocity finds a solid, this flow exercises a pressure on it. At the exact point where the flow is perpendicular to the solid, called the stagnation point, the flow velocity is zero and the pressure caused by wind at this point is called the **dynamic pressure**. However, the flow in other points becomes turbulent and presents a non-zero velocity generating wind induced pressures at all the solid according to the ratio of the current fluid speed to the initial speed. The relation between the total pressure (p_s) by the dynamic wind pressure (q) at a specific point of the building is represented by a coefficient, called the **pressure coefficient** (C_p). ^{48; 51}

Wind generates an external pressure due to the aerodynamic shape of the building. In addition, due to openings or leakages the wind can also generate an internal pressure. To calculate the pressure coefficient, the combination of external and internal wind induced pressure effects must be described in each wall of the building. ^{52; 53; 54}

Some national standards recommend different pressure coefficients considering local or global effects. It means that the pressure coefficients for the design of large elements or to verify the global stability of a structure can be different of those to design specific and small elements, as façades fixing or joints. However, local winds

are not always considered correctly by the national codes, sometimes they provide non-conservative responses.^{55; 56}

2.1.2.1. External pressure coefficients

To obtain the dynamic pressure, the velocity intensity must be determined at each point. Wind tunnel tests can provide these results, producing a complete description of the dynamic pressure distribution on a building. This pressure distribution, due to the geometry of the building, can be expressed by the **external pressure coefficients**. Although the wind tunnel measurements are reliable, they can take a lot of time and be economically expensive.

For simple building shapes, most national standards offer pre-defined values of external pressure coefficient intending to facilitate the design process. In all cases it is important to consider the different wind directions and differentiate positive pressure effects and the negative pressure ones (suction).

2.1.2.2. Internal pressure coefficients

If the building is completely sealed, the wind flow will generate pressure only on the external faces of the building. However, the buildings have openings (windows, doors or even gaps) and the wind can pass through the building generating an internal pressure. This **internal pressure coefficient** will be calculated as a function of the opening area and the opening location on a façade, that is called **building permeability**. The definition of a realistic internal pressure coefficient is not evident. We cannot adopt an overstated hypothesis, but incorrect hypothesis on internal pressures or even unexpected openings due to flying debris, for example, can generate high pressure values. These unplanned high pressures have been a critical cause of accidents, especially with openings on windward faces.^{57; 58; 59}

Different cases must be analyzed as a single dominant opening in one wall (windward wall, sidewall or leeward wall), multiple wall openings or the effect of wall permeability. Despite the different opening combinations, walls with a dominant opening present an important interaction between internal and area-averaged external pressure, and the wall corners are more susceptible to high suction pressures.^{60; 61; 62}

If the building presents cross-openings, the internal pressure coefficients are not uniform. In some cases, cross-openings may present critical values more important than a single dominant windward opening.⁶³

2.2. International standard comparison

The different national building codes follow the same idea of the wind loading chain of Davenport. The coefficients and the composition of each parameter may change in each code, such as the wind speed and wind-induced pressures calculation. However, all national standards recommend the evaluation of the same variables:

- Basic wind speed: obtained for statistical treatment of historic meteorological data series;
- Surface roughness and neighborhood effects;
- Topography and height of the building;
- Shape-factors: the building dimensions have influence on the gust factor and on the pressure coefficients determination

These are the basic parameters considered by the building codes. However, other variables may be considered by some codes, as wind directionality and localized effects, for example. A comparison of different international codes was done by different authors to compare the dynamics considerations of each code and the wind speed parameters used on each standard. ^{39; 50; 64; 65}

On this work, the Brazilian standard for wind actions (NBR 6123:1988) is compared with three other wind codes: the European (EN 1991-1-4:2005), the USA (ASCE 7-10) and the Australian and New-Zealand (AS/NZS 1170.2:2011) standards. This comparative analysis aims to identify similarities and the main differences on the definition of wind-induced pressure on façades systems and their components. A description of the different global or local parameters and coefficients used in each code is presented, followed by a comparative example to illustrate.

2.2.1. Characteristic wind speed

2.2.1.1. Wind speed definition

The basic wind speed, also called the reference wind speed in some standards, is always a value measured at 10m height in a flat and opened terrain. Although, the gust factor and the recurrence period change from one standard to another. Table 8 summarizes the different averaging time and return period for the studied standards. The AS/NZS 1170.2:2011 is the only code that presents the wind speed as a function of different return periods ³⁹. After having defined the basic wind speed, following

standard measuring parameters, this value must be corrected to represent the wind speed in a specific condition of terrain, height and exposure of the building.

Table 8: Basic wind speeds parameters for different national codes.

Standard	Averaging time	Return period
NBR 6123:1988	3 s	50 years
EN 1991-1-4:2005	10 min	50 years
ASCE 7-10	3 s	50 years
AS/NZS 1170.2:2011	3 s	1 to 10000 years

Source: adapted from Holmes (2013).

2.2.1.2. Correction factors

All the analyzed standards use correction factors to adapt the basic wind speed to each specific construction. Only the American code applies the correction factors on the dynamic pressure. The other codes include these factors modifying the wind speed according to terrain roughness, topography and building height. ^{66; 67; 68; 69}

Table 9 shows a description of how each code considers wind speed modifications for each construction condition. Topography, roughness and height effects are considered in all codes even if with different values or laws. For example, the Australian and the European code use a logarithmic law to describe the speed variation with height, while the American and the Brazilian ones use a power law.

Wind directionality is assessed in all codes, except in the Brazilian one. The Australian and New-Zealander code, for example, defines a site wind speed for each cardinal direction ($V_{sit,\beta}$) and takes the most critical case, i.e. the largest value, to the design ($V_{des,\theta}$). In most cases, neglecting the wind directionality results in a conservative analysis. But in other cases, this consideration may be convenient to avoid an oversizing design, for example. Neglecting the wind directionality may provide a wind speed more than 2 times greater than the actual speed, but sometimes the available meteorological data are not sufficient to describe the directional distribution of the wind. ⁷⁰

Table 9: Wind speed parameters in different international codes.

Standard	Parameter	Definition	Wind speed
NBR 6123:1988	V_0	<u>Basic wind speed</u> 3s gust wind speed for annual probability of exceedance of 63% in a return period of 50 years.	$V_k = V_0 S_1 S_2 S_3$
	S_1	<u>Topographic factor</u> Considers the relief variation of the construction site. It is equal to 1,0 on flat terrain and it is less than 1,0 in wind-sheltered valleys or more than 1,0 in slopes.	
	S_2	<u>Roughness factor</u> Classifies a terrain according to its roughness and takes into account the building height using a power law.	
	S_3	<u>Statistic factor or importance factor</u> Defines the annual probability of exceedance. Also considers the importance of the building according to its occupation and the gravity in case of ruin.	
EN 1991-1-4:2005	v_b	<u>Reference wind speed</u> Basic wind speed corrected by wind directionality factors. Generally, the directionality factor taken is equal to 1,0.	$v_m(z)$ $= v_b c_r(z) c_o(z)$
	$c_r(z)$	<u>Roughness coefficient</u> Corresponds to the S_2 factor of the Brazilian standard. However, uses a logarithmic law instead of a power one.	
	$c_o(z)$	<u>Orographic coefficient</u> Corresponds to the S_1 factor of the Brazilian standard, but with different recommended values.	
AS/NZ 1170.2:2011	V_R	<u>Regional speed</u> Regional 3s gust wind speed for annual probability of exceedance of 1/R, given by the national wind charts	$V_{sit,\beta}$ $= V_R M_{(z,cat)} M_s M_t M_d$
	$M_{(z,cat)}$	<u>Terrain/height multiplier</u> It corresponds to the S_2 factor of the Brazilian standard, but considering a logarithmic law.	
	M_s	<u>Shielding multiplier</u> Allows a reduction on the wind speed consideration in case of shielding provided by upwind buildings or other structures.	
	M_t	<u>Topographic multiplier</u> Corresponds to the S_1 factor of the Brazilian standard, but with different recommended values.	
	M_d	<u>Directional multiplier</u> Considers the wind directionality for each cardinal direction. It can be taken equal to 1,0 in general cases, for a conservative analysis.	

Source: author.

Defining the characteristic wind speed, it is possible to calculate the wind dynamic pressure. As exposed in Table 10, the dynamic pressure is the product of the mass air density by the square of the characteristic wind speed. The ASCE code applies the correction multipliers at this stage, adopting an exposure (K_z), a topographic (K_{zt}) and a directionality (K_d) coefficients. The Eurocode includes an exposure coefficient (c_e) on the dynamic pressure definition to take into account the turbulence intensity in addition to roughness and orographic considerations. This factor is height-dependent and converts the dynamic pressure into a gust pressure.

Table 10: Wind-induced pressures from different international codes.

Standard	Dynamic pressure	Mass air density* ρ (kg/m ³)	Wind-induced pressure on a wall
NBR 6123:1988	$q = \frac{\rho_{air} V_k^2}{2}$	1,225	$p_s = C_p q$
EN 1991-1-4:2005	$q = c_e(z) \frac{\rho_{air} v_b^2}{2}$	1,250	$w_e = q c_{pe}$ $w_i = q c_{pi}$
ASCE 7-10	$q = \frac{\rho_{air} K_z K_{zt} K_d V^2}{2}$	1,225	$p_s = q(GC_p)$
AS/NZ 1170.2:2011	$q = \frac{\rho_{air} V_{des,\theta}^2}{2}$	1,200	$p_s = C_{fig} C_{dyn} q$

*defined at standard atmosphere and sea level pressure

Source: adapted from Holmes (2013).

2.2.2. Aerodynamic pressure coefficients

Aerodynamic coefficients are used to transform the dynamic pressure on wind-induced pressure giving the wind effects on a surface. Different forms to calculate the wind-induced pressure can be seen in Table 10, following the international codes.

All standards demand an analysis of the external and internal pressures caused by the wind. In the Eurocode, an explicit description of the external and internal pressure determination is found. Other codes present a unique pressure coefficient, which is then composed by the combination of external and internal effects on the building. ^{66; 67; 68; 69}

2.2.2.1. External pressure coefficients

External pressure coefficients are presented in all codes for rectangular buildings. The standards indicate a mean pressure coefficient for each wall of the

building according to the wind direction and the plan dimensioning of the building. A wind tunnel test is recommended for most complex combinations between building shapes and wind direction to give a precise aerodynamic characterization.

The ratio of elevation by plan dimensioning defines the external pressure coefficient of the building. Highest buildings are always the most critical cases. In all standards, a square building is the most critical configuration, because it implies on higher suction values on the leeward wall. A graphic schema is presented in Figure 12 representing the wind pressure distribution around a building plan.

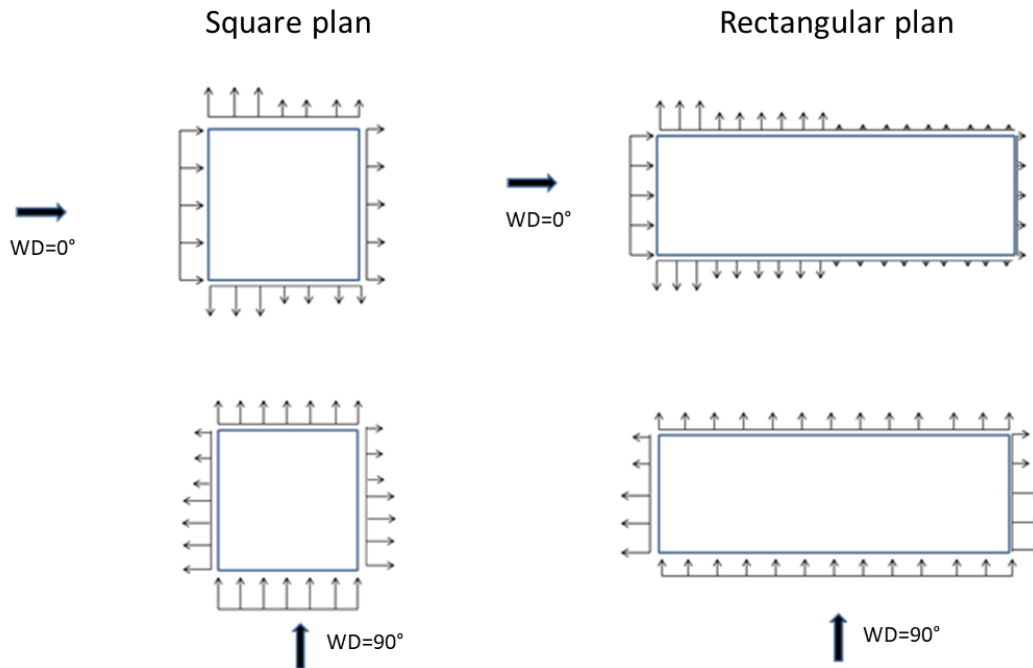
The Eurocode gives different external pressure coefficients (c_{pe}) as a function of the area of the element, less than 1m^2 for local effects considerations and more than 10m^2 for the design of major structural members (global effect). It explicitly recommends the use of local external pressure coefficient values to design claddings and façades fixing systems.

The ASCE wind code is subdivided in two parts: the Main Wind Force-Resisting System (MWFRS) design and the Components and Claddings design. For the first structure type, the design considers a global effect of the wind, and for the second one, local effects are taken into account. The gust factor is also considered on the pressure coefficient definition done by the GC_{pe} symbol.

The Australian code presents an aerodynamic shape factor (C_{fig}). It is composed by an external pressure coefficient multiplied by a local pressure factor (K_l) and by an area reduction factor (K_a) to consider local effects, mainly on claddings and façades design. A porous claddings reduction factor (K_p) is used for non-permeable claddings.

In the three presented cases, local wind effects result on higher pressure coefficients values. It means that local pressure effects are more important than the global one. On the other hand, the Brazilian standard doesn't consider any explicit differentiation of local and global wind effects. It gives a more conservative gust factor for the design of façades, but it recommends a low importance factor for this design. This combination implies on local pressure coefficients lower than the global ones, unlike the other studied standards.

Figure 12: Schema of wind pressure distribution on buildings plans.



Source: author.

2.2.2.2. Internal pressure coefficients

Most of the codes consider the ratio of dominant openings to the total open area on a wall to define the internal pressure coefficient. The ASCE 7-12 classifies the buildings in open, partially enclosed and enclosed, and attributes values between +0,55 and -0,55 of GC_{pi} based on this classification. The three other codes consider different opening situations to define the internal pressure.

Table 11 summarizes the internal pressure coefficient definition and the main values for the four compared standards. A negative value indicates suction effect on the wall and the positive ones indicate a positive pressure acting internally.

Table 11: Internal pressure coefficient definitions from different national codes.

Standard	Hypothesis	Criteria	Internal pressure coefficient
NBR 6123:1988	1) Two opposite faces permeable and other walls impermeable	Wind perpendicular to the permeable faces	+0,2
		Wind perpendicular to the impermeable faces	-0,3
	2) All faces equally permeable	Adopt the most critical	-0,3 or 0
	3.1) Dominant opening on windward wall	$A_{dom,open}/A_{suction}$	+0,1 to +0,8
	3.2) Dominant opening on leeward wall	Suction effect on the opening	C_{pe} of leeward wall
	3.3) Dominant opening on sidewall	Central zones (low suction region)	C_{pe} of leeward wall
		Highest suction regions	-0,4 to -0,9
4) All faces equally impermeable	Adopt the most critical	-0,2 or 0	
EN 1991-1-4:2005	1) One face with dominant opening	$A_{dom,open}/\sum A_{open} = 2$	$0,75 * C_{pe}$ of dominant face
		$A_{dom,open}/\sum A_{open} \geq 3$	$0,9 * C_{pe}$ of dominant face
	2) All faces equally permeable	$\mu = A_{suction}/A_{open}$	-0,5 to +0,35
	3) Impossible or non-justified permeability determination (μ)	Adopt the most critical	-0,3 or +0,2
ASCE 7-10	1) Open buildings	All faces with at least 80% of openings	0
	2) Partially enclosed buildings	I. $A_{dom,open}/\sum A_{open} > 1,1$ and II. $\min(A_{dom,open}/\sum A_{dom} > 0,1, A_{dom,open} > 0,37m^2)$ and III. $\sum A_{open}/A_{total} \leq 0,2$	-0,55 or +0,55
		3) Enclosed buildings	None of above criteria
AS/NZ 1170.2:2011	1) Two opposite faces permeable and other walls impermeable	Wind perpendicular to the permeable faces	+0,6
		Wind perpendicular to the impermeable faces	-0,3
	2) All faces equally permeable	Adopt the most critical	-0,3 or 0
	3.1) Dominant opening on windward wall	$A_{dom,open}/\sum A_{open}$	-0,3 to +0,2 or C_{pe} of windward wall
	3.2) Dominant opening on leeward wall		-0,3, 0 or C_{pe} of leeward wall
	3.3) Dominant opening on sidewall		-0,3, 0 or C_{pe} of sidewall
	4) All faces equally impermeable	Adopt the most critical	-0,2 or 0

Source: author.

2.3. Comparative example

A comparative study case is proposed to illustrate the differences of each standard and to compare the pressures done by each one. This exercise shows the quantitative difference for considering global effects or the local wind effects. It is also showed that the Brazilian standard recommendations imply less conservative results than other standards in case of local wind effects.

The standard typologies adopted by constructors for residential buildings are usually the rectangular plans or the H-plans buildings, as shown in Figure 13. The H-plan can be studied as a square plan, with simplified solutions on all standards. The square plan shape is the most critical case, mainly regarding negative pressures.

Figure 13: Building examples with standard plans. a) Rectangular building. b) H-plan building.



Source: Google Maps. Access on 27nd January, 2017.

Besides the square plan shape, this example considered:

- A 30-floor building, around 90 meters high;
- A building in São Paulo, Brazil, with a basic wind speed of 40 m/s;
- A flat terrain in a suburban housing area.

The parameters to obtain the characteristic wind speed, the dynamic pressure and the wind-induced pressure were presented according to the different standards. Wind directionality was neglected to simplify the comparative exercise. All analyses were done considering the worst case, that is, the suction effect at the corner of the windward wall.

2.3.1. Characteristic wind speed and dynamic pressure determination

2.3.1.1. Brazilian standard NBR 6123:1988

As shown in Table 9, the Brazilian standard adopts three modifier coefficients to define the characteristic wind speed: S_1 , S_2 and S_3 .⁶⁶

For a flat terrain, $S_1 = 1,0$.

The S_2 factor corresponds to a combination of building height, gust factor and terrain roughness. The suburban housing area is considered a terrain of Category IV on the Brazilian standard. The NBR standard indicates a 10s gusting time for high buildings (Class C) and a 3s gusting time for claddings and façades fixing or elements design (Class A). The S_2 value adopted is correspondent to the top of the building, at the highest point.

Different S_3 minimum values are required for the building design or the façades elements design. The S_3 value changes due to the different recurrence period chosen in each case. In general cases, the Brazilian standard considers a recurrence period of 50 years ($S_3 = 1,0$) but for façades and claddings design a recurrence period of 22 years ($S_3 = 0,88$) is indicated. However, a lower dynamic pressure is obtained for the design of local elements when adopting a reduced value for the S_3 factor. These results do not agree with the expected one, i.e., more important pressure values for local wind effects. For this reason, the same recurrence time of 50 years and the correspondent S_3 factor equal to 1,0 are even proposed for façades and claddings.⁴⁸ Table 12 presents the wind dynamic pressure obtained from those considerations.

Table 12: Wind speed and dynamic pressure defined by the Brazilian standard.

Wind effect	V_0 (m/s)	S_1	S_2	S_3	V_k (m/s)	q_0 (kPa)
Global effect	40,0	1,00	1,08	1,00	43,0	1,13
Local effect	40,0	1,00	1,12	0,88	39,4	0,95
Proposal for local effect	40,0	1,00	1,12	1,00	44,8	1,23

Source: author.

2.3.1.2. European standard EN 1991-1-4:2005

The expressions done by the European standard are based on a wind speed defined on 10min-average time measuring. As the basic wind speed of 40 m/s is

defined on a 3s-average time measuring, this value has to be converted as described on 2.1.1.1 to obtain the reference wind speed (v_b).

The orographic coefficient is equal to 1,0. The roughness terrain adopted is Category III. For this category at 90m-height the roughness coefficient is 1,23. The dynamic pressure is obtained using a gust factor (I_v) of 0,18 and a correspondent exposure coefficient (c_e) equal to 3,36.⁶⁹

At this stage, any differentiation between global and local effects are indicated, as shown in Table 13.

Table 13: Wind speed and dynamic pressure defined by the European standard.

Wind effect	V_0 (m/s)	v_b (m/s)	c_0	c_r	v_m (m/s)	c_e	q_p (kPa)
Local and global effect	40,0	27,0	1,00	1,23	33,2	3,36	1,50

Source: author.

2.3.1.3. North American standard ASCE 7-10

The modifier factors are applied only on the definition of the dynamic wind pressure. However, these coefficients are similar to those of other standards.

The directionality (K_d) and the orographic (K_{zt}) coefficients taken are 1,0. The exposure coefficient (K_z) is calculated for a building on a region classified as Exposure B by the American standard.⁶⁷

The dynamic pressure obtained is the same for local or global effects, as reported in Table 14. The differentiation of these effects is made for the pressure coefficients.

Table 14: Wind speed and dynamic wind pressure defined by the ASCE standard.

Wind effect	V_0 (m/s)	K_d	K_{zt}	K_z	q_z (kPa)
Local and global effect	40,0	1,00	1,00	1,35	1,32

Source : author.

2.3.1.4. Australian-New Zealand standard AS/NZS 1170.2:2011

Based on the same hypothesis used on the other standards, the directional coefficient (M_d), the topographic coefficient (M_t) and the shielding multiplier (M_s) are equal to 1,0.

The terrain/height multiplier is defined similar to the roughness coefficient on the Brazilian standard, but following a logarithmic law. The AS/NZS standard classifies the terrain as Category 3. This results in a terrain multiplier of 1,15 for a 90m-building. ⁶⁸

Local effects and gusting are not taken into account on the dynamic pressure definition, as indicated in Table 15.

Table 15: Wind speed and dynamic wind pressure defined by the Australian-New Zealand standard.

Wind effect	V_R (m/s)	M_d	M_t	M_s	M_z	$V_{des,\theta}$ (m/s)	q_z (kPa)
Local and global effect	40,0	1,00	1,00	1,00	1,15	46,0	1,30

Source: author.

2.3.1.5. Summary of dynamic wind pressure results

Comparing the results, Table 16 shows that the Brazilian standard is the only one that differentiates the local and global effects of wind for the dynamic wind pressure definition. Despite considering these effects, the standard proposal penalizes local effects, resulting in a dynamic wind pressure much lower than other standards.

The results provided by the American and by the Australian-New Zealand standards are similar, even if they use different roughness laws. The European standard is the most conservative providing the greatest dynamic pressure value.

The proposal for local considerations on Brazilian standards explained on 2.3.1.1 provides results closer than the other national standards. Even if the dynamic pressure obtained stays the lowest, the value becomes comparable to the other codes.

Table 16: Summary of dynamic wind pressure results.

Standard	Variation on height	Wind effect	q_0 (kPa)
NBR 6123:1988	Power law	Global	1,1
		Local	0,9
		Local – new proposal	1,2
EN 1991-1-4 :2005	Logarithmic law	Global and local	1,5
ASCE 7-10	Power law	Global and local	1,3
AS/NZ 1170.2:2011	Logarithmic law	Global and local	1,3

Source: author.

2.3.2. Aerodynamic coefficients

According to what was presented in 2.2.2, the pressure coefficients recommended by each standard can be determined. For the external pressure coefficients, the dimensions of the building are an important entry parameter – a square building of 25mx25m was considered.

To define the internal pressure coefficients, hypothesis about the openings on the building must be formulated. As explained in 2.2.2.2 it is important to analyze in each project the realistic cases and the most critical combination for dominant openings, even considering potential accidental openings. In this example, the most critical internal pressure coefficient is compared to the usual assumption of a building with all faces equally impermeable. Neglecting the internal pressure considerations can imply on a non-safety design as well as on an oversizing and non-economical design. ⁵⁹

2.3.2.1. External pressure coefficients

Table 17 presents the critical values for external pressure coefficients on the different walls of a building. Positive values represent a positive pressure acting on the façade. Negative values represent a suction effect on the façade.

Observing the coefficients and the schema in Figure 12, the most critical case considering local effects is the suction on sidewalls at the corner closest to the windward wall. For global effects, in some standards the external pressure on windward wall may be more important than the suction. ⁵¹

Table 17: Critical external pressure coefficients by different standards.

Standard / Symbol	Wind effect	Windward wall	Leeward wall	Sidewalls
NBR 6123:1988 / C_{pe}	Global and local	+ 0,8	- 1,2	- 1,2
EN 1991-1-4:2005 / C_{pe}	Global	+ 0,8	- 0,7	- 1,2
	Local	+ 1,0	- 0,7	- 1,4
ASCE 7-10 / GC_{pe}	Global	+ 0,8	- 0,5	- 0,7
	Local	+ 0,9	- 1,8	- 1,8
AS/NZ 1170.2:2011 / $C_{p,e}$	Global	+ 0,8	- 0,5	- 0,65
	Local	+ 1,2	- 0,75	- 1,95

Source: author.

2.3.2.2. Internal pressure coefficients

Table 18 shows the internal pressure coefficients recommended by the four analyzed international codes. The usual value corresponds to a building with all faces equally impermeable to wind, or considered completely closed. The critical value is obtained for a building with an important dominant opening on the windward face, it means a large opening on the windward face and the three other faces assumed impermeable^{60; 62}. The internal pressure is presumed homogeneous in all internal faces, presupposing a building without internal partitions or internal partitions completely permeable to wind.

Table 18: Critical and usual internal pressure coefficients by different standards.

Standard / Symbol	Critical value	Usual value
NBR 6123:1988 / C_{pi}	+ 0,8	0
EN 1991-1-4:2005 / c_{pi}	+ 0,9	+ 0,2
ASCE 7-10 / GC_{pi}	+ 0,55	+ 0,18
AS/NZ 1170.2:2011 / $C_{p,i}$	+ 0,6	0

Source: author.

2.3.3. Wind-induced pressures

Critical or usual positive internal pressures result in an additional suction on the external wall. Then, these effects must be combined with the most critical external pressure values to obtain the net pressure coefficient on the building and the wind-induced pressure as expressed in Table 10.

Combining external and internal pressure, the most critical case is the suction effect at the sidewall corner close to the windward wall for global and for local effects. Usual values are calculated considering the most critical external pressure values and the usual internal pressure coefficients. The principal case must be the worst loading, because it is not possible to preview if an opening will appear during a windstorm.^{61; 71}

The most critical and the usual wind-induced pressures obtained for a 90m-height building are summarized in Table 19 as characteristic values. The values are presented without sign, because the most critical case or the usual case are considered acting both as a positive and as a negative pressure.

The ratio of the critical case value by the usual case indicates the important influence of the internal pressure determination. We can verify that the wind-induced pressure value on the critical case is 1,5 to 2 times of the usual value.

The ratio of local effects by global effects values is 1,1, 1,2 and 2,0 for the European, the American and the Australian/New Zealand codes, respectively. The Brazilian code gives a contrary result with a ratio of 0,85. The new proposal to correct the local effect provides a better result with a ratio of 1,1, which is closer to the European, even if the absolute value remains lower than the other standards.

Table 19: Characteristic wind-induced pressures for a 90m-height building.

Standard	Wind effect	q_{wk} (kPa) Critical case	q_{wk} (kPa) Usual case
NBR 6123:1988	Global	2,3	1,3
	Local	1,9	1,1
	Local – New proposal	2,5	1,5
EN 1991-1-4:2005	Global	3,1	2,1
	Local	3,4	2,4
ASCE 7-10 / GC_{pe}	Global	2,7	1,2
	Local	3,2	2,6
AS/NZ 1170.2:2011 / $C_{p,e}$	Global	1,6	1,1
	Local	3,3	2,5

Source: author.

2.4. Design wind load and design criteria – Brazilian standard

The design loads and the criteria for each limit state (ULS and SLS) have to be properly defined for the design of a structural system. Regarding a façade system, the ULS must be used to design the metal frame structure and the fixing systems, avoiding the collapse of the structure and the pull-through of the board.

Ensuring that the ULS is properly met, the SLS criteria must be verified. For high-rise buildings, serviceability is an important design consideration, although it is sometimes the least understood. Regarding the main structure of the building, Sarkisian (2012) defines these serviceability criteria as the drift, the damping and the maximum acceleration of the building. ⁷²

For the façades systems this work proposes to define the SLS by the maximum horizontal displacement of the complete façade panel and by the crack initiation on the

external façades elements. In the case of fiber cement external boards, the most critical zones for cracking are the fixing screwed points. The maximum horizontal displacement of a façade is already limited by the Brazilian standard NBR 15575:2013. However, based on the architectural significance of a façade, the presence of cracks can also be considered as a serviceability failure. The progression of cracking process, besides being an aesthetical problem, can compromise the water tightness of the building, increasing the building façade deterioration. For this reason, it is convenient to add a crack initiation criterion as a complement of the standards requirements.⁷³

The proposed design criteria may be assessed taking into consideration the different wind effects. Global wind effects affect the design of the structural metal frame and the maximum displacement evaluation, whilst the local wind effects influence the analysis of the fixing points, that is, the pull-through strength and the crack initiation on the external board.

Finally, the design loads are not the same considering ULS or SLS assessment. For safety reasons, the most critical case for wind loads determination will be used. It is important to reaffirm that a safety and economical solution demands a specific analysis for each project. For the ULS, the materials must fulfill all strength criteria. The Brazilian standards require using a load factor (γ_f) of 1,4 for wind loads.²⁹

Load considerations for SLS depend on the analyzed criterion. For example, Ferrareto (2017) proposes using the 50-years return period for a ULS analysis and 1-year or 10-year return period for a SLS analysis, mainly for comfort and dynamic analysis of the building structure. The serviceability wind load for cracks or irreversible damages due to excessive displacements can be defined using a load factor equal to 0,8. This load factor, recommended by the Brazilian performance standard, converts the wind pressure calculated for a 50-year return period into an equivalent 10-year return period pressure. Under this SLS load, the maximum horizontal displacement of a lightweight façade panel must be 175 times less than the height of the façade panel, as required by the same Brazilian standard.^{47; 73}

The proposal for ULS and SLS lightweight façades design criteria and its correspondent design (factored) wind loads is summarized in Figure 14. Taking the example presented in 2.3 and the results for the Brazilian standard shown in Table 19, the design wind loads can be defined. For the ULS criteria, the global wind-induced

pressure will be adopted as $q_{wd} = 3,2 \text{ kPa}$ and the local wind-induced pressure, as $q_{wd} = 3,5 \text{ kPa}$. The serviceability loads (SLS) will be equal to 1,8 kPa for global effects and 2,0 kPa for local ones.

Figure 14: Proposal for design wind loads and criteria to façade design, based on Brazilian standards requirements.

<p><u>Criterion:</u></p> <ul style="list-style-type: none"> Structural strength <p><u>Design wind load:</u></p> <ul style="list-style-type: none"> $q_{wd} = 1,4q_{wk,global}$ <p>Global effects:</p> <p>Metal frame and board design</p> <p><u>Criterion:</u></p> <ul style="list-style-type: none"> Maximum horizontal displacement ($\delta_h \leq h/175$) <p><u>Design wind load:</u></p> <ul style="list-style-type: none"> $q_{wd} = 0,8q_{wk,global}$ 	ULS	<p><u>Criterion:</u></p> <ul style="list-style-type: none"> Pull-through strength <p><u>Design wind load:</u></p> <ul style="list-style-type: none"> $q_{wd} = 1,4q_{wk,local}$ <p>Local effects:</p> <p>Board fixing design</p> <p><u>Criterion:</u></p> <ul style="list-style-type: none"> Crack initiation on external board <p><u>Design wind load:</u></p> <ul style="list-style-type: none"> $q_{wd} = 0,8q_{wk,local}$ 	SLS
--	------------	--	------------

Source: author.

2.4.1. Design wind load for different building heights

Following the same procedure exemplified in 2.3, the most critical design wind load can be defined for different building heights. Table 20 shows the results based on the Brazilian standard and on the considerations presented previously in this work.

Table 20: Critical design wind-induced pressures based on Brazilian standards.

q_{wd} (kPa)		<i>ULS</i>		<i>SLS</i>	
Floors	Height	Global	Local	Global	Local
10	30 m	2,2	2,5	1,3	1,4
15	45 m	2,5	2,8	1,4	1,6
20	60 m	2,8	3,1	1,6	1,8
25	75 m	3,0	3,3	1,7	1,9
30	90 m	3,2	3,5	1,8	2,0
35	105 m	3,3	3,6	1,9	2,0
40	120 m	3,4	3,7	2,0	2,1

Source: author.

2.5. Concluding remarks

The wind loads are the main forces to be considered for the design of a façade panel. Mainly in high buildings, those loads become quite relevant and all the façade components must be conceived to withstand the wind action. In addition, some of these components may be subjected to local wind effects, usually more severe than the global loads. For those reasons, the proper wind load definition is crucial to ensure a reliable design of a façade system.

Around the world, different building codes follow the same framework reasoning, called the Davenport wind loading chain, to calculate the wind load for a project. However, each local standard provides a specific way to define those loads including different factors, pressure coefficients or even distinct meteorological interpretations. The consideration of local and global wind effects is one of the most important differences among the four building codes compared in this chapter.

Contrary to the Brazilian standard, the three foreign codes present a clear distinction for a local or for a global wind analysis. Moreover, the wind pressure obtained by those codes are similar both for the critical case and the usual one. The Brazilian standard, conversely, has not had a precise differentiation of local or global effect. Furthermore, it is the only code that provides lower values for a local analysis, being less conservative than the other standards. Aiming to redress this particularity, a new importance factor was proposed in case of a local wind analysis.

Finally, the loads must be defined observing the safety factors correspondent to an ultimate (ULS) or a serviceability analysis (SLS). Making this ponderation, the wind loads for façades design were defined based on the building height. This final load definition was proposed considering a critical case, including extreme suction wind effects and the worst combination of internal and external pressure coefficients. These values cannot be generalized, and they must be reviewed and redefined regarding the specificities and the context of each different project.

3. FIBER CEMENT BOARDS

Numerical model input definition: Material behavior

Fiber cement boards have been widely used for roofing, claddings, internal closings and external façades. As a fiber reinforced composite, the mechanical performance of these boards is very singular. Understanding the formulation, the production process, the constitutive law and the aging mechanisms of the composite is fundamental to describe the contribution of these boards in a façade system. The raw materials choices, specially the fibers specifications, can significantly influence the composite behavior, creating different microstructures and being able to transform a quasi-brittle into a ductile material. The production process defines the global composite performance and how to properly model its mechanical behavior. Finally, the aging mechanisms can generate additional loads and modify the composite behavior due to deferred effects over time.

The constitutive law of the material starts by an elastic function, followed by a non-linear and ductile post-peak behavior dependent on the microstructure interactions between fibers and matrix. The laminated composite theory equations are resorted to properly represent the elastic phase of the boards, since its production process results in a laminated structure.

The fibers choice must optimize the composite performance along with ensuring costs and raw materials availability. The first fiber cement technology was initially proposed using asbestos fibers, but over time, due to health risks, asbestos fibers have been replaced by alternative non-asbestos materials. These non-asbestos products are usually produced by two different industrial process: the Hatschek process, a filtering process combined with an air curing or an autoclaved curing post-treatment; or the open-mesh process producing a monolithic board reinforced by an embedded glass mesh.

The air cured Hatschek process was firstly implemented using asbestos in fiber cement materials production. Nowadays, natural and synthetic fibers have been studied as substitutive raw reinforcing materials using the same production process. Celluloses, such as pine, sisal or jute, polyvinylalcohol (PVA), polyethylene (PE), alkali-resistance glass (AR-glass) and polypropylene (PP) are examples of alternative fibers used in non-asbestos Hatschek fiber cement products ^{74; 75}. Both natural and synthetic

fibers tend to increase toughness and ductility in the hardened composite. Multiple cracking behavior can be accompanied by a pseudo strain-hardening depending on the fiber content ^{77; 78}. These effects imply high ductility, large energy absorption capacity and high toughness of the material ^{76; 77; 78; 79}. Polypropylene fibers represent less expensive cost and bigger availability compared to PVA or PE fibers. PP fibers will improve strength, toughness and ductility if they are properly treated to improve the interfacial bonding with the cementitious matrix, enhancing the composite performance ^{80; 81; 82}.

The cementitious matrix leaves the composite susceptible to carbonation reactions during its service life. In addition, fiber cement boards have a high porosity, enabling a significant dimensional variation due to moisture. Both, carbonation and moisture variation, act together, generating in-plane stress and modifying the material microstructure along the boards service life.

This chapter describes and characterizes a fiber cement board produced in a Hatschek machine using a mix of cellulose-pulp fibers and PP fibers by an air-curing process. The cellulose acts as a processing fiber, due to its compatibility with the Hatschek process, helping on the filtering step. Polypropylene fibers, once they are stiffer and stronger than pulp, are used as the primary reinforcement of the composite.

First, the Hatschek air cured production process is presented. Then the constitutive law of the fiber cement is detailed with a description of the elastic and laminated theories, followed by a microstructure description of the fiber-matrix interactions and the main considerations regarding the fracture behavior of the composite. Next, the mechanical characterization of the boards is described through a three-point bending test and a direct tensile test. Lastly, a durability analysis is proposed to assess the carbonation level of an aged specimen and the aging consequences over the mechanical parameters, including stress-generated by moisture variation and shrinkage.

3.1. Manufacturing Hatschek process

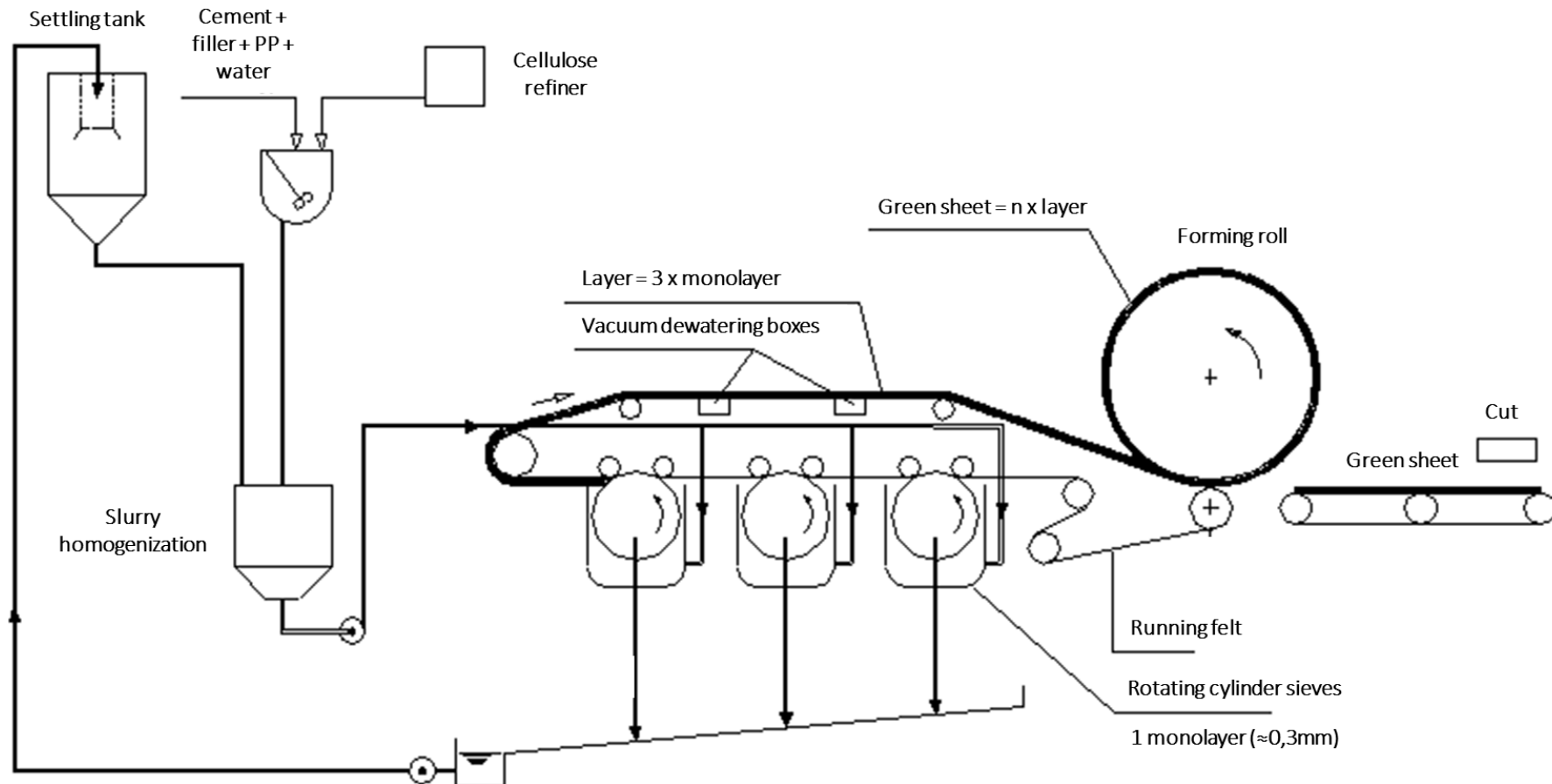
The process starts by mixing cement, water, cellulose-pulp, PP fibers and fillers according to the formulation, as illustrated in Figure 15. This dilute suspension of cement, such as a cement slurry, is filtered on rotating cylinder sieves or vats. A thin layer, called monolayer, of about 0,3 mm-thickness is transferred from each sieve and accumulated on an endless running felt. Passing through some sieves, usually three or four, a layer up to 1,2 mm-thickness is formed. This layer is wound around a format roll and the process is repeated as often as required to achieve the expected thickness of sheet. The diameter of the format roll defines the length of the sheet. Once the desired thickness is achieved, the composite is cut and conformed.⁷⁵

Fibers distribution should be ideally random. However, the production process promotes a partial fiber alignment in the longitudinal direction of the running felt. This fiber alignment, even partial, results in an orthotropic material with different behaviors in the longitudinal direction (fiber alignment) or in the transversal direction (orthogonal to the fiber alignment).

The water content of the material is very high after this process. The hydration process continues, and cement hardens by an exothermic chemical reaction with water. Curing and drying process are held in an open ambient, resulting in air-cured products with great toughness and ductile fibers. Autoclaved curing process can also be used, resulting in steam cured products, but the use of autoclaves demands special attention on the fibers choice, since this process leads to a less alkaline matrix.

Because the production process is based on laminating thin layers, delamination failure may be a big issue for the final board performance. Bond interaction between layers may be enhanced by applying polymer flocculants, as polyacrylamide, during the laminating process. Interlaminar bond strength may also be enhanced by applying a pressure at the end of the production process⁸³.

Figure 15: Layout of Hatschek machine. Example of production process using three cylinder sieves.



Source: adapted from Saint-Gobain (2017).

3.2. Constitutive law of fiber cement materials and fracture process

The behavior of the fiber cement material is dependent on the structure of the composite. To describe the material properties, it is important to consider the three aspects: the bulk cementitious matrix, the shape and distribution of the fibers and the fiber-matrix interface interaction. The microstructure around fibers is significantly different from that away from the interface. The cementitious matrix on this interfacial transition zone (ITZ) is much more porous than in the bulk paste. ⁷⁴

The reinforcing fibers play an important role on the stress redistribution in the composite. After the first crack, the stress strength may ascend or descend depending on the fiber performance and on the fiber-matrix interface. The fiber bridging across the cracked matrix may promote a strength increasing after the first crack. This ascending behavior of the stress-strain curve is called strain hardening. In addition, fibers act improving material toughness through energy absorption mechanisms, such as the debonding and the pull-out. Different from the fiber bridging, debonding and pull-out mechanisms may be present even with a descending stress-strain behavior after crack. The descending behavior of the curve is called stress softening. ⁷⁴

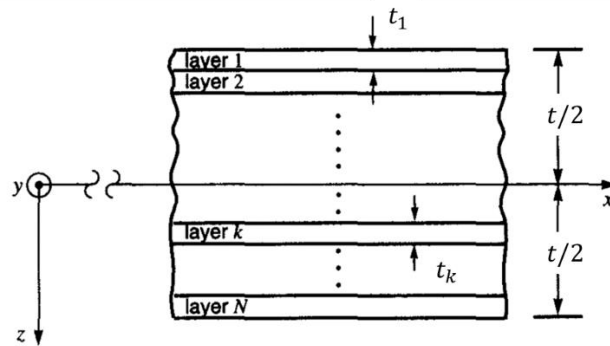
Usually, the stress-strain curve of a fiber cement presents, at least, three different stages. The first one, characterized by the Young's modulus (E) or modulus of elasticity (MOE), is linear up to the first crack reaching a stress called limit of proportionality (LOP) in flexural tests or bend over point (BOP) for direct tensile tests. The LOP and BOP values are affected by the matrix properties, the fiber type, the volume fraction and the interfacial properties. Beyond this point, a second stage begins and the material behavior is further affected by the fiber-matrix interface characteristics and the ability of the fiber to carry out the load. ⁷⁵ After, a third stage takes place corresponding to the fiber failure caused by the fiber rupture or by the fiber pull-out.

The use of cellulose fibers makes the composite sensitive to moisture content variations. The hygroscopic nature of the natural fibers implies changes on the composite behavior. In wet condition, the cellulose fibers lose stiffness and gain ductility, providing strength decreasing and toughness increasing. In dry condition, fiber-matrix bond is stronger, as the result of hydrogen bridges enhancing. The composite failure is frequently characterized by the fiber pull-out on wetting, but the dominated failure mode in dry condition is the fiber rupture. ⁷⁴

3.2.1. Elastic behavior – prior to cracking

Fiber cement boards produced by the Hatschek method may be modeled as a laminated material due to the laminating production process. Each single ply (monolayer) may be characterized in strength, stiffness, thermal and moisture dimensional variation. The behavior of the global composite can then be predicted using the laminated theory. Figure 16 illustrates a generic schema of a layered material. The cartesian coordinates x , y and z will be adopted as the longitudinal (along fibers), the transverse and the thickness direction, respectively.

Figure 16: Cross section view of a generic laminated material.



Source: Hyer (2009).⁸⁴

As presented in 3.1, fibers have a preferential orientation. Hence, the boards may be considered orthotropic in the plane of the layers, and mechanical properties must be defined in the direction along the fibers (longitudinal direction) and perpendicular to the fibers (transverse direction). Each layer is considered an isotropic transversal material.

Assuming the layer as a unidirectional material, its elastic linear behavior can be described by five independent elastic constants. Hooke's law is then written directly by (6) using the engineering matrix notation for stress and deformation fields. $\underline{\underline{C}}$ is the elastic stiffness tensor.⁸⁵

$$\underline{\underline{\sigma}} = \underline{\underline{C}} : \underline{\underline{\varepsilon}} \Rightarrow \begin{pmatrix} \sigma_{xx} \\ \sigma_{yy} \\ \sigma_{zz} \\ \sigma_{yz} \\ \sigma_{xz} \\ \sigma_{xy} \end{pmatrix} = \begin{pmatrix} C_{11} & C_{12} & C_{12} & 0 & 0 & 0 \\ C_{12} & C_{22} & C_{23} & 0 & 0 & 0 \\ C_{12} & C_{23} & C_{22} & 0 & 0 & 0 \\ 0 & 0 & 0 & 1/2(C_{22} - C_{23}) & 0 & 0 \\ 0 & 0 & 0 & 0 & C_{66} & 0 \\ 0 & 0 & 0 & 0 & 0 & C_{66} \end{pmatrix} \begin{pmatrix} \varepsilon_{xx} \\ \varepsilon_{yy} \\ \varepsilon_{zz} \\ \gamma_{yz} \\ \gamma_{xz} \\ \gamma_{xy} \end{pmatrix} \quad (6)$$

The elastic coefficients can also be represented by the engineering constants: elastic longitudinal modulus (E_L), elastic transverse modulus (E_T), shear modulus (G_{LT}) and the Poisson's coefficients (ν_{LT} , ν_{TT}). The engineering constants can be obtained by unidirectional tests and they are expressed by (7).⁸⁵

$$E_L = C_{11} - \frac{2C_{12}^2}{C_{22} + C_{23}}; E_T = C_{22} + \frac{C_{12}^2(C_{22} - 2C_{23}) + C_{11}C_{23}^2}{C_{12}^2 - C_{11}C_{22}} \quad (7)$$

$$\nu_{LT} = \frac{C_{12}}{C_{22} + C_{23}}; \nu_{TT} = \frac{C_{12}^2 - C_{11}C_{23}}{C_{12}^2 - C_{11}C_{22}}; G_{LT} = C_{66}$$

The modulus of elasticity of the composite can be predicted by the rule of mixtures. It must be considered as a variable dependent on the fiber volume fraction content (V_f) in a direction, and on the moduli of elasticity of the matrix (E_m) and fibers (E_f). As a plane orthotropic material, modulus of elasticity on each direction (x -longitudinal and y -transverse) is different. The elastic longitudinal modulus can be defined as (8), and the transverse elastic modulus is done by (9). Accordingly, the shear modulus can be written as (10). Assuming that fiber and matrix are isotropic materials, it is possible to obtain their respective shear modulus G_f and G_m using relation (11).⁸⁵

$$E_L = E_m(1 - V_f) + E_f V_f \quad (8)$$

$$\frac{1}{E_T} = \frac{(1 - V_f)}{E_m} + \frac{V_f}{E_f} \quad (9)$$

$$\frac{1}{G_{LT}} = \frac{(1 - V_f)}{G_m} + \frac{V_f}{G_f} \quad (10)$$

$$G = \frac{E}{2(1 + \nu)} \quad (11)$$

Since the fiber volume and its elastic modulus are relatively low, it can be noted that the composite elastic behavior is mostly driven by the matrix characteristics. However, even if they do not provide a relevant contribution for the elastic modulus enhancing, fibers contribute to increase the material strength and toughness. The fiber-matrix interaction is the main responsible for this fiber contribution. For this reason, different elastic moduli can be expected in the longitudinal or in the transverse direction

of the board. On the other hand, the ultimate strength and toughness are expected to be significantly higher in the longitudinal direction than in the transverse one. ^{74; 85}

3.2.2. Elastic behavior – laminated composite theory

In 3.2.1, the elastic behavior of a single fiber cement layer has just been presented. However, as described in 3.1, fiber cement boards are formed in a laminating process. The final material is a multi-layer material with stacked plies. Accordingly, the classical lamination theory can be used to represent the structural response of the boards. This approach becomes interesting in order to evaluate the influence of layer thickness and number of layers on the elastic behavior of the boards.

The classical lamination theory is based on the plates theory with additional hypothesis, taking into account an infinite combination of stacking arrangements and fibers orientation. In this study, the problem will be simplified even with a laminated material. Despite an orientating screw in each vat to promote the misalignments of fibers in a real machine, all layers can be presumed identical and disposed (stacked) on the same direction. Thus, the structural response formulation can be simplified. ⁸⁵

Each layer can be considered as a plate, in order to obtain its mechanical behavior description. A plate can be defined as a three-dimensional structure with one dimension (thickness) much lower than the others; thus, having a zero-stress constraint. For homogenous plates, displacements and rotations are described as a function of its mean surface.

If the ratio of the length by thickness is greater than 20 ($L > 20h$), plates are classified as “thin plates”. In this case, shearing may be neglected due to the small thickness, and the displacement field is described using the Kirchhoff-Love theory. On the other hand, with more important thickness values, plates are classified as “thick plates”. Thus, the Mindlin-Reissner plate theory can be applied, which considers the shear stress distribution through the board thickness, and proposes to represent it by a parabolic function. ^{84; 85; 86}

Considering that the fiber cement boards are commonly 10mm-thickness (at the most, 12mm), the Kirchhoff's hypothesis can be assumed ($\gamma_{xz} = \gamma_{yz} = 0$), and the board can be modeled as a thin plate. The displacement field assumption results in a deformation field, composed by a reference surface strain component and by a

reference surface curvature component. In addition, plane stress state was assumed, which results in $\sigma_{zz} = 0$.

With these hypothesis, the relation (6) is rewritten for each layer adopting the plane stress state. \underline{Q} is called local reduced stiffness matrix. The superscript σ is used to signal the plane stress formulation, shown in (12).

$$\begin{aligned} \underline{\sigma}^\sigma &= \underline{Q} : \underline{\varepsilon}^\sigma \Rightarrow \begin{pmatrix} \sigma_{xx} \\ \sigma_{yy} \\ \sigma_{xy} \end{pmatrix} = \begin{pmatrix} Q_{11} & Q_{12} & 0 \\ Q_{12} & Q_{22} & 0 \\ 0 & 0 & Q_{66} \end{pmatrix} \begin{pmatrix} \varepsilon_{xx} \\ \varepsilon_{yy} \\ \gamma_{xy} \end{pmatrix} \\ &= \begin{pmatrix} C_{11} - \frac{C_{12}^2}{C_{22}} & C_{12} - \frac{C_{12}C_{23}}{C_{22}} & 0 \\ C_{12} - \frac{C_{12}C_{23}}{C_{22}} & C_{22} - \frac{C_{23}^2}{C_{22}} & 0 \\ 0 & 0 & C_{66} \end{pmatrix} \begin{pmatrix} \varepsilon_{xx} \\ \varepsilon_{yy} \\ \gamma_{xy} \end{pmatrix} \end{aligned} \quad (12)$$

The standard hypothesis states that the total displacement is composed by a membrane behavior component and by a bending behavior component. Hence, the surface deformations are given by (13), where $\underline{\varepsilon}_m$ is the field of membrane strains and $\underline{\varphi}$ is the field of surface curvatures.

$$\underline{\varepsilon}^\sigma = \underline{\varepsilon}_m + z \underline{\varphi} \Rightarrow \begin{pmatrix} \varepsilon_{xx} \\ \varepsilon_{yy} \\ \gamma_{xy} \end{pmatrix} = \begin{pmatrix} \varepsilon_{xx}^0 \\ \varepsilon_{yy}^0 \\ \gamma_{xy}^0 \end{pmatrix} + z \begin{pmatrix} \varphi_x \\ \varphi_y \\ \varphi_{xy} \end{pmatrix} \quad (13)$$

Integrating equation (12) with the strain field done by (13), the resultants force (\underline{N}) and moment (\underline{M}) on the board are obtained. These resultant expressions are written in (14) and (15), respectively. \underline{N} is also called membrane forces.

$$\underline{N} = \underline{A} : \underline{\varepsilon}_m + \underline{B} : \underline{\varphi} \quad (14)$$

$$\underline{M} = \underline{B} : \underline{\varepsilon}_m + \underline{D} : \underline{\varphi} \quad (15)$$

Matrix \underline{A} , \underline{B} and \underline{D} are called laminated stiffness matrices. \underline{A} is the membrane stiffness matrix; \underline{D} is the bending stiffness matrix and \underline{B} is the membrane-bending-torsion coupling matrix. The laminated stiffness matrices are written as a function of the reduced stiffness matrix, thickness and orientation of each layer. In case of symmetric stacking sequences, there is no coupling effect between membrane and bending/torsion effects. Hence, $\underline{B} = \underline{0}$ for the boards studied in this work. ^{85; 86}

Once the layers are assumed identical, the tensor $\underline{\underline{Q}}$ is the same for each layer, as well as the thickness. Accordingly, tensors $\underline{\underline{A}}$ and $\underline{\underline{D}}$ are respectively given by (16) and (17), where t_k is the layer thickness, n is the total number of layers and z_k is the z -coordinate of the mean surface of layer k .

$$\underline{\underline{A}} = n \cdot t_k \cdot \begin{pmatrix} Q_{11} & Q_{12} & 0 \\ Q_{12} & Q_{22} & 0 \\ 0 & 0 & Q_{66} \end{pmatrix} \quad (16)$$

$$\underline{\underline{D}} = \left(\frac{n \cdot t_k^3}{12} + h \sum_{k=1}^n z_k^2 \right) \cdot \begin{pmatrix} Q_{11} & Q_{12} & 0 \\ Q_{12} & Q_{22} & 0 \\ 0 & 0 & Q_{66} \end{pmatrix} \quad (17)$$

The effect of the layer thickness and the number of layers can then be assessed in each case through the analysis of a direct tensile test, and of a 3-point bending test. In the first one, only the membrane effects will be observed, so the elastic homogenized parameters will be defined as a function of $\underline{\underline{A}}$. The second test, a pure bending analysis, will give results related to matrix $\underline{\underline{D}}$.

3.2.2.1. Direct tensile test formulation – membrane efforts

Consider a rectangular laminated board with a symmetric stacking sequence and infinite length, submitted to an axial force F on the same direction of the fibers. The force is distributed in a width equal to b , and it is taken as applied on the mean surface of the board, which thickness is t .

In this case, only membrane efforts are solicited. From equation (14):

$$\underline{N} = \underline{\underline{A}} : \underline{\underline{\varepsilon}}_m \Rightarrow \begin{pmatrix} F/b \\ 0 \\ 0 \end{pmatrix} = n \cdot t_k \cdot \begin{pmatrix} Q_{11} & Q_{12} & 0 \\ Q_{12} & Q_{22} & 0 \\ 0 & 0 & Q_{66} \end{pmatrix} \begin{pmatrix} \varepsilon_{xx} \\ \varepsilon_{yy} \\ \gamma_{xy} \end{pmatrix} \quad (18)$$

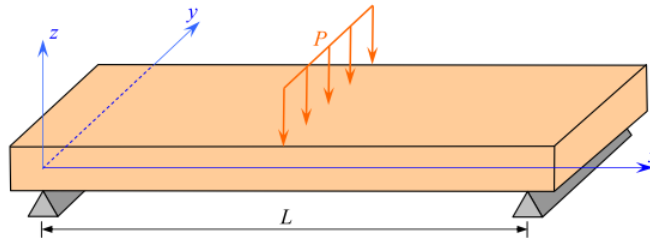
The equivalent global stress on the longitudinal direction is due to the distribution of N_x through the thickness t . Board thickness is given by the product of the number of layer by the layer thickness ($n \cdot t_k$). Hence, equation (18) shows that the longitudinal elastic modulus (E_L) of the laminated composite are independent of the layer thickness or the number of layers. Expressions (19) show the relation between the reduction stiffness coefficients and the engineering constants. Using the same reasoning, these conclusions can be extended to the transverse elastic modulus and the Poisson's coefficients too.

$$Q_{11} = \frac{E_L}{\left(1 - v_{LT}^2 \frac{E_T}{E_L}\right)}; Q_{22} = \frac{E_T}{E_L} Q_{11}; Q_{12} = v_{LT} Q_{22}; Q_{66} = G_{LT} \quad (19)$$

3.2.2.2. 3-point bending test formulation – pure bending efforts

Consider a board simply supported on two parallel edges. The distance between the supports are taken as L . The 3-point bending test consists of applying a linear distributed load trough the board width (b) at mid-span ($L/2$), as shown in Figure 17.

Figure 17: 3-point bending test configuration.



Source: Berthelot (2010).⁸⁵

Assuming the hypothesis of the vertical displacement is only a function of the x -direction (beam hypothesis), then $\varphi_y = 0$. In this case, there are only bending effects, and from equation (15):

$$\underline{M} = \underline{D} : \underline{\varphi} \Rightarrow \begin{pmatrix} -Px/2 \\ 0 \\ 0 \end{pmatrix} = \begin{pmatrix} D_{11} & D_{12} & 0 \\ D_{12} & D_{22} & 0 \\ 0 & 0 & D_{66} \end{pmatrix} \begin{pmatrix} \varphi_x \\ 0 \\ \varphi_{xy} \end{pmatrix} \quad (20)$$

Resolving (20), the maximum vertical displacement (w_c - at mid-span), the flexural stiffness (E_x), the maximum normal (σ_{xx}) and shear stress distribution (σ_{xz}) can be found. Expressions (21) to (24) show the results for the laminated with identical layers stacked on the same direction.⁸⁵

$$w_c = \frac{PL^3}{4bt^3E_x} \quad (21)$$

$$E_x = \frac{12D_{11}}{t^3} \quad (22)$$

$$\sigma_{xx} = \frac{3PL}{2bt^2} \quad (23)$$

$$\sigma_{xz} = \frac{3P}{4bt} \left(4 \left(\frac{z}{t} \right)^2 - 1 \right) \quad (24)$$

3.2.3. Fiber-matrix interaction

Assuming that the elastic strain (ε) in a point is the same for the matrix and for the fiber, the stress in the composite (σ_c) up to the first crack may be written as a function of the weighted average of the stress in the matrix (σ_m) and the stress in the fiber (σ_f). Equation (25) shows the composite stress in the longitudinal direction, improved by the fiber content.

$$\sigma_c = \sigma_m(1 - V_f) + \sigma_f V_f = E_m \varepsilon(1 - V_f) + E_f \varepsilon V_f = E_c \varepsilon \quad (25)$$

If the load-bearing capacity of the fibers ($\sigma_{fu} V_f$) is greater than the first crack load of the composite, catastrophic failure will be prevented. First crack stress can be written in function of the first crack strain of the matrix (ε_{mu}). Therefore, equation (26) defines the condition to be respected in order to avoid catastrophic failure. ⁷⁴

$$\sigma_{fu} V_f > E_c \varepsilon_{mu} \quad (26)$$

Li and his co-authors (1992) stated the microstructural conditions to improve toughness and ductility, promoting the so-called pseudo strain-hardening behavior of cementitious materials using short random fibers ^{87; 88; 89}. A critical fiber volume must be overcome to ensure the composite failure transition from quasi-brittle to a non-catastrophic mode. This critical value depends on the matrix toughness, on the interfacial bonding and on the geometry (length and diameter) of the fibers. When the fiber volume is below the critical value, then the composite presents a strain-softening behavior. If the fiber content is higher than the critical value, the fiber bridging transfers the stress on a crack-tip back into the matrix, forming more micro cracks, and the final failure occurs when one of these multiple cracks forms a fracture plane ⁹⁰.

The first crack on the composite is driven by the matrix properties and the fiber-matrix interaction. Beyond the crack, matrix is assumed to not contribute anymore to the composite strength. Therefore, fibers act increasing material toughness through dissipative means, such as fiber debonding or fiber pullout, and they control the crack growing by bridging mechanisms ⁷⁵. After the first crack, with an optimum fiber volume content, the stress is redistributed. In the cracked region, the stress in the matrix is transferred to the fiber, leading to a stress-free matrix at crack edges. Increasing external load, the additional stress will be redistributed by the fibers and withstood far away in other matrix points, creating new cracks. This process is called multiple cracking ⁷⁴.

External load is distributed between fiber and matrix by the development of an interfacial, non-uniform shear stress, along the interface. As fiber and matrix have a different elastic modulus, the stress transfer occurs providing the same strain at fibers and at the matrix. Before cracking, elastic shear stress transfer is the dominant mechanism, and it influences the LOP and BOP results. Once the interfacial stress reaches the adhesion shear bond strength (fiber-matrix shear strength), debonding initiates, and the stress transfer is driven by frictional slip.⁷⁴

Prior to cracking, the matrix to fiber stress-transfer occurs by elastic mechanisms. Different models were proposed based on the shear lag theory to predict the debonding. The stress in a matrix point is transferred to the fiber by a shear stress in the end zone of the fiber. The shear stress decreases gradually, building up tensile stress from fiber end moving inwards. In this elastic phase, tensile stress reaches its maximum at the center of the fiber and shear stress, at fiber ends.

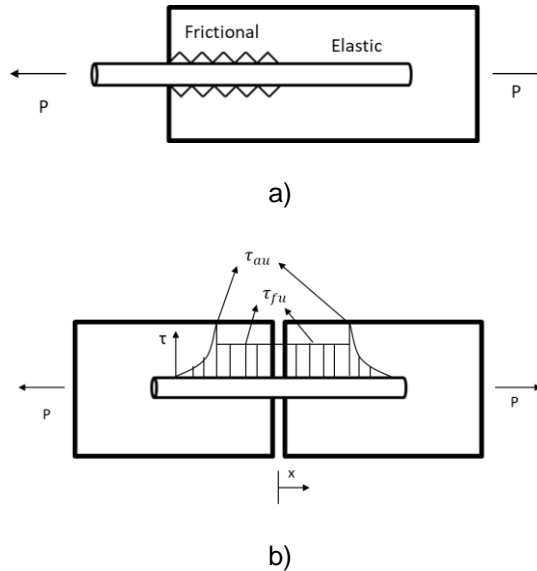
After cracking, once fiber-debonding was initiated, the shear stress distribution in the fiber can be described by a combination of frictional slip near the crack opening and elastic debonding away from it. These mechanisms are responsible to ensure the fiber bridge across the cracks, preventing catastrophic failures. The shear stress is governed by the fiber geometry (radius and length), by the modulus of elasticity of the fiber and by the shear modulus of the matrix. Figure 18 presents schematically the shear stress combined modes in a fiber after matrix cracking and fiber debonding. τ_{fu} is the frictional shear stress in the fiber and τ_{au} is the fiber-matrix shear strength.

The composite toughening is related to this fiber-matrix interface behavior. Fiber bridging is improved if fibers are able to slip, with friction, into the matrix. The material is more ductile if failure occurs by fiber pull-out than if the fibers break. Many models are proposed to represent the load-slip response of the fiber into a matrix. These models intend to represent the stress transfer and crack bridging. Interface strengthening mechanisms, such as fiber surface modification or fiber fibrillation, have been proposed by different authors^{91; 92}. These techniques intend to enhance the global behavior of the composite, optimizing the fiber-matrix interaction.

For asbestos-based products, for example, the fiber-matrix bonding was too high, and the material usually failed by fiber breakage with a reduced fiber slipping. High toughness PP-fibers provide a good fiber-matrix interaction, improving material

toughness, avoiding brittle failure and allowing the fiber-slippage before breaking⁸⁰. In addition, the fiber-matrix interface behavior of natural fibers has been studied in order to understand how to improve strength and toughness using cellulose fibers⁹³.

Figure 18: a) Partially debonded fiber configuration with combined elastic and frictional behavior. b) Interface shear stress distribution along a fiber immediately after cracking.



Source: adapted from Bentur and Mindess (2007).⁷⁴

3.2.4. Fracture mechanics and post-peak behavior

Fracture process in a material begins with the crack initiation followed by the crack propagation. The existence of micro cracks facilitates the crack propagation once the material is loaded. If the strain energy accumulated close to the initial crack reaches the energy required to create new surfaces, then crack grows.

Catastrophic crack occurs when the system releases more energy than it absorbs during crack growing. In these cases, once crack propagation initiates there is a fast process. This phenomenon can be described by the Griffith's theory, considering that crack propagation is imminent when the strain energy release rate is equal to the surface energy. The linear elastic fracture mechanics (LEFM) was the first approach used to predict material failure. LEFM assumes that the stress field on the crack region can be described by the theory of elasticity with a singularity at the crack tip. This approach is defined by two main parameters: the critical strain energy release rate (G_c) and the critical stress intensity factor, also called fracture toughness (K_{Ic}).^{75; 94}

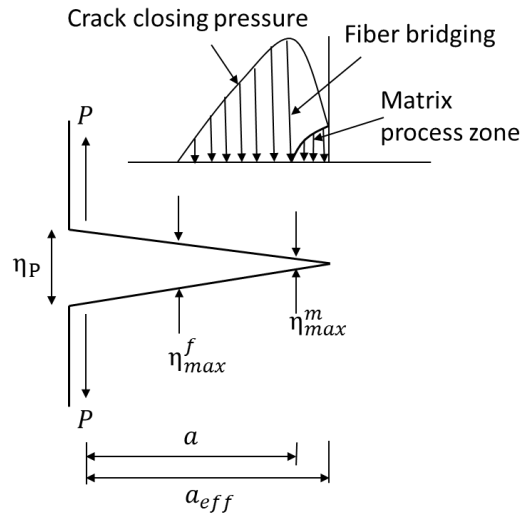
However, LEFM is adequate to describe brittle materials. A plastic model was created by Dugdale (1960), fitting very well the fracture behavior of metallic materials,

assuming the occurrence of a plastic zone near the crack tip. In this case, the strain energy release rate considers also a portion of plastic energy dissipation^{94; 95}. In case of fiber reinforced materials, to account for the post-cracking behavior, the elasto-plastic theory, or the non-linear fracture mechanics, appears as more accurate. The crack propagation in fiber cement boards is not catastrophic. Actually, fibers act inhibiting the unstable crack propagation. Contrary to the LEFM theory, in fiber cement materials there is a non-linear dissipative zone at the crack tip.

To model this crack stabilization, it is important to take into account the gradual decrease of stress at crack edges. Hillerborg et al. (1976) propose the fictitious crack model to represent fracture in fiber reinforced concrete⁹⁶. Their contribution is the assumption of a crack longer than the measured one, considering a process zone in the matrix where microcracking takes place. These cohesive crack models consider, in addition, a stress transferring from one face to another of the crack, once it is opened. They set the fracture energy (G_f) as the main parameter to describe the fracture process also considering this process zone and the cohesive stress field. Fracture energy is defined as the energy dissipated by area during cracking progress due to the additional deformation of the damage zone⁹⁷. Figure 19 illustrates the stress field around a crack, showing the three distinct zones: traction-free zone; fiber bridging and the matrix process zone. Li and his co-authors (1992) propose a steady-state cracking propagation theory for fiber cement materials⁸⁹. Their works aim to provide analytical models to account for stress softening and strain hardening in fiber cement composites^{98; 99; 100}. On these models, fibers are taken as elastic springs that are charged in case of strain-hardening composites, or unloaded to simulate a stress softening behavior.

The use of the tensile stress-strain curve was proposed by different authors as an experimental manner to determine the fracture energy of a cementitious composites^{101; 102; 103}. The RILEM recommends the three-point bend test on a notched beam to characterize the fracture energy, as defined by Hillerborg (1976)¹⁰⁴. However, it has been demonstrated that a size-effect must be considered in order to assess reliable results.

Figure 19: Idealized representation of the stress field around an advancing crack.



Source : Bentur and Mindess (2007).⁷⁴

3.3. Mechanical characterization

Three experimental tests were done in order to characterize the fiber cement material behavior. This experimental characterization provides the material input parameters for numerical modeling. The tests were chosen with different objectives:

- Three-point bending test: to characterize the bending behavior of the composite by means of the same test used in the quality control process of fiber cement boards production;
- Direct tensile test: to highlight the fiber cement cracking behavior and its effects. The stress-strain curve is obtained marking the multiple cracking, the fiber bridging and the fiber pullout processes;
- Work of fracture RILEM method: to measure the fracture energy of the composite. It is a three-point bending test on a notched beam. The work of fracture corresponds to the area under the force-displacement curve.

The analyses were performed on fiber cement boards samples produced in an air-cured Hatschek process, as described in 3.1. Table 21 indicates the raw composition of the boards, including the mass fraction content (m), the mass density of each material (ρ) and the correspondent volume fraction content (V). From the results on volume fraction content, the void fraction on the composite can be estimated around 45%.

Board specimens for all tests were cut in a water jet machine. The specimens were cut away from the board edges, in order to avoid or reduce any edge effect. The water jet cutting, as illustrated by Figure 20, ensures right and uniform edges, minimizing geometrical imperfections for any specimen shape.

Table 21: Raw materials composition of fiber cement board.

Component	m	ρ (g/cm ³)*	V^{**}
PP fiber	1,8%	0,9 ¹	3,0%
Cellulose fiber	3,2%	1,6 ²	3,0%
Cement	41,8%	3,1 ²	20,2%
Limestone filler	53,2%	2,8 ²	28,5%

*1) Houang et al. (2005) ¹⁰⁵; 2) Dias et al. (2010) ¹⁰⁶
^{**} $V_i = m_i \frac{\rho_c}{\rho_i}$, where ρ_c is the composite measured density of 1,5 g/cm³

Source: author.

Three different sample conditioning were adopted:

- Ambient condition: laboratory ambient conditions (23 °C and 50% RH);
- Wet condition: immersion in water at ambient temperature;
- Dry condition: drying in a ventilated oven at 60 °C.

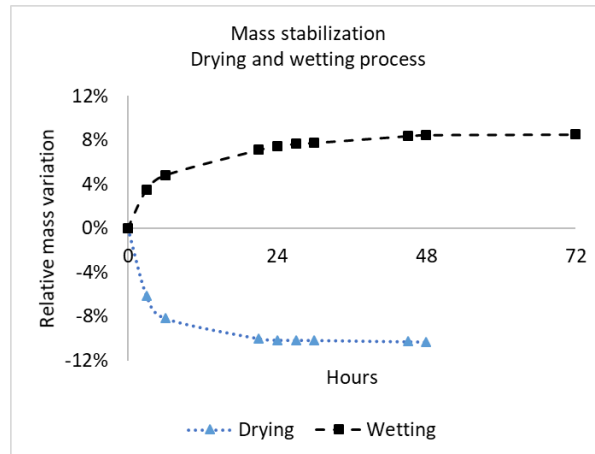
Figure 20: Water jet cutting machine. Samples preparation.



Source: author.

In all cases, tests were carried out after mass stabilization on the correspondent conditioning process. Mass stabilization was defined as a mass change less than 0,1% between two consecutive measures after at least 24 hours. Three measurements were done per day, with an interval of at least 3 hours between each one. It took the drying process of 10 mm boards at least 48 hours to achieve the mass stabilization condition, whereas wetting by immersion, around 72 hours as evidenced in Figure 21.

Figure 21: Mass stabilization during sample conditioning .



Source: author.

3.3.1. Three-point bending test

As a façade component, the flexural behavior of the fiber cement boards is an important characteristic of this structure. To assess the bending behavior, the three-point bending test is suggested by different standards and authors ^{34; 107; 108}. For this work, the three-point bending test was performed following the Brazilian standard for fiber cement products without asbestos – NBR 15498:2016.

Five samples of 250 mm x 250 mm x 10 mm were tested in each conditioning state. All samples were stored during 3 months in laboratory conditions. Testing was performed in a universal testing machine Instron with a controlled displacement and a load cell of 5 kN. The testing set-up is illustrated in Figure 22.

Figure 22: Test apparatus and sample positioning for the three-point bending test.



Source: author.

As the material is plane orthotropic, all samples were tested on the longitudinal and on the transverse direction. Modulus of elasticity (MOE), the first crack stress (LOP) and the ultimate flexural stress, or modulus of rupture (MOR), are calculated using the elastic bending theory, such as presented in 3.2.2.2 and as indicated on the

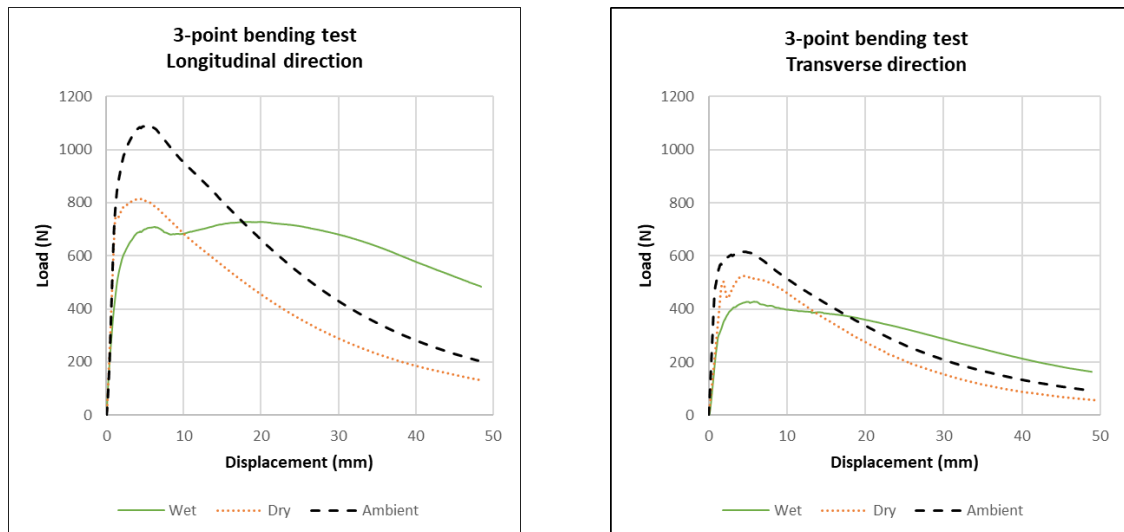
applicable standards The MOE is the slope of the initial straight-line of the force-displacement curve after the experimental grip device accommodation. The LOP is the equivalent stress obtained by the upper limit force of this straight-line. The MOR is the ultimate stress, obtained from the maximum force reached by the material. It is important to highlight that even if the standards indicate the use of linear equations to calculate the MOR, this ultimate stress is usually achieved beyond the elastic linear behavior of the material and this approximation can be inaccurate in this post-cracking regime, though. Another limitation of this test is the assumption of bending equations for small deflections: in the case of fiber cement boards, the deflections can reach high values, and the real bending moment is higher than the test provided value.

Figure 23 presents the average load-displacement curve obtained for dry, wet and ambient samples tested both in the longitudinal and transverse direction. A lower fiber contribution can be observed when the composite is solicited in the transverse direction, resulting in smaller strength values (MOR). The MOR relation between the two directions ($L/T \approx 1,7$) confirms the assumption of considering a preferential fiber orientation in the composite. On the other hand, the LOP values are quite closer for both directions ($L/T \approx 1,2$), confirming that this value is mainly driven by the cementitious matrix properties.

Furthermore, as expected, the material proves to have a non-linear behavior. Its linear limit is defined by the LOP value, and corresponds to the strength of the cementitious matrix. This linear behavior is observed only during the initial and lower displacements and its definition is not always clearly marked in the curves. The variability of the linear parameters (MOE and LOP), presented in Table 22, with coefficients of variation reaching 10% to 15%, indicates the variability of the materials and the limitation to take linear models to define it.

It can be seen that the hygrometric conditions have an important influence on the material strength and on the softening behavior (post-peak). The elastic behavior has a significant changing in a wet condition, with a significant reduction of the MOE. In terms of fracture mechanics, the main differences observed are the differences on the damage initiation point (LOP), the material strength (MOR), and on the fracture energy, obtained by the area under the load-displacement curve. The strain hardening, an indicator of the fibers' contribution, does not appear, even in the wetting condition.

Figure 23: Load-displacement average curve for the three-point bending test in different hygrometric conditions.



Source: author.

Finally, results showed that boards present the greatest ultimate strength in ambient conditions, without drying or saturation. However, the LOP was increased by the drying process, confirming that the cementitious matrix becomes strengthened in drier conditions. A reduction in the material porosity due to drying can explain this LOP and MOE increasing.^{109; 110} The water absorption promotes the reduction of fiber-matrix bond. As the cellulose absorbs a lot of water, the composite becomes significantly weaker when wet¹¹¹. On the other hand, material toughness is increased in saturated conditions due to fiber-slipping improvement.

Table 22: Flexural characterization of a 10mm-board in different hygrometric conditions following ABNT NBR 15498:2016. Average results from five samples for each condition.

Hygrometric condition	MOE (GPa)		LOP (MPa)		MOR (MPa)		Energy (N.m)	
	L	T	L	T	L	T	L	T
Ambient	8,4 ± 0,7	5,9 ± 0,9	5,9 ± 0,4	5,2 ± 0,9	14,1 ± 0,4	7,9 ± 0,3	28,4 ± 0,9	15,0 ± 0,9
Wet	4,2 ± 0,6	2,7 ± 0,4	4,5 ± 0,2	3,8 ± 0,5	9,4 ± 0,5	5,5 ± 0,2	31,2 ± 1,5	14,9 ± 1,7
Dry at 60°C	7,1 ± 0,6	5,7 ± 1,6	7,5 ± 0,6	6,5 ± 0,6	10,5 ± 0,7	6,7 ± 0,6	20,3 ± 2,0	12,1 ± 0,8

Source: author.

3.3.2. Direct tensile test

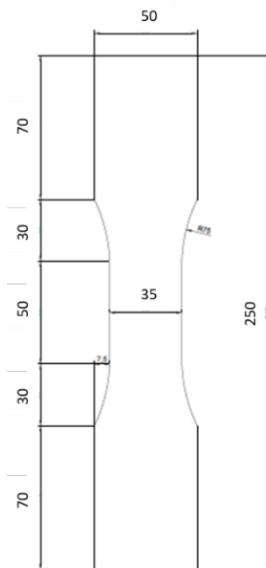
The direct tensile test has been proposed by different authors to demonstrate the tensile strain-hardening behavior and the enhanced ductility of fiber reinforced cementitious materials^{112; 113; 114; 115; 116}. Dogbone-shaped samples are used with

dimensions designed to avoid failure near the grips and to induce cracking at the central area of the specimen, as illustrated in Figure 24a.

The specimens were tested under displacement control in a 5 kN capacity Shimadzu AGS-X universal testing system. A displacement rate of 0,5 mm/min was adopted to simulate a quasi-static loading application. Additionally, the specimen positioning and the grips alignment must be done very cautiously intending to avoid the bending of the specimen. A bi-dimensional strain-gauge was glued at the center of the specimen, as evidenced in Figure 24b. The use of a bi-dimensional sensor allows the determination of the material Poisson's coefficient.

The tensile response of the material is characterized mainly by the first cracking tensile strength, also called Bend Over Point (BOP), and by the Ultimate Tensile Strength (UTS). The fracture energy (G_f) is estimated by the area under the force versus displacement curve. It was not possible to correctly measure the deformations after the first cracking formation using the strain-gauges, since the post-peak behavior engages large and plastic deformations beyond the measure range of these instruments. Nonetheless, elastic deformations were properly quantified.

Figure 24: a) Geometry of dogbone-shaped specimens. b) Test apparatus to direct tensile test in a specimen with strain gage.



a)



b)

Source: author.

Figure 25 highlights the fiber-bridging mechanism, and the different failure stages (matrix cracking, fiber-bridging and fiber pull-out) are marked when the board is loaded in both directions. The role of the fibers, such as in the three-point bending test, is easily visualized in wet condition for both directions. The fiber-bridging behavior implies multiple cracking process, as explained in 3.2.3, and evidenced in Figure 26. The main mechanical parameters obtained are summarized in Table 23.

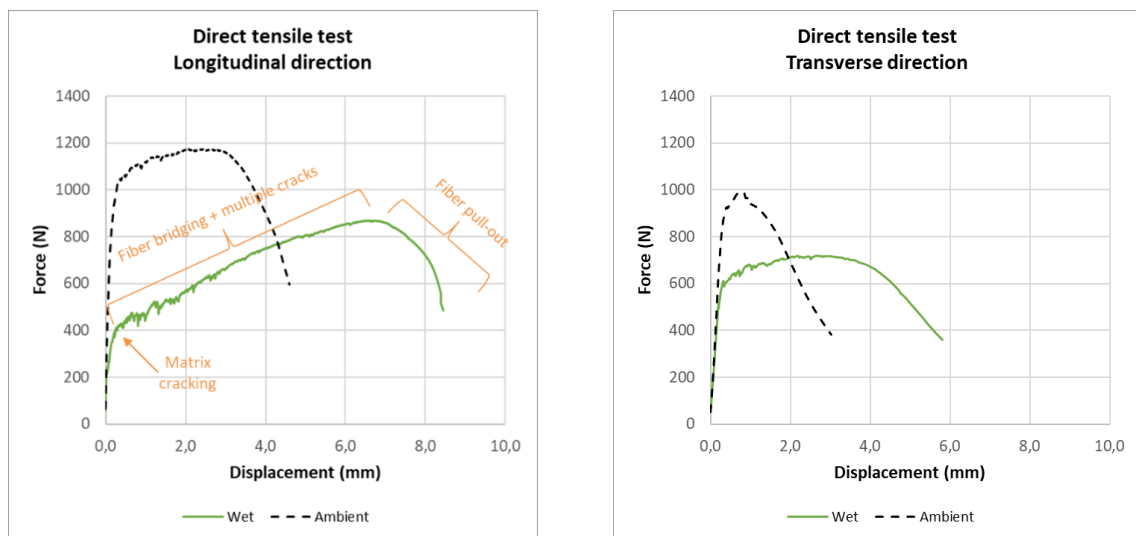
Table 23: Tensile characterization of a 10mm-board in wet and ambient conditions. Average results from three samples for each condition.

Hygrometric condition	E (GPa)		BOP (MPa)		UTS (MPa)		G _f (N/mm)	
	L	T	L	T	L	T	L	T
Ambient	4,2 ± 0,4	3,3 ± 0,2	3,0 ± 0,2	2,3 ± 0,1	3,3 ± 0,2	2,5 ± 0,1	14,8 ± 0,2	7,4 ± 0,1
Wet	3,4 ± 0,6	2,7 ± 0,5	1,2 ± 0,1	1,6 ± 0,1	2,5 ± 0,2	2,0 ± 0,1	18,6 ± 0,5	12,1 ± 0,3

Source: author.

The elastic moduli obtained by direct tensile test on longitudinal direction are lower than those obtained on the bending test. It may be a reflex of the load not applied exactly on the axis of the specimen. Additionally, Benouis (1995) suggests that on the bending test, a part of the thickness keeps resisting after the crack starts on the traction (bottom) surface, whilst on the direct tensile test the crack is quasi homogeneous through the thickness ¹¹⁷.

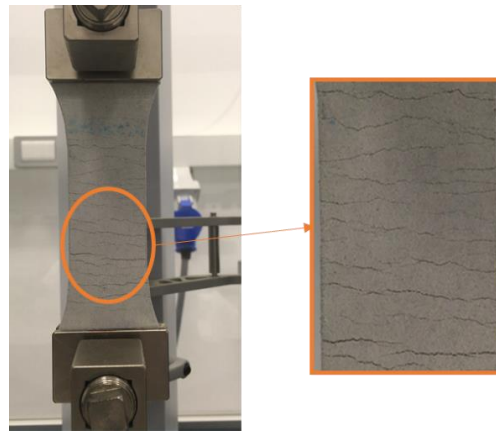
Figure 25: Tensile average response of the board in wet and in ambient conditions.



Source: author.

Furthermore, the MOR obtained with the three-point bending test is several times higher than the UTS obtained by the uniaxial tensile test. This difference, previously reported by many authors, is attributed to size effect, to the nature of the loading or even to the non-uniform fibers distribution in the composite ^{118; 119; 120}. In a direct tensile test, the polypropylene fibers are mobilized only under large strains. In turn, smaller deformations are sufficient to obtain strengthening in bending.

Figure 26: Multiple cracking process due to fiber-bridging in the direct tensile test.



Source: author.

3.3.3. Work of fracture

Aiming to verify the fracture energy of the fiber cement material, the RILEM method was used ¹⁰⁴. The test was worked out, as illustrated in Figure 27, in a Shimadzu AGS-X universal testing machine under a displacement rate of 1mm/min. Rectangular samples of 250mm x 50mm x 10mm were used, with a free span of 80mm.

Xu et al. (2018) showed that the fracture energy (G_f) is linearly correlated to the notch length and dependent on the boundaries of the so-called fracture process zone (FPZ) ¹²¹. A first approximation of the size-dependence of fracture results is obtained by testing two different notches length ($a = 10mm$ and $a = 20mm$). As expected, Figure 28 proves that the results are dependent on the notch length. The curves reaffirm, in addition, the influence of the wet condition in the material strength and toughness, such as observed in the previous bending and tensile tests.

The fracture energy values of the 20mm-notched samples are close to the values obtained by the direct tensile test, as summarized in Table 24. These results can be confirmed through a numerical analysis; however, a more extensive

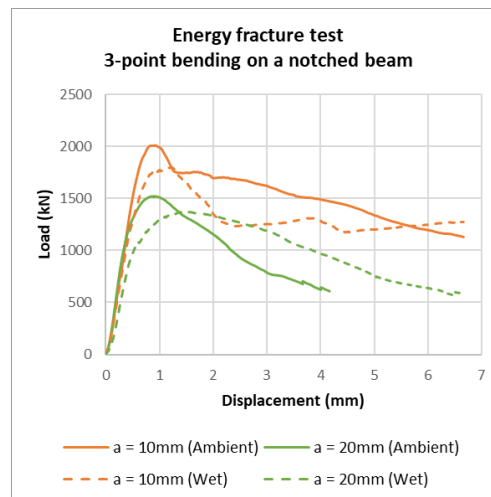
experimental program must be proposed if it is necessary to assess the complete size-dependence description of the fracture parameters.

Figure 27: RILEM work of fracture testing set-up.



Source: author.

Figure 28: Work of fracture results. Load versus displacement average curves for samples with different notch lengths and in different conditioning states.



Source: author.

Table 24: Fracture energy and crack initiation stress (σ_{cr}) obtained by the RILEM method. Average results from three samples for each condition.

Hygrometric condition	Notch length (mm)	σ_{cr} (MPa)	G_f (N/mm)	Fracture energy obtained in the direct tensile test (N/mm)
Ambient	10	8,9 $\pm 0,1$	27,3 $\pm 9,3$	14,8
	20	5,7 $\pm 0,1$	13,7 $\pm 0,9$	
Wet	10	7,6 $\pm 0,1$	42,0 $\pm 1,3$	18,6
	20	4,1 $\pm 0,1$	22,0 $\pm 1,0$	

Source: author.

3.4. Durability analysis

Aging of fiber cement composites results in changes in the mechanical behavior of the material. Changes in strength and toughness are the most common effects observed in long-term ^{123; 124}. These changes can be explained mainly by the matrix changes, by the fiber degradation due to the chemical attack and by the fiber-matrix microstructure and interaction modification. Different authors have been addressing this problem, investigating the influence of the fibers and of the matrix composition on the material aging, mainly regarding the use of natural fibers ^{122; 123; 124; 125}.

The main aging agents for fiber cement in façades are rain water, heating and carbonation ¹²⁶. Using PP fiber, aging effects act mainly on the matrix behavior. Fiber strength and fiber-matrix bond tend to remain constant, and the reinforcement PP fiber tends to maintain its toughness and strength over the years ¹²⁷. Elastic modulus of the matrix, however, increases over time, reducing the material ductility. The matrix densification can change the failure mode from fiber pull-out to fiber fracture.

Regarding natural fibers, a lot of studies have demonstrated that aging causes a marked change in the microstructure ^{128; 129; 130}. The cellulose fibers become petrified; a lot of carbonation products can be seen on the fiber-matrix interface, which was previously occupied by gel. The densification of the fiber-matrix interface provides a loss of strength and ductility. Conversely, the fiber embrittlement results in enhanced strength and reduced ductility. In order to avoid or mitigate the cellulose fiber degradation, some authors have proposed an accelerated carbonation during the early material age, for initial periods of curing ^{131; 132; 133; 134}.

Combining these effects, the composite presents strength and stiffness increasing, with a toughness reduction. Natural and accelerated aging in a CO₂ environment present the same results when both are completely carbonated, without any detection of calcium hydroxide (CH). Accelerated aging tests have been proposed to simulate the long-term effects on fiber cement materials. The fiber cement material can be aged in drying/wetting cycles using a carbonating environment ^{135; 136; 137}.

In a façade application, the aging process is not homogeneous, meaning that carbonation starts from the external surface, usually the more exposed, and it is governed by CO₂ diffusion through board thickness ¹³⁸. This non-homogeneous process may lead to an asymmetric load, resulting in board bowing.

The heat-rain variation produces cyclic loads on the material. The wet-dry process can produce a cyclic shrinkage degrading, by fatigue, the fibers themselves, in case of celluloses fibers, and their interaction within the matrix for all fibers. In addition, carbonation can produce an irreversible shrinkage, besides changing the material microstructure, reducing porosity and densifying the matrix once the carbonation products volume is larger than the CH consumed.

For all these reasons, the aging evolution of the mechanical parameters and of the shrinkage of the boards are important to define the external forces loading the boards. If these effects are neglected, they can generate cracks committing the aesthetic, water tightness and the mechanical performance of the façade. In order to evaluate the carbonation degree of a specimen, the increase of calcite content must be assessed in contrast with the C-S-H and portlandite consumption ¹³⁹. Furthermore, an increase in the bulk density and a reduction in the water absorption can be good indicators of the carbonation evolution also.

In this work, the mechanical behavior of natural aged boards has been compared to new boards. The natural aged samples were exposed for 3 years on a northeast façade in Capivari, Brazil. These boards were installed after 2 months of factory storage. The new samples were characterized after 3 months of their production and storage in laboratory conditions without weather exposition. The material composition was assumed to be the same for aged and new boards, as outlined in Table 21. The chemical composition of the particular raw materials obtained by means of X-ray fluorescence (XRF) are given in Table 25.

Table 25: Chemical composition of raw materials by XRF.

Compound	Cement (%wt.)	Limestone (%wt.)
CaO	61,7	30,9
SiO₂	14,1	5,8
MgO	5,3	16,7
Al₂O₃	3,9	1,6
SO₃	3,7	0,2
Others	4,3	2,2
Loss on ignition (L.O.I.)	6,9	42,6

Source: author.

3.4.1. Carbonation process

3.4.1.1. Carbonation index

An important characterization is assessing how carbonated the sample is. This information can indicate how old the sample is, and in which irreversible shrinkage stage the material is. The evolution of the calcium and magnesium linked to CO₂ rate provides a good estimation of the carbonation status of a sample. The definition of the carbonation status of a cementitious board can allow the estimation of the shrinkage that this board will be submitted during the rest of its service life.

The carbonation index (CI) has been defined as the percentage of carbonatable compounds that are completely carbonated at the analysis instant. Hence, this index is related to the rate of calcite production due to portlandite and C-S-H consumption, disregarding the carbonates (calcite and dolomite) that were already present in the raw material composition. Equation (27) expresses the carbonation index as a function of the different chemical combinations of calcium and magnesium oxides, as described.

$$CI = \frac{(CaO + MgO)_{CO_2} - (CaO + MgO)_{filler}}{(CaO + MgO)_{total} - (CaO + MgO)_{filler}} \quad (27)$$

The quantification of the carbonates present in the filler is done using the chemical composition of the raw materials, as presented in Table 25, weighted by the material formulation shown in Table 21. Similarly, by means of an XRF analysis, the total of calcium and magnesium content were determined in aged and new samples, as summarized in Table 26.

Table 26: Total calcium and magnesium oxides in new and aged samples by XRF analysis.

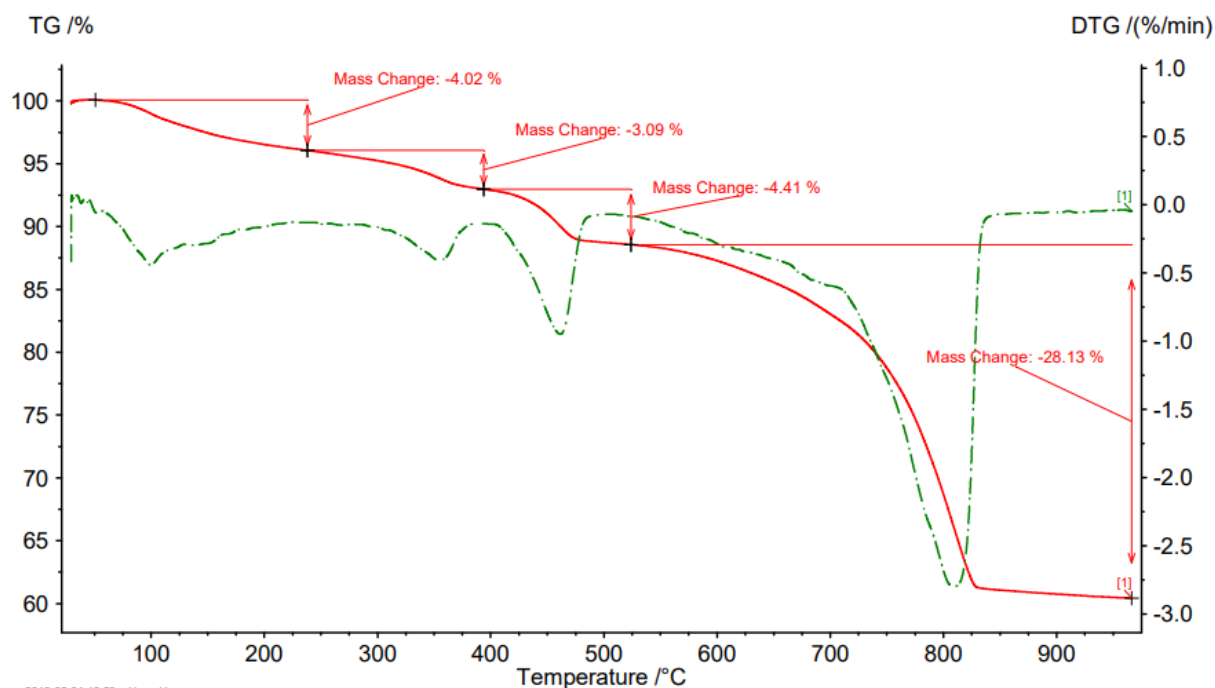
Compound	New sample (%wt.)	Aged sample (%wt.)
CaO	38,3	39,1
MgO	7,6	6,0

Source: author.

The analysis of the compounds linked to CO₂ can be made by means of a thermogravimetric analysis (TGA). The TGA of new and aged samples were conducted on a NETZSCH STA 449F3 instrument using a 55 mg sample in an Al₂O₃ crucible, in an inert atmosphere (nitrogen flow ratio equal to 60 mL/min), with a heating ratio of 10 °C/min from 30 °C up to 1000 °C. Prior to the test, the samples were finely ground in a

laboratory ball mill, then they were dried in a ventilated oven at 40 °C until mass stabilization, and stored in a desiccator for 24 hours at most.

Figure 29: TG and DTG curves of new samples.

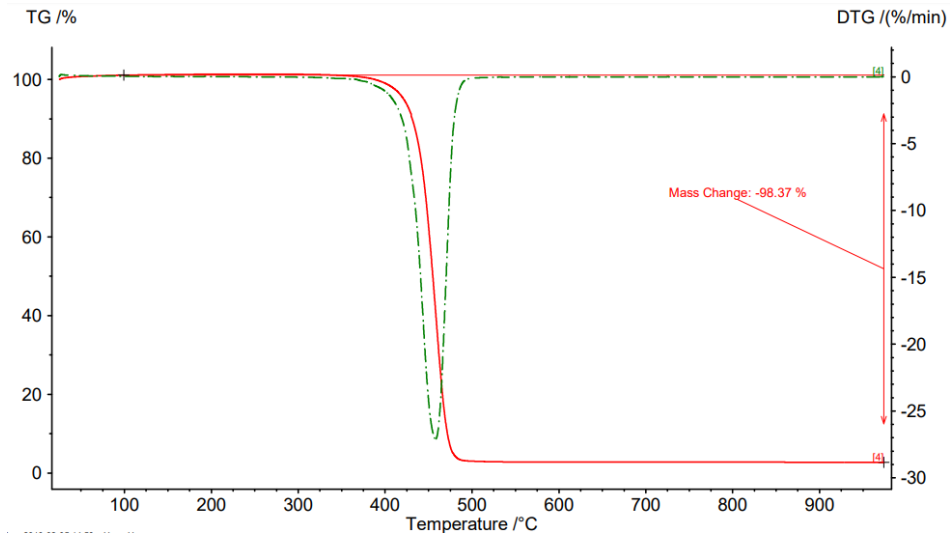


Source: author.

Figure 29 presents the thermogravimetric (TG) curve and its first derivative curve (DTG) for the new samples. The first peak (below 250 °C) corresponds to the thermal decomposition of C-S-H and ettringite, mainly. The second peak, from about 300 °C to 400 °C, indicates that the cellulose decomposition takes place. The third peak is the result of two simultaneous reactions: the PP fibers consumption, around 440 °C as evidenced in Figure 30, accompanied by the decomposition of the portlandite, around 450 °C. Finally, the decomposition of the dolomite and calcite occurs above 550 °C releasing CO₂.^{106; 140}

The TG and DTG peaks are in the same temperature ranges both for aged and new samples, as shown in Figure 31. Nevertheless, a significant difference can be noted in the mass change related to each peak, as indicated in Table 27. Assuming that the fiber content does not differ over time, a reduction on the C-S-H, ettringite and portlandite content is observed, accompanied by an increase of the carbonates amount. This confirms the occurrence of carbonation in the aged samples.

Figure 30: TG and DTG curves of PP fibers.



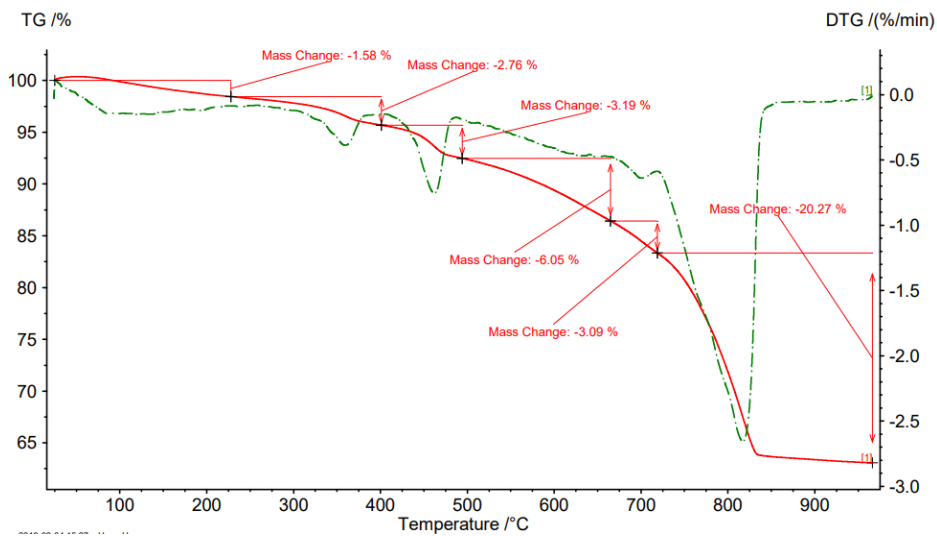
Source: author.

Table 27: Mass change observed for the different TG peaks for new and aged samples.

Peak	New sample (%wt.)	Aged sample (%wt.)
1 st (C-S-H + Ettringite)	4,0	1,6
2 nd (Cellulose)	3,1	2,8
3 rd (PP fiber + Portlandite)	4,4	3,2
4 th (Dolomite + Calcite)	28,1	29,4

Source: author.

Figure 31: TG and DTG curves of aged samples.



Source: author.

Calculating the carbonation index by (27), a CI of 27,9% was found for the new samples, and 35,9%, for the aged specimens. This result indicates that even if the material has been carbonating, after three years of natural exposition, the carbonation process has not ended yet. Observing the third peak in Figure 31, around 5,7% of portlandite remains, when considering 1,8%wt of PP fibers, which reaffirms that carbonation can still go on.

This conclusion shows that the carbonation process in a natural weathering is a slow process and takes more time to be complete than in a controlled ambient condition. Constant rain, high humidity and high temperatures inhibit the carbonation, which is greatest in 50% RH ¹⁴¹. A material completely dried or fully saturated slows down the carbonation process. Although the carbonation reaction needs water, the CO₂ diffusivity is reduced if the pores are filled by water.

Even if the results prove to be consistent, the raise of the CI would be expected to be quite more significant. In fact, this number was obtained assuming that the raw materials were exactly the same for new and aged samples. However, this assumption cannot be confirmed, since the characterization of the raw materials is not available for the aged boards. A proper characterization of these original raw materials for the aged specimens may lead to a more consistent CI value.

3.4.1.2. Bulk density and water absorption changes

Both bulk density (ρ) and water absorption (w_{abs}) parameters are measured and registered for each produced batch, as defined by ³⁴. Accordingly, the variation of these properties after aging can be compared. The original properties of the boards produced on September of 2015 were compared with the density and water absorption characteristics after 3 years of natural aging.

The methodology to determine these quantities is based on the Brazilian standard ³⁴. It consists of:

1. Samples immersed in water at ambient temperature until mass stabilization;
2. Sample volume (V) and the initial sample mass (m_i) measured in the saturated condition;
3. Sample dried in a ventilated oven at 100 °C until mass stabilization;
4. Sample final mass (m_f) measured in the dry condition.

The bulk density and water absorption results are respectively calculated by equations (28) and (29). Looking at Table 28, an increase in the bulk density can be noted along with a significant decrease in the water absorption. As previously explained, these two events contribute to reaffirm that the carbonation process has been effectively occurring in the exposed samples. The material densification and the water absorption reduction are related to the pore size reduction, a characteristic and expected effect of the fiber cement carbonation.

$$\rho = \frac{m_f}{V} \quad (28)$$

$$W_{abs} = \frac{m_i - m_f}{m_f} \quad (29)$$

Table 28: Bulk density and water absorption changes after natural aging.

Property	Measured on September, 2015	Measured on December, 2018 – after 3 years of natural aging
Bulk density (g/cm ³)	1,5 ± 0,2	1,7 ± 0,1
Water absorption (%)	24,3 ± 1,0	11,5 ± 1,2

Source: author.

3.4.1.3. Flexural behavior changes

In order to assess the consequences of natural aging in the mechanical properties, the flexural behavior of the aged samples was characterized following the methodology described in 3.3.1. The specimens were tested on the longitudinal direction in ambient and in wet condition.

The aging, mainly related to carbonation, has significantly changed the flexural behavior of the boards (Figure 32). It is possible to note an increase in the maximum load resistance in both cases after aging. On the other hand, the softening behavior of aged samples starts earlier, and it is sharper than that of the new one.

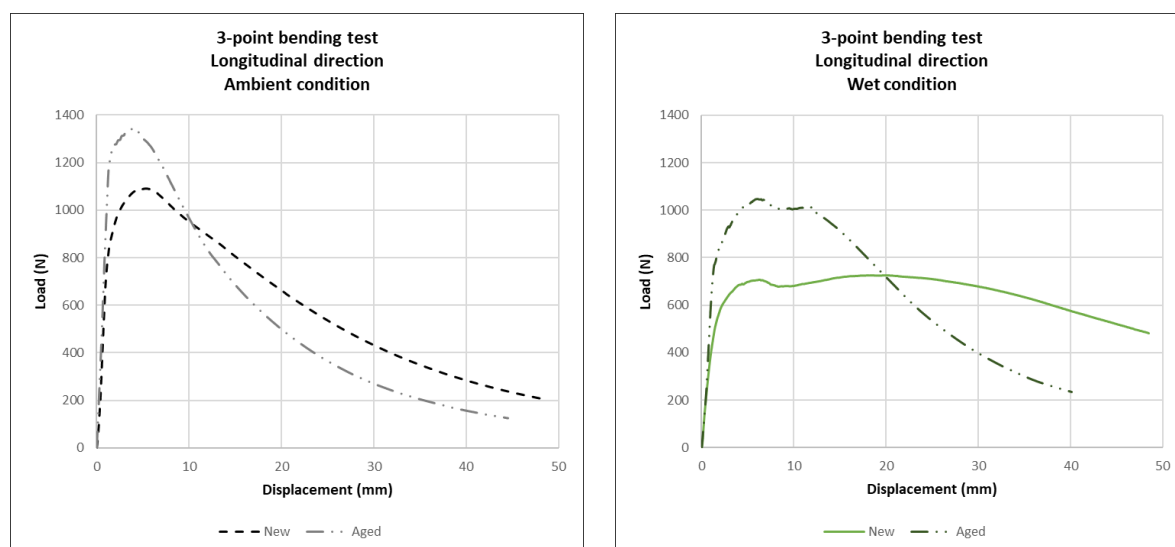
The results in Table 29 show that after 3 years of natural aging, the boards become more resistant, with a MOR increasing around 15% to 40%. Nevertheless, the fiber cement has lost ductility (energy decrease of about 15%) and has become more rigid, with 15% to 35% of MOE rising.

Table 29: Comparative flexural results of boards after natural aging.

Hygrometric condition	MOE (GPa)		LOP (MPa)		MOR (MPa)		Energy (N.m)	
	New	Aged	New	Aged	New	Aged	New	Aged
Ambient	8,4 ± 0,7	9,4 ± 1,2	5,9 ± 0,4	14,2 ± 1,2	14,1 ± 0,4	17,4 ± 0,8	28,4 ± 0,9	24,8 ± 1,5
Wet	4,2 ± 0,6	6,3 ± 2,0	4,5 ± 0,2	9,1 ± 1,5	9,4 ± 0,5	13,5 ± 1,7	31,2 ± 1,5	26,5 ± 1,7

Source: author.

Figure 32: Comparative of the flexural behavior of aged and new samples in ambient condition.



Source: author.

3.4.2. Dimensional variation

Drying and carbonation processes imply shrinkage in cement-based materials. Material shrinks due to the moisture loss by capillarity and from the gel pore microstructure. The shrinkage strains in a fiber cement composite can assume important values, depending on its formulation and on its production process. This volume variation is linked to the cement ratio content, the use of moisture-sensitive fibers, such as cellulose, the high porosity of the composite, and the high drying rates of thin sheets as well. ⁷⁴

This dimensional variation may cause some issues in applications of the fiber cement boards. Bowing and micro cracking can be generated on the boards applied on façades, for example. The screwed connections of the board on the frame structure restrain its movement. Restrained shrinkage promotes tensile stress on the board, enhancing the risk of cracking. This is why it is important to study this problem more cautiously, detailing the stress distribution around the connection's regions. ⁷⁴

The shrinkage process initiates as soon as cement hydration starts. However, it becomes critical at old ages when boards are already installed. Natural soak-dry combined with cement carbonation are the main responsible processes to induce cracking along the service life of the boards. Souza (2014) has presented the main influence factors of shrinkage cracking. His work shows the shrinkage mechanisms, the difference of shrinkage by drying and by carbonation and their characteristic values for a fiber cement material. ¹³⁹

Soak-dry in a hardened material generates a reversible shrinkage. On the other hand, carbonation implies in an irreversible dimensional variation ¹⁴¹. It is important to consider the combination of these two processes to calculate the total shrinkage and its correspondent hygrometric generated strain during time.

Accelerated tests provided by Souza (2014) in a PVA-based board, with 60% of cement mass fraction, have indicated a total shrinkage around 5,6 mm/m after more than 2 months of drying exposition in a CO₂ enriched environment. The important role of carbonation shrinkage was proved, with an irreversible dimension reduction of 2,7 mm/m ¹³⁹.

Thermal and hygrometric variations are defined as an intrinsic material property. The coefficients of thermal expansion (α) or moisture expansion (β) states the dimensional variation of a material in function of hygrometric conditions changes. Temperature (ΔT) and humidity (ΔRH) variations can induce loads in the board, influencing the design of the number and spacing of fixing screws. ^{86; 142}

Temperature and moisture variation produce a free expansion strain in a single layer in a stress-free state. Stress would be developed in the layer only if the hygrothermal strains were constrained. Considering that α and β are homogeneous in both directions, the stress induced in the layer due to the constrained hygrothermal strains can be written as (30). ^{86; 142}

$$\begin{pmatrix} \sigma_{xx} \\ \sigma_{yy} \\ \sigma_{xy} \end{pmatrix} = (-\alpha\Delta T - \beta\Delta RH) \begin{pmatrix} Q_{11} & Q_{12} & 0 \\ Q_{12} & Q_{22} & 0 \\ 0 & 0 & Q_{66} \end{pmatrix} \begin{pmatrix} 1 \\ 1 \\ 0 \end{pmatrix} \quad (30)$$

From (30), by integration, the normal forces and the bending resultant moments on the laminated can be found, induced by hygrothermal loads. Considering that all layers are identical and oriented in the same direction, the hygrothermal strains will be the same in case of uniform temperature and moisture variation through board

thickness. In cases when only a portion (some layers) of the laminated is concerned by hygrothermal variation, the hygrothermal strains are not the same through the thickness. This later assumption is important in case of using the fiber cement boards as an external façade envelope, where only the external face of the board will be subjected to moisture and thermal variations.

In both cases, membrane forces will be generated on the board if, and only if, the normal displacements are restrained. The normal resultants are proportional to the total thickness concerned by the hygrothermal variations. However, when only a few layers are affected by hygrothermal changes, then a bending moment will be generated independent of displacement restrictions. The bending moments are due to the non-uniform strain distribution, and they lead to board bowing.

Equation (31) describes the hygrothermal normal resultants in function of the depth of hygrothermal induced loads (t_{hyg}); it means the total thickness concerned by an hygrothermal variation. If all the board is subjected to the same moisture and temperature variation, then h_{hyg} is taken equal to t (total board thickness). In the case of moisture and temperature varying only in a quarter of the thickness, then h_{hyg} is taken equal to $t/4$, for example. It is important to remind that these hygrothermal forces are produced only in case of restrained displacements.

$$\begin{pmatrix} N_x \\ N_y \\ N_{xy} \end{pmatrix} = t_{hyg}(-\alpha\Delta T - \beta\Delta RH) \begin{pmatrix} Q_{11} & Q_{12} & 0 \\ Q_{12} & Q_{22} & 0 \\ 0 & 0 & Q_{66} \end{pmatrix} \begin{pmatrix} 1 \\ 1 \\ 0 \end{pmatrix} \quad (31)$$

The bending resultant moment can be written as (32), with the reference drawn in Figure 16. In case all layers are subjected to the hygrothermal strains, the stress in each layer ($\underline{\sigma}_k$) is constant. Therefore, the moment results zero, as shown in (33). In case of a non-uniform hygrothermal variation, the resultant moments are given by (34), where t_{hyg} is the same as defined previously.

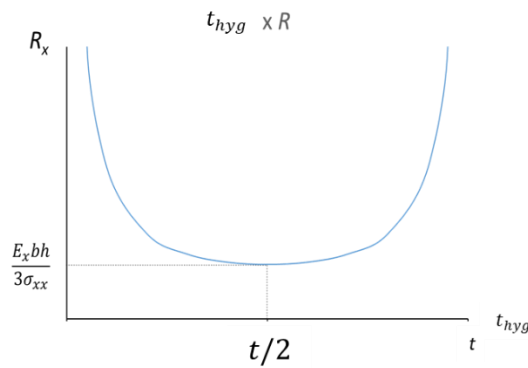
$$\underline{M} = \int_{-t/2}^{t/2} \underline{\sigma}_k z dz \quad (32)$$

$$\underline{M} = \int_{-t/2}^{t/2} \underline{\sigma}_k z dz = \underline{\sigma}_k \int_{-t/2}^{t/2} z dz = \underline{0} \quad (33)$$

$$\begin{aligned} \underline{M} &= \int_{(\frac{t}{2}-t_{hyg})}^{\frac{t}{2}} \underline{\sigma}_k z dz = \underline{\sigma}_k \int_{(\frac{t}{2}-t_{hyg})}^{\frac{t}{2}} z dz \\ &= \left(\frac{t^2}{4} - \left(\frac{t}{2} - t_{hyg} \right)^2 \right) (-\alpha \Delta T - \beta \Delta RH) \begin{pmatrix} Q_{11} & Q_{12} & 0 \\ Q_{12} & Q_{22} & 0 \\ 0 & 0 & Q_{66} \end{pmatrix} \begin{pmatrix} 1 \\ 1 \\ 0 \end{pmatrix} \end{aligned} \quad (34)$$

Admitting a linear relationship between moment and curvature, the board bowing magnitude can be described as a function of the t_{hyg} . Board bowing is done by the radius of curvature of the board (R). When R tends to the infinity, it means that the board is not bowing. The maximum bowing effect is reached when hygrometric loads act on half of the board thickness, resulting in a lower curvature radius value.

Figure 33: Bowing effect in function of the depth of hygrometric variation on a laminated board.



Source: author.

3.4.2.1. Shrinkage magnitude

Different formulations or different manufacturing processes will generate materials with different dimensional variation magnitudes. Maximum values can vary from around 1,2mm/m up to 6,0mm/m among boards available in the Brazilian market, for example ¹⁴³.

To get an order of magnitude of this shrinkage, the results presented by Souza (2014) ¹³⁹, with a PVA-based board and 60% of cement mass fraction, will be assumed. In this case, the dimensional variation values are taken as follows:

- 5,6 mm/m of irreversible shrinkage due to drying and carbonation along external board service life;
- Drying irreversible shrinkage occurs mainly during the first 14 days of drying, representing around 2,2 mm/m;

- Irreversible shrinkage by carbonation represents around 2,7 mm/m, and it is a slow process, lasting a few years;
- Dimensional variation due to soak-dry is a reversible process, representing approximately 2,1 mm/m.

These assumptions indicate that the behavior of the fixing systems depends on the stage of irreversible processes at the moment of board installation. If a board is installed after 14 days, a total of 3,4 mm/m of irreversible shrinkage can be estimated during the service life of the structure. The soak-dry dimensional variation of 2,1 mm/m must be additionally considered. The carbonation index (CI), presented in 3.4.1.1, can be used to estimate the current carbonation state of a board previous its fixation on the façade. This estimation allows the prediction of irreversible shrinkage that the board will be submitted once installed and during its service life.

The reversible shrinkage was assessed looking at fatigue effects at the fixing region. Matsumoto and al. (2010) reported a fatigue analysis of a PVA fiber reinforced composite. Under a cyclic loading varying from 0,05% compressive strain to 0,2% tensile strain, the tensile strength slowly decreases to 90% of its initial value during the first 100 cycles, and it sharply decreases to 10% from 100 to 1000 cycles ¹⁴⁴.

It is important to mention, as remarked by Wei et al. (2016), that during wetting the fiber cement may absorb more water than it loses in drying ¹³⁴. This fact reveals, indeed, that soak-dry shrinkage may be partially irreversible.

3.5. Concluding remarks

Understanding the production process and the influence of the fibers on the composite is important to define the appropriate equations to describe boards. Concerning the fracture process of fiber cement materials, the importance of fibers contributions and their interaction with the cementitious matrix has been shown. This fiber-matrix interaction promotes a failure process that cannot be described by LEFM, thus, a steady-state cracking theory can be adopted, considering cohesive models to represent the composite cracking.

The experimental characterization of the boards showed that results are influenced by hygrometric conditions of samples. Saturated boards presented lower strength instead of toughness and ductility improvement. The fiber bridging mechanism

is highlighted in a wet condition, with a lower matrix strength and the fibers enhancing the material performance. The three-point bending and the direct tensile tests provide different mechanical results because fibers are not requested in the same manner on each of them. Tensile tests have given a result closer to the true material behavior. The parameters obtained will be used to find the correct inputs for the numerical models to simulate the behavior of these boards in a façade system. Additionally, the results highlighted the variability of the material even if all samples were taken from the same batch. The variability of the production process was not assessed in this work, however, it is an important variable to be considered before extrapolate any result.

The three-point bending test results showed the limitation of the linear equations presented on current standards. The MOR values obtained are several times larger than the ultimate stress obtained in the direct tensile test. This fact is due to the inaccurate extrapolation of the linear equations to calculate the MOR that is reached in a non-linear stage of the material. In this regard, the LOP seems to be a more accurate value to be considered for design purposes and it provides a better estimation of the damage initiation on the material.

A proposal of durability assessment of the fiber cement boards has been presented. Samples of a board exposed in a natural aging condition were characterized after 3 years of weathering exposition. Even if the mechanical results have indicated an increasing in strength, a significant reduction of material ductility has been observed, meaning the boards are becoming more brittle over time. In addition, it has been verified that the carbonation process had not been finished after three years, since some hydration phases had remained not carbonated. These remarks are important because the material embrittlement and the irreversible shrinkage may generate cracks on the boards if they are not properly considered.

Finally, the importance of simultaneously considering the combination of wind loads, carbonation and moisture shrinkage has been shown. The characteristic values presented or obtained in this chapter will be used to assess the behavior of these boards under different fixings systems (stiffness, screws distance, etc.). Since the global behavior of the material has been properly characterized, including the mechanical modifications due to aging, the best numerical techniques can be found to simulate these boards and their fixations.

4. NUMERICAL MODELING OF FIBER CEMENT BOARDS

Numerical model input definition: Crack and damage modeling

Fiber cement was presented in chapter 3 as a multilayered composite material, which performance depends on the combined behavior of a cementitious matrix and natural and synthetic fibers. The experimental characterization showed that the constitutive law of the composite is highly influenced by the presence of the fibers and their interaction within the cementitious matrix. It has been shown that the fibers can promote a pseudo-strain hardening effect, increasing the material strength and its toughness after the first stress peak.

Hence, a numerical model will be considered adequate if it is able to correctly predict the elastic phase, the peak loads and the post-peak behavior both for hardening and softening cases, considering damage and cracking propagation on this material. Using the Finite Element Analysis (FEA), different approaches can be used to represent the behavior of fiber reinforced cementitious materials¹⁴⁵. These techniques have combined different strategies to represent the fiber effect within the composite and to simulate and predict the composite failure¹⁴⁶.

A lot of continuum constitutive models have been presented to simulate failure in fiber reinforced cementitious materials^{147; 148; 149; 150; 151}. A non-linear elasticity formulation or elasto-plastic-damage laws are examples of these continuum techniques, where damage is represented by a modification on the constitutive law of an element. On the other hand, some models propose a discontinuous approach to represent the crack propagation, introducing a physical discontinuity into the displacement field. The Cohesive Crack Model or the eXtended Finite Element Method (XFEM) are examples of these discontinuous crack representation methods^{152; 153; 154}.

Furthermore, some models are based on the physical representation of the fibers within the cementitious matrix^{155; 156; 157; 158}. These discrete techniques require the geometrical inclusion and an explicit representation of each fiber in the numerical model. Even if these discrete approaches can fit the experimental behavior by introducing a bond-slip law to represent the fiber-matrix interaction; usually, the discrete fiber representation can result in a heavy model, increasing calculation time.

The aim of this chapter is to find a numerical strategy, using FEA, able to simulate the global behavior of a fiber cement board, considering its main energetic

mechanisms. The objective is to identify proper models and techniques available in the software ABAQUS to fit the experimental curves. Simplified models are expected to be found capable of considering the fiber effect by means of a homogenized law, avoiding any fiber discretization.

The three-point bending test and the direct tensile test presented in the previous chapter are numerically simulated. For each test, a particular numerical model is proposed using 2D shell elements. The numerical analysis is done using ABAQUS Explicit with an automatic stable time step. Explicit analysis is preferred to an implicit one to simulate materials with ascending or softening behaviors. The implicit analysis needs iterative calculations, and when the material enters the softening phase, material stiffness becomes negative. Then, the global stiffness matrix is not positive and it is definite, generating a convergence problem. For the explicit analysis, the equation is solved at each step without any iteration procedure.

The material behavior is simulated by means of different techniques. A comparison is done among the XFEM technique, the Hashin damage model and the Concrete Damage Plasticity model available in ABAQUS¹⁵⁹. For each of these two experimental tests, an appropriated numerical technique is chosen and assessed, comparing the numerical and experimental results. The input parameters for each model are defined by an inverse analysis in order to properly fit the experimental curves. This analysis was limited by the availability of bi-linear damage models in ABAQUS for the XFEM and the Hashin modelization, though.

4.1. Failure simulation techniques

For composite materials, the damage onset is characterized by the microcracking initiation. The material failure, as presented in 3.2, may occur by the rupture of the matrix, the rupture of fibers or by the degradation of fiber-matrix interaction. The standard failure criteria used to describe the damage onset on laminated composites material may be classified in: maximum stress criteria, maximum strain criteria or energetic-based criteria, such as the Hashin's.¹⁶⁰

After damage initiates, its evolution may be controlled either by an energetic criterion or by the controlling of the critical displacement at failure. According to the failure criteria previously chosen, the critical fracture energy that controls the crack propagation in the material can be defined. As presented in chapter 3, cracking in fiber

cement board is a steady-state process with a cohesive behavior at the crack surfaces. It means that, once initiated, a crack needs an additional amount of energy to propagate in the material – cracking is not a catastrophic process.

Different numerical strategies may be adopted to represent the damage evolution. Three main classes of methods to represent a cracking process are: re-meshing techniques with adaptive meshes accompanying the crack evolution, homogenized models that change the constitutive law on damaged elements by degrading the material stiffness matrix, and numerical methods that represents crack as a physical discontinuity on the displacement field, without needing a re-meshing strategy, such as proposed by XFEM.

In this work, there is a comparison of three different numerical strategies available in ABAQUS: the XFEM formulation and the Hashin damage criteria using bi-linear cohesive zone models and the Concrete Damage Plasticity model. The aim of this study is to find a good technique to simulate the fiber cement boards, avoiding the need of fiber discretization and its explicit representation in the model. Before applying these techniques to model some experimental tests, a summary of the ABAQUS formulation for each damage model is presented.

4.1.1. eXtended Finite Element Method (XFEM)

The XFEM technique was first proposed by Belytschko and his co-authors to solve crack propagation problems without re-meshing ¹⁶¹. The use of XFEM has been reported to estimate failure in laminated composite structures ¹⁶², to study crack propagation in concrete ^{163; 164} or even to simulate damage in fiber reinforced structures ^{165; 166; 167; 168}. This technique allows the modeling of discontinuities, such as cracks, independently of the original mesh, using local enrichments functions ¹⁶⁹. The discontinuity representation is done by introducing a modified displacement field in the so-called enriched domain, i.e. in the cracked region.

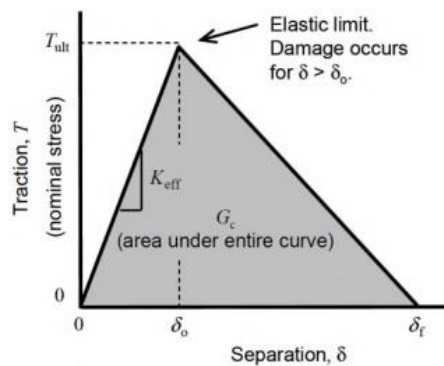
Hence, the displacement vector (\underline{u}) is approximated by enriched functions. In the ABAQUS formulation for XFEM ¹⁵⁹, asymptotic crack-tip functions ($F_\alpha(x)$) and discontinuous jump functions, such as the Heavside function ($H(x)$), are added to the usual nodal shape functions ($N_i(x)$) to respectively represent the singularities at the crack-tip and the discontinuity across the crack line or surface. As described by (35), the nodal enriched vectors \underline{a}_i and \underline{b}_i^α are modified by their associated enriched

functions. These enriched nodes are superposed on the original mesh, as phantom nodes. For this reason, once crack initiates, the modified nodes can move apart without changing the original mesh.

$$\underline{u} = \sum_{i=1}^n N_i(x) \left[\underline{u}_i + H(x) \underline{a}_i + \sum_{\alpha=1}^4 F_{\alpha}(x) \underline{b}_i^{\alpha} \right] \quad (35)$$

Failure can be represented in ABAQUS using a XFEM-based cohesive segment model. It means that to describe the complete cracking process a damage initiation criterion must be defined, and, once this criterion is met, the crack propagates following a user defined damage evolution law. The damage evolution law can be defined using a bilinear or an exponential traction-separation formulation. The definition of the failure stress and of the fracture energy is sufficient to define the damage evolution law, as illustrated in Figure 34.¹⁵⁹ These bi-linear or exponential formulations can represent the first limitation of this model, as implemented in ABAQUS, to simulate fiber reinforced materials^{170; 171}.

Figure 34: Traction-separation law for cohesive damage in ABAQUS.



Source: Zhang et al. (2016).¹⁶⁶

The available onset damage criteria in the software are the maximum principal or nominal stress, maximum principal or nominal strain, and quadratic traction-separation-interaction criteria. The maximum stress strength is used as the failure criterion parameter, since it can be easily determined. The maximum principal stress formulation, as presented in (36), indicates that damage initiates once the maximum principal stress (σ_{max}) reaches the maximum allowable principal stress (σ_{max}^0), that is $f = 1$. The use of the Macaulay brackets $\langle \cdot \rangle$ in the formulation indicates that damage cannot occur in a purely compressive stress state.

$$f = \begin{cases} \langle \sigma_{max} \rangle \\ \sigma_{max}^0 \end{cases}, \quad \begin{cases} \langle \cdot \rangle = 0, \text{ if } \cdot < 0 \\ \langle \cdot \rangle = \cdot, \text{ if } \cdot \geq 0 \end{cases} \quad (36)$$

4.1.2. Hashin damage model

The maximum stress and the maximum strain criteria are respectively defined by the stress strength and the rupture strain of the material. These criteria establish that damage initiates if any component of the stress or strain field (shear or tensile/compression stress in longitudinal or transverse direction) reaches the correspondent stress/strain strength. A limitation of both criteria is the supposition that the rupture mechanisms are independent. Aiming to overcome this limitation, energetic criteria have been proposed. These criteria are an extension of the Von Mises criterion, considering the orthotropic material behavior and the interaction between different failure mechanisms.¹⁶⁰

Hill (1948)¹⁷² was the first to extend the Von Mises criterion considering anisotropic materials, but without differentiating the tensile from the compression strength. Azzi and Tsai (1965)¹⁷³ adapted the Hill criterion proposing a failure formulation, called the Tsai-Hill criterion, for unidirectional composites. Hoffman (1967)¹⁷⁴ generalized the Hill criterion with a differentiation between tensile and compressive strengths. Tsai and Wu (1971)¹⁷⁵ reformulated the failure criterion in a tensor form, comprising anisotropy, unidirectionality and tensile/compression differentiation. All these presented criteria define the damage onset, but they are not able to identify the failure mode. Nor can they predict the material degradation and the damage evolution after the first failure.

Later, Hashin (1980)¹⁷⁶ presented his failure criteria for orthotropic materials based on four distinct failure modes: fiber tensile (F_f^t), fiber compression (F_f^c), matrix tensile (F_m^t) and matrix compression (F_m^c). Hence, the onset failure formulation for this model is provided by four distinct equations, as shown in (37), where X^T , X^C , Y^T , Y^C are respectively the longitudinal tensile and compressive strength, and the transverse tensile and compressive strength; S^L and S^T are the shear strength in the longitudinal and transverse direction; α is a scalar coefficient, determining the contribution of shear to the fiber tensile initiation criterion; σ_{11} , σ_{22} and τ_{12} are the components of the stress tensor. The initiation criterion is met when the criterion value (F) reaches 1.0 and then the correspondent failure mode can be identified.

These failure criteria have been proved to provide good results for fiber reinforced polymeric materials ^{177; 178}. Here, the objective will be to assess the availability of this method to fit a cementitious composite, and to find the correspondent input parameters.

$$\begin{aligned}
 F_f^t &= \left(\frac{\sigma_{11}}{X^T}\right)^2 + \alpha \left(\frac{\tau_{12}}{S^L}\right)^2 \\
 F_f^c &= \left(\frac{\sigma_{11}}{X^C}\right)^2 \\
 F_m^t &= \left(\frac{\sigma_{22}}{Y^T}\right)^2 + \alpha \left(\frac{\tau_{12}}{S^L}\right)^2 \\
 F_m^c &= \left(\frac{\sigma_{22}}{2S^T}\right)^2 + \left[\left(\frac{Y^C}{2S^T}\right)^2 - 1\right] \frac{\sigma_{22}}{Y^C} + \left(\frac{\tau_{12}}{S^L}\right)^2
 \end{aligned} \tag{37}$$

Once damage has been initiated, the material response is done by (38) using the damaged elasticity tensor (\underline{C}_d). In this elastic damage formulation, failure is represented in an analytical form, without including any physical discontinuity on the function domain. The damage variables reflect the current state of fiber damage (d_f), of matrix damage (d_m) and of shear damage (d_s), and $D = 1 - (1 - d_f)(1 - d_m)\nu_{LT}\nu_{TL}$. These variables also depend on the tensile and the compressive strength behavior.

$$\begin{aligned}
 \underline{\sigma} &= \underline{C}_d : \underline{\varepsilon} \Rightarrow \underline{\sigma} \\
 &= \begin{pmatrix} (1 - d_f)E_L & (1 - d_f)(1 - d_m)\nu_{TL}E_L & 0 \\ (1 - d_f)(1 - d_m)\nu_{LT}E_T & (1 - d_m)E_T & 0 \\ 0 & 0 & (1 - d_s)GD \end{pmatrix} \underline{\varepsilon}
 \end{aligned} \tag{38}$$

In addition to identifying the failure mode, the Hashin criteria is also able to describe damage propagation for the four different modes. Four different failure modes are considered, and the correspondent fracture energy must be defined for each case: tensile failure in fibers and in the matrix, and compression failure in them. The damage variable is calculated for each failure mode, and it is related to the equivalent displacement, as shown by (39). δ_{eq}^0 is the initial equivalent displacement, from which the initiation criterion for a particular mode was met; and δ_{eq}^f is the equivalent displacement, from which the material is completely damaged in the same failure mode. The corresponding equivalent stress is done by a linear damage law, similar to the one shown in Figure 34, whose evolution depends on the definition of fracture energy for the specific failure mode.

$$d = \frac{\delta_{eq}^f (\delta_{eq} - \delta_{eq}^0)}{\delta_{eq} (\delta_{eq}^f - \delta_{eq}^0)} \quad (39)$$

4.1.3. Concrete damage plasticity model

The Concrete Damage Plasticity model, or CDP, available in ABAQUS 6.14 was originally proposed to simulate the inelastic behavior of concrete structures based on a combination of an isotropic damaged elasticity model and an isotropic plasticity model. This elasto-plastic-damaged model is based on the models proposed by Lubliner (1989)¹⁷⁹ and modified by Lee and Fenves (1998)¹⁸⁰. In this model, the elastic stiffness of the material appears to be degraded when tensile or compressive strength is reached.

The yield surface, which defines the plastic initiation, is controlled by two hardening variables, that is, the equivalent tensile and compressive plastic strains ($\bar{\epsilon}_t^{pl}$ and $\bar{\epsilon}_c^{pl}$). This failure surface is based on classical criteria such as the Drucker-Prager's in compression regime, or the Rankine's in tensile regime. Hence, the yield function is defined in terms of effective stress, considering the stress state modifications under tensile and compressive forces. As shown in (40), the yield function is dependent on the effective hydrostatic pressure (\bar{p}), the Mises equivalent stress (\bar{q}), the maximum principal effective stress, and on the constitutive parameters α, β and γ , defining the flow and the shape of the function.

$$F = \frac{1}{1 - \alpha} \left(\bar{q} - 3\alpha\bar{p} + \beta \langle \hat{\sigma}_{max} \rangle - \gamma \langle -\hat{\sigma}_{max} \rangle - \bar{\sigma}_c (\bar{\epsilon}_c^{pl}) \right) \leq 0 \quad (40)$$

The direction and magnitude of the plastic deformations are governed by a potential flow function. This potential rule is written in (41), where e is the eccentricity, and defined as $e = 0.1$ by default; ψ is the dilatation angle, and σ_{t0} is the uniaxial tensile stress. The definition of the yield surface and of the potential flow functions for a fiber cement material will be based on the values obtained for concrete structures^{181; 182; 183} with a proper tensile behavior description.

$$G(\sigma) = \sqrt{(e\sigma_{t0} \tan\psi)^2 + \bar{q}^2} - \bar{p} \tan\psi \quad (41)$$

The non-linear behavior is a combined effect of plasticity and damage evolution, with damage mainly influencing the stiffness degradation and the unload behavior in cyclic loading. In the CDP model, damage is represented by a scalar parameter (d),

growing according to a damage evolution law. This scalar multiplies the stiffness matrix, acting as a stiffness reduction factor. Equation (42) shows the stress state as a function of the damage variable (d), the initial elastic tensor $\underline{\underline{C}}$, the total strain tensor $\underline{\underline{\varepsilon}}$ and the plastic strain tensor $\underline{\underline{\varepsilon}}^{pl}$. The cracking pattern is presented in this model by the maximum plastic strain field, that is, once the equivalent tensile plastic strain is greater than zero, it means that a crack was initiated.

$$\underline{\underline{\sigma}} = (1 - d)\underline{\underline{C}} : (\underline{\underline{\varepsilon}} - \underline{\underline{\varepsilon}}^{pl}) \quad (42)$$

This damage parameter can be calculated as a function of the plastic strains for tensile and compressive behavior. The material behavior can also be defined in a tabular form, indicating the effective stress versus plastic strain curve. Post-failure in tensile behavior, for example, is described as a tension stiffening effect, considering the stress-strain cracking curve.

Hence, the CDP model proposed in the software ABAQUS, is defined by a yield hardening surface and by softening damage parameters. In this work, the compressive behavior of fiber cement boards was taken similar to a concrete material, whilst the tensile behavior was defined by an inverse analysis, according to the experimental uniaxial tests results.

4.2. Numerical modeling of experimental tests

4.2.1. Three-point bending test

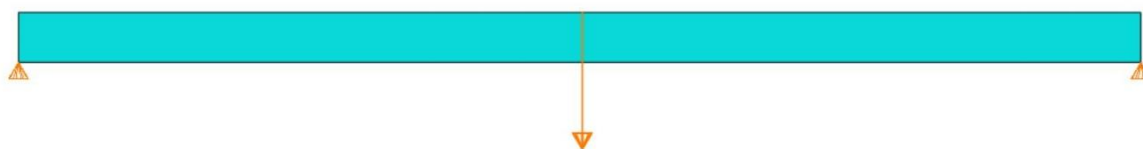
The three-point bending test was first modelled using a 2D model, assuming plane stress. The specimen was meshed with quadrilateral elements. The element used was the CPS4, an ABAQUS element for 2D solid sections with a plane stress formulation, four integration nodes and a bilinear interpolation function. ¹⁵⁹

The undamaged material behavior was assumed linear elastic. After damaging, a non-linear behavior was defined. Elastic properties were obtained by the experimental material characterization, such as presented in Table 22. Through the numerical FEA simulation, the damage initiation and the fracture energy were defined for each condition, fitting the numerical results to the experimental curves.

The three-point bending test was simulated in two-dimensions by a rectangular simply supported beam, with a 215mm span and 10mm thickness, as shown in Figure 35. The supports were represented by two restrained nodes on vertical displacement.

Crosshead displacement was represented by a progressive displacement applied on the top of the beam at its midspan. The applied displacement was considered distributed on 1mm to avoid stress concentration under a unique displacement application point.

Figure 35: Boundary conditions of 3-point bending model.



Source: author.

4.2.1.1. XFEM and Hashin model

Figure 36 shows that XFEM and Hashin simulations present a good agreement with experimental results on the linear elastic behavior, whatever the hygrometric content. On the other hand, the non-elastic behavior prediction is not properly fitted for all testing conditions. When the material presents a stress softening behavior after the first peak load, it can be noted that numerical results appropriately estimate the maximum load and the post-peak behavior. It is the case of the mechanical behavior in ambient and in dry condition.

In wet condition, the fiber cement tested shows a quite hardening behavior after the first peak load. In this situation, neither XFEM nor Hashin is able to capture the hardening effect on the material. In both numerical methods, the degradation process is uniform and irreversible after the damage initiation.

In each hygrometric condition, a sensibility analysis was made in order to understand how the variability of the fracture parameters influences the material load-displacement predicted response. Damage initiation criterion was adopted as the maximum principal stress, and the fracture propagation law is the energy-based law available in ABAQUS. Stress strength (σ_u) and fracture energy (G_f) were defined in Table 30, in order to achieve a relative error less than 3% in maximum load and energy prediction for all conditioning states. Table 31 summarizes the maximum predicted load and the calculated energy for each hygrometric configuration.

There is a slight difference between the XFEM fracture strategy and the Hashin damage model in ABAQUS. For Hashin model it is important to emphasize that the

damage initiation and the cracking progress is dependent of a more complete characterization, not held on this work, of longitudinal and transverse material tensile and compression strength. However, even with quite different parameters, both methods are able to properly capture the material behavior if there is any strain hardening event.

Table 30: Fracture flexural parameters defined to XFEM and Hashin numerical simulations.

Conditioning	Ambient		Wet		Dry	
	σ_u (MPa)	G_f (N/mm)	σ_u (MPa)	G_f (N/mm)	σ_u (MPa)	G_f (N/mm)
XFEM	5,6	16,5	3,5	35,0	4,1	12,0
Hashin	5,8	14,0	4,0	32,0	4,7	11,0

Source: author.

Table 31: Maximum load and energy predicted by XFEM and Hashin numerical simulations.

Conditioning	Ambient		Wet		Dry	
	P_{max} (N)	Energy (N.mm)	P_{max} (N)	Energy (N.mm)	P_{max} (N)	Energy (N.mm)
Experimental	1091,9	28437	726,9	31178	815,6	20299
XFEM	1105,7	28051	713,4	30996	812,1	20392
Hashin	1086,6	28728	718,2	31083	808,0	21764

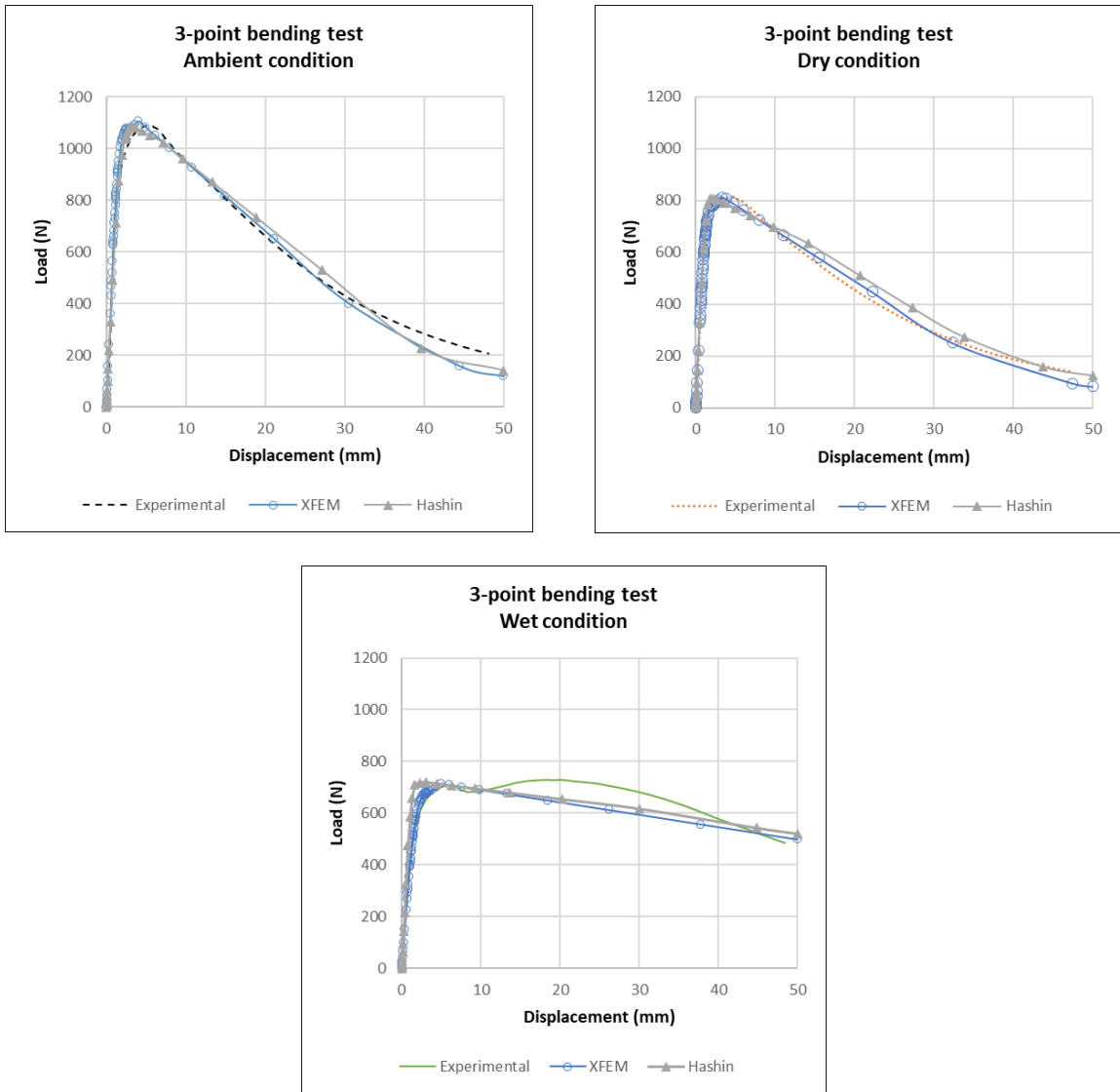
Source: author.

Considering only the elastic behavior of the material combined with damaged criterion is a significant limitation of these models. However, they are adequate to simulate the flexural behavior of the board, since no significant strain hardening effect was observed. It means that the proposed models are able to predict with a good agreement the maximum load withstand by the board; thereby, they can estimate the first crack formation and propagation, using the failure stress and the fracture energy values obtained from the simulations.

4.2.1.2. CDP model

The same exercise was done to calibrate the CDP model. Aiming to characterize the tensile material strength, the compressive failure was neglected in this analysis. Table 32 presents the input parameters defined according to the experimental flexural data. This material definition provides reliable results as shown by the load-displacement curves in Figure 37, with a good agreement for the maximum load prediction, as summarized in Table 33.

Figure 36: Load-displacement simulated flexural response using XFEM and Hashin model.



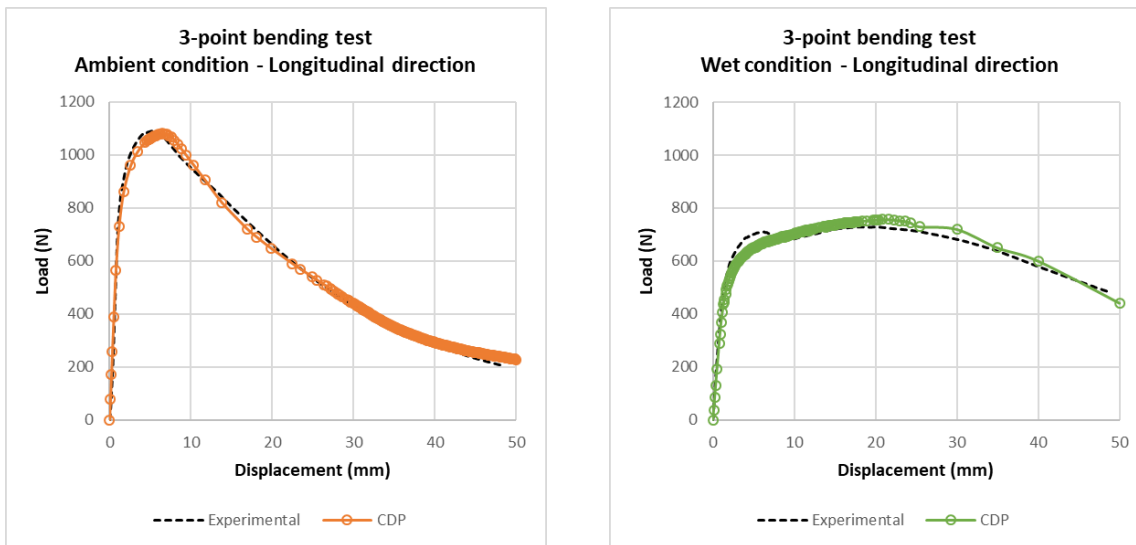
Source: author.

Table 32: Tensile plastic material behavior definition based on the flexural experimental data.

Ambient		Wet	
σ_t^y (MPa)	$\tilde{\epsilon}_t^{pl}$	σ_t^y (MPa)	$\tilde{\epsilon}_t^{pl}$
5,6	0,0	3,5	0,00
3,0	16,0	3,4	0,03
0,5	50,0	3,8	0,08
		3,5	1,00
		2,5	15,0

Source: author.

Figure 37: Load-displacement response of the 3-point bending test simulated by the CDP model.



Source: author.

Table 33: Maximum load and energy predicted by CDP numerical simulations.

Conditioning	Ambient		Wet	
	P_{max} (N)	Energy (N.mm)	P_{max} (N)	Energy (N.mm)
Experimental	1091,9	28437	726,9	31178
CDP	1080,7	28862	747,1	31856
Absolute relative error	1,0%	1,5%	2,8%	2,2%

Source: author.

4.2.2. Direct tensile test

To simulate the direct tensile test, the specimen was modeled in 2D, as shown in Figure 38. Vertical displacements are restrained at the bottom region, and a progressive displacement was applied at the top region of the geometry. Hardening effect and fiber-bridging effect are really marked on this test, as shown in 3.3.2.

4.2.2.1. XFEM and Hashin model

A first model using only the elastic parameters and the fracture energy was proposed. However, this numerical strategy was not capable to depict the non-linear effects, neither with XFEM nor with the Hashin formulation. Both damage formulations were not able to represent the fiber-bridge effect without a discrete modeling of the fibers, and without any interface element. Figure 39 illustrates this difficulty to model the direct tensile response using XFEM or Hashin strategy.

Figure 38: Geometry and boundary conditions to the direct tensile test.

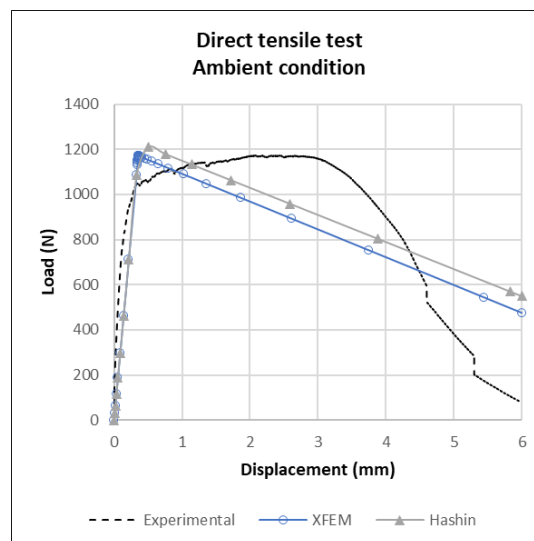


Source: author.

4.2.2.2. CDP model

Using the CDP elasto-plastic-damage model, the microcracking and the fiber effect are represented by an equivalent plastic behavior, such as explained in 4.1.3. Even if the cracking process, in this case, is not physically represented, it is possible to verify that the model has a good agreement with experimental results, providing a well fitted pseudo-strain behavior. Cracking pattern can be visualized by the progressive maximum principal plastic strain.

Figure 39: Load-displacement curve. Direct tensile response using XFEM and Hashin model.



Source: author.

The fiber cement material was modeled considering that its behavior in compression is similar to a standard concrete. Table 34 summarizes the compressive plastic parameters used both in ambient and wet material conditioning. Hence, the correspondent input parameters for ABAQUS were calculated.

Table 34 : Compressive plastic parameters of fiber cement board for the CDP model.

ψ	ε	α	γ	σ_c^y (MPa)
40°	0,1	0,12	3,0	40

Source: author.

Such as presented in the 3-point bending case, the tensile material behavior was defined based on the experimental data. Once plastic strains could not be correctly measured in the proposed experimental methodology, all parameters were obtained by means of an inverse analysis fitting the experimental curve. Table 35 shows the stress and plastic strain values defined to represent the pseudo-strain hardening and the damage of the material for each conditioning state. These final values endorse the elastic approximation to calculate material stress from internal forces; however, the strains could not be approximated by the same linear-elastic equations. Rather, after the first cracking, the development of a pseudo-plastic regime was observed accompanied by the non-linear evolution of strains.

Table 35: Tensile plastic material behavior definition based on the direct tensile experimental data.

Ambient		Wet	
σ_t^y (MPa)	ε_t^{pl}	σ_t^y (MPa)	ε_t^{pl}
1,90	0,000	0,75	0,000
3,00	0,001	1,20	0,002
3,35	0,028	1,50	0,015
3,30	0,150	2,00	0,023
2,00	1,500	2,30	0,025
0,50	2,000	2,48	0,039
		2,00	0,800
		0,50	1,200

Source: author.

Figure 40 presents the stress-strain curve simulated by the CDP model. In both cases it can be noted that the numerical simulation has a good agreement with the experimental curves. The elastic phase, the pseudo-strain hardening and the post-peak behavior were properly captured by the CDP model with a less than 3,0% deviation in load and in energy prediction, as indicated in Table 36.

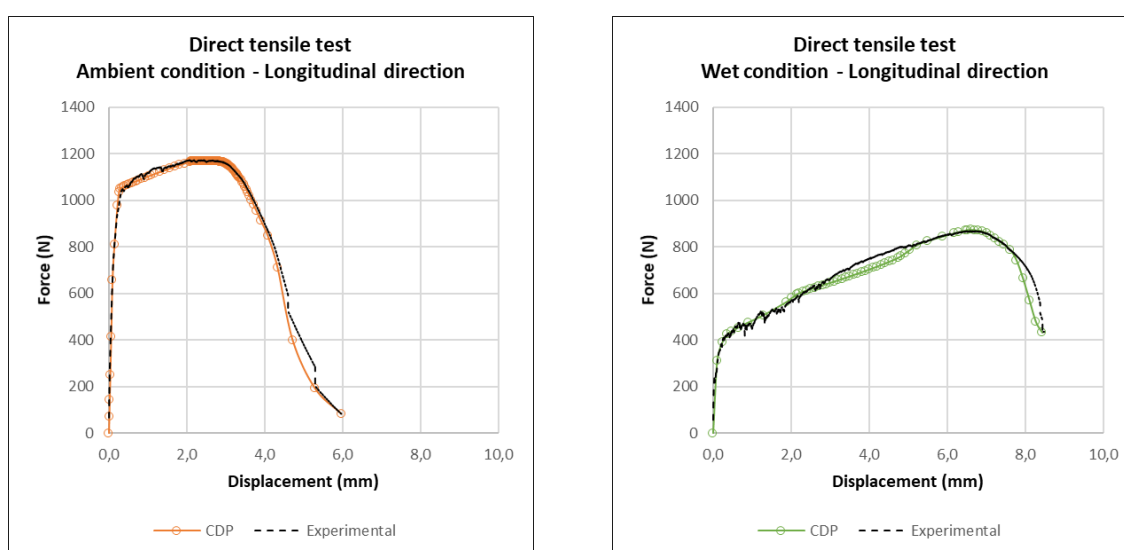
Table 36 : Maximum load and energy predicted by CDP simulation.

Conditioning	Ambient		Wet	
	P_{\max} (N)	Energy (N.mm)	P_{\max} (N)	Energy (N.mm)
Experimental	1173,6	5181	868,9	6493
CDP	1170,6	5479	873,5	6289
Absolute relative error	0,3%	2,4%	0,5%	3,0%

Source: author.

These results confirm the capability of the CDP model to represent the effect of the fiber reinforcement in a cementitious matrix, without needing a fiber discrete representation. The material behavior is properly fitted by the plastic-damage formulation, and the fiber bridging is well represented as hardening. In comparison with the XFEM or with the Hashin formulation in ABAQUS, the CDP model is more adequate to simulate the homogeneous tensile behavior of the fiber cement board.

Figure 40: Force-displacement response of the direct tensile test simulated by the CDP model.



Source: author.

4.3. Concluding remarks

Distinct numerical techniques can be used to simulate failure and damage in cementitious materials. Using the formulations available in the software ABAQUS, the XFEM and the Hashin model using a bi-linear cohesive zone model and the CDP model have been described and calibrated to simulate the three-point bending test and the direct tensile test. These three techniques have been chosen to model the mechanical behavior of the fiber cement through a homogenized formulation, dismissing a discrete numerical representation of the fibers.

The experimental tests highlight different material behaviors: the fiber cement board has presented a marked fiber-bridging effect in the direct tensile test, whilst the post-peak obtained in the three-point bending experiment has been set by a softening curve. The CDP, an elasto-plastic-damage model, has been able to capture the pseudo-strain hardening behavior, highlighted in the direct tensile test, representing the fibers action as a plasticizing phenomenon. XFEM and Hashin model have been demonstrated adequate to simulate the three-point bending test predicting the elastic-phase, the peak load and the post-peak softening behavior with a good agreement.

Even if the three techniques have been able to simulate the flexural behavior in the three-point bending test, only the CDP model has had a good fit in the direct tensile simulation. Therefore, this last technique has been considered as the most appropriate to describe the behavior of a fiber cement board, including this post-peak strengthening performance. However, in cases when the interest is to define only the first peak or a softening behavior, the other techniques can be useful, specially due to their easier implementation. Furthermore, the use of trilinear, or even multilinear cohesive models can be proposed to enhance the capability of the XFEM technique and the Hashin model to fit the fiber cement behavior. The implementation of these multilinear cohesive zone models in ABAQUS and the parameter calibration to fiber cement materials can be suggested as a continuation of this present work.

The material properties defined by simulations have been slightly different, according to the technique choice, specially the ultimate strength stress (σ_u). This discrepancy can be explained by the approximations done in each model and those intrinsic of each formulation. Nevertheless, those differences have been numerically insignificant, particularly in a global analysis. In addition, the material parameters

obtained by the numerical have confirmed that the MOR, calculated in the three-point bending test, is not a good indicator of the material behavior, as shown in Table 37

Table 37: Comparative between experimental and numerical ultimate strength (σ_u) results.

(MPa)	Material stress calculated by linear equations based on the experimental results			Material stress obtained by the calibration of numerical models*	
		Ambient	Wet	Ambient	Wet
3-point bending	MOR	14,1	9,4	5,6	3,8
	LOP	5,9	4,5		
Direct tensile		3,3	2,5	3,4	2,5

*The results of the CDP modeling were taken for the comparison.

Source: author.

In the experimental methodology, the final material strength is calculated by linear elastic equations from forces, a simplification ignoring damage and the non-elastic material behavior. Thereby, the numerical results have indicated that the material strength is overestimated by the MOR. This value, as defined in national standards, does not represent the material strength and cannot be directly used to the material law definition. On the other hand, the LOP shows to be a good approximation for the material strength and it can be used for design purposes and to define the damage initiation criteria of the material.

5. FIXING SYSTEM

Numerical model input definition: Screw contact and fixing modeling

The behavior of the connectors has a direct influence on the final structural capacity of a lightweight façade system. An accurate design of connections, mainly considering their stiffness and strength, is crucial to prevent cracks and to avoid the structural failure. The design of boards fixings must consider two main effects: the in-plane board movement and the board perpendicular loads.

In-plane loads are generated by cyclic dimensional variations and moisture shrinkage, as discussed in 3.4.2, whilst wind action is the most severe perpendicular load acting on the façade system, as presented in chapter 2. These actions can cause the pullout of the board or trigger an evolving degradation of the screwed connection if they are not properly considered. However, in the literature, the modeling of screws and connectors is often addressed considering mainly their pullout behavior.

Loading distribution and the definition of a fastener load depend on the mechanical characteristics of the connection; they are particularly dependent on the stiffness and strength parameters. Experimental studies ^{184; 185; 186; 187} have presented laboratorial methods to define pullout capacity equations for the design of fasteners connections. In addition, their results have demonstrated that most design codes are inadequate in predicting pullout capacities ¹⁸⁷. Based on experimental data, mathematical functions can be proposed to represent the connection behavior. Along the years, nonlinear and piecewise linear models have been proposed ^{188; 189; 190; 191} to depict the load-displacement behavior of those connections.

Recent works ^{188; 192; 193; 194} have shown that a connection is partially withdrawn during peak wind gusts, and failure may occur due to the accumulation of damaging peaks events. In addition, the connection behavior changes along the material aging process. A common way to estimate an average fastener load is dividing the total load by the number of fasteners. Therefore, some authors ^{194; 195; 196; 197} have demonstrated that this averaging method provides inaccurate or non-optimized results, since there is a load transfer between adjacent fasteners. Different methodologies have been described in the literature to take into account this load transfer due to local failures on fixing systems ^{188; 198; 199}.

Finite element modeling has been used^{200; 201} to simulate the global structural behavior based on the screw parameters. Fixing connectors have been usually represented by relying rotation, displacements and nodal forces of two different points by a spring link or by defining a particular stiffness matrix¹¹⁷. The interaction between connector and material has been commonly considered in this fixing definition.

The proposal of this chapter is to assess the behavior of a screw-board connection in function of aging and screws type. The two effects, in-plane and pull-through loads, will be considered separately. A theoretical analysis of the in-plane board displacements is proposed and complemented by a numerical study, to validate drilling recommendations and an optimized positioning of the screws. The pull-through effect is studied by the proposal of an experimental methodology, to characterize the behavior of the screw-board connection in different ages and hygrometric conditions. Therefore, a numerical model is calibrated to represent those screw connections.

5.1. Screw-board interaction

During the assembly and drilling process, a preload is applied on the board. The tightening torque implies a first compression load on the board, and a small elongation of the screw. This initial torque has to be properly controlled, in order to avoid any micro cracking nucleation due to an excessive compression. During the service life, the fixing system will be subjected to axial and transversal loads, generating a pull-through and a shearing efforts. The pull-through behavior is initially elastic with a post-peak, usually governed by the interaction of the screw head and the board. The shearing forces result from the lateral contact between a fastener and the board.

Different systems may be used to fix fiber cement boards on lightweight façades frames²⁰². Screws and rivets are the most used board connectors for LSF structures. The fixation is ensured by a pressure perpendicular to the fiber cement board, exerted by the screw head and the support profile. The anchor points may be fixed or sliding; it means blocking or allowing the displacements in the board plane. Sliding, or gliding, points are obtained by a gap between the screw or rivet axis and the hole on the board, for example. When the fixing system limits these dimensional movements, this implies in-plane stresses acting on the fiber cement board, and increasing the risk of cracking. Following this reasoning, it is preferable to use a minimum of fixed points, ensuring the necessary to prevent a rigid body motion of the board, but avoiding in-plane stresses.

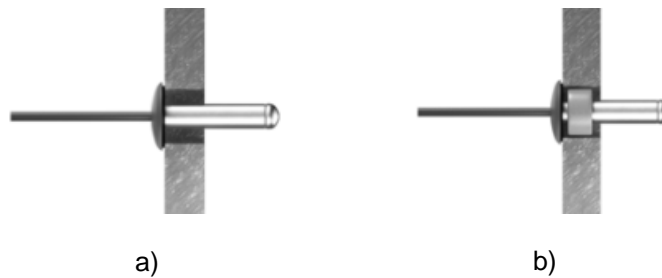
Some manufacturers recommend the use of pre-drilled holes bigger than the screw or rivet diameter to ensure the free space for a sliding point ^{203; 204; 205}. In all cases, at least two fixed points must be defined in each board with all other gliding points allowing movement. Figure 41 shows an example of the choice of fixing points in a mounted board. As the pre-hole is bigger than the diameter of the screw or rivet, a fixed point is formed using rivets with sleeve (Figure 42) or screws with washers (Figure 43) in these specific points.

Figure 41: Example of fixing and gliding points positioning.



Source: Equitone (2018). ²⁰³

Figure 42: Fixing system using rivets. a) Sliding point. b) Fixed point using a rivet sleeve.



Source: Cembrit. (2019). ²⁰⁴

Figure 43: Fixing system using screws. a) Sliding point. b) Fixed point using washers.



Source: Cembrit. (2019). ²⁰⁴

In Brazil, the common fasteners for board screwing on steel structures are self-drilling screws with flat or wafer head ^{206; 207; 208}. The boards are directly screwed without pre-drilling, and the screws can be winged or not, as shown in Figure 44. The wings enlarge the hole, allowing the threads to pass through the board without engaging the fiber cement material. Yet, they produce a small gap between the board and the screw, allowing a free displacement at the hole. In case of flat head screws, the conical part of the screw becomes embedded below the board surface (~1mm). This embedment can block the in-plane board displacement, resulting in a fixed point.

Figure 44: Self-drilling screws. a) Flat head with wings, b) Wafer head without wings.



Source: a) Brasilit (2019). ²⁰⁸ b) Ciser (2019). ²⁰⁹

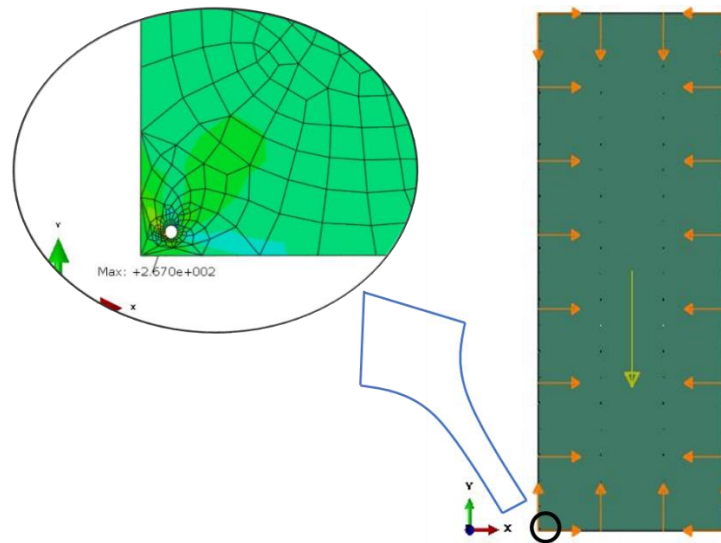
Alternatively, boards can be chemically fixed on the metal structure. Tapes and structural adhesives have been proposed as invisible fixing systems. These chemical fasteners may increase the final façades aesthetic and productivity, besides contributing to avoid edge cracks. However, the quality of these adhesives application is highly dependent on favorable climatic conditions, and it demands boards with regular, plane and cleaned surfaces.

5.2. In-plane loads

The modeling of structure connectors is a boundary condition problem. Resolving this problem implies the imposition of relative displacements and rotations between two or more points. The different fasteners can be defined by specific force-displacement equations that will be exemplified in 5.3.2.

A first and simple analysis can be made considering each connecting point as a fixed point, and assessing mechanical effects or damages by the resultant material stresses. Based on this assumption, a preliminary simulation of shrinkage effects has been proposed, using the software ABAQUS for a Finite Element Analysis. A standard screwed board has been modeled, and each screwed connection has been represented by blocking the three translational degrees-of-freedom (dof).

Figure 45: Localization of the maximum stressed connecting point due to in-plane loads.



Source: author.

It can be observed, as illustrated in Figure 45, that fixations at the corners of the board are the most stressed in case of in-plane loads, such as shrinkage. However, modeling screwed connections as fixed points is a highly conservative approach. This model has generated overestimated stresses, or it can even result in an overconstrained numerical problem.

A more realistic approach, therefore, is to consider the fixed points as springs characterized by their respective elastic stiffness. This assumption alleviates the overconstraining, holding a mechanical condition to represent fixings. This strategy provides good predictive results for comparative analysis, for example, regarding the influence of fixing stiffness on crack initiation and propagation.

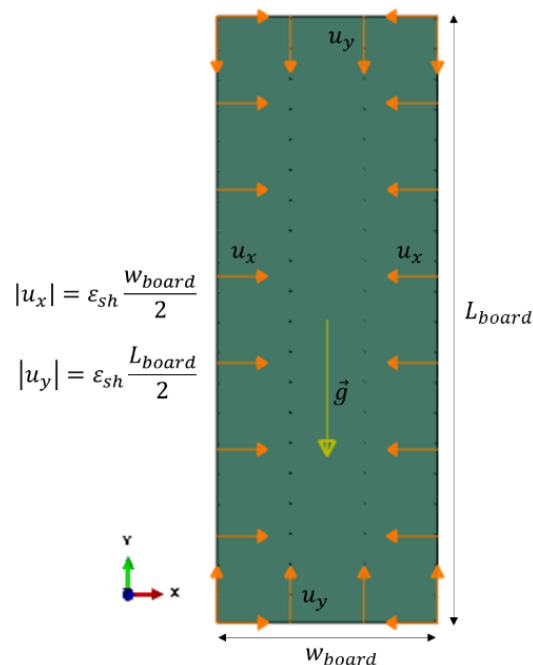
In addition to the fixing stiffness, the geometrical parameters of the façade, such as the board size, screws spacing and studs distance have a clear influence on mechanical stresses and damage results. In order to define the influence of each of those parameters, the study focused on the fastener in the corner of the board and its resultant displacements and forces during shrinkage.

This study started with the definition of an analytical approach to estimate the displacement field generated by shrinkage. Board in-plane displacements were calculated by considering a free displacement connector without any fixed point. Afterwards, the influence of the connector elastic stiffness was assessed by comparing different stiffness and the correspondent cracking results.

5.2.1. Free board displacements

Consider a rectangular board of width w_{board} and length L_{board} . If this board is subjected to a shrinkage equal to ε_{sh} , the field of displacements can be described by the equivalent displacements u_x and u_y applied at the free edges of the board, as indicated in Figure 46, where \vec{g} represents self-weight loads. By symmetry, the model can be simplified taking one single fixing point at the corner of the board. The influence area of this fixing point is illustrated in Figure 47, and it can be defined in function of studs distance (d_{st}) and screws spacing (s_{screw}).

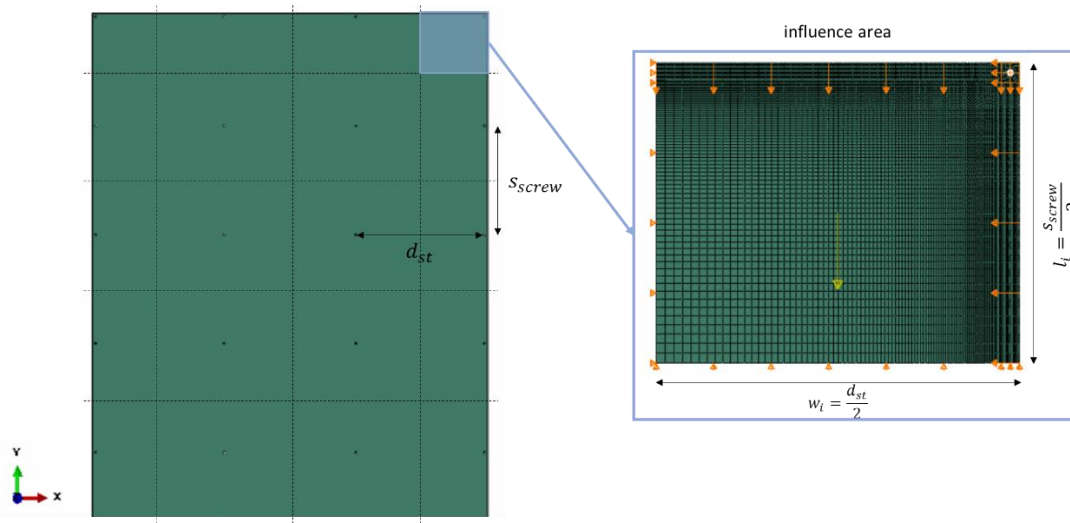
Figure 46: Field of displacements generated by a shrinkage loading.



Source: author.

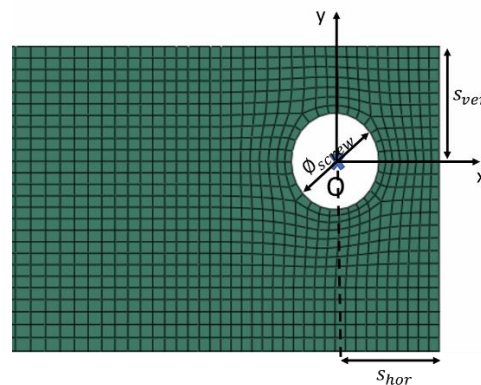
Avoiding the need of a geometrical representation of connectors, the fastener is represented here by one point. This single point O is located as shown in Figure 48, where s_{ver} and s_{hor} are the distances of the point to both free edges. The same point is the center of a hole with diameter ϕ_{screw} , which represents the space created by drilling. This hole is equal to the screw diameter in case of self-drilling screws, or it can be larger than the connector diameter in case of pre-drills. Displacements at the edge of the drilled hole are coupled with those at the fixing point.

Figure 47: Influence area and symmetric boundary conditions of the corner fixing.



Source: author.

Figure 48: Position of the fixing point – distance to free edges and screwed hole diameter.



Source: author.

Therefore, free displacements at the point O can be estimated by a linear relation, decreasing from u_x or u_y at the correspondent free edge to zero at the opposite symmetry axis. This linear relation, in turn, can be written in function of the geometry, of the influence area, and of the coordinates of a point in relation to the free edges. Hence, the free displacements at the fixing point can be written as a multiple of the board shrinkage, as shown by equation (43), where ζ_x and ζ_y are linear multipliers defined by the geometrical conditions, representing an equivalent influence length.

$$\begin{aligned}
 u_{x,0} &= \left(\frac{w_i - s_{hor}}{w_i} \right) u_x = \left(\frac{w_i}{w_i + s_{hor}} \right) \left(\frac{w_{board}}{2} \right) \varepsilon_{sh} = \zeta_x \varepsilon_{sh} \\
 u_{y,0} &= \left(\frac{l_i - s_{ver}}{l_i} \right) u_y = \left(\frac{l_i}{l_i + s_{ver}} \right) \left(\frac{L_{board}}{2} \right) \varepsilon_{sh} = \zeta_y \varepsilon_{sh}
 \end{aligned}
 \tag{43}$$

Table 38 indicates ζ_x and ζ_y values for different studs and screw spacing for a 1200mm by 3000mm board, assuming that there is no dependency of displacements in different directions. These results allow, for example, the estimation of the diameter of a pre-drill, or the displacements reduction when increasing the distances of the corner fastener to the free edges.

As an example, consider an irreversible shrinkage of 3,4mm/m, as estimated in 3.4.2.1, and the worst case scenario for both directions. A gap of 2,0mm between the screw thread and the board would be sufficient to avoid the contact and the creation of a fixed point in the horizontal direction (x). By the same reasoning, a minimum gap of 5,0mm is needed in the vertical direction (y) to ensure only free in-plane displacements. In case of the contact between the screw and the board, a complementary analysis is needed, thus adding the influence of the screw stiffness.

Table 38: Equivalent influence lengths for a 1200mmx3000mm rectangular board.

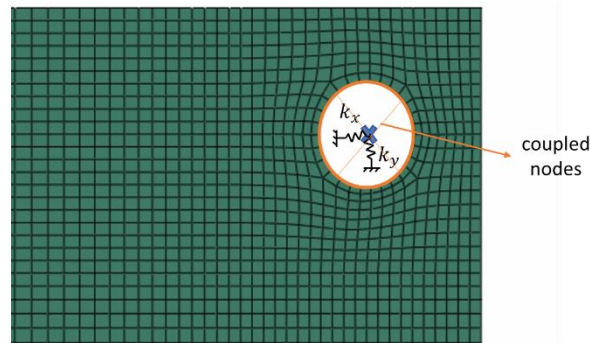
ζ_x (m)	d_{st} (mm)		ζ_y (m)	s_{screw} (mm)		
s_{hor} (mm)	400	600	s_{ver} (mm)	150	300	400
10	0,57	0,58	10	1,32	1,41	1,43
15	0,56	0,57	25	1,13	1,29	1,33
20	0,54	0,56	50	0,90	1,13	1,20
25	0,53	0,55	100	0,64	0,90	1,00
30	0,51	0,54	150	0,50	0,75	0,86

Source: author.

5.2.2. Fixed and sliding fasteners modeling

A fixing system can be designed to hold boards by tied fasteners blocking all movements or by slack fasteners exerting a sufficient perpendicular pressure, whilst allowing free lateral and in-plane displacements. It is possible to simulate the behavior of those fasteners and their interaction with the board without their geometrical representation, as commented in 5.2.1. Restrained movements, in that case, can be represented by springs supports as illustrated in Figure 49.

Figure 49: Fasteners model using springs supports and coupled nodes.



Source: author.

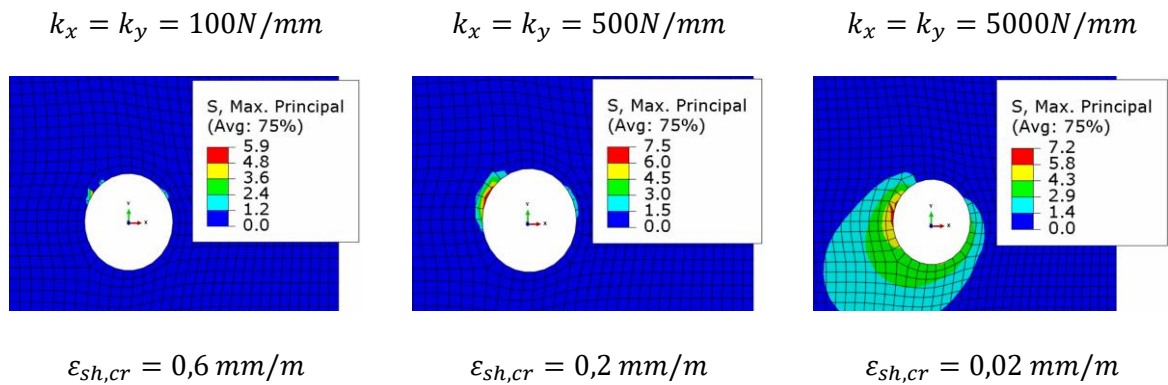
This displacement constraint is dependent on the definition of the spring stiffness. Rigid connections, as tied fasteners, are simulated by high stiffness values. In order to assess the influence of those values, the results of a shrinkage simulation on a fiber cement board in ambient conditions have been compared.

The board was modeled considering its orthotropic behavior and using the XFEM parameters, as described in 4.2, to evaluate the crack propagation. The corner fastener was assumed to be located at 10mm from the free edges. A comparative analysis of crack initiation and propagation was done for different spring stiffness magnitudes: 100N.mm; 500N.mm and 5000N.mm. Figure 50 presents the crack evolution, comparing the critical shrinkage, which causes the initial cracking ($\varepsilon_{sh,cr}$) and the crack length (l_{cr}) for each case. This parametric analysis was done considering a shrinkage up to 3,0mm/m and using the personalized algorithm *spring_screws.py*.

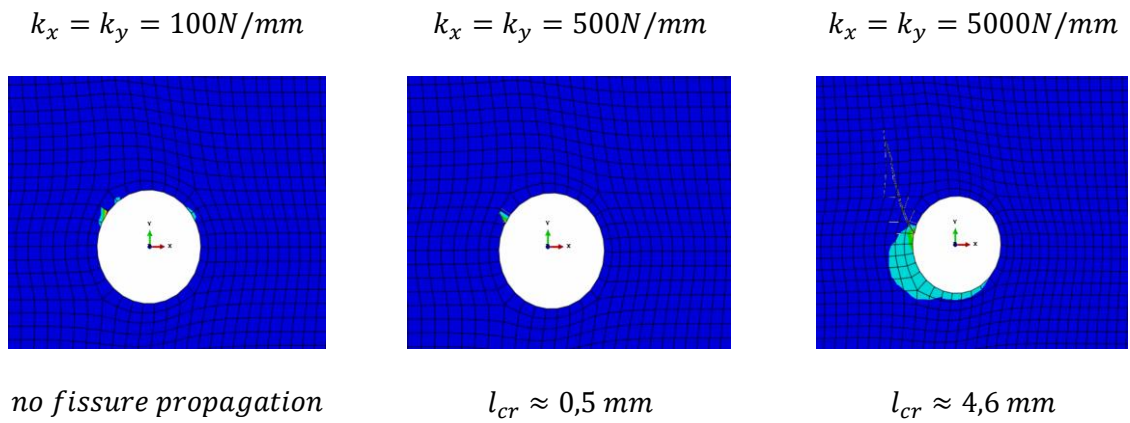
From these results, more rigid connections have implied earlier cracks. Furthermore, the cracking path and its length increase are different according to the spring stiffness definition. Since the fastener-board contact results in blocked movement, the highest stiffness value may be assumed to represent this tied connection. Moreover, the cracking path gotten from the simulation with a 5000N.mm spring has a similar pattern to those currently observed in real cases, as illustrated in Figure 51. Finally, it was observed that when using low stiffened springs, the cracking process starts later, and there is no crack propagation even in an advanced shrinkage stage. This last conclusion is also valid in a free-displacement case, i.e, using sliding points.

Figure 50: Influence of fastener stiffness on cracking results.

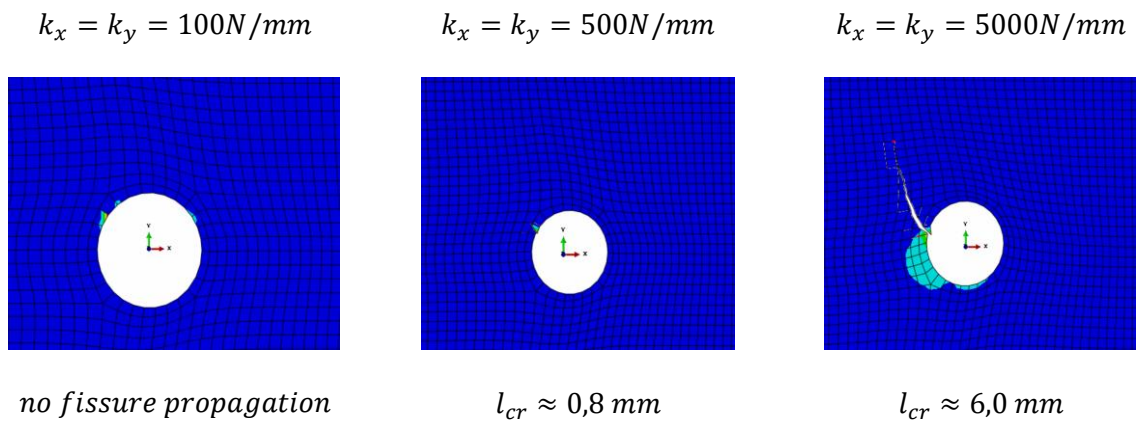
Crack initiation



Intermediate stage - $\epsilon_{sh} = 1,0 \text{ mm/m}$

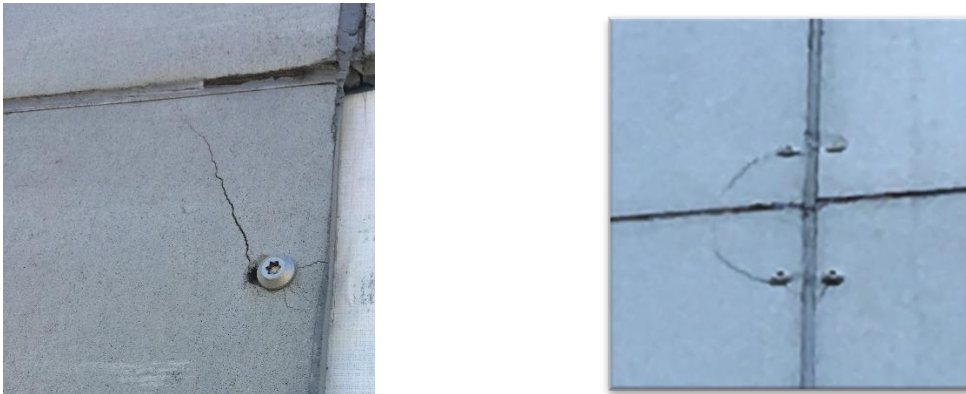


Advanced stage - $\epsilon_{sh} = 3,0 \text{ mm/m}$



Source: author.

Figure 51: Examples of cracking path in real façades cases.



Source: author.

In case of sliding points, such as using pre-drilled fasteners, the shrinkage analysis must be made in two stages, at least. The first stage corresponds to the free shrinkage of the board, without any restrained in-plane displacement. Afterwards, once the lateral contact between the fastener and the board is initiated, the spring support is activated and the successive displacements will generate material stresses and initiate a presumed board cracking.

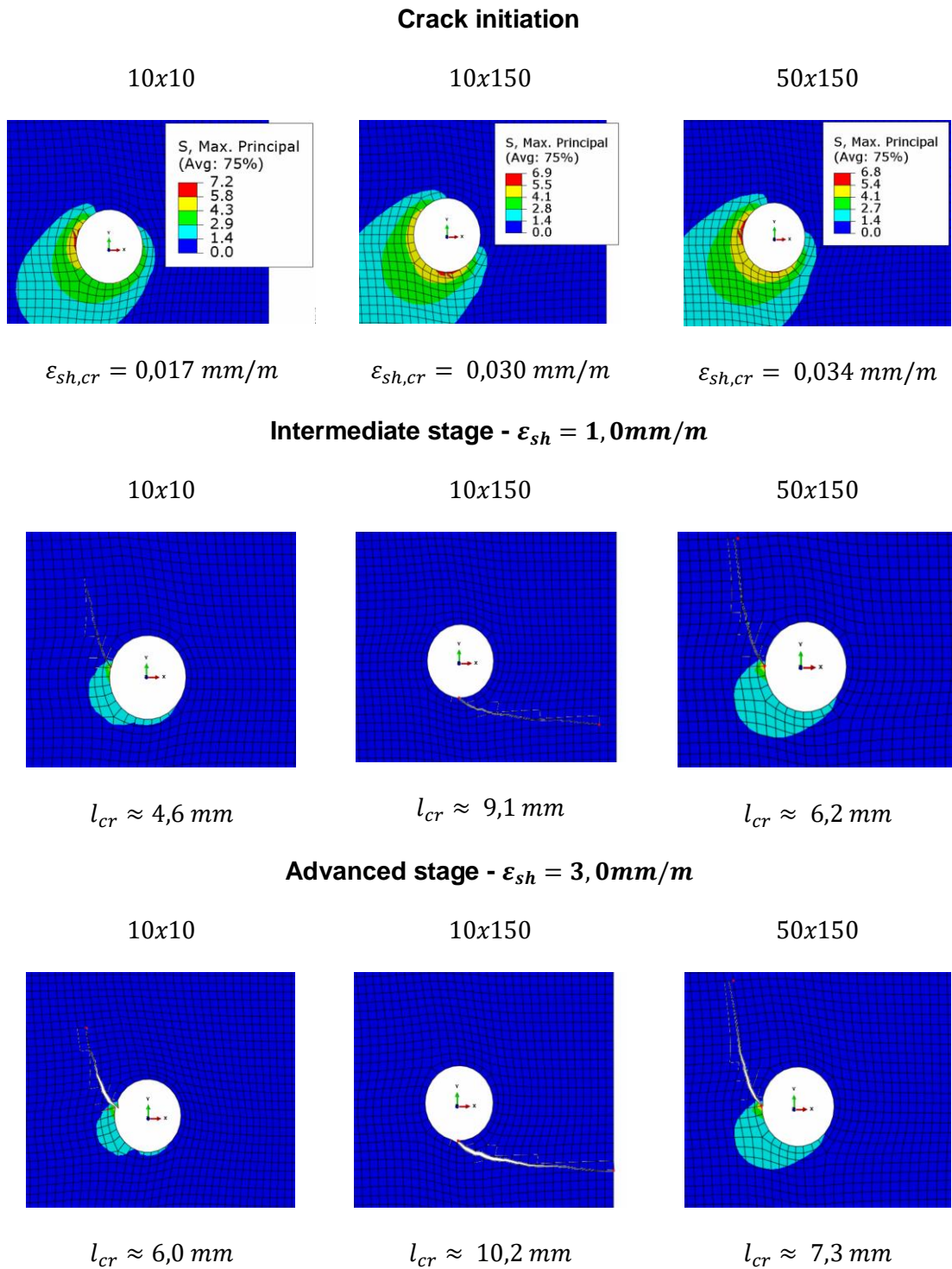
5.2.3. Minimum edge distances

It was shown in 5.2.1 that the fixing distance to the edge influences the connector displacement results caused by in-plane loads. Assuming a linear displacement field, the closer the connector is to the edge, the larger the displacements are. This way, the definition of the edge distances has a direct impact on the cracking initiation and propagation on the board.

The same numerical model proposed in 5.2.2 was used to provide a comparative analysis of different edge distances of a fixed point. Assuming that the smaller dimension of the board is parallel to axis x , the increase of the y -distance (meaning the distance of the screw to the smaller edge) has a bigger influence on results than the change of the x -distance. An optimized choice of edges distances may slightly retard the crack initiation ($\varepsilon_{sh,cr}$), besides reducing its final length, as exemplified by Figure 52.

However, even if minimum edge distances can retard the cracking process, they cannot avoid cracks in the case of using fixed points. To eliminate or mitigate this risk, the optimized connector design must include a reduced connector stiffness or the use of pre-drills, in addition to the minimum edges distance.

Figure 52: Influence of edge distances on cracking results.



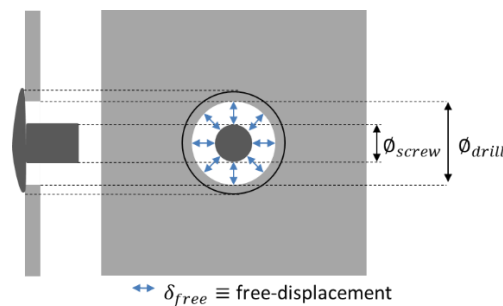
Source: author.

5.2.4. Effect of pre-drilling

The best way to avoid a stress concentration on a fixing point is allowing free in-plane displacements. The pre-drilling is a common solution to ensure this free movement, as presented in 5.1. This free space is limited, and it can be estimated by the difference between the drill and the screw diameters, as indicated in equation (44) if considering a perfectly centered connector as illustrated by Figure 53.

$$\delta_{free} = \pm \frac{\phi_{drill} - \phi_{screw}}{2} \quad (44)$$

Figure 53: Pre-drill schema.



Source: author.

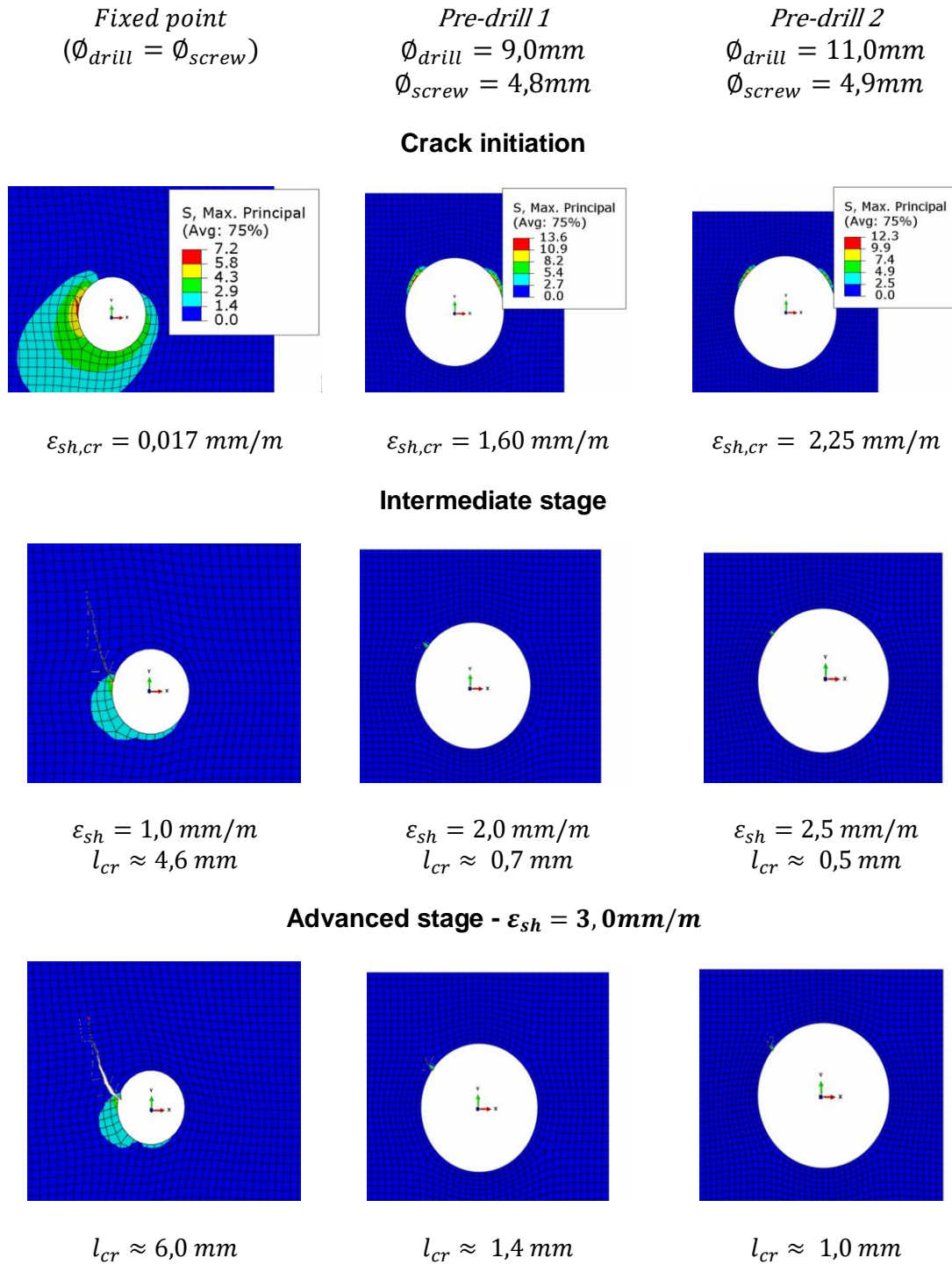
A numerical study is proposed to verify the efficiency of pre-drills for the reduction of cracking risks. The numerical model is the same previously used in this chapter, adding the new information of a pre-drill in the calculation of the displacement field evolution. A specific routine called *pre_drill.py* was created, and it runs the analysis of the shrinkage effect in 2 steps:

- 1st step - before the contact between the board and the screw thread: considering the free-displacement of the connector until reaching the δ_{free} value.
- 2nd step – after the contact between the board and the screw thread: considering a stiffened connection, such as described in 5.2.2, in the direction where u_0 exceeds δ_{free} .

Two pre-drilling solutions were analyzed and compared with the fixed point behavior. Both solutions were assessed assuming that fixing is ideally centralized and neglecting any eccentric effect. The first solution considers a rivet with 4,8mm of diameter and a pre-drill of 9mm and the second one taking a rivet of 4,9mm and a drill of 11mm. Figure 54 shows the results for the different drilling conditions. The use of

larger drills reduces significantly the risk of cracking due to shrinkage, even for the worst edge distance cases with screws nearer the edges. The initial gap between the board and the screw enables a first stress-free stage, delaying the crack initiation and, hence, its propagation.

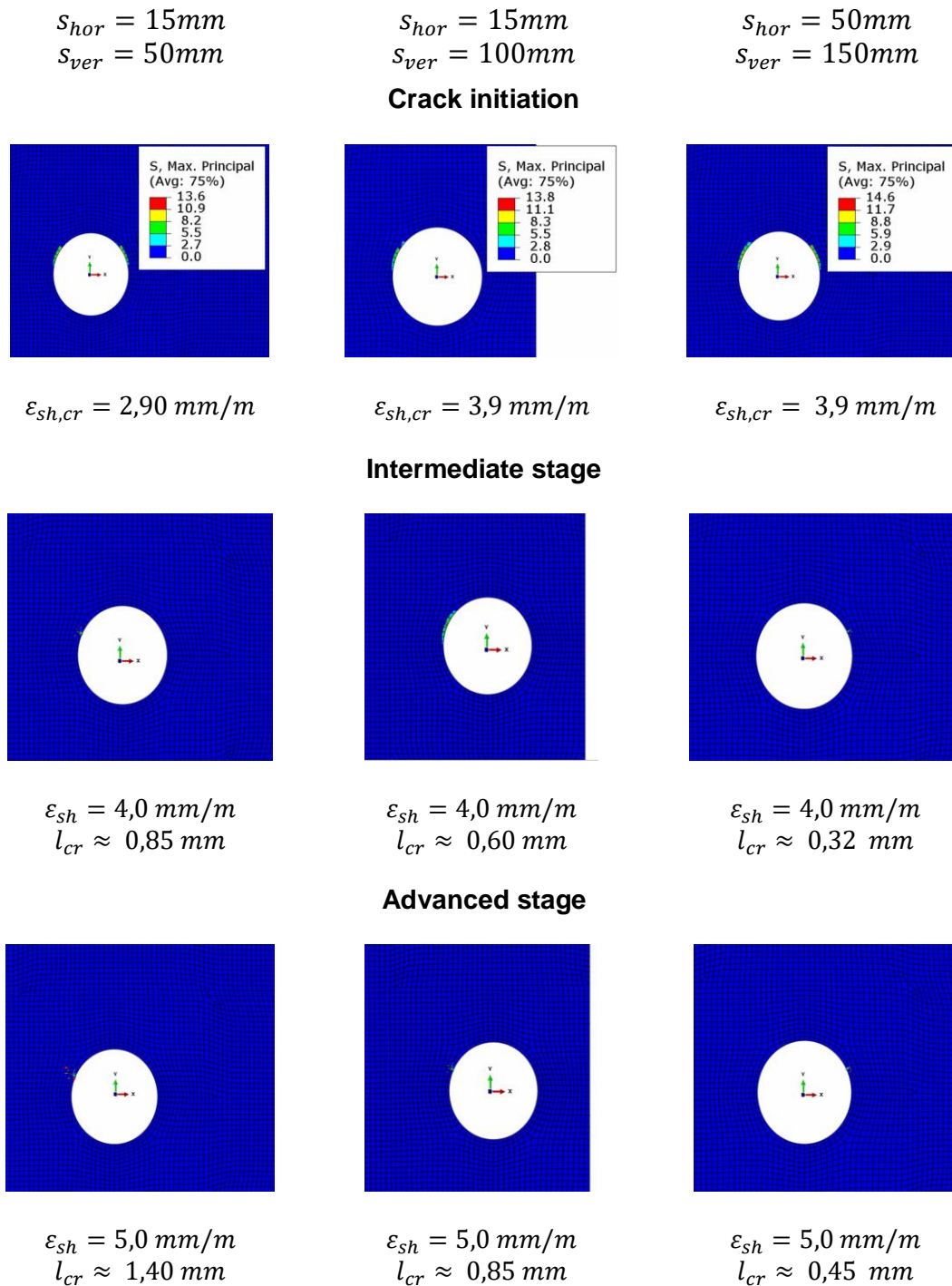
Figure 54: Effect of pre-drilling considering 10mm of edges distances.



Source: author.

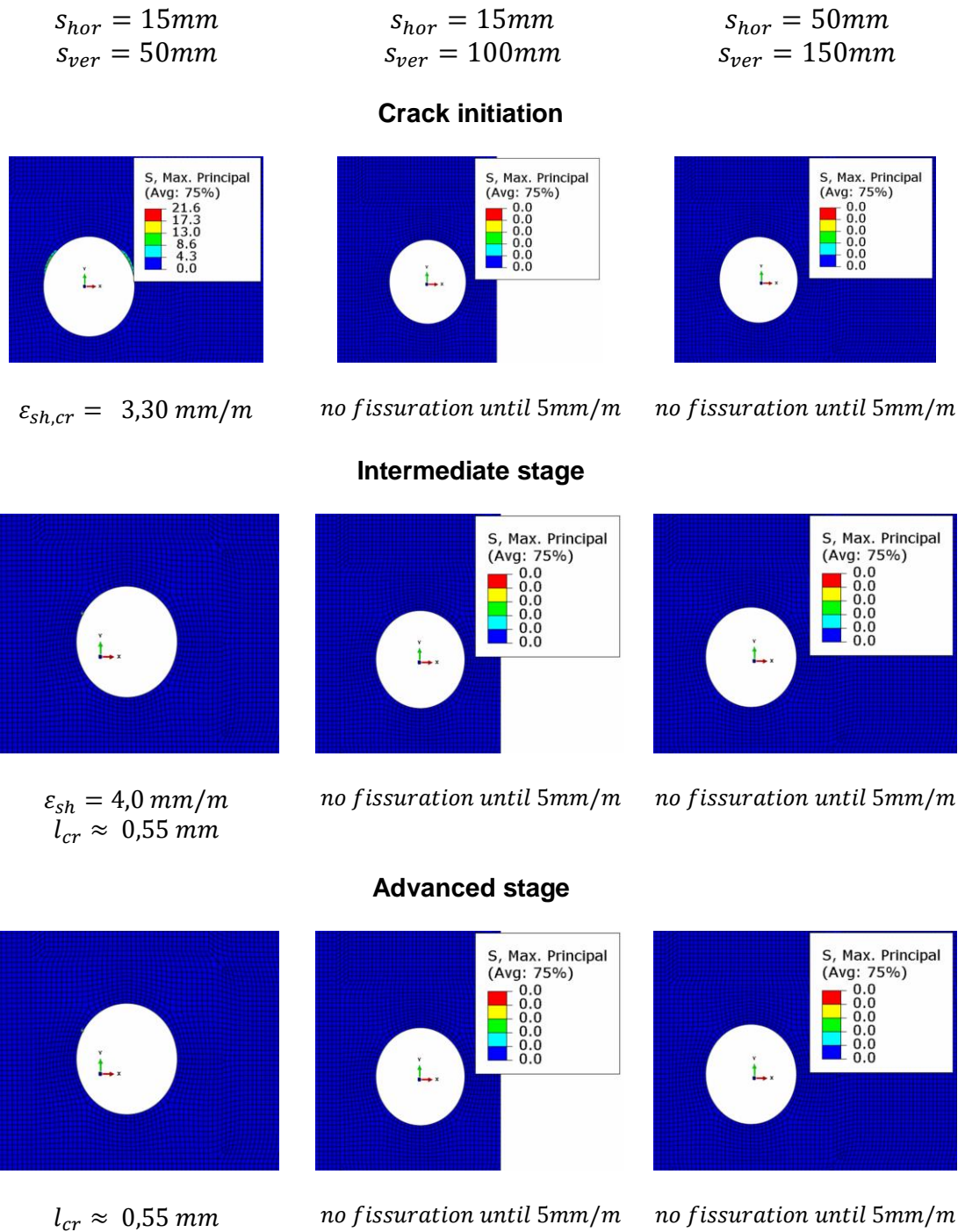
The good results already provided by the large drills solutions can be still improved by combining pre-drills with minimum edges distances. Figure 55 and Figure 56 show that the risk of cracking can be conveniently eliminated or roughly mitigated by increasing the minimum edges distances by using both pre-drilled solutions.

Figure 55: Combined effect of pre-drilling and minimum edge distance for pre-drilled solution 1.



Source: author.

Figure 56: Combined effect of pre-drilling and minimum edge distance for pre-drilled solution 2.



Source: author.

It can be noted that the results have been more affected by changing the vertical edge distance (relative to the smaller edge). Moreover, changing the minimum horizontal distance has provided only a slight improvement, and, therefore, the configuration 15mm x 100mm with large drills has been pointed as an optimized choice to avoid major cracking risks due to shrinkage.

5.3. Pull-through loads

5.3.1. Experimental characterization of self-drilling screws

These tests aim to provide the maximum screw pull-through strength and the connection stiffness of two self-drilling stainless steel screws commonly used in the Brazilian market. The pull-through was measured both in samples stored in ambient conditions and in soaked samples, in order to verify the influence of the humidity content on the board-screw behavior. New and natural aged samples are also compared to assess potential changes on the fastener behavior due to aging.

5.3.1.1. Methodology

The pull-through tests were made following the ASTM D1037 standard ²¹⁰. Board samples measure 150mm x 150mm and their thickness is 10mm (+/- 0,3mm). Screws are driven through the center of the board perpendicular to the surface, as shown in Figure 57. Two types of 4,2mm x 32mm screws were tested: a flat head winged screw and a wafer head screw without wings, as presented in 1.3.4.

The assembly test is shown in Figure 58. A support with a 76mm-diameter central hole is used to block the board in the vertical direction. Samples are placed with screw threads up. Load is applied by a tensile non-shift wedge grip. Testing was performed in a universal testing machine Shimadzu AGS-X, 5kN-load cell capacity, with a controlled displacement rate of 1,5mm/min.

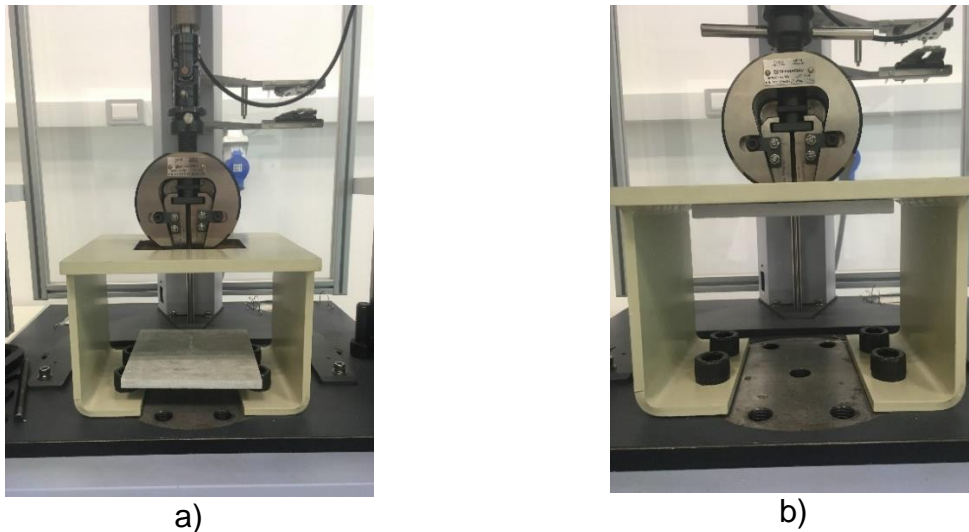
Figure 57: Screws driven through board samples.



Source: author.

Samples considered as “Ambient” were tested after at least 7 days in laboratory ambient conditions (23 ± 5 °C and 50 ± 10 % of RH). Samples called “Wet” were tested after 24 hours immersed in water at ambient temperature. In both cases, screws are drilled before the sample conditioning to simulate a real case of water saturation in presence of a screw on the board.

Figure 58: Test assembly for measuring screw pull-through resistance. a) Board positioning with screw threads up. b) Test starting with board blocked by the support fixture.



Source: author.

For aging effect analysis, samples were taken from boards exposed to natural aging for 3 years. The reference samples considered as “New” were taken from boards after 3 months in factory storage without temperature controlling. The aging quantification and analysis of the samples were presented in 3.4.

5.3.1.2. Results and analysis

Five samples were tested for each combination of screw type, sample conditioning and aging. The results are identified by the combination description (“Flat head screw new wet” or “Wafer head screw aged ambient”, for example). The average load-displacement curve is presented for each testing condition.

A graphical analysis indicates the maximum pull-through force and the elastic parameters for each configuration. Figure 59 shows those experimental pull-through results. From the graphs, it can be remarked that the main difference between the two types of screw is their post-peak behavior. Even if the first peak value is statistically similar for both screws, the absence of wings imply a stiffer screw-board connection, as shown in Table 39. The first peak, however, is independent of the wings presence. It corresponds to the matrix failure caused by the screw head and it occurs when the head of the screw completely passes above the material surface, at approximately 1mm of vertical displacement.

Table 39: Pull-through strength results for new samples.

Parameter	Flat head winged screws		Wafer head screws without wings	
	Ambient	Wet	Ambient	Wet
k (N/mm)	786,3 ± 82,6	557,2 ± 56,4	887,9 ± 95,4	663,8 ± 73,0
1st crack (N)	637,8 ± 108,4	399,2 ± 42,4	562,1 ± 94,3	369,4 ± 44,4
F_{max} (N)	637,8 ± 108,4	399,2 ± 42,4	840,8 ± 96,9	644,6 ± 58,0

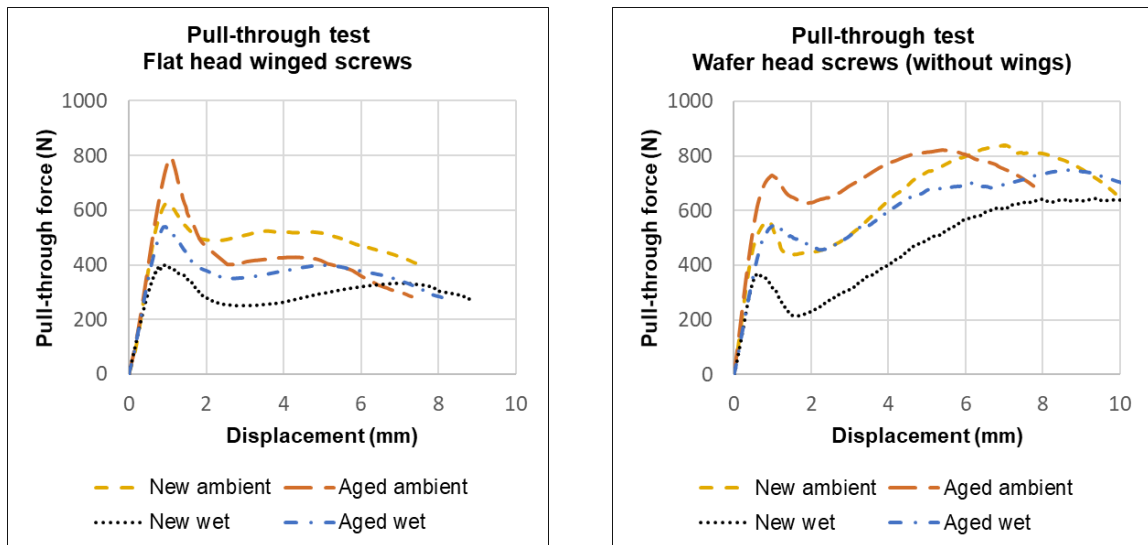
Source: author.

Despite being a more rigid fastener, screws without wings promote an increasing of the post-peak pull-through resistance. After the complete screw head penetration above the surface, the connection threads-board and the wafer shape of the screw head work on resisting the applied force. This non-linear behavior suggests that after the first crack at the surface, the fibers act holding the screw displacement and increasing the pull-through force. In case of winged screws, the pull-through force drops after the first peak load, without any significative recovering. This behavior may be explained by the “pre-hole” created by wings that facilitates the head screw passing-through after the first surface cracking. Table 39 summarizes these values, showing that the maximum pull-through force is bigger than the first crack resistance for screws without wings, while the pull-through force corresponds to the first crack resistance in case of winged screws.

Fastening stiffness increases after aging. As shown in Table 40, the connection stiffness is bigger for both screws and hygrometric conditions. In addition, the pull-through resistance rises too. This rising of these connection parameters is due to the cementitious matrix changes after aging and the irreversible board deformations. As explained in 3.4.1, aging produces a densification of the matrix, reducing pores and leaving the material more resistant, even less ductile. The combination of carbonation and soak-drying processes can also cause irreversible deformations with the shrinkage of the board, leading to a tighter screw-board connection.

Effectively, in new samples, a bigger difference has been observed between the maximum pull-through force and the first-crack resistance for wafer head screws. The pull-through force increases around 50%-70% after the first crack in new samples, whilst it raises around 13%-30% for the aged ones. These results reveal that aging influences more the first peak than the maximum force, if they are different. Yet, it reaffirms the relation between the first-peak load and the matrix behavior.

Figure 59: Load-displacement pull-through curves.



Source: author.

Finally, observing the values presented both in Table 39 and in Table 40, the loss of strength and stiffness can be noted when the boards are tested in a wet condition. This remark behaves the same way as the results presented in 3.3, since the presence of water degrades the matrix resistance and increases the fiber-matrix slipping and the material ductility. It is interesting to highlight that the strength decreasing is more important for new samples (~35%-50%) than for aged ones (~13%-25%). This difference is due to the different water absorption of samples. After aging, samples absorb less water due to the pores reduction.

Table 40: Pull-through strength results for aged samples.

Parameter	Flat head winged screws		Wafer head screws without wings	
	Ambient	Wet	Ambient	Wet
k (N/mm)	811,2 ± 79,9	638,2 ± 114,9	963,1 ± 76,7	741,8 ± 69,1
1st crack (N)	798,2 ± 44,9	570,7 ± 34,3	729,8 ± 51,1	585,9 ± 52,7
F_{max} (N)	798,2 ± 44,9	570,7 ± 34,3	823,3 ± 10,2	745,3 ± 11,3

Source: author.

5.3.2. Mathematical models

From the characterization presented in 5.2, the pull-through behavior of the screwed connections has been demonstrated to be non-linear. In order to avoid complexity in further analysis, the pull-through behavior can be simplified. Khan (2012) presents different piecewise linear models and a curvilinear load-displacement model to represent a connection withdrawing. These functions can define the load-displacement curve up to the failure capacity of the connection, neglecting softening effects. Failure capacity is defined as the maximum withstood load by a connection.

5.3.2.1. Flat head winged screws

For the flat head screws with wings, experiments showed a linear behavior up to the maximum load followed by an irreversible drop of strength. Therefore, the load-displacement behavior can be simple represented by a linear model up to the failure capacity. The parameters of this model are the failure capacity (F_C), the failure displacement (d_C) and the connection stiffness (k_C), defined as the slope of the load-displacement line. Figure 60 exemplifies the definition of the linear model up to the failure capacity of the connection. Linear model parameters for all sample conditionings are presented in Table 41.

Table 41: Linear model parameters for flat head winged screws pull-through on fiber cement boards.

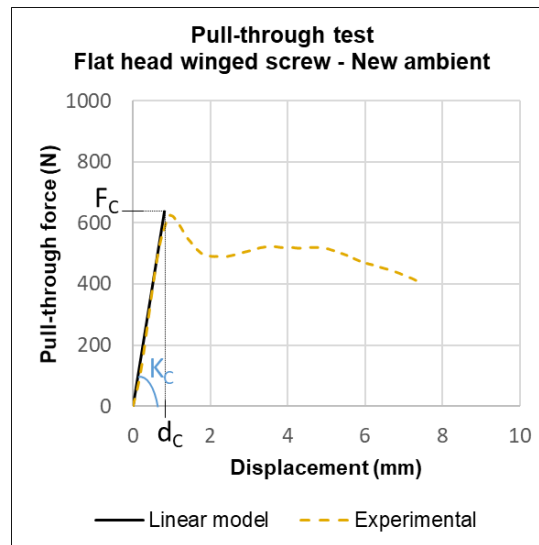
Flat head winged screwed samples	F_C (N)	d_C (mm)	k_C (N/mm)
New ambient	637,8	0,81	786,3
New wet	399,2	0,72	557,2
Aged ambient	798,2	0,98	811,2
Aged wet	570,7	0,89	638,2

Source: author.

According to this model, the pull-through load function is written as (45), where F is the pull-through force, d is the displacement of the screw orthogonally through the board and K_C is the connection stiffness as defined previously.

$$F(d) = k_C d, \quad 0 \leq d \leq d_C \quad (45)$$

Figure 60: Load-displacement linear model example.



Source: author.

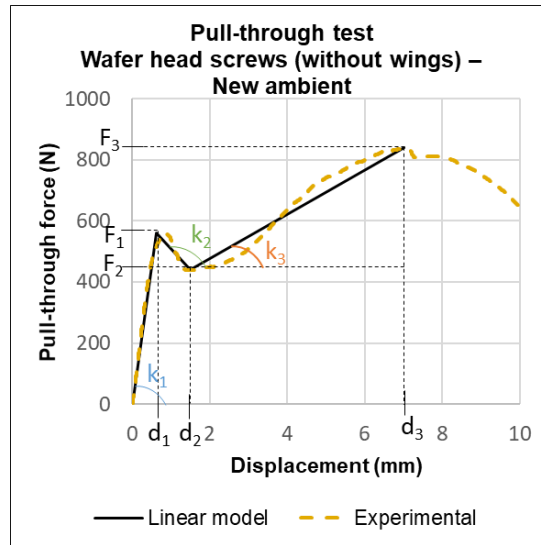
5.3.2.2. Wafer head screws without wings

As shown in Figure 59, screws without wings have presented a linear behavior up to the first peak load, followed by a small drop, and recovering by an increasing of the resistive force. This behavior can be represented by a piecewise linear function or by a curvilinear function. The piecewise form considers three different slopes to represent the first peak load, the small drop and the strength recovering. In case of a curvilinear model, the global behavior can be represented neglecting the strength decreasing after the first peak, but maintaining the first peak identification followed by a strength increasing up to the maximum pull-through force.

Figure 61 gives the example of a piecewise model definition. To write the piecewise linear function, three line slopes must be given or three force-displacement pairs. The three different pieces of the function correspond to the first peak load (F_1); the minimum load reached after the first crack (F_2) and the maximum force resistance after the first crack, or the failure capacity (F_3). Table 42 shows the model parameters for all sample conditionings.

Therefore, the piecewise linear function is written in (46), where F_i is the force on the i -piece, d_i is the correspondent displacement and k_i is the equivalent line slope. The function is, however, not monotonic.

Figure 61: Load-displacement piecewise linear model example.



Source: author.

$$\begin{aligned}
 F(d) &= k_1 d, & 0 \leq d \leq d_1 \\
 F(d) &= k_2 d, & d_1 < d \leq d_2 \\
 F(d) &= k_3 d, & d_2 < d \leq d_3
 \end{aligned}
 \tag{46}$$

Table 42: Piecewise linear model parameters for wafer head screws without wings pull-through on fiber cement boards.

Wafer head screws samples without wings	F ₁ (N)	d ₁ (mm)	k ₁ (N/mm)	F ₂ (N)	d ₂ (mm)	k ₂ (N/mm)	F ₃ (N)	d ₃ (mm)	k ₃ (N/mm)
New ambient	562,1	0,63	887,9	439,8	1,49	-142,7	840,8	7,01	72,6
New wet	369,4	0,56	663,8	214,8	1,76	-128,8	644,6	7,74	71,9
Aged ambient	729,8	0,76	963,2	623,8	1,72	-110,2	823,3	5,15	58,2
Aged wet	585,9	0,79	741,8	476,9	2,02	-88,6	745,3	7,97	45,1

Source: author.

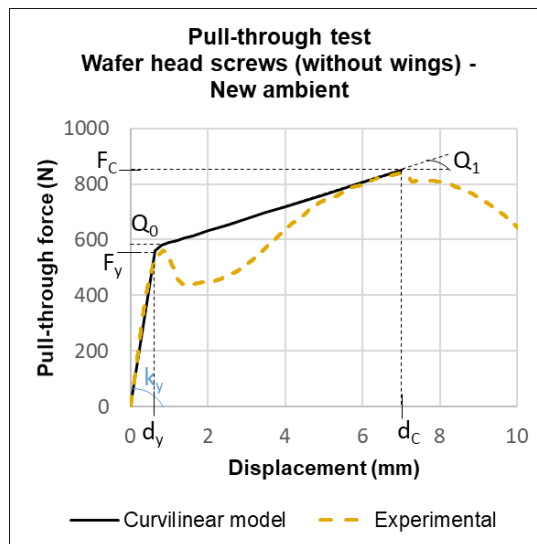
The curvilinear model can be interpreted as a plastic model. The function is defined by a linear behavior up to the yield capacity (F_y). Afterwards, the connection presents a non-linear behavior up to failure capacity (F_c). Assuming that the post-peak increasing can be represented as a plastic phenomenon, and neglecting the strength drop after the first peak, the load-displacement relationship adapted from Khan (2012) is given by (47).

$$F(d) = k_c d, \quad 0 \leq d \leq d_y$$

$$F(d) = F_y + \left(Q_0 + Q_1(d - d_y) \right) \left(1 - e^{\left(\frac{k_y(d_y - d)}{Q_0} \right)} \right), \quad d_y < d \leq d_c \quad (47)$$

This function, despite not representing the exact post-peak behavior, may be suitable to describe the global behavior. This model indicates the maximum connection capacity by a strictly increasing function. A monotonic function can be preferable to others for being numerically easier to apply. The graphic representation of the function is exemplified in Figure 62. The model parameters are presented in Table 43.

Figure 62: Load-displacement curvilinear model example.



Source: author.

Table 43: Curvilinear model parameters for wafer head screws without wings pull-through on fiber cement boards.

Wafer head screws samples without wings	F_y (N)	d_y (mm)	k_y (N/mm)	Q_0 (N)	Q_1 (N/mm)
New ambient	562,1	0,63	887,9	10	43
New wet	369,4	0,56	663,8	12	38
Aged ambient	729,8	0,76	963,2	5	20
Aged wet	585,9	0,79	741,8	13	21

Source: author.

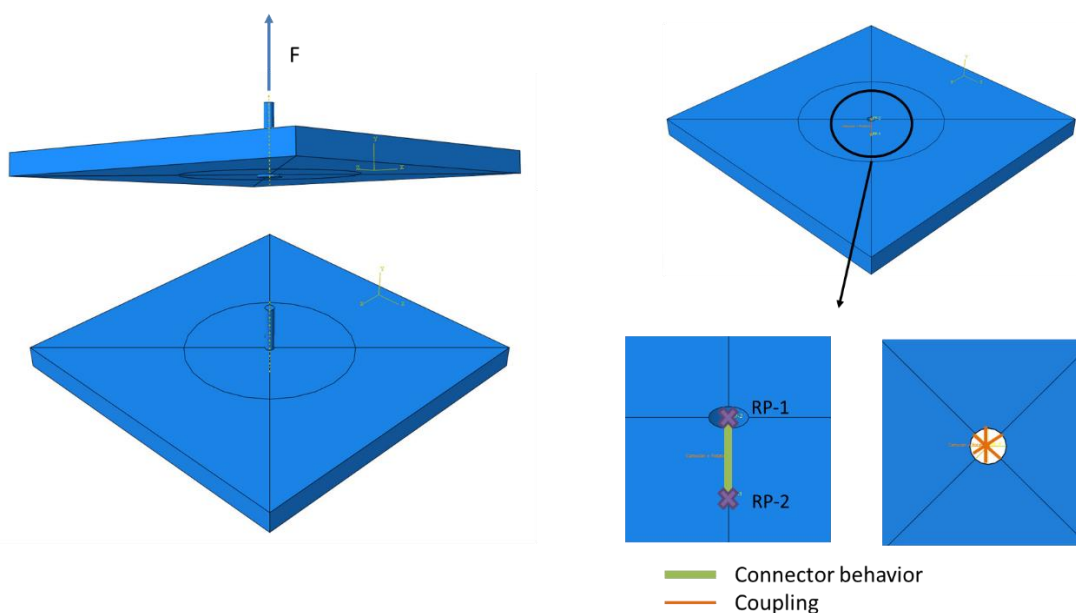
5.3.3. Numerical pull-through modeling

The numerical representation of the connector may be done by two main ways, as illustrated in Figure 63: an explicit modeling of the connector and its interaction with the board or by virtual wires relying nodes by defining behavioral equations, including the material interaction.

The first choice, despite being more realistic, is costlier to implement due to the difficulty of characterizing and representing the fastener-board contact and the material damage or failure in the pull-through process. The interaction between the connector and the material plays an important role and must be considered for a proper modeling. However, stress concentration in the contact region may generate numerical instabilities, and distort the damage prediction accuracy in this case.

The second model has a simpler implementation, since all behavioral equations were directly obtained by the experimental analysis. Moreover, those equations implicitly comprise the interaction between the screw and the board. In this case, failure is assessed by the connector failure itself and not explicitly by a material criterion; and the pull-through failure criteria will be directly represented as the connector damage, avoiding any contact modeling problem.

Figure 63: Numerical modeling of pull-through test. Calibration of the screw-board interaction behavior.



Source: author.

The implementation of the second modeling choice is facilitated by using the ABAQUS options to model a connector behavior ¹⁵⁹. The numerical models were calibrated considering the different behavior options that could best represent each fixing solution. These numerical calibrations were done using the personalized model *connector_design.cae*. The linear connector behavior is defined by its stiffness. The non-linear post-peak behavior with strengthening was defined as a “pseudo-hardening” behavior, and it was modeled by defining explicitly the yield force by plastic motion ordered pairs. Finally, the maximum pull-through force was adopted as the failure criteria in both cases.

5.3.3.1. Flat head winged screws

For the flat head winged screws, the numerical model was set to fit the elastic behavior of the connector. The connection is only assumed activated before reaching its F_{max} , due to the sharp drop in the pull-through strength after the peak. Indeed, there is no interest to pursue the analysis after the connector failure. For this reason, after reaching this maximum strength, it is assumed that the connector is fully broken, and the board is completely released at this respective point.

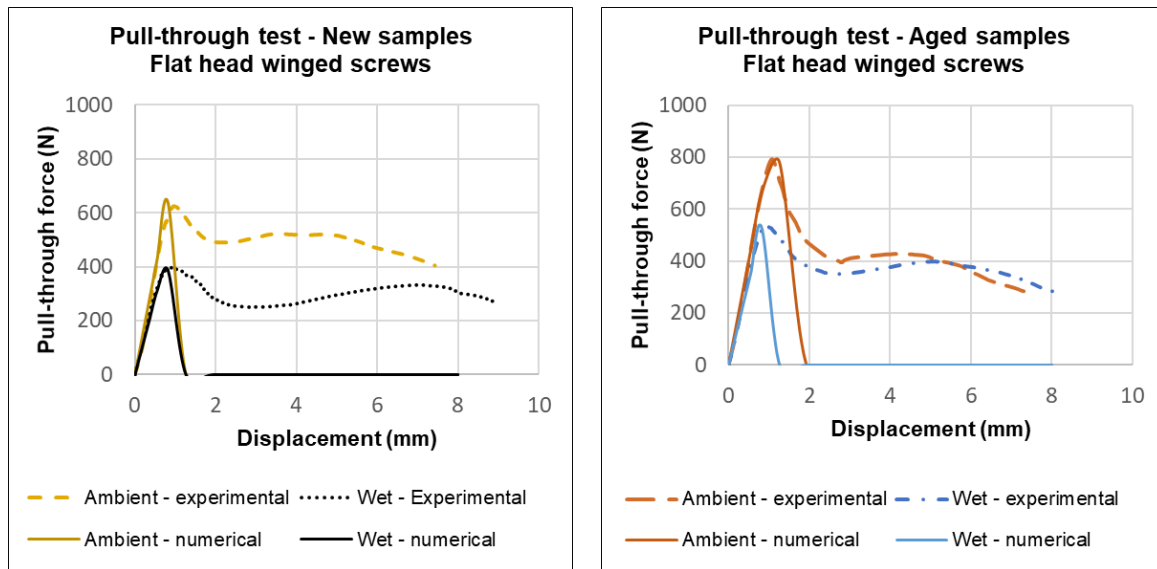
The numerical model was calibrated using the definitions presented in 5.3.2.1. Therefore, Table 44 summarizes the input parameters obtained for the simulations. As observed in Figure 64, the numerical model has a good fit to predict the elastic performance of the connection and its pull-through. After the peak, the connector fails, and the numerical curves do not represent the experimental results anymore.

Table 44: Numerical model parameters to simulate a flat head winged screwed connection.

ABAQUS option	Elastic behavior	Failure criterion
Flat head winged screws	Elastic stiffness (N/mm)	Upper bound - F_{max} (N)
New ambient	786	638
New wet	557	400
Aged ambient	811	875
Aged wet	638	571

Source: author.

Figure 64: Numerical calibration of winged screws pull-through.



Source: author.

5.3.3.2. Wafer head screw without wings

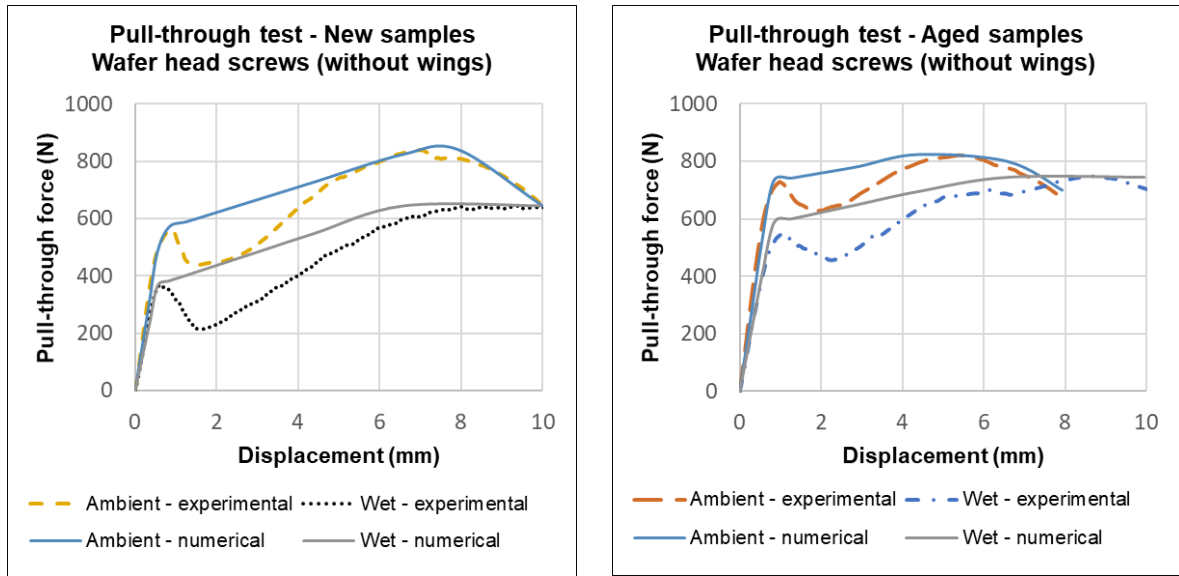
In the case of using a wafer head screw without wings, two numerical models are proposed following the reasoning explained in 5.3.2.2. In both cases, the connector is considered with a plastic behavior to capture the strengthening effect after the first pull-through peak. The difference of the two modeling choices is the plastic curve definition: for a monotonic curve, only two points are defined ((F_1, p_1) and (F_3, p_3)), and in the case of using a piecewise function, an intermediate point ((F_2, p_2)) is needed to represent the slight softening after the first peak.

Table 45: Input parameters for the numerical models of wafer head screws without wings.

ABAQUS option	Elastic behavior	Plastic behavior		
		(F_1, p_1)	(F_2, p_2)	(F_3, p_3)
Flat head winged screws	Elastic stiffness (N/mm)			
New ambient	888	(600,0)	(400,1)	(841,5)
New wet	664	(369,0)	(200,1.3)	(645,5.5)
Aged ambient	963	(730,0)	(624,0.96)	(823,3.8)
Aged wet	742	(586,0)	(450,1.3)	(745,7.2)

Source: author.

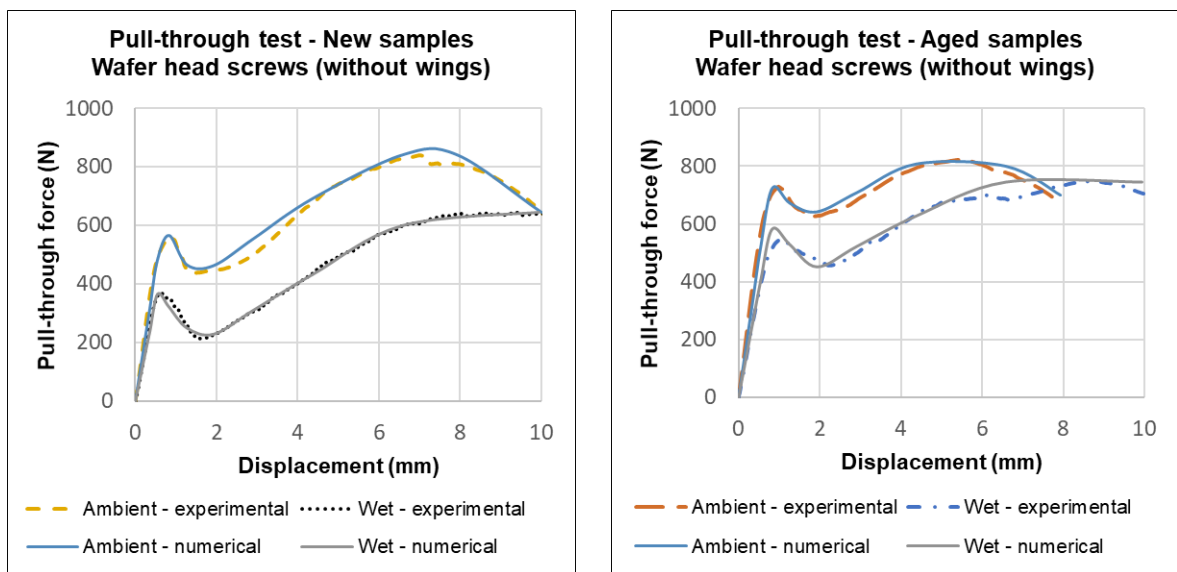
Figure 65: Numerical calibration of no-winged screws using a monotonic curvilinear function.



Source: author.

Table 45 presents the numerical parameters for the plastic behavior simulation. Figure 65 and Figure 66 depict the numerical curves obtained for each modeling choice. It can be noted that it is possible to get a good agreement between the experimental and the numerical results despite the function choice. In addition, it can be highlighted that in this plastic case the connection behavior is fully represented, including its post-peak behavior.

Figure 66: Numerical calibration of no-winged screws using a piecewise function.



Source: author.

5.4. Concluding remarks

The design of the connectors to fix the fiber cement board in a façade must consider both in-plane and out-of-plane actions. The dimensional variation by shrinkage or carbonation and the wind load actions have been demonstrated to be the main loads acting on the façade system. Each of those actions generates different risks related to the fixing system, and it implies complementary analysis to define the connectors parameters and their positioning. Furthermore, if the tightening torque is not controlled during screwing, it can result in an excessive compression of the board, initiating micro cracking on the fixing regions.

The dimensional variations may cause cracks on the boards if the connections are too stiff or quite close to the edges. It has been demonstrated, by computational simulations, that the best strategy to avoid the risk of cracking is the use of sliding points instead of fixed ones. If the screw diameter is close to the drill size, the connection becomes rigid and cracks will appear, whatever the fixing distancing to the edges is. On the other hand, the use of pre-drills with a drilling diameter higher than the connector gauge allows the free board displacement in case of shrinkage, mitigating the cracks. By combining pre-drills and the definition of minimum edge distances, the risk of cracks can be conveniently eliminated. It was defined, for the case studied in this work, that a pre-drill of 11mm for a rivet with 4,9mm is sufficient to avoid any crack until a dimensional variation of 5mm/m, provided a minimum horizontal edge distance of 15mm and a minimum vertical one of 100mm.

Regarding the wind loads effect, the major engendered risk is the pullout of the board due to the fasteners failure. The assessment of this out-of-plane response depends on the connector behavior and its interaction with the board at the screwed regions. An experimental protocol has been implemented to characterize the fixing behavior, including the board interaction. The pull-through analysis has shown the different performance of a winged screw and a screw without wings in different hygrometric conditions and aging.

As expected, in wet conditions the connector stiffness and the maximum strength are reduced in all cases. The use of screws without wings has resulted in an enhanced post-peak behavior and in the increasing of the pull-through strength, despite creating a more rigid connection. Moreover, it has been demonstrated that aging improves the pull-through strength, whilst promoting a material embrittlement.

However, this embrittlement is not a major issue, since the convenient pre-drill and edge distances have been well defined to prevent cracks. Therefore, the worst case scenario for the pull-through analysis has been the new samples.

Based on the experimental characterization, numerical models have been proposed to simulate those connections in a finite element analysis. In order to simplify the modeling strategy, connectors have been represented by virtual wires with a behavior defined by a mathematical function. Those equations have been defined already comprising the interaction between the board and the screws, and failure has been directly defined as the maximum point of the connector behavior function.

An elastic-linear model has been sufficient to represent the behavior of the winged screw, whose failure is reached after the pull-through peak. In the case of a no-winged screw, there is a strengthening in the post-peak behavior with a force recovering after a slight drop in the force-displacement curve. Elastic-plastic models have been set to fit this “pseudo-hardened” experimental behavior with a good agreement. The definition of these numerical modeling strategies will be useful to represent the fixing system in a macroscale analysis of the overall façade panel performance.

All analyses were done assuming the superposition of effects, by assessing separately the effects of pull-through and in-plane displacements. In addition, the fixing point was considered ideally centered within the drilling hole. In this way, the conclusions presented in this work have to be carefully considered and it is recommended that any extrapolation has to be complemented by particular analyses considering a combined bending and axial forces that could be generated by an expected eccentricity.

6. NUMERICAL MODELING OF A FAÇADE PANEL

Final numerical model: General boundary conditions and results

The definition of the design parameters of a façade system depends on the validation of all structural requirements proposed in this work. Since those requirements have been postulated linked to the systemic performance of the façade, their verification demands an overall analysis including all components and their interactions. As presented in chapter 1, this global analysis will be done considering a façade panel composed by the metal frame, the fiber cement boards and the fixing system, assumed as the most relevant pieces for the structural performance setting.

Therefore, the numerical model ability to simulate general façade performance depends on the definition of:

- The general boundary conditions, including the metal frames modeling and their supports;
- A model to simulate the board material behavior;
- A model to simulate the connectors behavior;
- The loads applied to the structure.

The previous chapters described the last three points of the above list. Hence, this final chapter starts by presenting a discussion about the steel profiles modeling and the general boundary conditions. Next, the validation framework is revisited to clarify how each criterion is verified in the numerical analysis, and which the design loads are, and the limit values considered on the design of a 30-floor building façade. Then, the façade modeling is presented with all components considerations.

Finally, a set of numerical results is used to assess the façade mechanical performance in different configurations. Optimized combinations of studs and screws distancing are obtained by ensuring that the structural requirements are fulfilled in both ULS and SLS safety limit states. The analyses include considerations about the hygrometric conditions and the aging effect on board and connector behaviors.

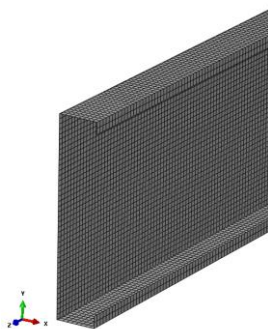
It is important to highlight that all results presented here have been obtained considering the most critical hypotheses for the design loads definitions, as described in 2.3.3 and in 3.4.2. Those values and the optimized design parameters must be properly defined for each specific project, preventing any generalization.

6.1. Structural frame modeling

In order to validate the stud design, as presented in 1.3.2, a modeling strategy was proposed using the finite element method (FEM). An ABAQUS routine called *stud_design.py* was created to generate these analyses. Studs were modeled using the shell element S4 available in the software ABAQUS. This element is a general-purpose quadrilateral shell element with 4-nodes, linear interpolation and full integration. The S4-element is recommended to allow a finite-strain formulation, to avoid hourglass modes, and to provide accurate solutions for in-plane bending and membrane responses. After a convergence study, a refined mesh was adopted with 5x5mm-size S4 elements, as illustrated in Figure 67.

The steel behavior was assumed as elastic until the yield stress limit. The elastic behavior was characterized by the Young's modulus (E) of 200 GPa and by a Poisson's coefficient of 0,3. Mass density was adopted as 7850 g/cm³. The yield stress was taken as 230 MPa, for a steel classified as ZAR 230. However, considering a safety factor of 1,15, the elastic limit was considered at 200 MPa for dimensioning purposes. A static analysis was done with wind load applied as an equivalent distributed load along the web edge of the stud. A geometrical nonlinear formulation was assumed.

Figure 67: Mesh detailing. 5mmx5mm S4 elements.



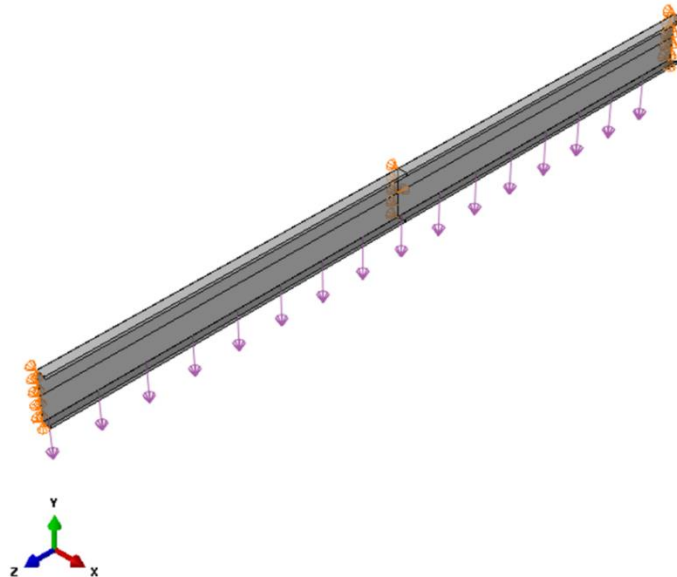
Source: author.

Three different models were proposed to simulate the stud behavior: a first model representing a pinned-supported stud, as assumed on the analytical analysis; a second model introducing boundary conditions, representing the inserts geometry; and a third proposal, simulating the lateral restraints provided by the boards. The example of the 200 x 40 x 12 x 1,25 stud was taken to illustrate the results, with a ULS wind load of 3,2kPa correspondent to a 30-floor building horizontal load.

6.1.1. Simply-supported stud

This first model intends to simulate the same boundary conditions adopted on the analytical design, i.e., a simply-supported C-stud with a transversal displacement restrained at mid-span, due to bracing straps. Accordingly, in the numerical modeling in ABAQUS, the in-plane translational displacements of the web edges were blocked ($U_x = U_y = 0$) at both stud extremities, as shown in Figure 68. Restraining only the web displacements, warping and local cross-section distortions remain free. The longitudinal displacement along the stud length was restrained ($U_z = 0$) in a central point, avoiding stress concentration at the supported edges.

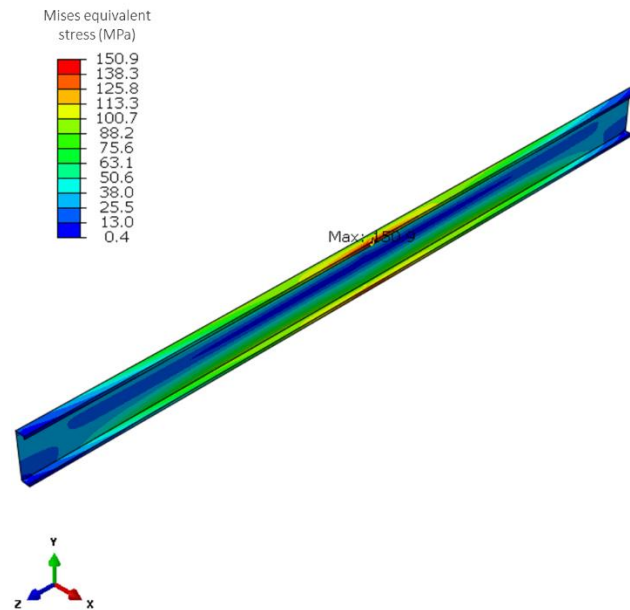
Figure 68: Boundary conditions of a simply-supported C-stud. Model 1.



Source: author.

Figure 69 shows the stress field results for the exemplified stud. The maximum stress remains lower than the ULS limit of 200 MPa ($f_y/1,15$). Figure 70 depicts the displacements field of the same stud. Table 46 presents the results of the maximum horizontal loads determined by numerical simulation for some proposed C-profiles. It can be observed a slight difference between these values and those in Table 4, which are obtained by analytical equations. The symbols ▲ and ▼ indicate when the numerical results are respectively greater or lower than those defined analytically.

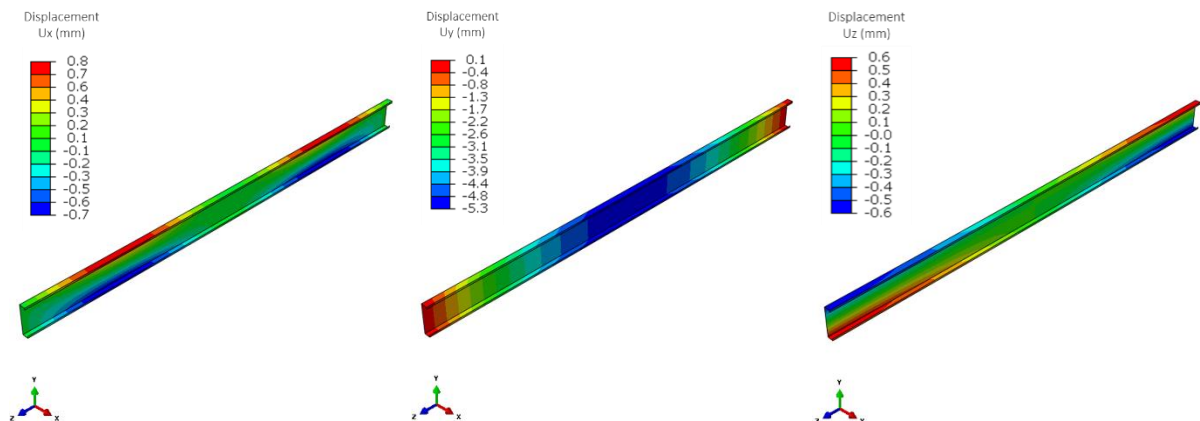
Figure 69: Mises equivalent stress of Model 1.



Source: author.

These differences are due to the approximations of the linear analytical formulation, such as those for the calculation of effective sections²¹¹. Furthermore, the geometrical properties determination, as inertia or section modulus, is not exact: tabulated values were used on the analytical approach, whereas the geometrical stiffness is calculated element-by-element in FEM. Analytical formulations are easy to apply, and give a good approximated solution. However, numerical methods, such as FEM, can be helpful to optimize the structure design, since they are able to capture some local or specific effects that do not appear in the analytical equations.

Figure 70: Displacement field of Model 1.



Source: author.

Table 46: Maximum design horizontal loads calculated by means of FEM for a 3-meters high C-stud.

C-stud LSF profile (ZAR 230)	Maximum design wind pressure - q_{wd} (kPa)	
	400 mm	600 mm
90 x 40 x 12 x 0.8	1,4	0,9
90 x 40 x 12 x 0.95	▼ 1,7	▼ 1,1
90 x 50 x 12 x 0.95	▼ 1,9	▼ 1,2
90 x 40 x 12 x 1.25	▼ 2,3	▼ 1,5
140 x 40 x 12 x 0.95	2,9	▲ 1,9
140 x 50 x 12 x 0.95	▼ 3,2	▼ 2,1
200 x 40 x 12 x 0.95	▲ 4,6	▲ 3,1
200 x 50 x 12 x 0.95	▲ 5,0	▲ 3,5
140 x 40 x 12 x 1.25	▼ 3,9	▼ 2,7
200 x 40 x 12 x 1.25	▲ 6,3	▲ 4,2

Source: author.

Based on this numerical results and on the loads defined in 2.4.1, a list of recommended C-profiles is proposed for different building heights. Table 47 summarizes these indicated C-stud profiles for LSF façades. The standard notation was used to indicate the profiles, including a last number defining the stud spacing of 400mm or 600mm each. The choices were made based on the mechanical results before the defined loads for each building height, and also looking for the most economical option in terms of steel consumption, assessed by the ratio of the total steel mass by square meter of façade.

Table 47: Suggested profiles for LSF façades studs. Minimum geometries.

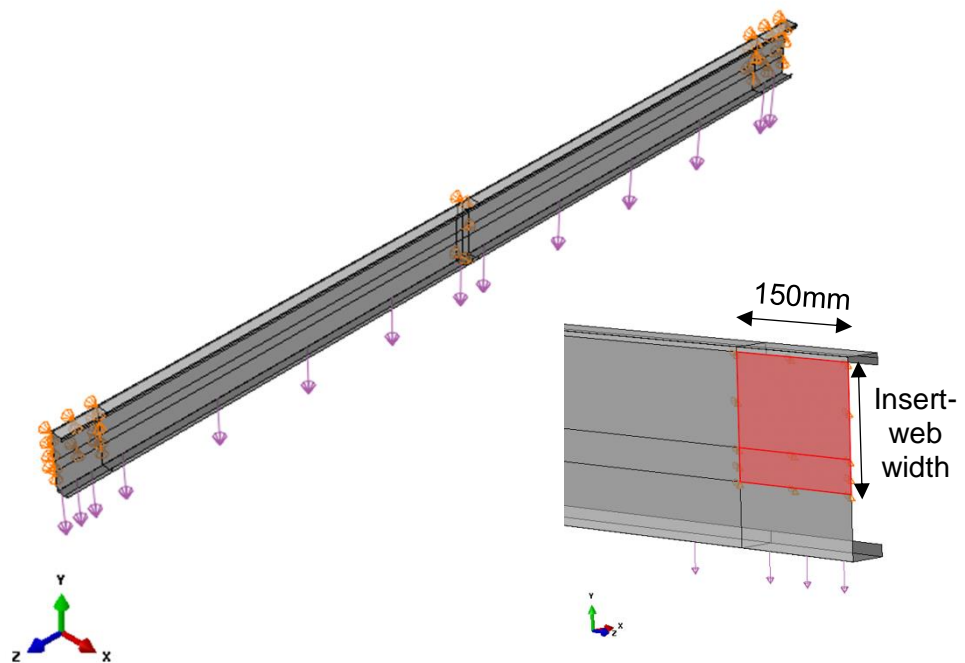
Floors	Height	Global load (kPa) ULS	Suggested profiles	
			studs at each 400mm	studs at each 600mm
10	30 m	2,2	90 x 40 x 12 x 1,25	140 x 50 x 12 x 1,25
15	45 m	2,5	140 x 40 x 12 x 0,95	200 x 40 x 12 x 0,95
20	60 m	2,8		
25	75 m	3,0	140 x 50 x 12 x 0,95 or 200 x 40 x 12 x 0,95	200 x 40 x 12 x 1,25
30	90 m	3,2		
35	105 m	3,3		
40	120 m	3,4	200 x 40 x 12 x 0,95	

Source: author.

6.1.2. Inserts modeling as restrained displacements

In case of choosing to represent the stud closer to the real application, a second modeling strategy is proposed, changing the boundary conditions of the problem. As shown in Figure 71, the inserts may be represented by displacements restrained at a portion of the web surface in the stud extremities. Inserts were assumed with a length of 150mm and a variable width to simulate the insert-web contact at the ends.

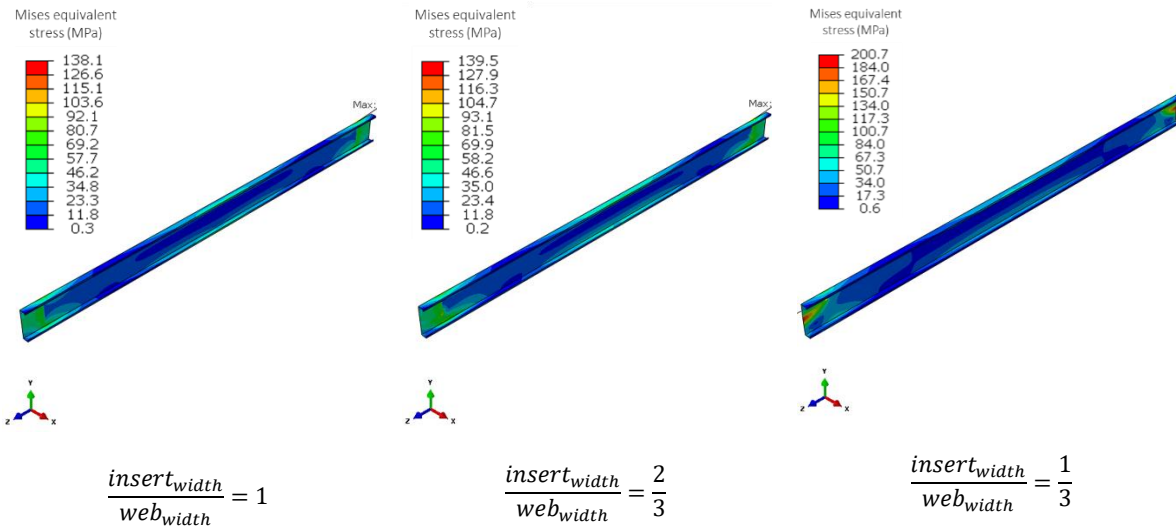
Figure 71: Boundary conditions with insert geometry simulation. Model 2.



Source: author.

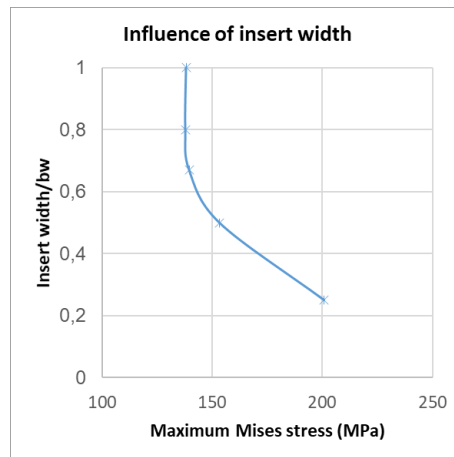
Even if this model is more representative of the real problem, it leads to a problem of stress concentration in the support corners, demanding a careful analysis on these regions. The stress concentration is dependent on the size of the support region, indicating the influence of the insert dimensioning and positioning on the stud design. As evidenced in Figure 72 and in Figure 73, a minimum of $2/3$ of the web width must be in contact with the insert to avoid an important stress increase. Specific modeling of the inserts is necessary to design the insert geometry and shape; this detailing is out of the scope of this work.

Figure 72: Stress increasing with reduced web-insert contact.



Source: author.

Figure 73: Influence of insert width in stress concentration.

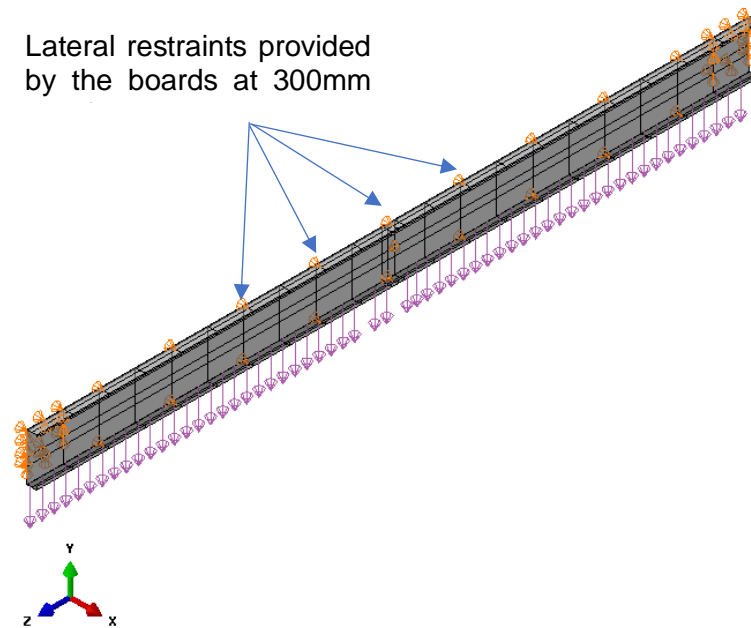


Source: author.

6.1.3. Contribution of the boards as a lateral in-plane restriction

Considering that the load acts on the board, it is coherent to consider that the boards restrain the lateral in-plane displacement of the flanges. To represent this configuration, a third model was proposed with lateral displacements restraints at the screw fasteners locations along the stud height, as exemplified in Figure 74. Screws spacing of 150mm, 300mm, 400mm and 600mm were simulated, comparing the effects of these point restrictions in relation to the bracing strap simulation.

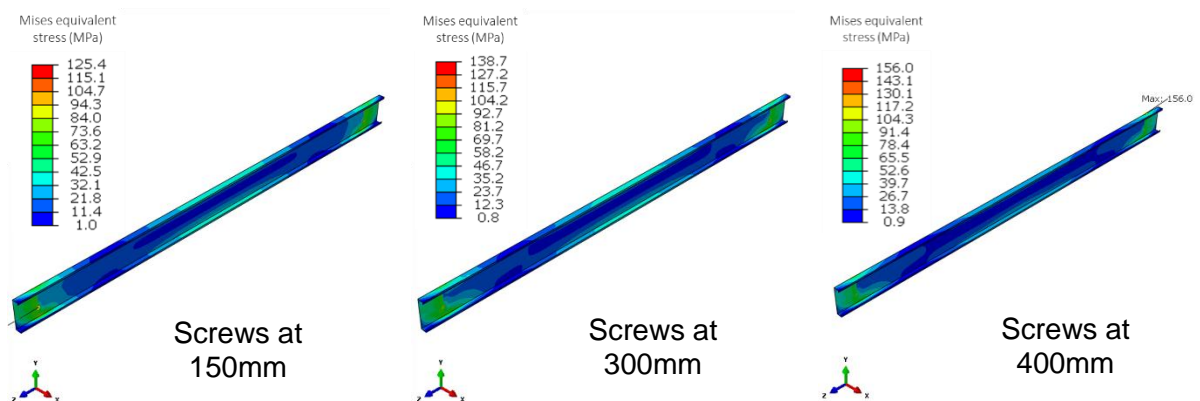
Figure 74: Boundary conditions considering lateral in-plane restraints provided by screws. Model 3.



Source: author.

The results, evidenced in Figure 75, showed that in case of boards screwed in both sides of the metal frame, the lateral restraints provided by the boards correspond to the bracing strap only if screws are spaced 300mm each, at most. If screw spacing is higher than 300mm, the maximum stress increasing becomes significant, although screws still provide a slight bracing effect. In case of considering a board screwed only in one side of the stud, for a siding wall for example, the screw points do not contribute to the lateral stud stability, and bracing straps become mandatory independent of the screw fastener spacing.

Figure 75: Stress increasing in function of screws spacing.



Source: author.

6.2. Requirements validation framework

At the beginning of this work, a generic set of criteria were proposed for the design of a lightweight façade system. It has been demonstrated that wind and shrinkage are the main actions to be considered in this design assessment. The definition of the imposed loads or imposed strains magnitudes have been shown as dependent of the specific conditions for each project and each material. In order to exemplify the use of this framework, Figure 76 summarizes the values that have been considered in the analysis of a 30-floor building façade.

Figure 76: Design criteria for a 30-floor building lightweight façade.

<p><u>Criterion:</u></p> <ul style="list-style-type: none"> Structural strength <p><u>Design wind load:</u></p> <ul style="list-style-type: none"> $q_{wd} = 3,2 \text{ kPa}$ <p>Global effects:</p> <p>Metal frame and board design</p> <p><u>Criterion:</u></p> <ul style="list-style-type: none"> Maximum horizontal displacement ($\delta_h \leq h/175$) <p><u>Design wind load:</u></p> <ul style="list-style-type: none"> $q_{wd} = 1,8 \text{ kPa}$ 	ULS	<p><u>Criterion:</u></p> <ul style="list-style-type: none"> Pull-through strength <p><u>Design wind load:</u></p> <ul style="list-style-type: none"> $q_{wd} = 3,5 \text{ kPa}$ <p>Local effects:</p> <p>Board fixing design</p> <p><u>Criterion:</u></p> <ul style="list-style-type: none"> Crack initiation on external board <p><u>Design wind load:</u> $q_{wd} = 2,0 \text{ kPa}$</p> <p><u>Design shrinkage:</u> $\varepsilon_{sh} = \frac{5\text{mm}}{m}$</p>	SLS
--	------------	---	------------

Source: author.

A specific façade configuration, including the design parameters such as the stud and screw distancing, will be validated if the complete set of criteria is properly fulfilled. These assessments can be done by numerical simulations using the different models proposed in this work. Table 48 clarifies how each requirement can be assessed and which numerical routine can be used to the respective analysis.

It can be noted from Table 48 that the shrinkage analysis and the metal frame design are considered already covered in previous items of this work. Assuming a stud profile as instructed in 6.1 and the screwing recommendations of 5.4, the requirements 1 and 5 are consequently fulfilled. Hence, the complete façade model can be created considering only the wind load effect, and the analysis will be focused on the board stress results, the overall displacements and the connector resultant forces.

Table 48: Requirements validation framework.

Limit state	Effect	Criterion	Requirement validation	Numerical routine
ULS	Global	Structural strength	1) <u>Metal frame</u> : design presented in 6.1. 2) <u>External board</u> : the principal stress in the span must be lower than the ultimate board strength.	<u>Metal frame</u> : <i>stud_design.py</i> <u>External board</u> : <i>facade_design.py</i>
	Local	Pull-trough strength	3) <u>Connector</u> : the maximum force cannot reach the pull-trough strength of the respective connector, that already considers the interaction with the board.	<i>facade_design.py</i>
SLS	Global	Maximum horizontal displacement	4) <u>Metal frame and external boards</u> : the maximum overall displacement must be lower than 17,1mm, considering a façade of 3m-height.	<i>facade_design.py</i>
	Local	Crack initiation	5) <u>Shrinkage</u> : the use of pre-drills and the minimum edge distances defined in 5.4 are sufficient to fulfill this requirement. 6) <u>Wind loads</u> : the principal stress must be lower than the yield stress of the board in all points and the connectors cannot fail.	<u>Shrinkage</u> : <i>pre_drill.py</i> <u>Wind loads</u> : <i>facade_design.py</i>

Source: author.

6.3. Façade modeling

The numerical model of a façade panel was conceived by assembling the metal frames and the fiber cement boards. The interaction of these two parts is done by a fastener modeling that connects the points representing a screw. In order to facilitate a parametric analysis of different geometries and material properties, the routine *façade_design.py* was created. This routine allows the parametrization of all variables related to the façade modeling, such as the profiles and board geometries, the screws distancing and properties, and the material behaviors.

To exemplify this façade modeling strategy, and to complete the validation of a façade panel for a 30 floor-building, a numerical model was created using the ABAQUS software. The façade typology was simplified considering only the metal frame (including studs and tracks) and the fiber cement board. Different studs and screws distancing were tested in order to reach the most optimized and safest solution. Besides these parameters variations, some premises were assumed to the modeling:

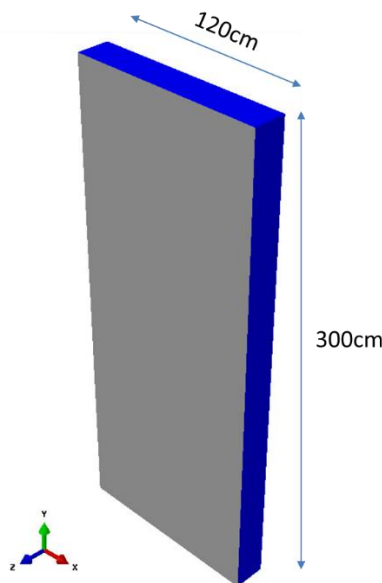
6.3.1. Geometry

A façade frame was adopted in the same dimension of one fiber cement board for a conventional floor-to-floor height. Hence, the façade panel has 1,2m-width by 3,0m-height. The metal frame is composed by studs (vertical elements) 400mm or 600mm apart, and tracks (horizontal elements) disposed at 1,5m of height. The connection between studs and tracks is assumed to be rigid. The geometry of the LSF profiles was adopted according to Table 47 for a 30-floor building:

- Studs (C-profile): 200 x 40 x 12 x 0,95 for 400mm of studs distancing and 200 x 40 x 12 x 1,25 for 600mm of studs distancing;
- Tracks (U-profile): 200 x 39 x 0,95 or 200 x 39 x 1,25.

Since its thickness is quite smaller than the other dimensions, the board was modeled as a plate structure. Figure 77 illustrates the geometry of the façade panel model. This single-board frame allows the study of the screws and studs distancing, whose conclusions can be even used for larger panels. In case of longer panels, using more than one board, the inserts design and positioning become important variables to be taken into account. This insert conception was not assessed in this work, and must be done accordingly to each specific project.

Figure 77: Façade frame geometry.



Source: author.

6.3.2. Materials

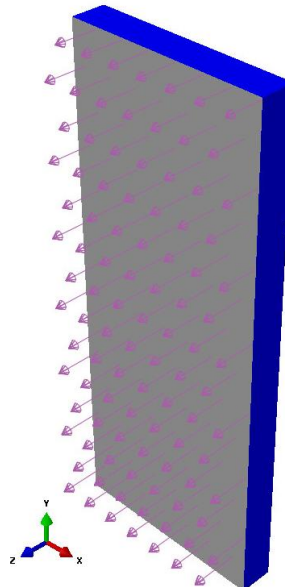
Two materials were used in this model: the steel for the metallic structure and the fiber cement for the board. The steel behavior was defined in 6.1. The fiber cement modeling was considered as described in 4.2. Since bending is the most relevant internal reaction in the case of perpendicular external loads, the material parameters were taken, as characteristic values, from 4.2.1, using the CDP model. The design strength is obtained by using a reduction factor of 1,4; it results in the ultimate board design values $\sigma_{u,ambient} = 4,0MPa$ and $\sigma_{u,wet} = 2,7MPa$.

6.3.3. Loads and boundary conditions

The external loads, defined in Figure 76, are applied as perpendicular loads acting over the board, as illustrated in Figure 78. The boundary conditions, however, are applied on the metallic structure as described in 6.1.2, and illustrated in Figure 79.

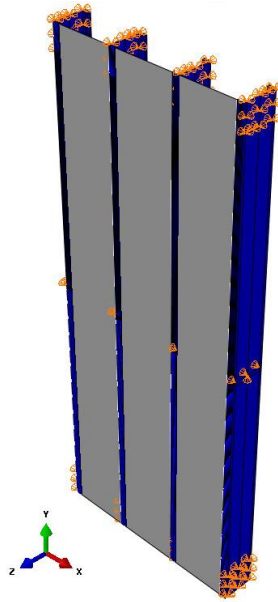
The intermediary track plays the role of bracing, ensuring the torsional strength of the studs. As the studs were dimensioned as simply-supported beams, each of them is supported by inserts in their extremities, replacing the upper and the bottom tracks, to relieve the model geometry.

Figure 78: External wind load.



Source: author.

Figure 79: Boundary conditions. Inserts positioning.

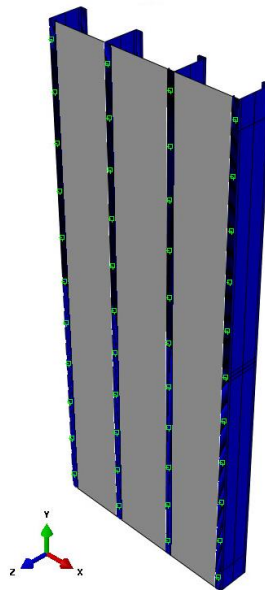


Source: author.

6.3.4. Connectors interactions

The connectors are modeled by relying the displacements and rotations of nodes from the studs and the boards, as illustrated in Figure 80. The behavior equations were described in 5.3.3.

Figure 80: Connectors interactions.



Source: author.

6.3.5. Finite elements and meshing

The façade panel was modeled using the shell element S4, as explained in 6.1. The metallic studs were meshed with 5mmx5mm elements to have at least 2 elements in the smallest part of the profiles (lateral stiffeners of 12mm). The board was meshed with 10mmx10mm elements. Both element sizes were verified by a mesh convergence analysis, comparing the maximum displacement obtained in a linear analysis.

6.4. Design parameters optimization

This work defines as the main design variables of a lightweight façade system: the metal frame and the board geometries; the vertical studs distance and the screws positioning, including their spacing and edges distance. The board geometry was assumed as standard; the metal profile definition was given in 1.3.2 and confirmed in 6.1, and the assessment of the optima screws-to-edges distance was presented in 5.2.

Therefore, here the overall analysis of a single façade panel is presented, aiming to complete this design parameters definition. The influence of the vertical studs distance and the screws spacing is evaluated through numerical models including all materials behavior and geometry definitions. This analysis is completed by considering the effects of wetting, aging and the use of a non-winged screw on the global performance of the façade.

6.4.1. Studs and screws optimum distance

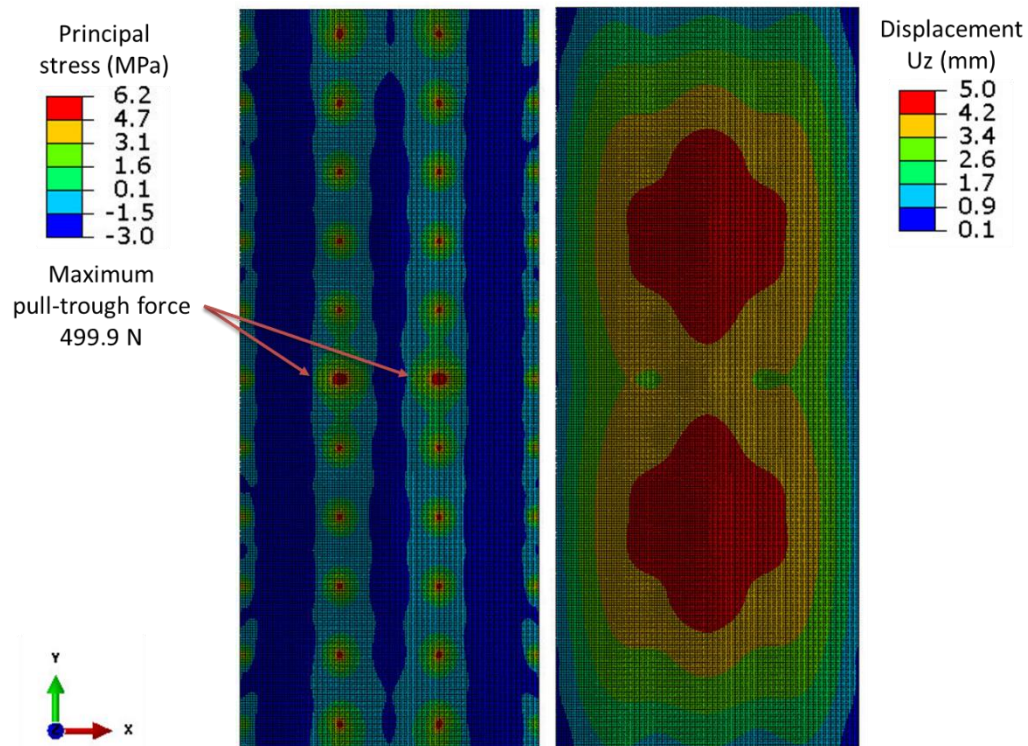
This analysis starts with a maximum distance of 400mm between studs and a vertical screws spacing of 300mm, which is the standard recommendation used in the construction market. The screws spacing increase is assessed using 400mm and 600mm screws distances. Lastly, the same study is done for studs spaced each 600mm. All analyses, in this first moment, are made considering the board and the fixing behaviors at ambient conditions (models defined in 4.1.3 and in 5.3.3.1).

6.4.1.1. Studs distance of 400mm

The configuration 400mm x 300mm (studs distance x screws distance) using winged screws presents a satisfactory behavior in the ULS analysis. Figure 81 shows that the maximum pull-through force stays lower than the allowable connector force ($F_{d,pull-through} = 638N$), and the principal stress, in absolute value, is under the board flexural strength ($\sigma_u = 5,6MPa$) in all regions, apart from the screw points. In these

punctual regions there is a stress concentration, and, then, the criteria to be verified is the pull-through equivalent force and not the board stress, as stated in 6.2. Although the maximum displacement is defined as a SLS requirement, this criterion is already fulfilled, even considering the ultimate load combination.

Figure 81: Local ULS analysis considering studs and screws distance of 400mm x 300mm.

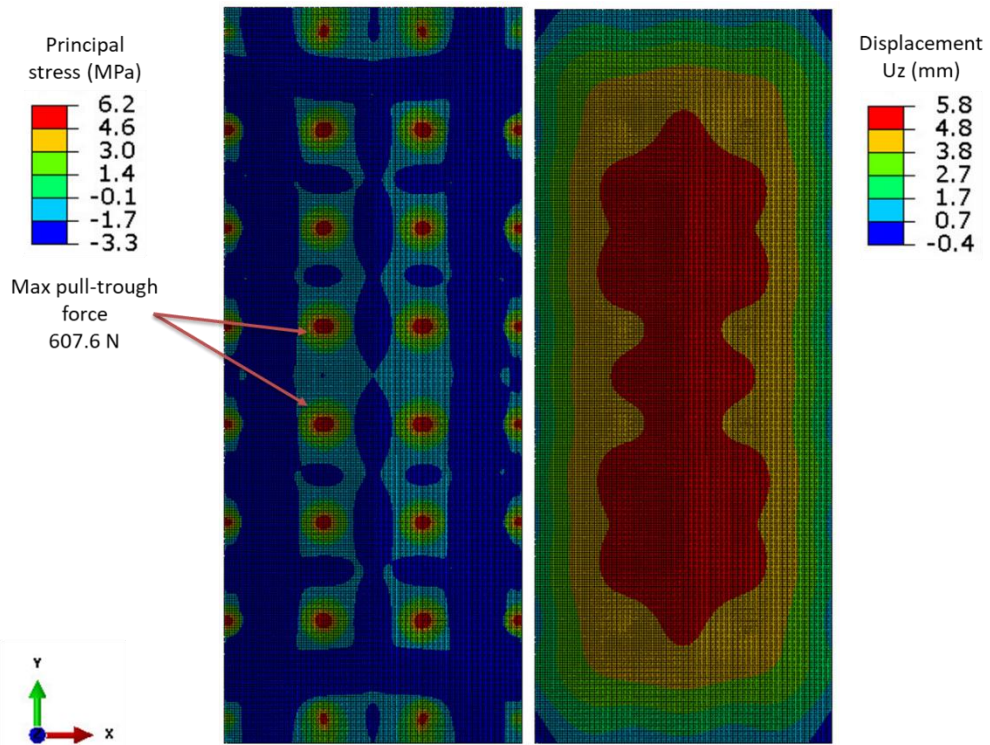


Source: author.

By increasing the screws spacing to 400mm, the façade panel maintains an adequate performance. Despite a slight increase of the maximum principal stress and maximum displacement, these values stay lower than the required ones as depicted in Figure 82. The connectors do not present any failure, though the maximum pull-through force has a significant rise.

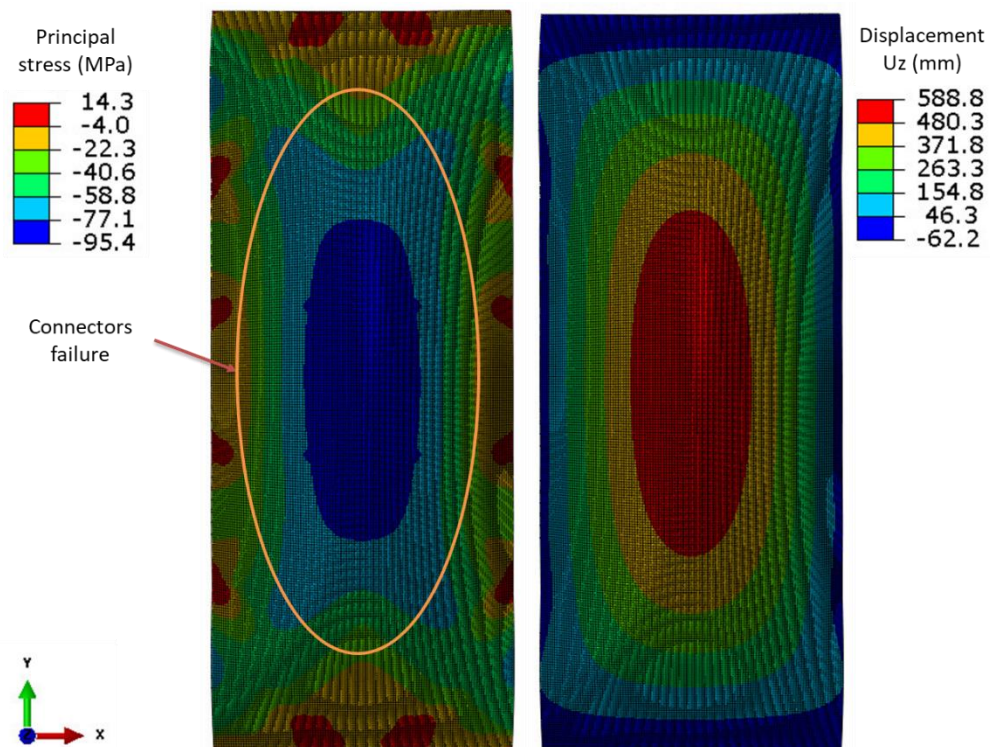
To compare these two solutions, a safety factor (γ_s) can be introduced as the ratio of the pull-through strength by the maximum pull-through force calculated in the numerical model. The 400mm x 300mm configuration has a γ_s of 1,28, whilst the 400mm x 400mm solution presents a safety factor of 1,05 in terms of pull-through capacity. This way, the use of screws at each 400mm can be prescribed, since it is acceptable to admit this reduction in the safety margin.

Figure 82: Local ULS analysis considering studs and screws distance of 400mm x 400mm.



Source: author.

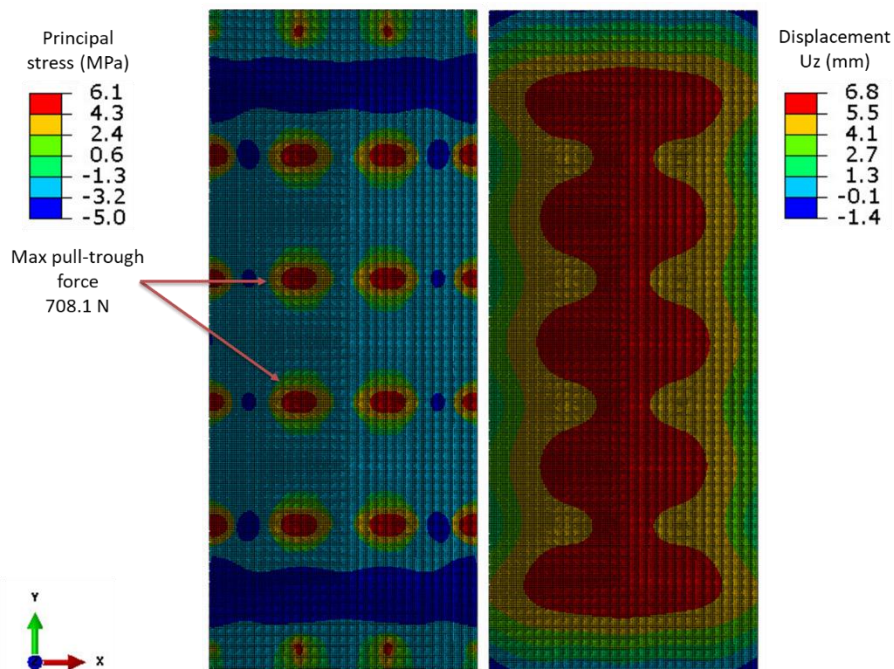
Figure 83: Local ULS analysis considering studs and screws distance of 400mm x 600mm.



Source: author.

Trying to go beyond, the screws were pushed to a 600mm-spacing. However, the failure of some of the connectors was observed, resulting in the complete releasing of the board. As shown in Figure 83, the displacements and the stresses values related to the ULS load (3,5 kPa) are unrealistic, since the connectors have already failed. Assessing one previous step, with an equivalent load of 3,0 kPa, the principal stress and the pull-through forces had already reached their limit values, as illustrated by Figure 84. These results invalidate the choice of a screw distance of 600mm.

Figure 84: Façade panel configuration of 400mm x 600mm under a horizontal load of 3,0kPa.



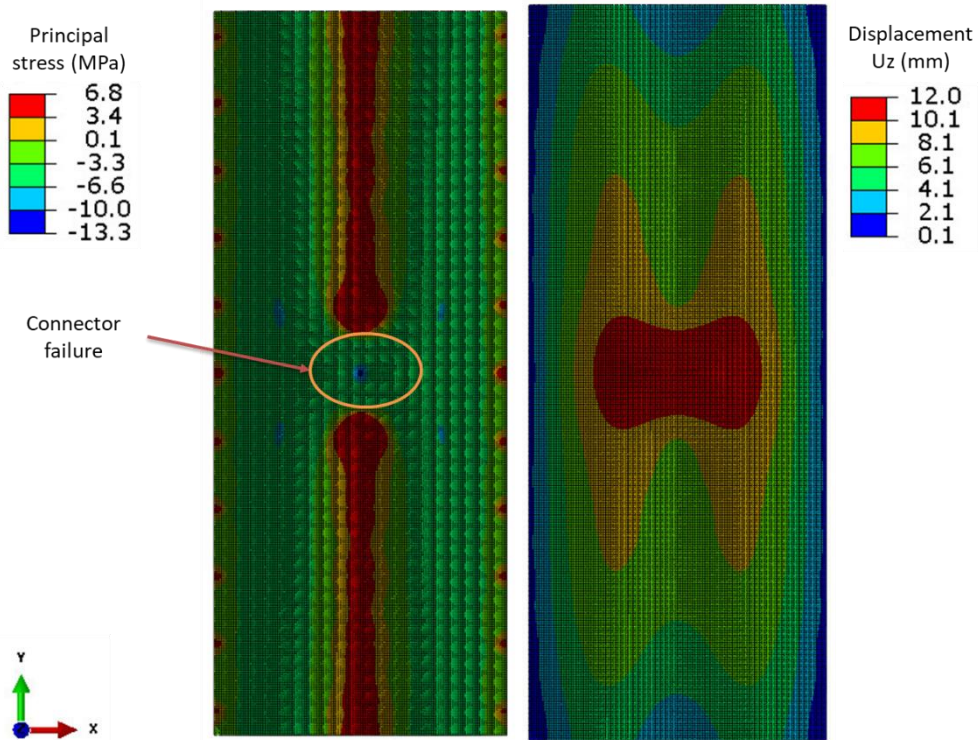
Source: author.

6.4.1.2. Studs distance of 600mm

The same analysis presented in the previous item is done for a façade panel considering studs at each 600mm. Starting by the common screw spacing of 300mm, the Figure 85 reveals that the central connector fails in the ULS analysis. This failure is sufficient to disapprove this design configuration.

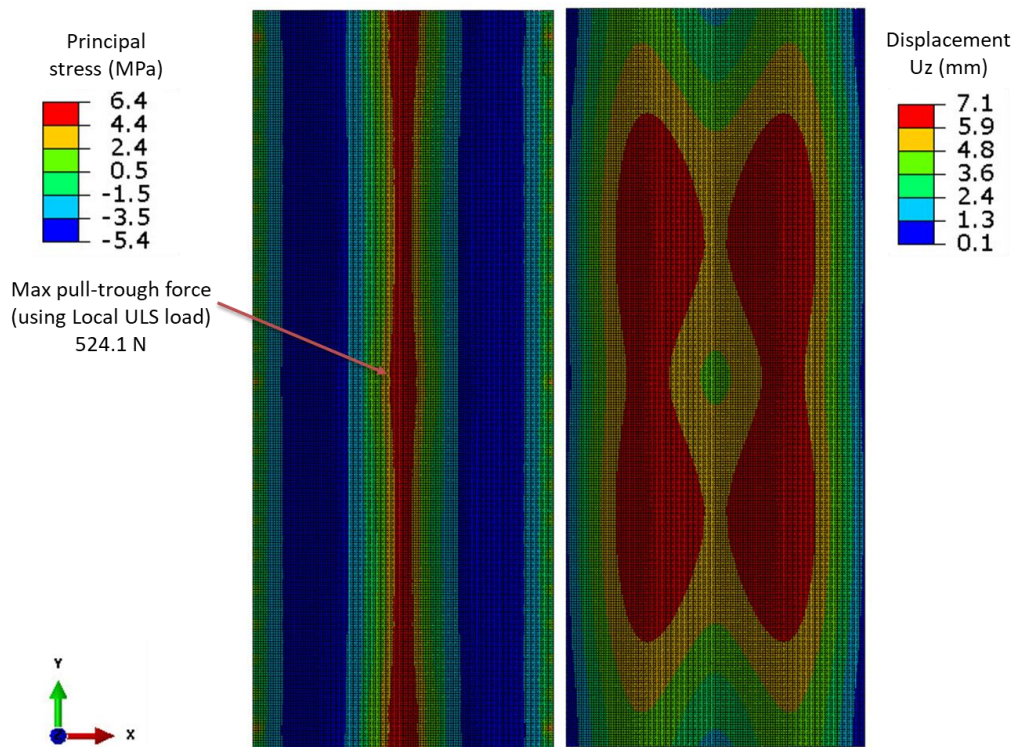
The reduction of the screws distance to 150mm is proposed as an alternative. Figure 86 shows that, indeed, the pull-through and the maximum displacement requirement are fulfilled with this new design. However, using the global design loads of 3,2kPa, the principal stress reaches the board design strength causing its failure in the region between studs. For this reason, no configuration using 600mm of studs distance is recommended for a 30-floor lightweight façade building with this board.

Figure 85: Local ULS analysis considering studs and screws distance of 600mm x 300mm.



Source: author.

Figure 86: Global ULS analysis considering studs and screws distance of 600mm x 150mm.



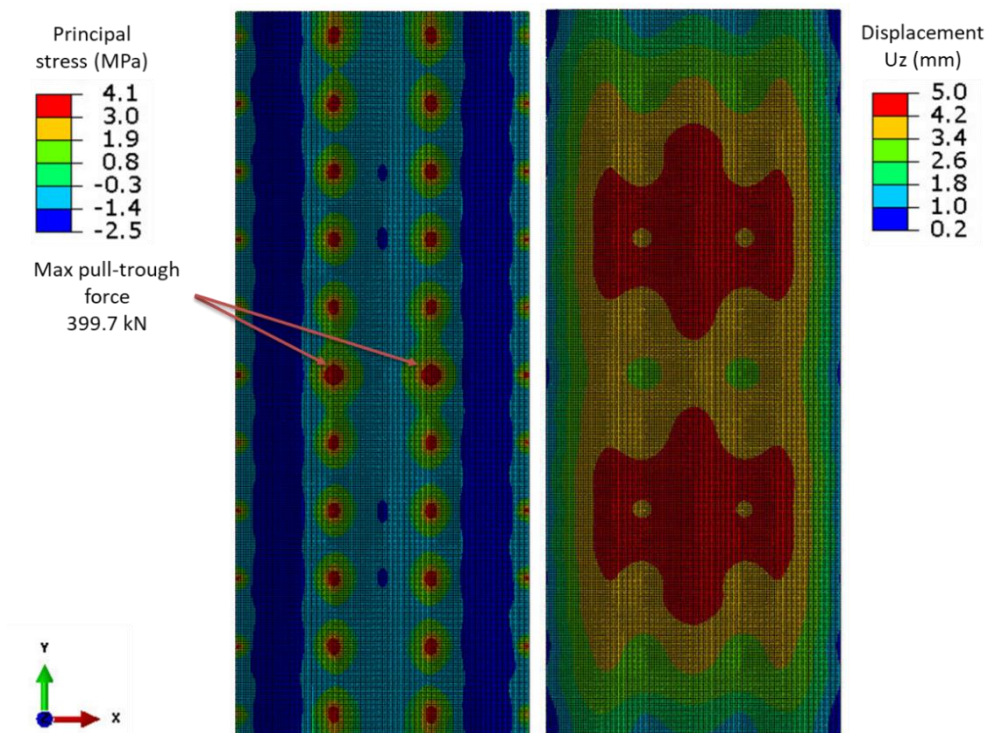
Source: author.

6.4.2. Hygrothermal condition influence

All the analyses are usually done using the material performance at ambient conditions. Aiming to verify the façade performance in most critical cases, simulations were run in a wet condition. The objective is to understand the limits of the design assumptions stated in 6.4.1, when using extreme material parameters.

The façade configuration 400mm x 300mm with winged screws is assessed taking the saturated material inputs. The board behavior was taken from 4.2.1.2, and the screw modeling is the same as presented in 5.3.3.1, both considering the wetting results. Since the water saturation reduces the board and the pull-trough strength, the wet façade can withstand a maximum wind load of 3,0 kPa, as shown in Figure 87. Under a wind load of 3,5 kPa the system fails, as illustrated by Figure 88.

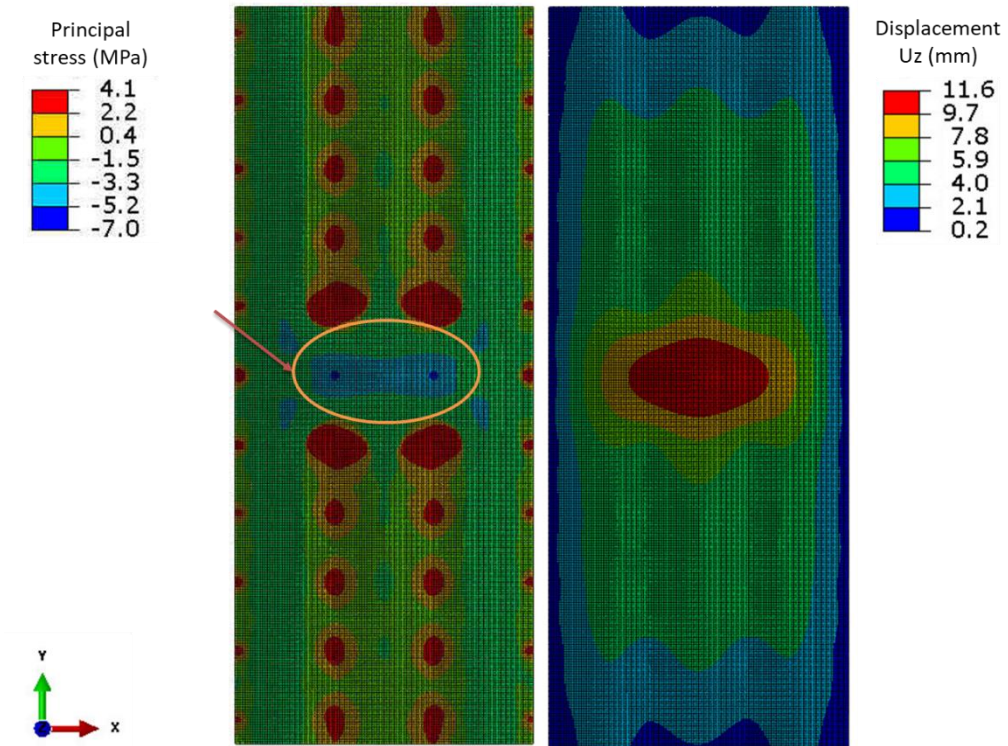
Figure 87: Façade panel of 400mm x 300mm in wetting condition, under a horizontal load of 3,0kPa.



Source: author.

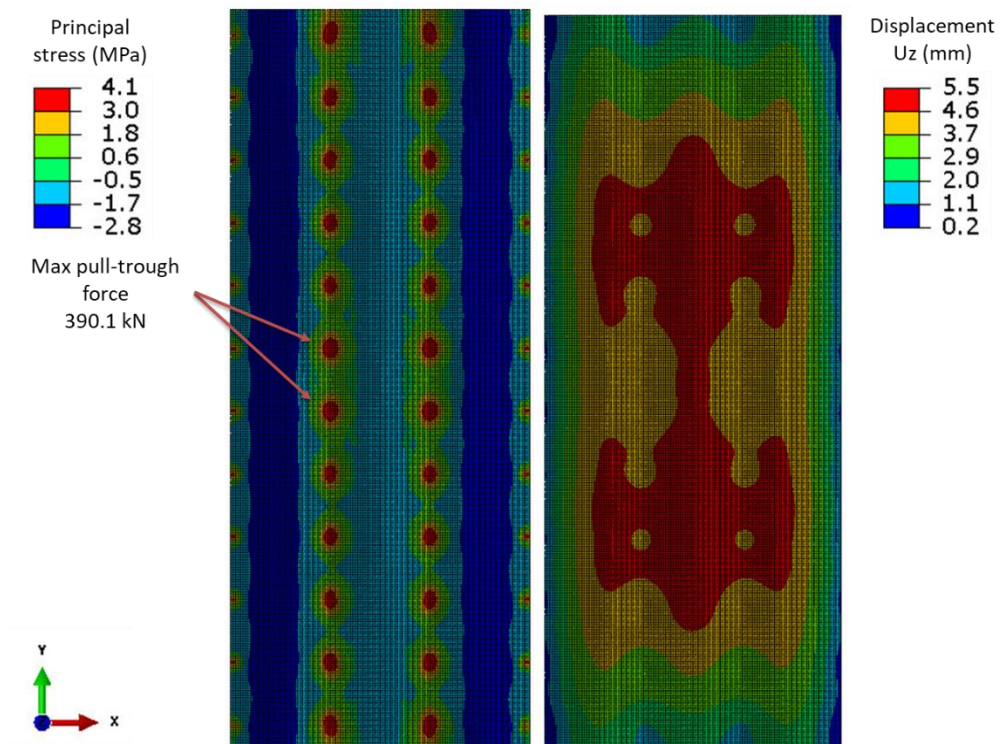
This result confirms that there is an important influence of the hygrothermal conditions on the façade system performance. In case of using completely saturated boards, the façade behavior can be degraded due to the drop of the material strength. However, it has to be pointed out that this condition of fully saturation was achieved after 48 hours with the board completely immersed in water, representing an extreme event.

Figure 88: Local ULS analysis in wet condition, with studs and screws distance of 400mm x 300mm.



Source: author.

Figure 89: Local ULS analysis in wet condition, with studs and screws distance of 400mm x 270mm.



Source: author.

Even in this critical condition, a slight change on the screws spacing can help mitigate the risks. The use of a maximum screw spacing of 270mm, instead of the 300mm initially proposed, is sufficient to ensure that any connector will not fail under 3,5 kPa. Figure 89 presents these results, and it can be noted that the maximum pull-through force in this case is 390 kN, representing an equivalent safety factor of 1,03 for this wetting case.

6.4.3. Aging effects

Regarding the aging effects, it was demonstrated that there is an increase on the material strength along the time. This rising promotes an improvement of the façade system performance, since the drilling process is sufficient to accommodate the shrinkage along the time, maintaining the free in-plane displacements. The system tends to withstand more important loads, despite its embrittlement.

For this reason, the façades configurations that are validated in the “new” condition will stay verified in an aged situation. Moreover, this performance improvement can be observed even in the wet condition where the 400mm x 300mm configuration meets the requirements, presenting a safety factor of 1,18 for the pull-through performance after aging.

6.4.4. Screws type influence

The screws choice has a direct influence on the admissible pull-through load, as demonstrated in 5.3. Indeed, the use of non-winged screws results in strengthened connections. Even if there is a drop in the first pull-through strength, the connector recovers its pull-through capacity after the peak. By changing the winged screws for a non-winged choice, the connections capacity increases around 30%, on average, whatever the condition. Therefore, these screws are a reasonable option when the pull-through requirement is the limiting factor.

That is the case of the façades with studs at each 400mm, mainly to validate the parameters in a wet condition. Both configurations considering a screw spacing of 300mm or 400mm present a satisfactory behavior with safety factors, in ambient conditions of 1,73 and 1,39, respectively. The configuration considering screws at each 600mm still remains out of requirements. The stiffer behavior caused by those non-winged connectors cannot be neglected. That is why the pre-drilling process is specially recommended in this case to mitigate the related in-plane cracking risks.

6.5. Concluding remarks

A global analysis has been presented in order to validate the façade system performance. A numerical model has been conceived to represent the interactions between the boards, the connectors and the metal frame. The material and the connectors behavior have been previously validated and calibrated through experimental analyses. The metal frame model has been defined in order to better simulate the boundary conditions of the frame support, including the inserts representations and the bracing restraining.

A validation framework has been defined, indicating the design loads to be considered for a 30-floor building façade. A set of requirements has been drawn, by differentiating the ULS and the SLS assumptions and, in addition, the global and the local analyses. This framework has been completed by a clear description of variables that have to be monitored in the board, the fixing or in the metal frame parts.

The optimization of the main design parameters has been proposed through a numerical analysis of the complete façade system. This façade modeling regrouped the material, the connector and the geometry definitions for a single lightweight façade panel, comprising one fiber cement board screwed in the metal studs. The assessment of the different façade configurations has been based on the evaluation of the maximum stress, the maximum displacement and the maximum pull-through load reached on each case. Figure 90 summarized the results obtained with winged screws.

In ambient conditions, and considering 400mm of studs distancing, the connectors have had a satisfactory performance with 300mm and 400mm of screws spacing. The board strength has also respected the design limits, since it stayed in the elastic phase without damages in the span regions. Moreover, the maximum displacement stays lower than the maximum allowed, even using the ULS design load. Using a 600mm of screws distance, a lot of connectors have failed, and the board has been released, resulting in unrealistic displacement values in the numerical model.

For the studs at each 600mm, the screws distance would be limited in 150mm to avoid any connector failure. Using the common 300mm of screws spacing, it has been observed that one connector failed, surcharging its adjacent fixing points. Despite the connector analysis, it has been noted that the board stress exceeds the material

strength in both situations. Therefore, the case of 600mm of studs distance cannot be considered for the described 30-floor building façade due to the board failure risk.

Figure 90: Summary of façades design validation for a 30-floor building using winged screws.

Façade design for a 30-floor building using winged screws				ULS			SLS	
				Global (structural strength)		Local	Global	Local*
Frame	Studs (mm)	Screws (mm)	Condition	Metal frame	External board	Pull-trough	Horizontal displacement	Crack initiation
200 x 40 x 12 x 0.95	400	300	Ambient	ok	ok	ok ($\gamma_s = 1,28$)	ok	ok
			Wet	ok	out of limits	out of limits	ok	ok
			Aged wet	ok	ok	ok ($\gamma_s = 1,18$)	ok	ok
200 x 40 x 12 x 0.95	400	400	Ambient	ok	ok	ok ($\gamma_s = 1,05$)	ok	ok
			Wet	ok	out of limits	out of limits	ok	ok
			Aged wet	ok	ok	out of limits	ok	ok
200 x 40 x 12 x 0.95	400	600	Ambient	ok	out of limits	out of limits	ok	ok
			Wet	not assessed				
			Aged wet	not assessed				
200 x 40 x 12 x 1.25	600	150	Ambient	ok	out of limits	ok ($\gamma_s = 1,22$)	ok	ok
			Wet	not assessed				
			Aged wet	ok	ok	ok ($\gamma_s = 1,12$)	ok	ok
200 x 40 x 12 x 1.25	600	300	Ambient	ok	out of limits	out of limits	ok	ok
			Wet	not assessed				
			Aged wet	not assessed				

*considering minimum edges distance of 15mm x 100mm with an appropriate pre-drilling

Source: author.

Once again, it has been demonstrated that wetting can degrade the mechanical performance of the façade system. The reduction of the material capacity in wet condition has resulted in restricted configurations able to withstand the maximum wind load. The maximum screws spacing, in this case, has to be limited to 270mm. Nevertheless, this analysis represents an extremely critical condition, considering the board fully soaked, after many hours in water immersion. Therefore, the wet results must be carefully analyzed for each project, taking into account the real exposure conditions of the façade to avoid any oversizing or over restriction.

Finally, aging and the use of non-winged screws have been demonstrated to be beneficial to the façade performance improvement. The natural aging has increased the mechanical strength, improving the board performance. On the other hand, the use of non-winged screws has raised the safety factor in all configurations where the pull-trough is the limiting factor. This connector capacity increasing has validated the use of the 400mm x 300mm and the 400mm x 400mm façade configurations whatever the hygrothermal condition.

CONCLUSIONS

General remarks

The lightweight façades have been gradually implemented in the Construction Industry. In Brazil, in particular, a clear definition of technical requirements is needed to ensure the mechanical performance of the façade system. The development of specific assessment tools can help and support these new developments, providing reliability and optimization. The proposal of a scientific methodology to evaluate façades helps increase the market confidence in these new systems, whilst contributing to promote sustainability, by improving the productivity and the quality of civil constructions in Brazil and around the world.

A system evaluation demands the description of the components and their combined behavior. Predictive models have been proposed to assess the system performance, preventing cracking, large-displacements and pullout. This work proposes the definition of a design framework based on numerical models to assess the mechanical performance of lightweight façades in high buildings. This framework defines a set of requirements for global and local performance analysis, ensuring both ULS and SLS limit states design. The criteria are related to structural strength, to the metal frame and board behavior, and to the fixing design.

The definition of each requirement has been explored through a literature review, international standards comparison, numerical modeling and experimental tests. The framework has been particularly validated for the case of a 30-floor building façade. This work has focused on the analysis of a façade playing the role of the building envelope, and composed by the metal frame, the external fiber cement-boards and their fixing systems. No joint treatment and no monolithic rendering or coating were considered in this work. In addition, this study contributes to different areas such as: the characterization of fiber cement boards before and after aging; the numerical modeling of non-linear cracking process using different numerical techniques or even the definition of appropriated wind loads to be considered in a façade design project.

Wind loads

For high-building application, the wind load has been defined as the main action to be considered for the façade design, with its worst effect in suction. Moreover, local wind effects can generate more important loads imposed on the smaller façades

components, such as the connectors. Compared to other international standards, the Brazilian standard has been the only one that does not present a clear differentiation of global and local wind effects, generating a less conservative wind load prediction. To mitigate this gap, this study has proposed a slight increasing in the Brazilian S_3 factor, whose nomenclature was adopted as the importance factor, for the local design load definition for façades. In addition, a safety factor of 1,4 has been adopted for the ULS analyses, whilst 0,8 has been defined as the SLS wind load factor. Therefore, the design loads for a 30-floor building façade case have been defined varying from 3,5 kPa for local ULS assessment to 1,8 for the global SLS evaluation, considering a critical case of wind suction combined with a high internal pressure coefficient.

Fiber cement boards

A detailed description of the fiber cement material has been presented. An overview of its production process and its theoretical constitutive behavior has been provided to demonstrate the main mechanisms and interactions that are expected to be represented in a numerical model. This theoretical description has been completed by the experimental characterization of the mechanical behavior of the boards. This experimental methodology has shown the influence of the hygrothermal content on the board behavior. The results have indicated that wetting causes a board strength reduction, whereas it increases the material toughness.

A durability analysis has also been proposed to verify the mechanical behavior evolution of the boards over time. It has been demonstrated that after 3 years of natural exposition, the fiber cement boards presented a significant increase of strength, despite showing a ductility reduction. Nevertheless, a chemical analysis has been applied, and verified that the natural exposed sample was not fully carbonated yet, meaning that the natural aging process still continued even after 3 years of the fiber cement exposure. Finally, the shrinkage magnitude related to the combined carbonation and drying processes has been reported. The irreversible shrinkage can reach more than 5mm/m, whilst the reversible process represents around 2mm/m. The combination of both processes have been crucial to be considered in the board fixing design, in order to mitigate and reduce cracking risks. However, it has to be highlighted that the analyses were done without considering any joint treatment or monolithic coating. In the case of designs including closed joints and coatings, it is recommended

to assess the behavior of those materials, specially their elasticity and their ability to accommodate the moisture movement of the boards. Special designs or formulations may be required for the joints and coatings in case of high dimensional variation values.

Aiming to simulate the mechanical behavior of this fiber cement material, three different numerical models have been tested and calibrated using the available formulations in the software ABAQUS. These models have shown how the different damage criteria and cracking simulation techniques can be used to represent the fiber cement behavior. The XFEM technique associated to a maximum stress damage criterion and a bi-linear cohesive zone model has provided acceptable results to predict the flexural behavior of the board, with a good agreement with the experimental data, even in the softening post-peak behavior. The same satisfactory results have been obtained using the Hashin model. However, none of those models have been able to capture the hardening post-peak, since their original crack propagation bi-linear formulation is based on linear elastic fracture mechanics. This gap has been mainly highlighted in the direct tensile test modeling.

Indeed, the CDP model has proved to be the best indicated technique to represent the fiber cement behavior without the need of a discrete fiber modeling within the material. The use of the CDP formulation has provided positive results for the flexural and for the direct tensile board behavior, showing a good fit for both softening and hardening post-peaks. The inconvenience of this technique is that it demands more data than the others, such as some stress versus strain points to describe the elastic and the pseudo-plastic behaviors.

Finally, it has been observed that the material strength defined by numerical models calibration is close to the values obtained experimentally. In the case of the 3-point bending test, this assumption is true if using the LOP value as the material parameter for design. This result evidences that the MOR parameter, calculated as defined by several country standards, cannot be used for design purposes nor to predict the mechanical performance of the material. Since those equations are based on linear and non-damaged assumptions, they are limited until the LOP point. After this point, cracking is initiated and the material is no more linear or elastic. The MOR can, indeed, be used as a standard reference parameter to compare different boards, but it cannot be used for design purposes, since it is not a proper material parameter.

Fixing system

A numerical study has been proposed to verify the minimum edge distances of fasteners that have to be respected to avoid cracking due to shrinkage. It has been demonstrated that the combination of an adequate pre-drilling and minimum edge distances is necessary to roughly reduce and mitigate cracking risks.

The pullout of the fixings has been assessed by an experimental methodology that characterized the pull-tough behavior of two self-drilling screws. The screw without wing has shown a bigger strength, despite being a more stiffened connector.

For each screw, a proper numerical model has been calibrated. A linear model has been proven to be sufficient to represent the winged connector, whilst a curvilinear model has been verified to be appropriate to simulate the non-winged screw pullout.

Façade model

The façade design parameters have been finally verified through a numerical analysis that is able to simulate the complete system behavior, including the board description and the connectors modeling. Different numerical routines have been created to simulate and to validate the façades parameters. For example, the numerical analysis has confirmed the choice of LSF stud profiles of 200 x 40 x 12 x 0,95 spaced at each 400mm or 200 x 40 x 12 x 1,25 at each 600mm to ensure the structural performance of a 30-floor building façade.

Regarding the other parameters, it has been demonstrated that the choice of studs spaced at each 600mm is not indicated due to the risk of the failure of the external board. Moreover, using the 400mm-stud configuration, the simulations have shown that the screw distance must be limited to 400mm at the most. If this distance is reduced to 300mm, the safety pullout factor increases from 1,05 to 1,28.

In addition, it has been proven that the aging and the use of non-winged screws, combined with a pre-drilling process, can improve the mechanical performance of the façade. In this particular case, the suggested configuration ensures a proper façade system behavior, even in the most critical hygrothermal conditions, such as in a wetting case with a fully-saturated board.

Final statement

It has been confirmed that the proposed numerical modeling strategy is able to simulate materials, connectors and the global façade behavior. The tools that have been created will help verify all the requirements of the framework suggested in this work. This way, a clear description and an operational strategy have been presented and validated to assess the mechanical behavior of a lightweight façade, allowing to optimize its design and to ensure its performance.

However, all conclusions were drawn based on ideal conditions, in order to illustrate and to validate the applicability of the proposed assessment framework. It means that any imperfection, such as geometrical misalignments, fixing eccentricities or even the material variability, can create boundary conditions or loads that were not considered in this work. A rigorous quality control of the construction process is crucial to mitigate or avoid those imperfections. The number of variables and the use of manual work, instead of industrialized processes, hind this quality controlling, though. For this reason, each project has to be verified considering its particularities and the extrapolation of any conclusion demands a careful analysis or even a complementation from future researches.

Suggestions for future researches

As a complex subject, the study of a constructive system includes a lot of materials and different areas to be explored. In this work, the scope was limited by the numerical analysis of some of the façades components, such as the external board, the connectors and the structural frame. For this reason, in some areas of knowledge, only a few of initial inputs have been provided. Among those topics, it could be further examined in future works:

- The impact of imperfections, such as fixing eccentricities, and material variability on the mechanical performance of the façade system;
- The characterization of the joints and the coating behavior, including their numerical modeling, the definition of basic requirements and the validation of a design guidance for the different applications (closed joints, monolithic basecoats, etc.);
- The impact of thermal variation on the façade system, considering thermal cycles of heating and cooling;

- The optimization of the internal pressure coefficients recommended for residential buildings, through experimental and numerical analysis;
- The development of a numerical model for the fiber cement board considering its multi-layer composition, the real fiber orientation and the delamination risk;
- The validation of other numerical modeling strategies, such as the use of a discrete fiber representation, tri and multilinear cohesive models to simulate the fiber cement behavior;
- The refinement of the carbonation curve and the carbonation rate, by correlating accelerated aging in laboratory to natural aging over time;
- The instrumentation and monitoring of a real façade prototype to measure the reversible and irreversible dimensional variations;
- The experimental characterization of other connectors to increase the list of available screws, and to include the assessment of the shear behavior of the fixings and the combined effect of bending and traction;
- The analysis of larger façade panels to design joints and inserts;
- The fire safety risk assessment of façades systems, to define the main requirements, to identify the critical components and to propose optimized solutions to mitigate the risk.

REFERENCES*

- 1 **BARROS, M. M. B. D.; SABBATINI, F. H. Diretrizes para o processo de projeto para a implantação de tecnologias construtivas racionalizadas na produção de edifícios.** EPUSP. São Paulo, p.24. 2003
- 2 **FGV/IBRE. Produtividade na Construção.** Sinduscon SP. São Paulo. 2015
- 3 **CARDOSO, S. S. Tecnologia construtiva de fachada em chapas delgadas estruturadas em light steel framing.** 2016. (Master's dissertation). Universidade de São Paulo, São Paulo.
- 4 **ROCHA, A. C. D. Análise comparativa de planejamento e custo de fachadas de edifício de múltiplos pavimentos com as tecnologias tradicional e com chapas delgadas estruturadas em light steel framing.** 2017. (Master's dissertation). Universidade de São Paulo, São Paulo.
- 5 **SAINT-GOBAIN. Internal Report: Design Thinking - Projeto Fachadas.** Saint-Gobain. São Paulo. 2017
- 6 **CARVALHO, J. C. Estudo comparativo entre fachadas em alvenaria de bloco cerâmico revestidas com argamassa e fachadas executadas com placas cimentícias.** 2015. (Undergraduation project). Universidade Federal do Rio de Janeiro, Rio de Janeiro.
- 7 **ANTUNES, G. R. Estudo de Manifestações Patológicas em Revestimento de Fachada em Brasília - Sistematização da Incidência de Casos.** 2010. (Master's degree). Departamento de Engenharia Civil e Ambiental, Universidade de Brasília, Brasília.
- 8 **CENTRO BRASILEIRO DE CONSTRUÇÃO EM AÇO. Cenário dos fabricantes de perfis galvanizados para light steel frame e drywall.** 2018
- 9 **HANDA, D. K. C. Identificação das principais manifestações patológicas em fachadas em chapas delgadas estruturadas em light steel framing - estudos de caso.** 2019. (Master). Faculdade de Engenharia Civil, Arquitetura e Urbanismo, Universidade Estadual de Campinas, Unicamp.
- 10 **BEVILAQUA, R. Estudo comparativo do desempenho estrutural de prédios estruturados em perfis formados a frio segundo os sistemas aporticado e light steel framing.** 2005. (Master's dissertation). Universidade Federal de Minas Gerais, Belo Horizonte.

* according to the numbered model of ABNT NBR 6023:2018²¹²

- 11 STEEL CONSTRUCTION INSTITUTE. **Residential Buildings - Guidance for Architects, Designers & Constructors**. SCI, 2008.
- 12 EUROPEAN LIGHT STEEL CONSTRUCTION ASSOCIATION. **European lightweight steel-framed construction**. Bruxelles: Arcelor, 2005.
- 13 LAWSON, R. M. **Light steel modular construction (ED014)**. 2012
- 14 STEEL ALLIANCE. **Multi-storey steel buildings. Part 2: Concept design**. 2008.
- 15 OLIVIERI, H. et al. Adopting new construction systems to reduce the use of resources in construction sites: light steel framing. **Ambiente Construído**, v. 17, n. 4, p. 45-60, 2017.
- 16 TAVAKOLI, D. B. et al. Investigation of LSF structure effect on economy and sustainable housing in Iran. Case study: 50m² units. **Review of European Studies**, v. 9, n. 3, p. 30-35, 2017.
- 17 YANDZIO, E.; LAWSON, R. M.; WAY, A. G. J. **Light steel framing in residential construction**. Berkshire: SCI, 2015.
- 18 SANTIAGO, A. K.; FREITAS, A. M. S.; CRASTO, R. C. M. D. **Steel framing: Arquitetura**. 2nd. Rio de Janeiro: Instituto Aço Brasil / CBCA, 2012.
- 19 BARREIROS, T. S. **Modelagem numérica de forças de vento em painéis de fechamento não estruturais para edifícios de múltiplos pavimentos**. 2013. (Master's dissertation). Instituto de Pesquisas Tecnológicas do Estado de São Paulo, São Paulo.
- 20 OLIVEIRA, L. A. D. **Metodologia para desenvolvimento de projeto de fachadas leves**. 2009. (PhD thesis). Universidade de São Paulo, São Paulo.
- 21 EOTA - EUROPEAN ORGANISATION FOR TECHNICAL ASSESSMENT. **EAD 090119-00-0404: Kits for external wall claddings of mineral boards with renderings applied in-situ**. Brussels: EOTA: 81 p. 2018.
- 22 _____. **EAD 090062-00-0404: Kits for external wall claddings mechanically fixed**. Brussels: EOTA: 81 p. 2018.
- 23 _____. **EAD 090129-00-0404: Kits for non-load bearing mineral board external wall systems**. Brussels: EOTA: 82 p. 2018.

- 24 _____ . **EAD 090019-00-0404: Kits for ventilated external wall claddings of lightweight boards on subframe with rendering applied in situ with or without thermal insulation.** Brussels: EOTA: 63 p. 2016.
- 25 _____ . **EAD 040089-00-0404: ETICS with renderings for the use on timber frame buildings.** Brussels: EOTA: 66 p. 2016.
- 26 DUBEY, A.; REICHERTS, J. **Lighthweight cement boards in exterior wall construction and finish systems.** 6th RILEM Symposium on Fibre-Reinforced Concretes. Varenna, Italy, 2004. 477-492 p.
- 27 ABNT - ASSOCIAÇÃO BRASILEIRA DE NORMAS TÉCNICAS. **ABNT NBR 15253: Perfis de aço formados a frio, com revestimento metálico, para painéis estruturais reticulados em edificações - Requisitos gerais.** Rio de Janeiro: ABNT: 30 p. 2014.
- 28 _____ . **ABNT NBR 7008: Chapas e bobinas de aço revestidas com zinco ou liga zinco-ferro pelo processo contínuo de imersão a quente.** Rio de Janeiro: ABNT: 14 p. 2012.
- 29 _____ . **ABNT NBR 14762: Dimensionamento de estruturas de aço constituídas por perfis formados a frio.** Rio de Janeiro: ABNT: 93 p. 2010.
- 30 _____ . **ABNT NBR 6355: Perfis estruturais de aço formados a frio - Padronização.** Rio de Janeiro: ABNT: 36 p. 2012.
- 31 RODRIGUES, F. C.; CALDAS, R. B. **Steel framing: Engenharia.** Rio de Janeiro: IBS / CBCA, 2016.
- 32 AMERICAN IRON AND STEEL INSTITUTE. **Design example for analytical modeling of a curtainwall and considering the effects of bridging.** AISI. Washington, USA. 2018
- 33 LANG, J.; NAUJOKS, B. Behaviour of cold-formed steel shear walls under horizontal and vertical loads. **Thin-Walled Structures**, v. 44, p. 1214-1222, 2006.
- 34 ABNT - ASSOCIAÇÃO BRASILEIRA DE NORMAS TÉCNICAS. **ABNT NBR 15498: Placa de fibrocimento sem amianto - Requisitos e métodos de ensaio.** Rio de Janeiro: ABNT: 29 p. 2015.
- 35 KNAUF. **Build exterior walls faster using drylining methods.** KNAUF 2011.
- 36 STOPANEL. **Application Guide.** STOCORP 2019.

- 37 DAVENPORT, A. G. **Note on the distribution of the largest value of a random function with application to gust loading.** Proceedings of the Institution of Civil Engineers, 1964. 187-196 p.
- 38 MAYNE, J. R. The estimation of extreme winds. **Journal of Industrial Aerodynamics**, v. 5, p. 109-137, 1979.
- 39 HOLMES, J. D. **Wind Loading of Structures.** 3rd. New York, USA: CRC Press, 2017.
- 40 PALUTIKOF, J. P. et al. A review of methods to calculate extreme wind speeds. **Meteorological Applications**, v. 6, p. 119-132, 1999.
- 41 TIELEMAN, H. W. et al. Extreme value distributions for peak pressure and load coefficients. **Journal of Wind Engineering and Industrial Aerodynamics**, v. 96, p. 1111-1123, 2008.
- 42 MOONEGHI, M. A. **Experimental and analytical methodologies for predicting peak loads on building envelopes and roofing systems.** 2014. (PhD thesis). Florida International University, Miami, USA.
- 43 PENG, X. et al. A comparison of methods to estimate peak wind loads on buildings. **Journal of Wind Engineering and Industrial Aerodynamics**, v. 126, p. 11-23, 2014.
- 44 GEURTS, C. P. W.; STAALDUINEN, P. C. V.; WIT, M. S. D. Towards a reliable design of facade and roof elements against wind loading. **Heron Journal**, v. 49, n. 2, p. 171-187, 2004.
- 45 IRWIN, P.; DENOON, R.; SCOTT, D. **Wind tunnel testing of high-rise buildings: An output of the CTBUH Wind Engineering Work Group.** Council on Tall Buildings and Urban Habitat. Chicago, USA. 2013
- 46 DAVENPORT, A. G. Chapter 12. In: PLATE, E. J. (Ed.). **Engineering Meteorology: Fundamentals of Meteorology and their Application to Problems in Environmental and Civil Engineering.** Oxford: Elsevier, 1982. cap. 12,
- 47 FERRARETO, J. A. **Human comfort in tall buildings subjected to wind-induced motion.** 2017. (PhD thesis). Universidade de São Paulo, São Paulo.
- 48 GEURTS, C. P. W. **Wind-induced pressure fluctuations on building facades.** 1997. (PhD thesis). Eindhoven University of Technology, Eindhoven, Netherlands.

- 49 GONCALVES, R. M. et al. **Ações do vento nas edificações - Teoria e Exemplos**. São Carlos: SET/EESC/USP, 2007. 138
- 50 ZHOU, Y.; KIJEWski, T.; KAREEM, A. Along-wind load effects on tall buildings: comparative study of major international codes and standards. **Journal of Structural Engineering**, v. 128, n. 6, p. 788-796, 2002.
- 51 IRWIN, P. Pressure model techniques for cladding loads. **Journal of Wind Engineering and Industrial Aerodynamics**, v. 29, p. 69-78, 1988.
- 52 LOU, W. et al. Experimental and zonal modeling for wind pressures on double-skin façades of a tall building. **Energy & Buildings**, v. 54, p. 179-191, 2012.
- 53 JENDZELOVSKY, N.; ANTAL, R.; KONECNA, L. Investigation of the external pressure coefficients on the facade of the triangular high-rise structure with curved corners. **Procedia Engineering**, v. 190, p. 398-405, 2017.
- 54 YUAN, K.; HUI, Y.; CHEN, Z. Effects of facade appurtenances on the local pressure of high-rise buildings. **Journal of Wind Engineering and Industrial Aerodynamics**, v. 178, p. 26-37, 2018.
- 55 KOPP, G. A.; SURRY, D.; MANS, C. Wind effects of parapets on low buildings: Part 1. Basic aerodynamics and local loads. **Journal of Wind Engineering and Industrial Aerodynamics**, v. 93, p. 817-841, 2005.
- 56 HABTE, F.; CHOWDHURY, A. G.; ZISIS, I. Effect of wind-induced internal pressure on local frame forces of low-rise buildings. **Engineering Structures**, v. 143, p. 455-468, 2017.
- 57 HOLMES, J. D. **Mean and fluctuating internal pressures induced by wind**. 7th Asia-Pacific Symposium on Wind Engineering. Taipei, Taiwan, 1979. 435-450 p.
- 58 HOLMES, J. D.; GINGER, J. D. Internal pressures - The dominant windward opening case - A review. **Journal of Wind Engineering and Industrial Aerodynamics**, v. 100, p. 70-76, 2012.
- 59 GERHARDT, H. J.; JANSER, F. Wind loads on wind permeable facades. **Journal of Wind Engineering and Industrial Aerodynamics**, v. 53, p. 37-48, 1994.
- 60 VICKERY, B. J. Internal pressure and interactions with the building envelope. **Journal of Wind Engineering and Industrial Aerodynamics**, v. 53, p. 125-144, 1994.

- 61 BESTE, F.; CERMAK, J. E. Correlation of internal and area-averaged external wind pressures on low-rise buildings. **Journal of Wind Engineering and Industrial Aerodynamics**, v. 69-71, p. 557-566, 1997.
- 62 IRWIN, P.; SIFTON, V. L. Risk considerations for internal pressures. **Journal of Wind Engineering and Industrial Aerodynamics**, v. 77-78, p. 715-723, 1998.
- 63 KARAVA, P.; STATHOPOULOS, T. **Wind-induced internal pressures in buildings with large façade openings**. 11th Americas Conference on Wind Engineering. San Juan, Porto Rico 2009.
- 64 KIJEWSKI, T.; KAREEM, A. Dynamic wind effects: a comparative study of provisions in codes and standards with wind tunnel data. **Wind and Structures**, v. 1, n. 1, p. 77-109, 1998.
- 65 HOLMES, J. D.; TAMURA, Y.; KRISHNA, P. **Comparison of wind loads calculated by fifteen different codes and standards for low, medium and high-rise buildings**. 11th Americas Conference on Wind Engineering. San Juan, Porto Rico 2009.
- 66 ABNT - ASSOCIAÇÃO BRASILEIRA DE NORMAS TÉCNICAS. **ABNT NBR 6123: Forças devidas ao vento em edificações**. Rio de Janeiro: ABNT: 69 p. 1988.
- 67 ASCE - AMERICAN SOCIETY OF CIVIL ENGINEERS. **ASCE 7-10: Minimum design loads for buildings and other structures**. Reston, VA, USA: ASCE: 658 p. 2010.
- 68 STANDARDS AUSTRALIA LIMITED; STANDARDS NEW ZEALAND. **Structural design actions. Part 2: Wind actions**. Sydney, AU / Wellington, NZ: SAI Global Limited and Standards New Zealand: 101 p. 2011.
- 69 CEN - COMITÉ EUROPÉEN DE NORMALISATION. **EC 1-1-4: Actions sur les strucutres. Actions générales - Actions du vent**. Saint-Denis, FR: AFNOR: 124 p. 2005.
- 70 SIMIU, E.; FILLIBEN, J. J. Wind direction effects on cladding and structural loads. **Engineering Structures**, v. 3, p. 181-186, 1981.
- 71 SHARMA, R. N.; RICHARDS, P. J. Net pressure on the roof of a low-rise building with wall openings. **Journal of Wind Engineering and Industrial Aerodynamics**, v. 93, p. 267-291, 2005.

- 72 SARKISIAN, M. **Designing tall buildings: structure as architecture**. New York, USA: Routledge, 2012.
- 73 ABNT - ASSOCIAÇÃO BRASILEIRA DE NORMAS TÉCNICAS. **ABNT NBR 15575-4: Edificações habitacionais - Desempenho. Parte 4: Requisitos para os sistemas de vedações verticais internos e externos - SVVIE**. Rio de Janeiro: ABNT: 75 p. 2013.
- 74 BENTUR, A.; MINDESS, S. **Fibre reinforced cementitious composites**. New York, USA: Taylor & Francis, 2007.
- 75 MOBASHER, B. **Mechanics of fiber and textile reinforced cement composites**. Florida, USA: CRC Press, 2012.
- 76 LI, V. C. From micromechanics to structural engineering - the design of cementitious composites for civil engineering applications. **Journal of Structural Mechanics and Earthquake Engineering**, v. 10, n. 3, p. 37-48, 1993.
- 77 LIN, Z.; LI, V. C. Crack bridging in fiber reinforced cementitious composites with slip-hardening interfaces. **Journal of the Mechanics and Physics of Solids**, v. 45, n. 5, p. 763-787, 1997.
- 78 LI, V. C.; WANG, S.; WU, C. Tensile strain-hardening behavior of polyvinyl alcohol engineered cementitious composite (PVA-ECC). **ACI Materials Journal**, v. 98, n. 6, p. 483-492, 2001.
- 79 ARDANUY, M.; CLARAMUNT, J.; FILHO, R. D. T. Cellulosic fiber reinforced cement-based composites: A review of recent research. **Construction and Building Materials**, v. 79, p. 115-128, 2015.
- 80 IKAI, S. et al. Asbestos-free technology with new high toughness polypropylene (PP) fibers in air-cured Hastchek process. **Construction and Building Materials**, v. 24, p. 171-180, 2010.
- 81 ALHOZAIMY, A. M.; SOROUSHIAN, P.; MIRZA, F. Mechanical properties of polypropylene fiber reinforced concrete and the effects of pozzolanic materials. **Cement and Concrete Composites**, v. 18, p. 85-92, 1996.
- 82 LI, V. C. On Engineered Cementitious Composites (ECC) - A review of the material and its applications. **Journal of Advanced Concrete Technology**, v. 1, n. 3, p. 215-230, 2003.

- 83 KUDER, K. G.; SHAH, S. P. Processing of high-performance fiber-reinforced cement-based composites. **Construction and Building Materials**, v. 24, p. 181-186, 2010.
- 84 HYER, M. **Stress Analysis of Fiber-Reinforced Composite Materials**. Lancaster, USA: DEStech Publication, Inc., 2009.
- 85 BERTHELOT, J.-M. **Mécanique des matériaux et structures composites**. Le Mans, France: Institut Supérieur des Matériaux et Mécanique Avancés - IMANS, 2010.
- 86 GÜRDAL, Z.; HAFTKA, R. T.; HAJELA, P. **Design and optimization of laminated composite materials**. New York, USA: John Wiley & Sons, 1999.
- 87 LI, V. C.; WU, H. C. Pseudo strain-hardening design in cementitious composites. In: REINHARDT, H. W. e NAAMAN, A. E. (Ed.). **High Performance Fiber Reinforced Cement Composites**. London, UK: E&FN Spon, 1992. p.371-387.
- 88 _____. Conditions for pseudo strain-hardening in fiber reinforced brittle matrix composites. **Applied Mechanics Review**, v. 45, n. 8, p. 390-398, 1992.
- 89 LI, V. C.; LEUNG, C. K. Y. Steady-state and multiple cracking of short random fiber composites. **Journal of Engineering Mechanics**, v. 118, n. 11, p. 2246-2264, 1992.
- 90 LI, V. C. Engineered Cementitious Composites (ECC) - Material, Structural and Durability Performance. In: NAWY, E. (Ed.). **Concrete Construction Engineering Handbook**: CRC Press, 2008.
- 91 LI, V. C.; STANG, H. Interface property characterization and strengthening mechanisms in fiber reinforced cement based composites. **Advanced Cement Based Materials**, v. 6, p. 1-20, 1997.
- 92 SINGH, S.; SHUKLA, A.; BROWN, R. Pullout behavior of polypropylene fibers from cementitious matrix. **Cement and Concrete Research**, v. 34, p. 1919-1925, 2004.
- 93 FERREIRA, S. R. et al. Influence of natural fibers characteristics on the interface mechanics with cement based matrices. **Composites Part B**, v. 140, p. 183-196, 2018.
- 94 ANDERSON, T. L. **Fracture Mechanics Fundamentals and Applications**. Boca Raton, FL: CRC Press, 1995.

- 95 DUGDALE, D. S. Yielding of steel sheets containing slits. **Journal of the Mechanics and Physics of Solids**, v. 8, p. 100-104, 1960.
- 96 HILLERBORG, A.; MODEER, M.; PETERSSON, P. E. Analysis of crack formation and crack growth in concrete by means of fracture mechanics and finite elements. **Cement and Concrete Research**, v. 6, p. 773-782, 1976.
- 97 HILLERBORG, A. The theoretical basis of a method to determine the fracture energy (G_f) of concrete. **Materials and Structures**, v. 18, p. 291-296, 1985.
- 98 LI, V. C. Applicability of J-integral to tension-softening materials. **Journal of Engineering Mechanics**, v. 123, n. 5, p. 531-533, 1997.
- 99 YANG, E.-H. et al. Fiber-bridging constitutive law of Engineered Cementitious Composites. **Journal of Advanced Concrete Technology**, v. 6, n. 1, p. 181-193, 2007.
- 100 YANG, E.-H.; LI, V. C. Strain-hardening fiber cement optimization and component tailoring by means of a micromechanical model. **Construction and Building Materials**, v. 24, p. 130-139, 2010.
- 101 LI, V. C.; CHAN, C.-H.; LEUNG, C. K. Y. Experimental determination of the tension-softening relations for cementitious composites. **Cement and Concrete Research**, v. 17, p. 441-452, 1987.
- 102 WANG, Y.; LI, V. C.; BACKER, S. Tensile properties of synthetic fiber reinforced mortar. **Cement and Concrete Composites**, v. 12, p. 29-40, 1990.
- 103 LI, V. C.; MAALEJ, M.; HASHIDA, T. Experimental determination of the stress-crack opening relation in fibre cementitious composites with a crack-tip singularity. **Journal of Materials Science**, v. 29, p. 2719-2724, 1994.
- 104 RILEM. **Determination of the fracture energy of mortar and concrete by means of three-point bend tests on notched beams.** RILEM Recommendations for the Testing and Use of Construction Materials: E & FN SPON: 99 - 101 p. 1985.
- 105 HOUANG, P. et al. **Fiber cement: corrugated sheets for roofing and flat panels using new polymeric fibers.** Composites in Construction. HAMELIN. Lyon, France 2005.
- 106 DIAS, C. M. R.; SAVASTANO JR., H.; JOHN, V. M. Exploring the potential of functionally graded materials concept for the development of fiber cement. **Construction and Building Materials**, v. 24, p. 140-146, 2010.

- 107 CEN - COMITÉ EUROPÉEN DE NORMALISATION. **EN 12467: Fibre-cement flat sheets - Product specification and test methods**. London, UK: BSI Standards Limited: 68 p. 2012.
- 108 SASMAL, S.; AVINASH, G. Investigations on mechanical performance of cementitious composites micro-engineered with poly vinyl alcohol fibers. **Construction and Building Materials**, v. 128, p. 136-147, 2016.
- 109 DIAS, C. M. R. **Fibrocimentos com gradação funcional**. 2011. (PhD). Escola Politécnica, Universidade de São Paulo, São Paulo.
- 110 MECHTCHERINE, V. et al. Coupled strain rate and temperature effects on the tensile behavior of strain-hardening cement-based composites (SHCC) with PVA fibers. **Cement and Concrete Research**, v. 42, p. 1417-1427, 2012.
- 111 COUTTS, R. S. P.; KIGHTLY, P. Bonding in wood fibre–cement composites. **Journal of Materials Science**, v. 19, p. 3355-3359, 1984.
- 112 LIMA, P. R. L.; FILHO, R. D. T.; LIMA, J. M. F. Mecanismo de fissuração sob tração direta de compósitos cimentícios reforçados com fibras curtas de sisal. **ENGEVISTA**, v. 15, n. 1, p. 95-103, 2013.
- 113 TRAN, T. K.; KIM, D. J. Investigating direct tensile behavior of high performance fiber reinforced cementitious composites at high strain rates. **Cement and Concrete Research**, v. 50, p. 62-73, 2013.
- 114 CHOI, J.-I. et al. Ultra-high-ductile behavior of a polyethylene fiber-reinforced alkali-activated slag-based composite. **Cement and Concrete Composites**, v. 70, p. 153-158, 2016.
- 115 YU, K.-Q. et al. Development of ultra-high performance engineered cementitious composites using polyethylene (PE) fibers. **Construction and Building Materials**, v. 158, p. 217-227, 2018.
- 116 YU, K. et al. Direct tensile properties of engineered cementitious composites: A review. **Construction and Building Materials**, v. 165, p. 346-362, 2018.
- 117 BENOUIS, A. **Comportement mécanique des ouvrages en plaques de plâtre sur ossature métallique**. 1995. (PhD thesis). Ecole nationale des ponts et chaussées, Paris.
- 118 SORANAKOM, C.; MOBASHER, B. Correlation of tensile and flexural responses of strain softening and strain hardening cement composites. **Cement and Concrete Composites**, v. 30, p. 465-477, 2008.

- 119 TAILHAN, J.-L.; ROSSI, P.; BOULAY, C. Tensile and bending behaviour of a strain hardening cement-based composite: Experimental and numerical analysis. **Cement and Concrete Composites**, v. 34, p. 166-171, 2012.
- 120 MAJUMDAR, A. J.; LAWS, V. Composite materials based on cement matrices. **Philosophical Transactions of the Royal Society of London. Series A, Mathematical and Physical Sciences.**, v. 310, n. 1511, p. 191-202, 1983.
- 121 XU, P. et al. Fracture Energy Analysis of Concrete considering the Boundary Effect of Single-Edge Notched Beams. **Advances in Civil Engineering**, p. 1-10, 2018.
- 122 BENTUR, A.; AKERS, S. A. S. The microstructure and ageing of cellulose fibre reinforced autoclaved cement composites. **International Journal of Cement Composites and Lightweight Concrete**, v. 11, n. 2, p. 111-115, 1989.
- 123 _____. The microstructure and ageing of cellulose fiber reinforced cement composites cured in a normal environment. **International Journal of Cement Composites and Lightweight Concrete**, v. 11, n. 2, p. 99-109, 1989.
- 124 WEI, J.; MEYER, C. Degradation mechanisms of natural fiber in the matrix of cement composites. **Cement and Concrete Research**, v. 73, p. 1-16, 2015.
- 125 CEFERINO, G. E. U. **Accelerated carbonation: a study of the parameters, mineral additions effect, type cellulosic pulp and durability in fiber-cement**. 2016. (PhD). Faculdade de Zootecnia e Engenharia de Alimentos, Universidade de São Paulo, Pirassununga.
- 126 WEI, J.; MEYER, C. Degradation rate of natural fiber in cement composites exposed to various accelerated aging environment conditions. **Corrosion Science**, v. 88, p. 118-132, 2014.
- 127 HANNANT, D. J. Durability of polypropylene fibers in portland cement-based composites: eighteen years of data. **Cement and Concrete Research**, v. 28, n. 12, p. 1809-1817, 1998.
- 128 AGOPYAN, V. et al. Developments on vegetable fibre-cement based materials in São Paulo, Brazil: an overview. **Cement and Concrete Composites**, v. 27, p. 527-536, 2005.
- 129 AHMED, S. F. U.; MIHASHI, H. A review on durability properties of strain hardening fibre reinforced cementitious composites (SHFRCC). **Cement and Concrete Composites**, v. 29, p. 365-376, 2007.

- 130 SILVA, F. D. A. et al. Physical and mechanical properties of durable sisal fiber-cement composites. **Construction and Building Materials**, v. 24, p. 777-785, 2010.
- 131 TONOLI, G. H. D. et al. Effect of accelerated carbonation on cementitious roofing tiles reinforced with lignocellulosic fibre. **Construction and Building Materials**, v. 24, p. 193-201, 2010.
- 132 SOROUSHIAN, P.; WON, J.-P.; HASSAN, M. Durability characteristics of CO₂-cured cellulose fiber reinforced cement composites. **Construction and Building Materials**, v. 34, p. 44-53, 2012.
- 133 PIZZOL, V. D. et al. Effect of accelerated carbonation on the microstructure and physical properties of hybrid fiber-cement composites. **Minerals Engineering**, v. 59, p. 101-106, 2014.
- 134 WEI, J.; MA, S.; THOMAS, D. S. G. Correlation between hydration of cement and durability of natural fiber-reinforced cement composites. **Corrosion Science**, v. 106, p. 1-15, 2016.
- 135 AKERS, S. A. S.; STUDINKA, J. B. Ageing behaviour of cellulose fibre cement composite in natural weathering and accelerated tests. **International Journal of Cement Composites and Lightweight Concrete**, v. 11, n. 2, p. 93-97, 1989.
- 136 MACVICAR, R.; MATUANA, L. M.; BALATINECZ, J. J. Aging mechanisms in cellulose fiber reinforced cement composites. **Cement and Concrete Composites**, v. 21, p. 189-196, 1999.
- 137 SOROUSHIAN, P. et al. Development of accelerated processing techniques for cement-bonded wood particleboard. **Cement and Concrete Composites**, v. 25, p. 721-727, 2003.
- 138 YILDIRIM, G. et al. Self-healing performance of aged cementitious composites. **Cement and Concrete Composites**, v. 87, p. 172-186, 2018.
- 139 SOUZA, R. B. D. **Estudo da retração em fibrocimento reforçado com fibra polimérica**. 2014. (PhD). Escola Politécnica, Universidade de São Paulo, São Paulo.
- 140 DIAS, C. M. R. et al. Long-term aging of fiber-cement corrugated sheets - The effect of carbonation, leaching and acid rain. **Cement and Concrete Composites**, v. 30, p. 255-265, 2008.

- 141 MINDESS, S.; YOUNG, J. F.; DARWIN, D. **Concrete**. New Jersey, USA: Prentice Hall, 2002.
- 142 CSTB. **Traité de physique du bâtiment. Tome 2: Mécanique des ouvrages**. Paris, FR: CSTB, 1999. 484
- 143 SAINT-GOBAIN BRASILIT. **Fiber cement boards benchmarking**. Internal report. 2016
- 144 MATSUMOTO, T. et al. Uniaxial tension–compression fatigue behavior and fiber bridging degradation of strain hardening fiber reinforced cementitious composites. **International Journal of Fatigue**, v. 32, p. 1812-1822, 2010.
- 145 HOFSTETTER, G.; MESCHKE, G. **Numerical Modelling of Concrete Cracking**. Udine, Italy: International Centre for Mechanical Sciences, 2011.
- 146 TEJCHMAN, J.; BOBINSKI, J. **Continuous and discontinuous modelling of fracture in concrete using FEM**. New York: Springer, 2013.
- 147 HUANG, T.; ZHANG, Y. X.; YANG, C. Multiscale modelling of multiple-cracking tensile fracture behaviour of engineered cementitious composites. **Engineering Fracture Mechanics**, v. 160, p. 52-66, 2016.
- 148 LU, C.; LEUNG, C. K. Y.; LI, V. C. Numerical model on the stress field and multiple crackinh behavior of Engineered Cementitious Composites (ECC). **Construction and Building Materials**, v. 133, p. 118-127, 2017.
- 149 LANÇIONI, G.; ALESSI, R. Modeling micro-cracking and failure in short fiber-reinforced composites. **Journal of the Mechanics and Physics of Solids**, v. 137, p. 1-34, 2020.
- 150 JOBIN, G. et al. Behavior of plain concrete beam subjected to three point bending using concrete damaged plasticity (CDP) model. **Materials Today: Proceedings**, v. 4, p. 9742-9746, 2017.
- 151 TYSMANS, T. et al. Finite element modelling of the biaxial behaviour of high-performance fibre-reinforced cement composites (HPFRCC) using Concrete Damaged Plasticity. **Finite Elements in Analysis and Design**, v. 100, p. 47-53, 2015.
- 152 LI, X.; CHEN, J. An extended cohesive damage model for simulating multicroack propagation in fibre composites. **Composite Structures**, v. 143, p. 1-8, 2016.

- 153 HUANG, T.; ZHANG, Y. X. Numerical modelling of mechanical behaviour of engineered cementitious composites under axial tension. **Computers and Structures**, v. 173, p. 95-108, 2016.
- 154 JAVANMARDI, M. R.; MAHERI, M. R. Extended finite element method and anisotropic damage plasticity for modelling crack propagation in concrete. **Finite Elements in Analysis and Design**, v. 165, p. 1-20, 2019.
- 155 KUNIEDA, M. et al. **Fracture analysis of strain hardening cementitious composites by means of discrete modeling of short fibers**. VII International Conference of Fracture Mechanics on Concrete and on Concrete Structures (FraMCoS-7). S. Korea, 2010. 501-508 p.
- 156 KUNIEDA, M. et al. Tensile fracture process of strain hardening cementitious composites by means of three-dimensional meso-scale analysis. **Cement and Concrete Composites**, v. 33, p. 956-965, 2011.
- 157 BITENCOURT JR, L. A. G. **Numerical modeling of failure processes in steel fiber reinforced cementitious materials**. 2015. (PhD thesis). Structure Engineering, Universidade de São Paulo, São Paulo.
- 158 AFSHAR, A.; DANESHYAR, A.; MOHAMMADI, S. XFEM analysis of fiber bridging in mixed-mode crack propagation in composites. **Composite Structures**, v. 125, p. 314-327, 2015.
- 159 DASSAULT SYSTÈMES. **ABAQUS Analysis User's Manual** Providence, USA. v.6-14 2017.
- 160 LI, S.; SITNIKOVA, E. A critical review on the rationality of popular failure criteria for composites. **Composites Communications**, v. 8, p. 7-13, 2018.
- 161 BELYTSCHKO, T.; BLACK, T. Elastic crack growth in finite elements with minimal remeshing. **International Journal for Numerical Methods in Engineering**, v. 45, n. 5, p. 601-620, 1999.
- 162 ABDULLAH, N. A. et al. Transversal crack and delamination of laminates using XFEM. **Composite Structures**, v. 173, p. 78-85, 2017.
- 163 FERRETTI, D.; MICHELINI, E.; ROSATI, G. Cracking in autoclaved aerated concrete: Experimental investigation and XFEM modeling. **Cement and Concrete Research**, v. 67, p. 156-167, 2015.
- 164 AL HAMD, R. K. S. et al. **Crack propagation for concrete flat plates using XFEM method**. 9th International Conference on Fracture Mechanics of

- Concrete and Concrete Structures (FraMCoS-9). Berkeley, USA. May, 29 - June, 1, 2016. p.
- 165 WANG, H. W. et al. Application of extended finite element method in damage progress simulation of fiber reinforced composites. **Materials and Design**, v. 55, p. 191-196, 2014.
- 166 ZHANG, D.; WANG, Q.; DONG, J. Simulation study on CFRP strengthened reinforced concrete beam under four-point bending. **Computers and Concrete**, v. 17, n. 3, p. 407-421, 2016.
- 167 SWATI, R. F. et al. Extended finite element method (XFEM) analysis of fiber reinforced composites for prediction of micro-crack propagation and delaminations in progressive damage: a review. **Microsystem Technologies**, v. 25, n. 3, p. 747-763, 2018.
- 168 RUKAVINA, T.; IBRAHIMBEGOVIC, A.; KOZAR, I. Fiber-reinforced brittle material fracture models capable of capturing a complete set of failure modes including fiber pull-out. **Computers Methods in applied mechanics and engineering**, v. 355, p. 157-192, 2019.
- 169 BELYTCHKO, T.; GRACIE, R.; VENTURA, G. A review of extended/generalized finite element methods for material modeling. **Modelling and Simulation in Materials Science and Engineering**, v. 17, p. 1-24, 2009.
- 170 MAIMÍ, P. et al. **A thermodynamically consistent damage model for advanced composites**. National Aeronautics and Space Administration. 2006
- 171 CAMANHO, P. P.; MAIMÍ, P.; DÁVILA, C. G. Prediction of size effects in notched laminates using continuum damage mechanics. **Composites Science and Technology**, v. 67, n. 13, p. 2715-2727, 2007.
- 172 HILL, R. A theory of the yielding and plastic flow of anisotropic metals. **Proceedings of the Royal Society A**, v. 193, p. 281-297, 1948.
- 173 AZZI, V. D.; TSAI, S. W. Anisotropic strength of components. **Experimental Mechanics**, v. 5, p. 268-288, 1965.
- 174 HOFFMAN, O. The brittle strength of orthotropic materials. **Journal of Composite Materials**, v. 1, n. 2, p. 200-206, 1967.
- 175 TSAI, S. W.; WU, E. M. A general theory of strength for anisotropic materials. **Journal of Composite Materials**, v. 5, p. 58-80, 1971.

- 176 HASHIN, Z. Failure criteria for unidirectional composites. **Journal of Applied Mechanics**, v. 47, p. 329-334, 1980.
- 177 GU, J.; CHEN, P. Some modifications of Hashin's failure criteria for unidirectional composite materials. **Composite Structures**, v. 182, p. 143-152, 2017.
- 178 DUARTE, A. P. C.; DÍAZ SÁEZ, A.; SILVESTRE, N. Comparative study between XFEM and Hashin damage criterion applied to failure of composites. **Thin-Walled Structures**, v. 115, p. 277-288, 2017.
- 179 LUBLINER, J. et al. A plastic-damage for concrete. **International Journal of Solids Structures**, v. 25, p. 299-326, 1989.
- 180 LEE, J.; FENVES, G. L. Plastic-damage model for cyclic loading of concrete structures. **Journal of Engineering Mechanics**, v. 124, p. 892-900, 1998.
- 181 GENIKOMSOU, A. S.; POLAK, M. A. Finite element analysis of punching shear of concrete slabs using damaged plasticity model in ABAQUS. **Engineering Structures**, v. 98, p. 38-48, 2015.
- 182 CHI, Y. et al. Finite element modeling of steel-polypropylene hybrid fiber reinforced concrete using modified concrete damaged plasticity. **Engineering Structures**, v. 148, p. 23-35, 2017.
- 183 MIARKA, P.; SEITL, S.; CORTE, W. D. Notch tip displacements of the concrete Brazilian disc test with central notch analysed by the concrete damaged plasticity model. **Theoretical and Applied Fracture Mechanics**, v. 102, p. 122-150, 2019.
- 184 WALFORD, J. L. J. M. N. P. Q. B. A simplified model for withdrawal of screws from end-grain of timber. **Construction and Building Materials**, v. 29, p. 557-563, 2012.
- 185 LOVISA, A. C. et al. Characterising fatigue macrocrack initiation in profiled steel roof cladding. **Engineering Structures**, v. 125, p. 364-373, 2016.
- 186 MYURAN, K.; MAHENDRAN, M. Unified static-fatigue pull-through capacity equations for cold-formed steel roof battens. **Journal of Constructional Steel Research**, v. 139, p. 135-148, 2017.
- 187 SIVAPATHASUNDARAM, M.; MAHENDRAN, M. New pull-out capacity equations for the design of screw fastener connections in steel cladding systems. **Thin-Walled Structures**, v. 122, p. 439-451, 2018.

- 188 KHAN, M. **Load-sharing of toe-nailed, roof-to-wall connections under extreme wind loads in wood-frame houses**. 2012. (Master of Engineering Science). The University of Western Ontario, Ontario.
- 189 RILEY, M. A.; SADEK, F. **Experimental testing of roof to wall connections in wood frame houses**. National Institute of Standards and Technology. 2003
- 190 FOSCHI, R. O. **Modeling the hysteric response of mechanical connections for wood structures**. World Conference on Timber Engineering. Vancouver: University of British Columbia, 2000. p.
- 191 SHANMUGAN, B.; NIELSON, B. G.; PREVATT, D. O. Statistical and analytical models for roof components in existing light-framed wood structures. **Engineering Structures**, v. 31, n. 11, p. 2607-2616, 2009.
- 192 MORRISON, M. J.; HENDERSON, D. J.; KOPP, G. A. The response of a wood-frame, gable roof to fluctuating wind loads. **Engineering Structures**, v. 41, p. 498-509, 2012.
- 193 JI, X. et al. Vulnerability analysis of steel roofing cladding: Influence of wind directionality. **Engineering Structures**, v. 156, p. 587-597, 2018.
- 194 MAHAARACHCHI, D.; MAHENDRAN, M. Wind uplift strength of trapezoidal steel cladding with closely spaced ribs. **Journal of Wind Engineering and Industrial Aerodynamics**, v. 97, p. 140 - 150, 2009.
- 195 WOLFE, R. W.; MCCARTHY, M. **Structural performance of light-frame roof assemblies. Part I: Truss assemblies with high truss stiffness variability**. Forest Product Laboratory. Madison, USA. 1989
- 196 WOLFE, R. W.; LABISSONIERRE, T. **Structural performance of light-frame roof assemblies. Part II: Conventional truss assemblies**. Forest Products Laboratory. Madison, USA. 1991
- 197 MORRISON, M. J.; KOPP, G. A. Performance of toe-nail connections under realistic wind loading. **Engineering Structures**, v. 33, p. 69-76, 2011.
- 198 MAHAARACHCHI, D.; MAHENDRAN, M. A strain criterion for pull-through failures in crest-fixed steel claddings. **Engineering Structures**, v. 31, p. 498-506, 2009.
- 199 MYURAN, K.; MAHENDRAN, M. New test and design methods for steel roof battens subject to fatigue pull-through failures. **Thin-Walled Structures**, v. 119, p. 558-571, 2017.

- 200 MEGHLAT, E.-M. et al. A new approach to model nailed and screwed timber joints using the finite element method. **Construction and Building Materials**, v. 41, p. 263-269, 2013.
- 201 SATHEESKUMAR, N. et al. Finite element modelling of the structural response of roof to wall framing connections in timber-framed houses. **Engineering Structures**, v. 134, p. 25-36, 2017.
- 202 FONTENELLE, J. H. **Sistema de fixação e juntas em vedações verticais constituídas por placas cimentícias: estado da arte, desenvolvimento de um sistema e avaliação experimental**. 2012. (Master's dissertation). Universidade de São Paulo, São Paulo.
- 203 EQUITONE. **Planning & application guide**. MATERIALS, E. F. C. 2018.
- 204 CEMBRIT. **Cembrit facade on steel - Installation** 2019.
- 205 PLYCEM. **Installation guide for Tek Facade** 2019.
- 206 ETERNIT. **Soluções construtivas Eternit - Eterplac** 2017.
- 207 KNAUF. **Sistema de Fachada Knauf Aquapanel** 2018.
- 208 SAINT-GOBAIN BRASILT. **Manual de Montagem - Construções industrializadas com placa cimentícia**. SAINT-GOBAIN. São Paulo 2019.
- 209 CISER. **Catálogo de produtos** 2019.
- 210 ASTM - AMERICAN SOCIETY FOR TESTING AND MATERIALS. **ASTM D1037: Standard test methods for evaluating properties of wood-base fiber and particle panel materials**. West Conshohocken, PA, USA: ASTM: 31 p. 2012.
- 211 BATISTA, E. D. M. Effective section method: A general direct method for the design of steel cold-formed members under local-global buckling interaction. **Thin-Walled Structures**, v. 48, p. 345-356, 2010.
- 212 ABNT - ASSOCIAÇÃO BRASILEIRA DE NORMAS TÉCNICAS. **ABNT NBR 6023: Informação e documentação - Referências - Elaboração**. Rio de Janeiro: ABNT: 74 p. 2018.